Numerical and experimental study of boiling flows : Application to quenching

Charles Brissot

PSL UNIVERSITÉ PARIS

THÈSE DE DOCTORAT

DE L'UNIVERSITÉ PSL

Préparée à MINES Paris

Numerical and experimental study of boiling flows Application to quenching

–

Étude expérimentale et numérique des processus d'ébullition Application à la trempe

Soutenue par

Charles Brissot

Le 14 avril 2022

École doctorale n°364

Sciences Fondamentales et Appliquées

Spécialité

Mécanique numérique et Matériaux

Composition du jury :

Pr. Emmanuelle ABISSET-CHAVANNE Arts et Métiers ParisTech	*Rapportrice*
Pr. Alvaro COUTINHO Universidade Federal do Rio de Janeiro	*Rapporteur*
Pr. Médéric ARGENTINA Institut de Physique de Nice	*Président*
Pr. Asst. Guillaume LAJOINIE Université de Twente	*Examinateur*
Pr. Rudy VALETTE Mines Paris	*Directeur de thèse*
Pr. Elie HACHEM Mines Paris	*Directeur de thèse*

MINES ParisTech | PSL

À ma marraine Régine...

Acknowledgements

À Rudy, plus camarade que directeur, plus ami que collègue, plus enfant qu'adulte, un immense merci. Pour tes conseils avisés qui sont la source principale de la qualité de ce travail. Pour les nombreuses discussions (ou devrais-je dire disputes) scientifiques. Pour ton snobisme qui se transforme en exigence. Pour ton art théâtral de la dramaqueenerie qui réussira toujours l'exploit à la fois de me navrer, de me faire hausser les sourcils, de me faire rire et m'attendrir. Pour ton anticyclone capillaire. Pour ta mémoire de daurade méditerranéenne. Pour toutes ces discussions à rallonge, ces cas de conscience psychologiques, ces projets avortés pour renverser le grand patronat. Pour tous ces messages WhatsApp qu'on ferait mieux d'effacer. Pour notre combo rythmique qui n'a rien à envier à Paul Jackson et Mike Clark. Bon... un peu quand même, ok (boomer). Anyway, tu as grave de quoi être fier de ce que tu es et fais. Merci vieux con !

À Elie le boss, le bosseur, le provocateur, un grand merci. Pour ton suivi malgré mes échappées théoriques. Pour les nombreuses disputes (ou devrais-je dire discussions) scientifiques. Pour ta force de travail qui pourrait déplacer des montagnes dans l'intérêt de ses étudiants. Pour ton pragmatisme scientifique. Pour ta disponibilité dans les moments importants. Pour la confiance que tu m'as accordée. Pour ces délicieux barbecues libanais ! Bon vent sur la route du succès déjà bien tracée. J'espère que tu sauras rester à l'écoute et au service de ton entourage.

À Léa, la VRAIE stagiaire, un merci sincère. Pour ton énergie, ton soutien scientifique et ta sur-motivation sur cette collaboration. Pour ces sessions expérimentales déjantées. Pour cette voix fantastique qui fait vibrer le labo entier. Pour les after-works que je n'oublierai pas. La partie expérimentale de ces travaux de thèse te doit beaucoup, de même que ce que je suis devenu. Force, sagesse et courage pour ta carrière de chercheuse, j'ai pleinement confiance en ta capacité à te faire une place de renom. Et à Romain, soutien technique infaillible, un merci poilu ;p. Pour tes conseils d'expérimentateur avisé aux jeunes profanes que nous étions. Et pour ton talent photographique si précieux, you rocked !

À Lulu, mon colocataire de galère, initiateur de montagne, partenaire de râleries et de commérage, un merci profond. Pour l'ouverture au monde que tu proposes aux gens. Pour tes blagues (presques toujours) drôles et (parfois) fines. Pour cette motivation sans faille à partager tes passions. Pour ta générosité sans limite. Pour m'ouvrir les yeux sur d'autres horizons culinaires exotiques. Pour toutes ces discussions à rallonge, ces cas de concsience psychologiques, ces projets avortés pour renverser le grand patronat (j'ai l'impression de me répéter moi...). Je crois en toi, la route est presque finie ! Tu en ressortiras la tête haute, et tu trouveras ta voie mon Lulu, j'en suis convaincu. Et à Théophile, l'autre partenaire

des montagnes et des airs, l'ours au grand coeur, un merci chaleureux. Pour ces nombreux week-ends le nez en l'air et les pieds dans l'herbe (ou parfois l'inverse !). La vie est un pique-nique, et tu en es un très bel opinel bien aiguisé.

Aux zicos à qui j'ai cassé les oreilles: David, compagnon de la première heure, graine de compositeur aux multiples talents. Pardon pour ma trahison, on va mettre ça sur le dos des circonstances sanitaires ! Cynthia, pianiste électrique dont les doigts sont plus véloces que son (mon ?) rythme de parole. Pour toutes tes vannes, tes biscuits et autres attentions en période de rédaction, qui m'auront bien aidé. Et Anselmo, le seule vrai musicien parmi nous, l'homme serein, minutieux, perfectionniste. Si ta vie était un film, je l'appellerais "l'homme à la vanille". Tu auras décidément élevé notre niveau de jeu (et de blagues !). Merci à vous trois pour tous ces moments de bonheurs mélodieux. Musicalement votre !

À mes camarades de trempe: Ali tout d'abord, collègue de bureau chaleureux et convivial. Pour toutes nos discussions et débats scientifico-politico-religio-culturels. D'ici à ce que Luffy trouve le One Piece, on devrait avoir encore de quoi papoter ! Joe, l'homme parfait. Que dire de plus :). Que vienne le règne de la martensite ! Faudra que tu m'apprennes à jouer de la darbouka et du cajón. Ghaniyya, maîtresse des solveurs numériques, ta discrétion masque un beau tempérament et des valeurs qui mériteraient d'être connus de tous. J'espère qu'on aura réussi à te faire apprécier ton séjour dans le sud, loin de ton cercle rouennais. Sacha, la douceur et la bienveillance faite doctorante. Grâce à toi j'aime le café ! Pour tous ces dessins de soutien qui ensoleillaient mes journées ! À vous quatre, un merci en acier trempé !! Et puis à Rémi et Ramy, duo (comique ?) de voisins de couloir, vous qui avez aussi partagé les galères sur CIMlib et animé de nombreux débats politiques. Merci pour l'ambiance que vous avez apportée !

À tout le reste de la team UPR (franchement, j'en reviens pas que ça ait tenu cette histoire...), camarades de cafés, soirées, sorties montagnes, voyages...: Clément, pour ces soirées geek qu'on pouvait se permettre à l'époque, Yacine, pour ces soirées tout court (go go pour ton Capes), Mehdi, pour tes anecdotes qui animaient toujours nos discussions, Émile, pour nous initier aux sensations de la moto, Ichrak, pour cette année trop courte en ta pétillante compagnie, Tiphaine, pour cet amour partagé de la pâtisserie (merci pour la recette de l'amandine !), Coraline, pour être notre SAM sûre, Victor, pour ton art de la punchline (un jour je t'apprendrai à prononcer correctement "moins" :p). À vous tous, merci pour cette super ambiance étudiante qui aura repoussé encore un peu la sensation de devenir adulte et responsable.

Aux anciens qui m'ont montré la voie de la sagesse: Robinou et Jonathan, pour nos ronchonnements communs autour de repas ou jeux de société. J'ai vraiment passé un bien meilleur confinement grâce à vous deux ! Et puis quand on gratte votre vernis de râleurs, on se rend vraiment compte de quelles chouettes personnes vous êtes. Chachou et Gabriel, mes éternels "3ème année" qui m'avez initié aux joies de CIMLib, avant que Lucas ne vienne m'en élever au rang d'expert (merci pour m'avoir supporté malgré toutes ces questions à la limite du harcèlement :p), au point de moi-même y initier Giulia (j'espère que tu ne m'en veux pas trop pour ce cadeau), Émilie, pour tous ces thés partagés, cette boule à thé Pikmin si adorable, et autres joyeusetés dont ta seule bonne humeur rayonnante a le secret, et enfin Romain, pour ton soutien psychologique à distance après

nous avoir montré le difficile et rude chemin de la rédaction. Merci à vous pour toutes ces attentions !

Aux permanents qui ont aussi oeuvré à la bonne ambiance du labo: Jean-Luc, pour nos taquineries quotidiennes, Aurélien, pour toutes ces discussions scientifiques, culturelles et politiques diverses et variées, Franck, gloire aux nombres sans dimension :p, Florence, pour ton punch et ton positivisme à toute épreuve, Patrice, je te dirais ce que je pense du nucléaire après mon année au CEA haha, Edith, pour ton smile systématique de bon matin, Philippe, pour cette belle initiation à la théorie des instabilités, Arnaud et Francis pour la mise en place et le soutien technique sur la manip' expérimentale. Merci pour vos conseils et votre bienveillance !

À tous les autres doctorants, avec qui j'ai pu apprécier plus brièvement la merveilleuse compagnie: Hassan, Jeff, Aakash, Wassim, Marion et Marion, Thibault et Thibault, Laurianne, Georges, Kindness, Jen, Aurèle, Pablo, Adrien, Iman, Loris (et j'en oublie plein ...). Merci pour ces tranches de rire en votre compagnie, j'aurais volontier pris encore plus de temps pour mieux vous connaitre !

À mes camarades d'école avec qui j'ai tant vécu de choses incroyables par le passé. Citer toutes leurs qualités me prendrait beaucoup trop de pages en plus, il me faut me résigner à ne citer que leurs noms: Baptiste, Arnaud, Laurie, Tommy, Corentin, Billax, Barrou, Robin, Romain, Mathilde, Vincent, Lucas, Antoine. Tout de même une mention spéciale à Aurel qui aura aussi traversé cette épreuve qu'est la thèse avec bravoure avant moi, et à Dog et Marin (force à toi pour ta soutenance prochaine, #709forever) qui l'auront traversée en même temps que moi. Merci pour tous nos échanges à distance, et vos nombreux accueil à Paris. Quelle bénediction que ce Slack pour garder contact, j'ai l'impression de ne jamais vous avoir quittés. Ça m'aura vraiment soutenu durant ces trois ans. Vous êtes tous de belles personnes, le sang des Mines.

À mes camardes de prépa aussi: Valou, Nico, Maxou, Clément, Keivan, Justine, Robin, Quentin, Simon, avec qui j'ai traversé une autre catégorie d'épreuve. Merci pour tous ces beaux moments passés ensembles, qui m'auront forgé pour affronter sereinement la thèse. Et à mes camarades de lycée: Bobo, Pierre, Julien, Corentin, Théotim, qui ont vu naître en moi ma vocation de scientifique. Merci pour cette amitié qui tient le coup malgré le temps qui file.

Et enfin le meilleur pour la fin, à ma famille. Mes oncles et tantes: Philippe, Céline, Sussu, Chantal, et les cousins cousines: Julien, Marie, Lucie, Adri, Chacha, Nana et Cloclo, aux côtés de qui j'ai passé de nombreux été dans la peau d'un gosse épanoui. Mes papi mamie de Lanau, encore bien vaillants et que j'embrasse tendrement, et mamie de Bédoin, qui j'espère garde quelques souvenirs de moi malgré son Alzheimer bien établi. Et pour finir mes deux soeurs, Zozo et Coco, et mes parents, toujours là pour moi, dont cet ingrat de fils ou de frère ne dit jamais assez à quel point il les aime.

Contents

Nomenclature

Variables

t	Time (s)
$\vec{u}$	Velocity vector ($\mathrm{m\,s^{-1}}$)
$\vec{u_\mathrm{I}}$	Interface velocity vector ($\mathrm{m\,s^{-1}}$)
p	Pressure (Pa)
T	Temperature (K)
e	Specific energy ($\mathrm{J\,m^{-3}}$)
h	Specific enthalpy ($\mathrm{J\,m^{-3}}$)
q	Conductive heat flux ($\mathrm{W\,m^{-2}}$)
q_R	Radiative heat flux ($\mathrm{W\,m^{-2}}$)
$\vec{\dot{m}}$	Surface mass transfer rate vector ($\mathrm{kg\,m^{-2}\,s^{-1}}$)
$\vec{\gamma_\alpha}$	Surface tension vector ($\mathrm{J\,m^{-2}}$)
$\boldsymbol{\sigma}$	Cauchy stress tensor (Pa)
$\boldsymbol{\tau}$	Viscous stress tensor (Pa)
$\dot{\boldsymbol{\varepsilon}}$	Strain rate tensor ($\mathrm{s^{-1}}$)
h_HTC	Heat transfer coefficient ($\mathrm{W\,m^{-2}\,K^{-1}}$)

Material properties

ρ	Density ($\mathrm{kg\,m^{-3}}$)
η	Dynamic viscosity (Pa s)

ν Kinematic viscosity ($\mathrm{m^2\,s^{-1}}$)

c_p Specific heat capacity at constant pressure ($\mathrm{J\,kg^{-1}\,K^{-1}}$)

k Thermal conductivity ($\mathrm{W\,m^{-1}\,K^{-1}}$)

D Thermal diffusivity ($\mathrm{m^2\,s^{-1}}$)

T_sat Saturation temperature of the fluid at atmospheric pressure (K)

$\mathcal{L}$ Specific enthalpy of vaporization at saturation temperature ($\mathrm{J\,kg^{-1}}$)

γ_0 Surface tension coefficient ($\mathrm{J\,m^{-2}}$)

α_T Thermal expansion coefficient ($\mathrm{K^{-1}}$)

ε Emissivity ($\mathrm{K^{-1}}$)

Thermal parameters

$\Delta T_w = T_w - T_\mathrm{sat}$ Overheating (K)

$\Delta T_\infty = T_\infty - T_\mathrm{sat}$ Subcooling (K)

Physical constants

g Gravitational acceleration ($9.81\,\mathrm{m\,s^{-2}}$)

σ_SB Stefan-Boltzmann constant ($5.67\times10^{-8}\,\mathrm{W\,m^{-2}\,K^{-4}}$)

Vapour film and bubble characteristics

e Vapor film thickness (m)

λ Interface wavelength (m)

v_r Interface wave velocity ($\mathrm{m\,s^{-1}}$)

f Frequency (Hz)

Dimensionless number

Re Reynolds number

Nu Nusselt number

Pe Péclet number

Pr	Prandtl number
Ra	Rayleigh number
Gr	Grashlof number
Ja	Jakob number
Bi	Biot number
Ma	Mach number

Indices

L	Liquid
V	Vapor
S	Solid
w	Wall
min	Minimum value
max	Maximum value
CHF	Critical Heat Flux
MHF	Minimum Heat Flux
ONB	Onset of Nucleate Boiling
c	Characteristic
exp	Experimental
eq	Equivalent

Mathematical and Geometric functions

$\vec{x}$	Position vector (m)
x, y, z	Cartesian coordinate (m,m,m)
r, θ, z	Cylindrical coordinate (m,rad,m)
$\vec{n}$	Normal vector of the liquid-vapor interface

d Distance function (m)

α Level Set function (m)

H_α Heaviside function

δ_α Dirac function (m^{-1})

κ_α Curvature (m^{-1})

ε Characteristic length of the smoothed interface (m)

$\vec{\nabla}$ Gradient operator

$\vec{\nabla}\cdot$ Divergence operator

Δ Laplace operator

$\mathbb{1}$ Identity tensor

$\mathcal{S}$ Surface (m^2)

$\mathcal{V}$ Volume (m^3)

$\mathrm{d}S$ Infinitesimal surface (m^2)

$\mathrm{d}V$ Infinitesimal volume (m^3)

Numerical parameters

h Mesh size (m)

Δt Time step (s)

Chapter 1

Introduction

Contents

Résumé en Français

Ce chapitre présente le contexte général de la thèse. Le développement de la trempe s'intègre dans un long processus d'amélioration des connaissances et techniques des humains en matière de travail des métaux. Ces progrès sont d'ailleurs intimement liés aux développements économiques des sociétés préhistoriques. La trempe, permettant d'aboutir à des composés métalliques de meilleure qualité et aux propriétés mécaniques intéressantes, a principalement servi à la confection d'armes plus robustes, avant d'être plus récemment employée pour tous types de pièces subissant des contraintes importantes. C'est le cas par exemple de certains composants de machines tournantes comme les turbines ou les moteurs.

Une trempe peut être réalisée dans un gaz ou un liquide. Dans les deux cas, une première approche pour étudier le comportement thermique de la pièce trempée consiste à considérer un coefficient d'échange thermique qui modélise le comportement du fluide aux bords de la pièce. Cette approche permet une première estimation du refroidissement de la pièce. Cependant elle souffre de biais importants notamment dans le cas d'une trempe liquide, où l'ébullition du fluide met en jeu des phénomènes transitoires multi-échelles complexes non représentés par le coefficient d'échange.

L'ébullition est décrite via la courbe d'ébullition par quatre modes (classés par température croissante) : la nucléation partielle et la nucléation complète sont très efficaces pour dégager de l'énergie, et existent jusqu'à une température critique associée à un flux critique très intense (OdG $10^6\,\mathrm{W\,m^{-2}}$). À plus haute température, le dégagement plus important de vapeur rend le transfert thermique moins intense (mode d'ébullition transitoire). Au-delà de la température de Leidenfrost, un film de vapeur permanent recouvre la pièce (mode de caléfaction). Cette description simplifiée donne un aperçu général de l'ébullition, mais différents paramètres viennent complexifier les phénomènes et changer les températures et flux en jeu: la nature du fluide, la température du fluide, l'état de surface du solide, la géométrie de la surface, l'agitation forcée dans le fluide, etc.

Face à cette complexité, la simulation numérique a émergé comme une alternative pour décrire les phénomènes en jeu. Différentes approches existent dans la littérature concernant le traitement numérique des équations physiques, les manières de représenter les interfaces et de gérer les transitions des quantités physiques à travers ces interfaces. L'approche de cette thèse est alors détaillée pour présenter les choix de modélisation, leurs performances et leur applicabilité.

1.1 The quenching process

1.1.1 Origins of quenching

Crafting metallic items have been linked to the history of humankind for millennial as tools are central in the development of human civilisations. Metal casting and work have been related to technological breakthroughs to a point that development of bronze and iron metallurgy gave their names to ages of civilisation developments.

The development of copperworks and tinworks during the Neolithic is usually dated to around -3000 BC [1], though debated findings may link its appearance to periods as far back as the -5000 BC [2]. The period of major spreading of bronze depends on the location around the globe. It played a major role in the development of humanity as the master of bronze crafting gave the advantage of better weapons and tools, but also shaped society structures, trade and the spread of art and cultures. Trade related to bronze items like the pin shown in Figure 1.1 allowed developments of rich communities that had copper and tin available on their ground, or that were advanced in blacksmith techniques. For example, in Europe the spread of bronze lead to the creation of a tangle network of trade routes, as well as the emergence and collapse of elites from 2500 to 1600 BC [1]. Iron melting might

Figure 1.1: Bronze pin for clothes from around 1000 BC (from Inrap [1]).

Figure 1.2: Double quenched katana with "Hamon Notare" finition (from Géry PARENT).

have been first developed by proto–Hittites in 2200–2000 BC in Turkey, near the plateau of Anatolia and then spread among the Hittite elites in 1400–1200 BC in the Middle East [3]. The appearance of iron signed the end of bronze dominance in many civilisations near 1000 BC and signed another important change of social and trade structures. This change of paradigm is however not universal. For example, Chinese populations never really replaced bronze until the emergence of imperial dynasties. Iron was available in larger quantities in European soils, leading to the collapse of current trade routes. Crafting became a full time occupation, and the first European state structures emerged [1]. Weapons began to replace imported items such as jewellery as a symbol of power.

With iron crafting came quenching. This is the process of plunging a hot metallic part into a cooling fluid to obtain beneficial changes of microstructure. Blacksmiths discovered the improvement of material structures by the mixing of iron and carbon

that resulted in steel. Its material properties could be improved by heat treatment processes that were first dedicated to weapons like swords [4]. The first known mention of quenching is given by Homer (-800 BC), but it may have been developed earlier [4]. Though theoretical knowledge of microstructure have only been developed in the middle of the nineteenth century, blacksmiths already had notions of toughness and hardness, and soon began to developed empirically quenching techniques to improve material qualities [4]. Different quenching fluids were mentioned, like water but also urine, blood or vinegar. For some applications clay was used to quench separately different part of weapons, as it is the case for the crafting of Japanese blades (see Figure 1.2). From these ancient days until the end of the Middle Age period, few mentions of quenching processes are available. The art of quenching requires rich knowledge and practice, hence intellectual property might be the main reason why the literature is not exhaustive at this time.

1.1.2 Benefits of quenching

The organisation of atoms of carbon and iron inside steel as well as their proportions lead to different material qualities. The stable states of carbon iron mixture can be represented thanks to phase diagrams (see Figure 1.3). At high temperature (around 800–1000 °C depending on the carbon concentration), the iron crystal form (γ) gives space for inclusions of carbon atoms. It is thus easy for carbon atoms to diffuse inside steel and being integrated in the crystalline network. This is called austenite. At low temperature, the configuration of iron crystal (α) gives little space to carbon atoms, leading to a hard diffusion of carbon. This phase is ferrite. Moreover, the carbon precipitates with iron to become cementite (Fe_3C) [5]. The mixture of ferrite and cementite is called perlite.

As diffusion of carbon atoms is not possible at ambient temperature, inclusion of carbon must be done at high temperature. However, if the metal is slowly cooled, carbon atoms have time to migrate and precipitate into cementite. The mechanical properties of perlite are not very interesting as it contains defaults and grains making the metal fragile and not so hard. To prevent the precipitation of carbon, the solution is to move out of the thermodynamic state by a rapid cooling as shown in Figure 1.4. Doing so, carbon atoms do not have the time to diffuse, and are still properly dispersed inside iron, resulting in a new configuration: martensite. This configuration reveals very interesting properties as it is twice to four time as hard as perlite [6]. The rapid cooling is possible thanks to quenching.

1.1.3 Modern industrial practices

Nowadays, quenching has evolved with technological improvements. Manufacturers are increasingly keen to control their manufacturing processes, in order to improve

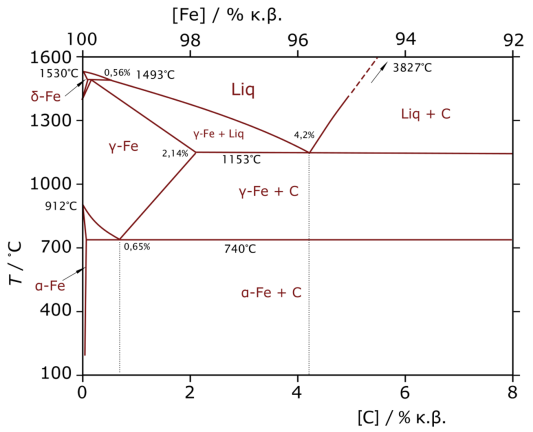

Figure 1.3: Iron Carbon phase diagram. At high temperature and low carbon concentration, the austenite phase is stable. However, if this phase is cooled down slowly, it turns into perlite. The desired martensite phase is not on this graph as it is not a thermodynamical optimum (from MARKELLOS).

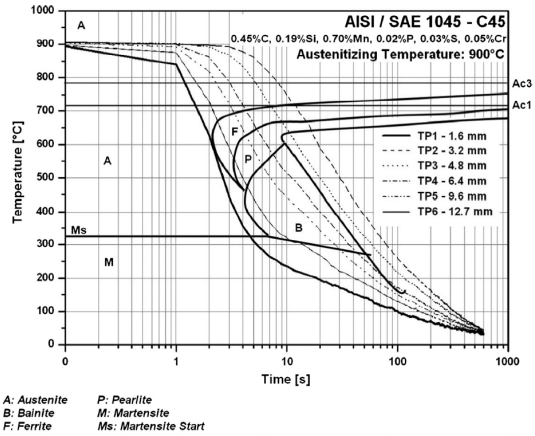

Figure 1.4: An example of Continuous Cooling Transformation diagram. If the cooling time is slow, the state line goes through the Perlite state. If the cooling time is fast, it passes only trough Austenite and Martensite states, which is stable at low temperature though not the thermodynamical optimum (from [6]).

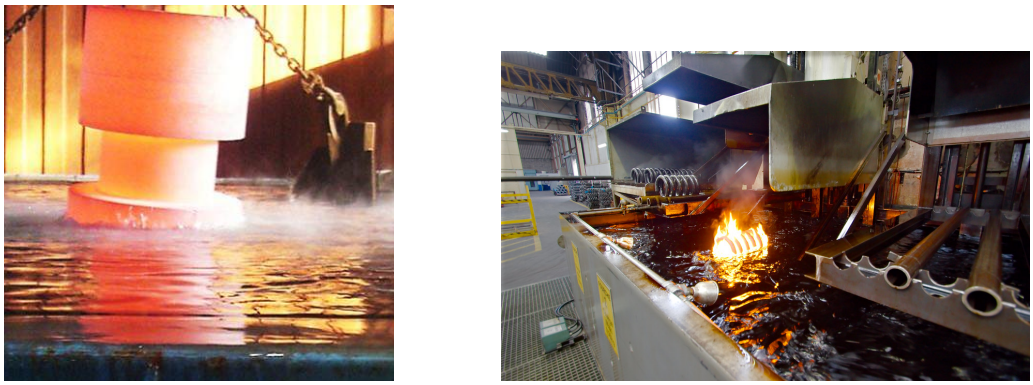

(a) Industrial quench of a hollow cylinder. *(b) Industrial quench of a metallic spring.*

Figure 1.5: Examples of industrial quenches.

performance, quality and reduce production costs. A large panel of metallic parts are quenched from engine turbine blades to nuclear reactor vessels (see Figure 1.5). Industrial furnaces ensure high initial temperatures (around 1000 °C) with good precision. Gas coolants are mostly air or nitrogen, and liquid coolants are mostly water or organic oils. A good control of quenching is essential to correctly control the phase changes that take place within the alloy, and thus the microstructure.

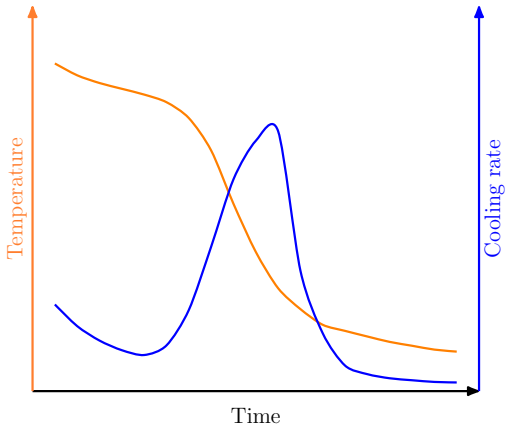

Figure 1.6: Typical temperature and cooling rate evolution during a quench. The cooling rate is moderate during the calefaction mode. Then a sudden increase is observed due to the nucleate boiling mode that drasticaly reduces the temperature. Finaly, the part cools down with a slow rate in natural convection.

Different parameters are controlled by the manufacturers, such as the quenching time, the chemical and thermal qualities of the coolant, or the number and arrangement of parts quenched together. The main factor to ensure the quality of the microstructure is the cooling rate of the part. Other secondary factors, such as the deformation or residual stresses experienced by the part are also monitored. The cooling rate is strongly conditioned by the behavior of the fluid that surrounds it and extracts heat from it. In this study we are interested in liquid coolants that can evaporate on contact with the hot part. These boiling phenomena have a critical influence on the heat transfer. Figure 1.6 shows a classical cooling curve for a liquid quenching. The cooling rate is not constant and usually presents a peak at a certain surface temperature.

The orders of magnitude of the temperatures involved imply boiling phenomena during the majority of the process. The last part of the quench is only driven by convection. This is mainly true for water whose saturation temperature is low in regard to organic oils' ones. Understanding boiling is therefore crucial to properly control the quenching process.

1.1.4 Heat Transfer Coefficient

1.1.4.1 Definition of the HTC

In order to monitor the cooling rate of every industrial part, two solutions exist. A priori approximations thanks to models, and a posteriori estimations thanks to experiments.

Although this process is ancient, many questions still remain open and the a priori estimation is a delicate task. Even today, when a new part is produced, a lot of experimental tests are carried out in order to adjust the quenching parameters to cool the part properly. However, these tests are long, expensive and not always scalable. This is the case whatever the coolant nature, but it is especially true when the coolant can vaporise. Convection and boiling phenomena being relatively chaotic and complex to understand, heat transfers between a solid and a fluid are always difficult to estimate. It is therefore customary to use a Heat Transfer Coefficient (HTC) model:

$$q_w = h_{\mathrm{HTC}} \Delta T_w \tag{1.1}$$

where $\Delta T_w = T_w - T_{\mathrm{sat}}$ is the overheating. T_{sat} is the saturation temperature of the coolant at a given pressure. Depending on the modeling choices, ΔT_w can be replaced in (1.1) with $\Delta T_w + \Delta T_\infty = T_w - T_\infty$ where T_∞ is the liquid temperature far away from the part and ΔT_∞ is the subcooling. Doing so, h_{HTC} integrates the effects of the fluid temperature.

h_{HTC} is a coefficient averaged over a given surface, whose characteristic size is large compared to the scale of convection or boiling phenomena. This consideration allows to strongly reduce the complexity of the modeling. Depending on the degree of simplification, the HTC is or is not temperature dependent.

Although this formulation by an equivalent HTC is not recent in the case of quenching, manufacturers still use this model to characterise the cooling of parts (see for example, [7] in the context of heat treatments of Zirconium and Hafnium alloys). For a given part and a given quenching configuration, the knowledge of the HTC allows to trace the temperature evolution of the part, and thus to know its micro-structural characteristics.

The major problem with such model is that the HTC expression is not known a priori. It varies depending on the quenching conditions, the geometry of the part, the nature of the fluid, etc. In the literature, some tests performed on similar reference samples allow estimations of HTC values. These tests can give first order approximations, but the samples in the literature often have simple geometries far from the complex ones of industrial parts. Moreover the quenching conditions are not flexible. Thus industrials often have to carry out tests and deduce from them the HTC with an inverse method. This second solution is more accurate but quite expensive as it requires some iterations. Furthermore it remains case dependent and only relevant for one set of quenching parameters.

1.1.4.2 HTC estimation

A quenching test consists of temperature measurements at different points of the quenched sample. The estimation of the heat exchange and temperature profile

at any point of the part is therefore an inverse problem. On the one hand, the experiments leads to temperature data points plotted against the time ${T^{\text{mes}}}_i(t)$. On the other hand, a conduction model allows to compute the temperature evolution $T(\vec{x},t)$ of sensors located at position $\vec{x}_i$ for a given HTC that can be time and space dependent. The inverse problem consists in finding the best HTC function to fit the experimental results: ${T^{\text{mes}}}_i(t) \simeq T(\vec{x}_i,t)$. For example, Archambault et al. [8] explained the procedure in the case of the quench of a long metallic cylinder. The conduction model in cylindrical coordinates (r,ϑ,z) for an infinitely long cylinder reads :

$$\rho_{\text{S}} c_{\text{PS}} \frac{\partial T}{\partial t} = \frac{1}{r}\frac{\partial}{\partial r}\left(r k_{\text{S}} \frac{\partial T}{\partial r}\right) + \dot{Q}(r,t) \tag{1.2}$$

with ρ the density, c_{P} the specific heat capacity, k the thermal conductivity and the subscript S that stands for the solid properties. $\dot{Q}(r,t)$ is a volume heat source that can exist in the case of phase transformations inside the metallic part. If R is the radius of the cylinder, then the HTC to be estimated reads :

$$h_{\text{HTC}} = \frac{q_w}{\Delta T_w} = \frac{k_{\text{S}}}{\Delta T_w}\left(\frac{\partial T}{\partial r}\right)_{r=R} \tag{1.3}$$

More details on the mathematical aspect of the method are available in [8].

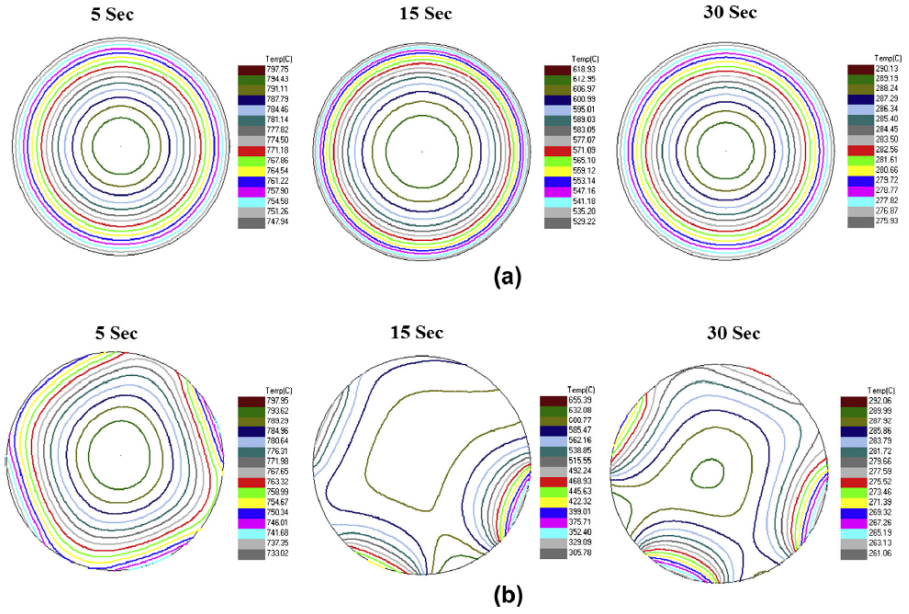

Figure 1.7: Evaluation of the temperature field within a quenched cylinder by inverse method, with a single global heat transfer coefficient (top), or with a separation into eight distinct thermal boundaries (bottom) (from [9]).

Ramesh et al. have presented a list of similar existing methods [9]. The vast majority is based on the estimation of a single global HTC. More recent methods propose localised HTC by partitioning the surface of the quenched part.

1.1.4.3 Weaknesses and biases

The general observation is that the best performing methods are very efficient for parts with simple geometries, such as cylinders (see [8, 9, 10, 11]). For example, Archambault et al. [8] succeeded in obtaining temperature evolution with errors not exceeding 0.1 %. However, it is specified that deviations are observed as soon as the geometry becomes more complex or if the sensors are improperly distributed. Sugianto et al. [11] also explained that the method works better in uniform cooling when the HTC is constant. Buczek et al. [10] observed that the method is more effective for oil quenching than for water quenching, which is more "brutal".

The presence of all the boiling modes at the same time brings great spatial disparities in heat transfer [12]. The global HTC description is then much less robust than that by local HTC. Sugianto et al. [11] showed that errors of the method with local HTC estimations are strongly reduced. Ramesh et al. [9] had the same conclusions and obtained up to 100 K difference between the two methods. Notably, even on a symmetric cylinder, they obtained asymmetric cooling results, which would not be modeled by a global HTC (see Figure 1.7).

Another problem raised by Srinivasan et al. is that this method generally relies on the solution of an "ill-posed" problem [13]. Depending on the geometry of the part and the position of the sensors, there is no guarantee that the solution is unique. In addition, it is usually difficult to get data in this environment, especially for complex parts. Desalos et al. [14] drew attention to the reproducibility of the quenching conditions between tests and production, not to mention the presence of sensors that disturb the part's thermics and the behavior of the fluid around it. Finally, this method remains in all cases totally dependent on the thermal evolution model of the part used, from which other errors may come. For all these reasons, the comprehension of boiling is of high interest to better assess the value of this HTC.

1.2 Boiling

1.2.1 Boiling curve

The boiling process on a surface w (or "wall") can be studied by different approaches. The most common one is to look at the surface heat flux q_w relative to a given overheating $\Delta T_w = T_w - T_{\text{sat}}$. This is the temperature difference between the hot surface and the saturation temperature of the fluid. The Jakob number $\text{Ja} = c_{\text{PV}} \Delta T_w / \mathcal{L}$ can

also be considered to scale with ΔT_w, but this is rarely done in practice in the literature. L and V subscripts stand for the liquid and the vapour phase respectively. $\mathcal{L}$ is the latent heat of vaporisation at a given pressure, in general the atmospheric pressure. The study of q_w versus ΔT_w leads to the boiling curve described by Figure 1.8. It is also called the Nukiyama curve in reference to the pioneer work of Nukiyama in 1934. He first described the four different modes of boiling [15] (orders of magnitude of temperatures and heat fluxes are given for saturated water on a horizontal heater):

(1) **Partial nucleate boiling:** ΔT_w from 5 to 10 K, q_w from 10^3 to 10^5 W m^{-2} (see Figure 1.9a). The first part of boiling, when small vapour bubbles form on preferential sites of the wall. They evacuate successively in the form of strings once the critical size is exceeded. It should be noticed that this mode does not start at $q_w = 0$ K but at the Onset of Nucleate Boiling (ONB) T_{ONB}. A sufficient amount of liquid must be superheated in a thermal layer close to the wall to exceed the energy barrier preventing the bubbles to form. For very low overheating, this is a superheated pure convection system (area (0) in Figure 1.8).

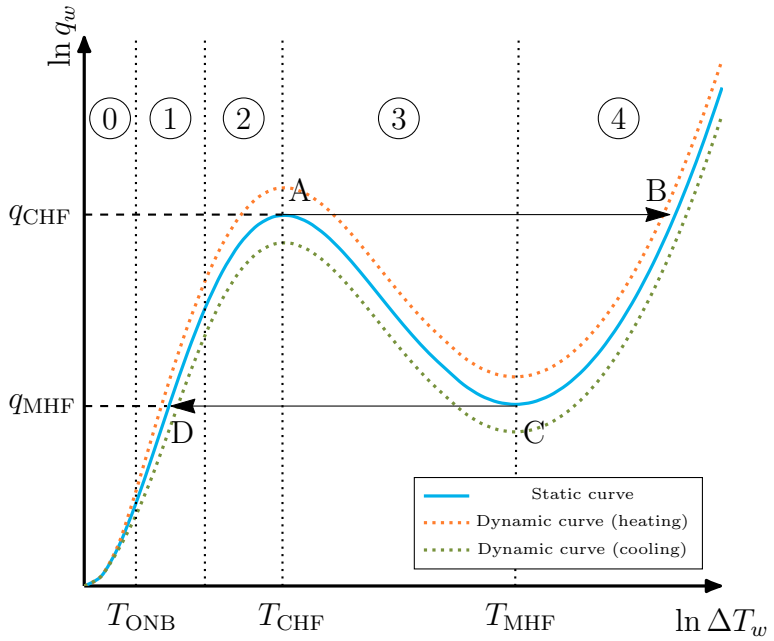

Figure 1.8: The boiling curve. The liquid is supersaturated (0) before the Onset of Nucleate Boiling. Nucleate boiling starts with partial (1) and fully developed (2) mode until it reaches the Critical Heat Flux (point A). Then the heat flux decreases during transition boiling (3) to reach the Minimum Heat Flux (point C). Then calefaction (4) starts and the heat flux increases slowly until radiation takes the lead at very high temperatures.

(2) **Fully developed nucleate boiling:** ΔT_w from 10 to 30 K, q_w from 10^5 to 10^6 W m^{-2} (see Figure 1.9b). The heat transfer is important enough for boiling to develop on most of the surface. The vapour bubbles are mobile, merge and create unstable mushroom-type vapour bulges or vapour stems. They break away from the surface in a chaotic manner. This is the main efficient cooling mode. The point of maximum heat flux is called Critical Heat Flux (CHF) q_{CHF} linked to the CHF temperature T_{CHF} (point A in the Figure 1.8).

(3) **Transition boiling:** ΔT_w from 30 to 300 K, q_w from 10^6 to 10^4 W m^{-2} (see Figure 1.9c). The boiling is so significant that in some places the water vaporises before it touches the hot surface. A partial vapour film begins to form. As the vapour has a lower conductivity, this reduces the heat transfer that results in a negative slope on the boiling curve (see the portion between points A and C in Figure 1.8). The point when all the vapour covers the heater surface is called the Minimum Heat Flux (MHF) q_{MHF} or sometimes the Leidenfrost heat flux linked to the Leidenfrost Temperature T_{MHF}. This is in reference to the Leidenfrost effect where a small drop of water levitates on a vapour cushion over a sufficiently warm heater [16].

(4) **Calefaction or film boiling:** ΔT_w above 300 K, q_w slowly rising from 10^4 W m^{-2} with temperature (see Figure 1.9d). Heat fluxes are significant enough to prevent permanent liquid contact with the wall. Thus a continuous vapour film covers the entire surface. The vaporisation takes place directly at the interface between the film and the liquid. At its creation, the film thickness is of the order of the millimeter.

The entire curve is observable providing a proper control of the wall temperature. This is the case in most of the studies where stationary flow and temperature are considered. The shape of the curve is the same whether the surface is progressively heated or cooled. However, transient phenomena can displace the curve when the temperature variation time is shorter than the relaxation time of the system. Auracher et al. [20] experimentally showed that in heating, the observed heat fluxes are more important than in stationary as shown in Figure 1.8. In cooling, it is the opposite, the fluxes are lower. A deviation of ±25 % is observed for fluorinated coolant (FC-72) at atmospheric pressure with a 4 K/s heating, and this increase can be up to ±300 % with heatings of around 50 K/s. Baudin [21] had the same conclusions and observed that the heating speed profile also had an impact on the temperature of shifting of boiling modes. A ramped heating tends to increase the start temperature of the calefaction mode (point C on Figure 1.8).

If the heat flux is controlled instead of the temperature, a hysteresis phenomenon appears linked to the transient boiling mode. This latter is indeed unstable for such configurations due to the negative slope of the boiling curve. A slight increase in

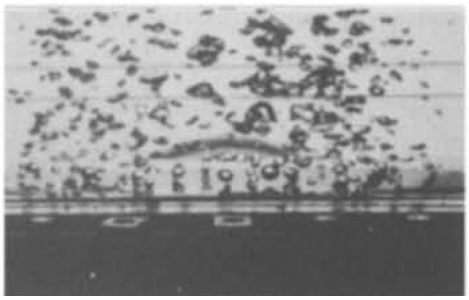

(a) Partial Nucleate Boiling on a vertical plate (from [17])

(b) Fully Developed Boiling on a vertical plate (from [17])

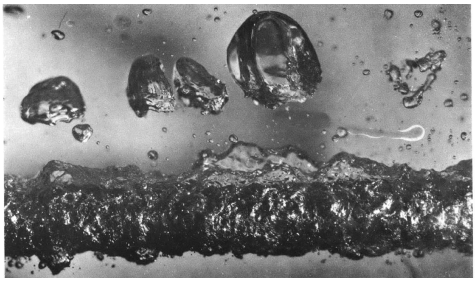

(c) Transition Boiling on a wire (from [18])

(d) Calefaction under a water drop over a heater (from [19])

Figure 1.9: Experimental view of each boiling mode.

the heat flux leads to a degradation of the cooling. The heater then receives more heat than it transfers to the fluid, increasing the temperature and degrading even more the cooling. If the temperature is increased, the system passes rapidly from the CHF to the film boiling of equivalent heat flux (from A to B on Figure 1.8. This phenomenon is called the boiling crisis or the burn out and is usually avoided in industrial processes as it leads to very high temperatures. Conversely during a cooling, the system quickly passes from the MHF to the partial nucleation point at equivalent heat flux (from C to D on Figure 1.8).

The quenching process is concerned by these two phenomena as explained by Murry [22]. This is indeed a transient process with modes going from the film boiling to the nucleation modes. The temperature variation of the metallic part can be very sudden, leading to a degraded cooling in comparison to the static boiling curve. And as the system cools down, the hysteresis leads to a transition from calefaction to nucleate boiling with an intense cooling rate. This explains the general form of the cooling curve represented in Figure 1.6, with a sudden decrease in temperature and a heat flux peak. Before this transition, the cooling rate is small due to the vapour film that insulates the part from the liquid. After the transition, the cooling rate is moderate as the overheating is small. The cooling is completed by the nucleation

mode and finally by pure convection until thermal equilibrium is reached. This is a simplified view of the reality, as several modes can be present at the same time during quenching. Most of the time, the vapour created from the bottom rises and feeds vapour films of the upper parts. Thus film boiling is more stable at the top and thus the Leidenfrost temperature is lower, delaying the apparition of wetting [12]. For moderate subcooling, this creates a vapour film front separating the nucleate boiling at the bottom and the calefaction at the top, as shown in Figure 1.10 [23, 9]. The cooling rate peak happens at different times depending on the location of the observed point, and is correlated with the film front location that moves with moderate speed. Ramesh et al. [9] found values around $5\,\mathrm{mm\,s^{-1}}$ for an Inconel probe quenched in mineral oil. However for very high subcooling or small parts, the wetting is a violent transition that happens at the same time over the entire part [24].

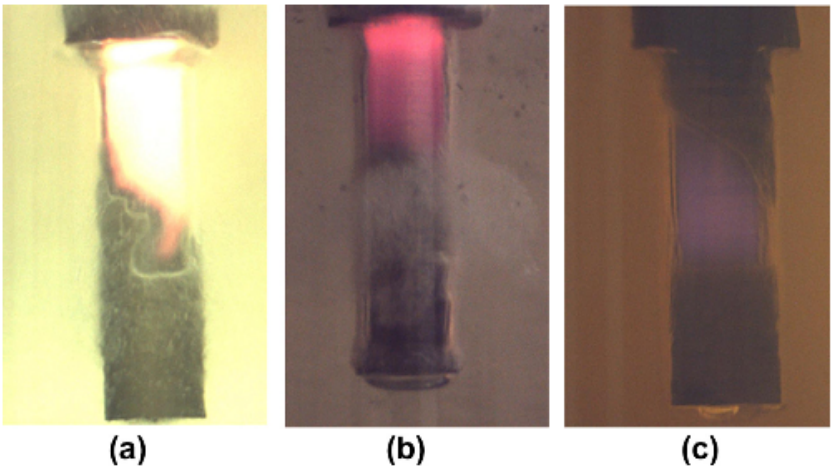

Figure 1.10: Pictures of vapour film fronts from Inconel probe quenched in (a) water, (b) aqueous polymer solution and (c) mineral oil (from [9]).

1.2.2 Influential factors

Boiling is usually characterised as a function of the overheating, but there are many other parameters involved such that:

- **Subcooling** $\Delta T_\infty = T_{\mathrm{sat}} - T_\infty$: This is the temperature of the liquid away from the heater. Large subcooling tends to increase the heat flux whatever the boiling mode. This is not surprising as the liquid is expected to consume a part of the heat delivered by the heater. Large subcooling then naturally raises q_{CHF} and T_{CHF} as well as q_{MHF} and T_{MHF}. In the context of quenching, this

means that the cooler the pool and the faster the film breaks. For example, in the experiment of Ebrahim et al. [25] where an Inconel-600 cylinder is quenched, the overheating at which the vapour film breaks increases from 250 to 450 K between subcooling of 2 to 30 K. This observation is confirmed by other authors [26, 24] and Ikkene et al. [27] that reported Leidenfrost temperatures above 800 °C ($\Delta T_w = 700$ K) for very high subcoolings ($\Delta T_\infty = 80$ K). Jouhara et al. [24] observed that the vapour film breakage nature was different depending on the subcooling. The wetting front was only possible for moderate subcoolings. For very high subcoolings, an explosive wetting was observed, meaning that the entire heater was wetted at the same time.

- **Fluid characteristics** like the density ρ, the specific heat capacity c_p, the thermal conductivity k, the dynamic viscosity η and the vaporisation temperature T_{sat}: the latter obviously shifts the boiling curve for a given overheating. Larger viscosities η_L and η_V lead to larger viscous stresses that prevent the liquid to replace the vapour at the surface of the heater. This decreases T_{CHF} and T_{MHF}. Larger volume heat capacities $(\rho c_p)_L$ and $(\rho c_p)_V$ imply that the fluid stores more energy per unit volume at a given temperature. Therefore it heats up more slowly, increasing the cooling rate. Higher conductivities k_L and k_V allow the fluid to release heat more quickly away from the part, also increasing heat transfers. Buczek et al. [10] highlighted these latter conclusions by using two oils with different characteristics. However a higher k_L might lower T_{MHF} as the vapour film is less insulating and can accept higher heat fluxes for lower overheating.

- **Wettability and surface roughness**: the roughness facilitates nucleation by providing more bubble nucleation sites and the wettability increases T_{MHF} facilitating permanent solid liquid contacts. Ebrahim et al. [25] quenched cylinders of different natures: stainless steel (SS), zirconium-702 (Zr) and Inconel-600. SS and Zr samples have similar effusivities, but the Zr sample wets better with a 20° difference in wetting angle. This leads to a q_{CHF} twice higher regardless of subcooling. As for T_{MHF}, it is higher for the Zr sample, especially at high subcooling. In general, a strong correlation is observed between the surface condition of the part and the heat transfer. Heat transfer is more important on the wetted zones. Auracher et al. [20] showed for example that a deposit on the surface of the hot plate shifts the Nukiyama curve to the right. Vakarelski et al. [28] pushed further the analysis with superhydrophobic and superhydrophilic samples. They showed that for superhydrophobic surfaces, the calefaction mode was the only boiling regime even for very low overheatings. For superhydrophilic surfaces, the considered range of temperature (up to 800 °C) did not allow the authors to observe the calefaction mode

(see Figure 1.11). This suggests that whatever the temperature of the solid, wetting effects always exist even during calefaction. However, in this latter regime, solid–liquid contacts are transient.

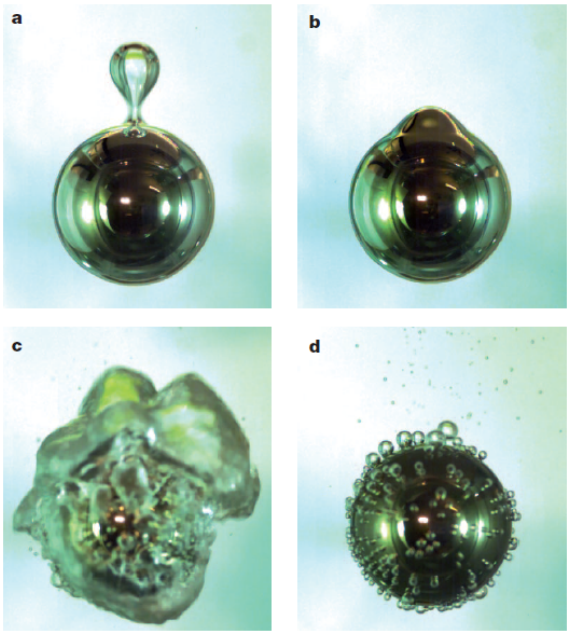

Figure 1.11: Pictures of 20 mm *steel spheres quenched in saturated water (a) Superhydrophobic sphere at* 200 °C*, (b) Superhydrophobic sphere at* 100 °C*: the vapour film is so stable that wetting never appeared, (c) Hydrophilic sphere at* 270 °C *during the boiling crisis (d) Hydrophilic sphere at* 200 °C *during nucleate boiling (from [28]).*

- **Orientation and geometry of the heater**: in partial nucleate boiling, thermal exchanges are favored for a face directed downwards, but this not the case anymore for fully developed nucleation [29]. Howard et al. [30] demonstrated that the orientation of the heater had a continuous impact on q_{CHF} which was maximum for upward facing heaters and minimum for downward facing heaters. The size of a quenched part also influences boiling around it. For example, surface tension effects are stabilizing the calefaction mode as wetting entails large curvatures.

- **Gravity**: its orientation and its magnitude also impact all the parameters of the boiling curve. A lot of studies working in micro gravity highlighted it [31].

- **Forced convection**: in the case of boiling inside a tube, this represents the input flow of liquid. For pool boiling or during quenching, this is related to the flow created by external agitators. The larger the convection, the larger

q_{CHF}, T_{CHF} [27] and T_{MHF} [26]. More generally forced convection improves the heat transfer providing that the convection velocity exceeds a minimum value around $10\,cm\,s^{-1}$ [24]. There are however some counterexamples, as shown by Ramezanzadeh et al. [32]. They numerically demonstrated configurations where forced convection can locally stabilise a vapour film. Figure 1.12 depicts the streamlines of two quenching simulations with two different liquid flows. The ledge created by the workpiece causes an obstacle that the liquid must bypass. At higher speeds ($50\,cm\,s^{-1}$), the detachment of the velocity lines traps a pocket of gas whose vorticity is very high. At low speed ($10\,cm\,s^{-1}$), liquid vortices remain close to the part but the vapour is not trapped.

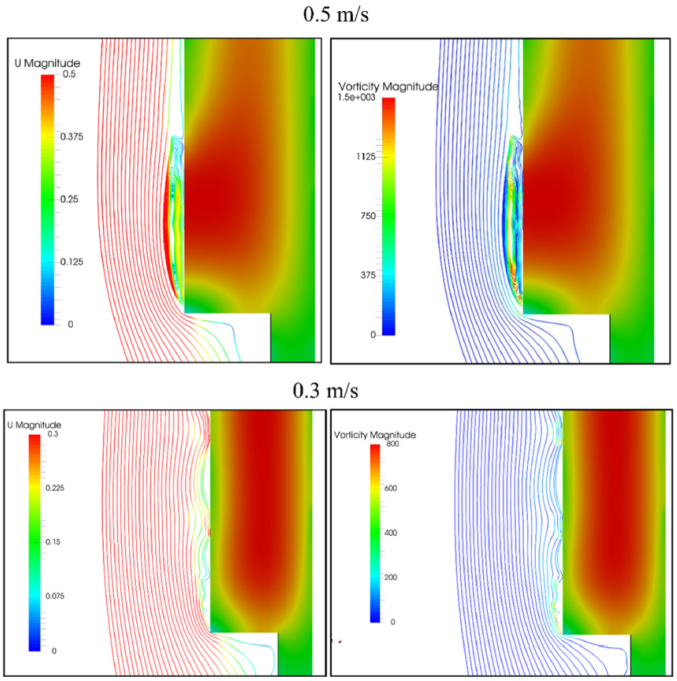

Figure 1.12: Velocity trajectories for two different input velocities. The entrapment of a vapour pocket is enabled by the high input velocity (from [32]).

- **Pressure**: higher pressure reduces superheating for the same temperature as the saturation temperature is higher. It naturally shifts the boiling curve to the right with increasing pressure. The vapour film is also thinned due to the compressibility of the vapour, according to [31], meaning higher heat fluxes in calefaction.

- **Solid thermal characteristics** like the density ρ_S, the specific heat capacity c_{pS} and the thermal conductivity k_S: in the case where the overheating

is not controlled, these characteristics also influence boiling phenomena characteristics at the surface of the heater. A larger $(\rho c_{\text{P}})_{\text{S}}$ characterises a solid that will tend to impose its temperature on the surface, as it will be more difficult to cool down. A larger k_{S} indicates that the material conducts well, and therefore also tends to impose its temperature at the interface. Indeed, if the temperature at the surface drops, this will be compensated by a quick heat input from the hot regions of the part. In both cases, the part cool down more uniformly. The Biot number $\text{Bi} = L_{\text{c}} h_{\text{HTC}} / k_{\text{S}}$ allows to characterise this last tendency in comparison with the characteristics of the fluid. Ebrahim et al. [25] used the effusivity $\sqrt{\rho_{\text{S}} c_{\text{PS}} k_{\text{S}}}$ of the material to characterise these effects. The effusivity of Inconel-600 being around 50% higher than the other materials, they observed that after the wetting the relaxation time of cooling of Inconel-600 was four times shorter than the other materials, whatever the subcooling. In the other materials, the core remained hotter and slowed down the cooling of the surface once q_{CHF} is exceeded.

1.2.3 State of the art of available correlations

Boiling entails a lot of different configurations with complex physics and many scales. An attractive solution is to draw correlations to pass over the complexity of the phenomena. The modes are too different for a unique simple correlation [33], thus correlations are usually dedicated to one mode. Only partial and fully developed nucleate boiling modes are sometimes gathered in one correlation. Integrated models are then a combination of every local heat transfer weighted by the void fraction, which is the proportion of vapour covering the solid [34].

1.2.3.1 Nucleate Boiling

This mode is subdivided into partial nucleate boiling and fully developed nucleate boiling.

At very low superheating, the liquid needs to exceed a certain supersaturation level for nucleation to start (the ONB). A thermal layer of supersaturated liquid of few millimetres exists close to the wall. Common correlations at saturation link T_{ONB}, q_{ONB} and the fluid pressure. Usually, T_{ONB} scales as q_{ONB} to the power x. x varies between 1/4 and 1/2 [35]. The combination of this law with correlations for nucleate boiling at atmospheric pressure leads to an estimation of T_{ONB} of few Kelvins for water, depending on the considered correlation.

Partial nucleate boiling is the most orderly mode of boiling: bubbles form at specific nucleation sites and are released once the critical size is exceeded. The sites are spaced far enough apart and the frequency of bubble creation is low enough to prevent the bubbles for merging with each other. The main three parameters are

the surface density of nucleation sites N_{NB}, the bubble critical diameter d_{NB} and the bubble release frequency f_{NB} (see Figure 1.13a). For example, Gaertner et al. [36] obtained for a copper plate values of surface density ranging from 0 to 175 sites per cm^2 according to the temperature difference. Cole [37] measured frequencies ranging from 1 to 50 Hz and starting diameters from 1 to 10 mm. Correlations dedicated to partial nucleate boiling were developed on these parameters [38, 39, 31]. The contribution of microlayer models are sometimes considered. It describes the thin layer of liquid at the bottom of the bubble that is superheated. It is believed to be the area where heat transfer is the most intense [31, 40].

However, studies to obtain these three parameters are tedious and not applicable for practical applications. In order to use this correlation, the approximation of some parameters is necessary. Furthermore, this theory does not fully extend to the fully developed nucleation, as these parameters make less sense. The surface fraction occupied by the vapour jets and the thickness of the thermal layer are often better descriptions.

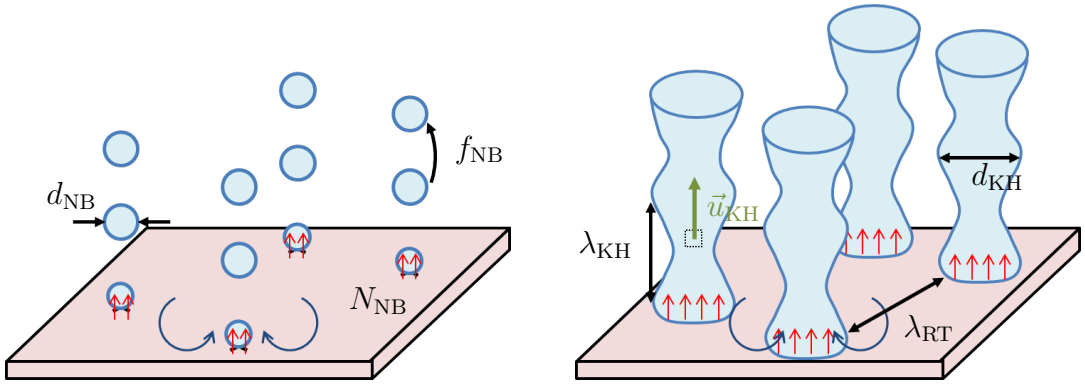

(a) Partial nucleate boiling. Bubbles of diameter d_{NB} leave the nucleation sites of density N_{NB} at a frequency f_{NB}.

(b) Vapour jets of fully developed boiling. The CHF is reached when u_{KH} and thus d_{KH} are so large that the liquid can't replace the vapour at the bottom of the jets.

Figure 1.13: Simplified vision of partial nucleate boiling (a) and fully developed nucleate boiling (b).

This is the reason why other laws that only scale with macro characteristics of the flow were proposed [33, 41]. Cooper suggested another approach by reduced properties. He proposed a scaling law based on data points without any particular theory, which is a sort of regression model extended to the whole nucleate boiling mode [42]. In addition to the fluid properties, this model only requires the pressure, the overheating and the roughness as parameters. It holds for saturated conditions. He obtained a heat flux scaling with a power 3 with the overheating which is a low

approximation as other existing correlations propose a value of 4 [31]. This approach has been completed by Liu et al. [43] and extended for subcooling conditions and also for the pure convection configuration. Further details are presented in Section 7.2.3.

1.2.3.2 Critical Heat Flux

Liang et al. [44] recently provided a complete review on the available correlation for the assessment of T_{CHF} temperature and q_{CHF}. The pioneer works of Zuber and Kutateladze [45, 46] are still one of the best known estimation of the CHF mechanisms. They suggested that the transition boiling appears when the replacement of liquid at the wall surface is prevented by Kelvin Helmholtz instabilities (see Figure 1.13b). These instabilities are expected to appear between the vapour jet that evacuates vapour from the surface, and the interstitial liquid phase. Jets are also believed to be allocated following the wavelength predicted by Rayleigh–Taylor instabilities. For a water vapour mixture, $\lambda_{\mathrm{RT}} \sim 1\,\mathrm{cm}$ which is coherent with experimental data [17]. This leads to a CHF value that only depends on the fluids properties. A correlation factor has been used to fit experimental data for horizontal pool boiling. Still for a water vapour mixture, $q_{\mathrm{CHF}} \sim 2{\times}10^{6}\,\mathrm{W\,m^{-2}}$. Combined with correlations of nucleate boiling, we can also estimate $T_{\mathrm{CHF}} \sim 125\,^{\circ}\mathrm{C}$. Figure 1.14a shows a visualisation of an experimental quench of a sphere at CHF by Linehard [17].

Liang et al. [44] then detailed some modifications of this correlation to account for subcooling, pressure as well as the orientation, contact angle and surface roughness of the heater. Details of this correlation with modifications are presented in Section 7.2.3. Other models based on other theories have been proposed: an intermittent behavior of coalescent vapour bubbles and consumption of the microlayer beneath the bubbles [47], the consideration of an irreversible growth of a dry spot area due to the proximity of bubbles [48], or the competition between the momentum of the vapour and the inertia of the liquid that tries to replace it [49].

1.2.3.3 Transition boiling

The unstable transition boiling can be seen as a localised alternation between nucleation and calefaction. Areas where liquid is wetting experience local nucleate boiling. Areas where vapour covers the surface (also called dry zones) experience local film boiling. Thus this mode is usually studied in term of surface void fraction [34].

Another approach is to consider that the heat flux is a weighting between q_{CHF} and q_{MHF}. Weights values are then functions of the temperature that is compared with T_{CHF} and T_{MHF}. Berenson observed a linear dependency of $\ln q$ versus $\ln(T - T_{\mathrm{CHF}})$ [18], whereas experimental curves of quenched probes of Ebrahim et al. [25] are closer to a linear dependency between q and $T - T_{\mathrm{CHF}}$ themselves.

Berenson's works [18] were extended by Ramilson et al. [50] to have a more accurate solution close to T_{MHF}. Writing $\ln q_{\mathrm{B}}$ as the prediction of Berenson in pure film boiling, then $(q - q_{\mathrm{B}})/\Delta T_w$ scales as $T - T_{\mathrm{MHF}}$ to the power 1/2. This static view can be corrected to account for hysteresis effects [51].

1.2.3.4 Minimum Heat Flux

The assessment of the MHF is a very important topic for quenching. This is the tipping point of the cooling as it is a transition between the moderate heat transfer of calefaction and the sudden increase of cooling rate of the transition and nucleate boiling modes.

Berenson showed that for low overheating horizontal film boiling, the bubble spacing and growth rate was still determined by Rayleigh Taylor instabilities as shown in Figure 1.15a [18]. It enabled him to get an estimation of the hydrodynamics of the film and to recover the heat flux. He considered with such profile the limit vapour flow rate to maintain the vapour film and obtained an estimation of q_{MHF}. This gives around $3{\times}10^4\,\mathrm{W\,m^{-2}}$ for water at atmospheric pressure. Combined with his estimation of the heat flux lead him to an estimation of T_{MHF}. This gives 272 °C for water at atmospheric pressure. Figure 1.14b shows a visualisation of an experimental film boiling around a wire at MHF by Linehard [17].

This correlation has been upgraded to account for subcooling with a linear dependency [52, 53], and with surface roughness effects [25]. These two parameters happen to have a large influence on the value of T_{MHF} [28], though the surface

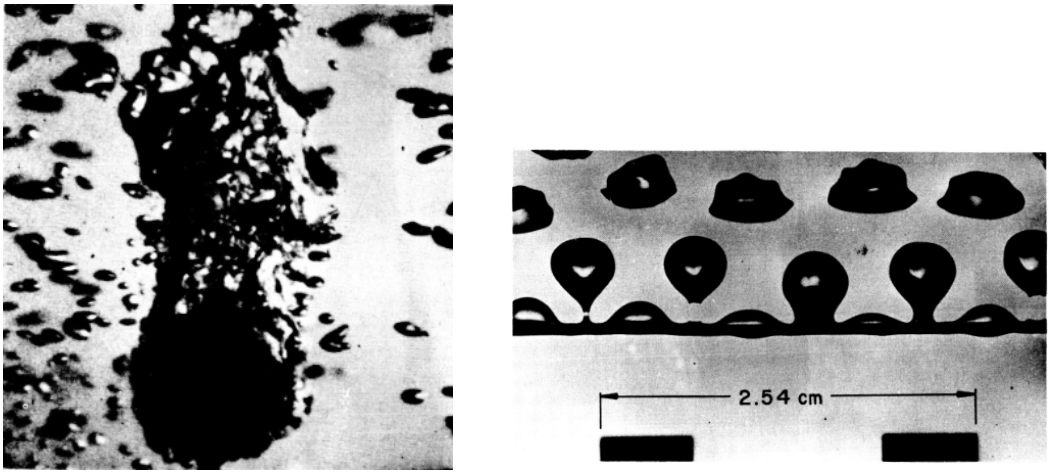

(a) Critical Heat Flux on a quenched sphere

(b) Vapour film around a wire just before wetting at Minimum Heat Flux

Figure 1.14: Experimental views of the CHF and MHF (from [17]).

roughness is always delicate to assess in industrial applications. The shift of T_{MHF} observed for water is on average between 6 and 10 K per kelvin of additional subcooling, depending on the material [25, 54, 55, 56].

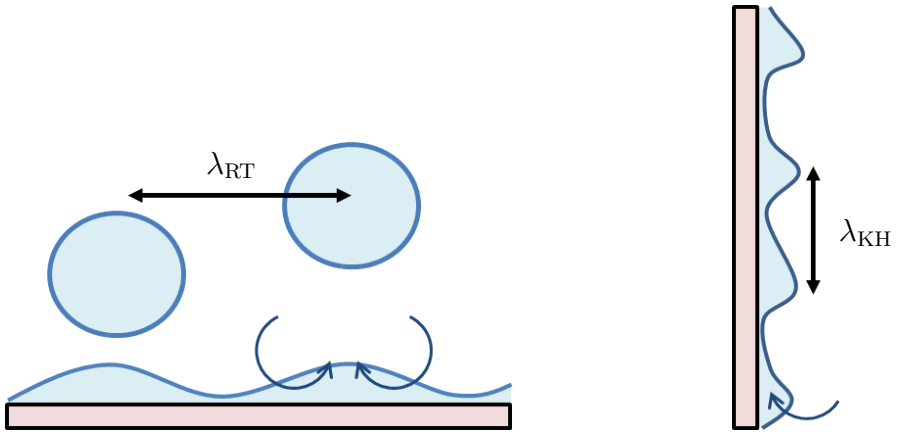

(a) Horizontal film boiling. Vapour bubbles are spaced from each other by the most unstable wavelength of the Rayleigh–Taylor instability theory. The liquid vaporise from the thin parts of the film to feed the bubbles.

(b) Vertical film boiling. The wavelengths of the vapour film are the most unstable ones of the Kelvin–Helmholtz instability theory. A major portion of the vapour comes from the bottom of the heater that feeds the film.

Figure 1.15: Schematic descriptions of film boiling in horizontal and vertical configuration.

1.2.3.5 Calefaction

The vapour film is never stable and interface waves exist whatever the orientation of the heater. A pure conduction model in the vapour film is usually considered as a first estimation of the film boiling heat transfer. Authors showed that this estimation underestimates the heat flux by a factor 25% for vertical film boiling [57]. This demonstrates that convection inside the film is also at play, but has a moderate impact in comparison with conduction. The vapour film thickness is then a good parameter to evaluate as it is directly linked with conductive fluxes.

For horizontal film boiling, Berenson's theory based on Rayleigh Taylor instabilities lead to heat flux that scales as of the overheating to the power 3/4 [18]. Klimenko [58] considered similar arguments except that the Rayleigh Taylor instability theory was considered with a finite vapour film thickness. This results in a heat flux that scales as the overheating to the power 2/3.

For vertical film boiling, boundary layer theories with pure conduction inside the vapour film have been developed for saturated conditions [12], with subcooling

[59, 60, 61, 57, 54, 24] and with forced convection [62, 63]. They predict a film thickness that scales as the height to the power 1/4, leading to a heat flux that scales as the height to the power −1/4. These models are interesting for a first approach. However, their reliability is limited. Moreover, the mean film thickness is not a convenient parameter as it is not necessarily an increasing function of the heat flux [21]. Kelvin–Helmholtz instabilities are generally present at the liquid vapour interface as shown in Figure 1.15b. These waves create very small film thickness that improve drastically the heat transfers. Meduri et al. suggested a correlation to account for those instabilities based on Berenson's one for horizontal configuration, scaling in a power 3/4 of the overheating [62]. Subcooling and forced convection are also taken into account as multiplicative factors.

Overall tendencies of the boiling curve are summarised in Figure 1.16.

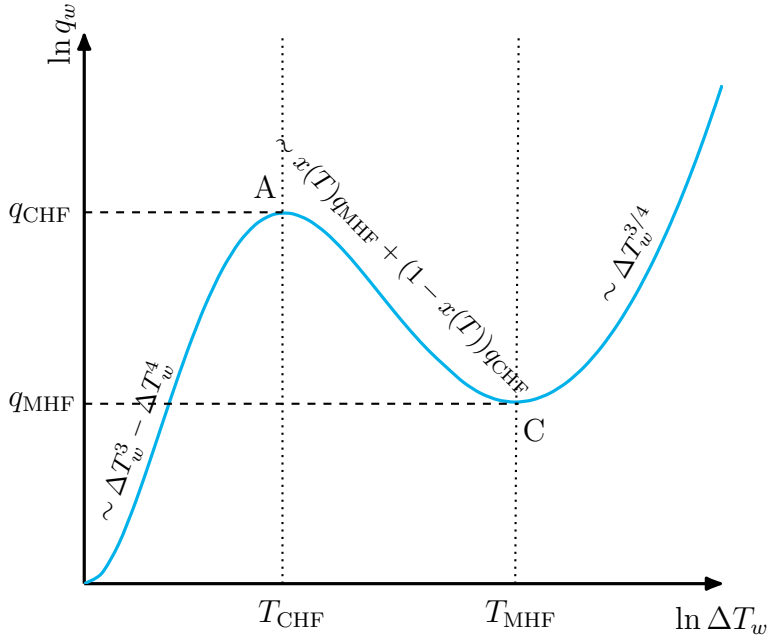

Figure 1.16: Tendancies of the boiling curve from correlations of the literature. The CHF (point A) can be assessed by Zuber's theory, and the MHF (point C) can be assessed by Berenson's theory.

1.3 Numerical simulation

All the correlations are restricted to specific conditions, from the geometry of the heater to the range of physical parameters. Moreover they do not take into account external influences like the supply of vapour from below during quenching. It has for example a huge impact on the CHF value that vary with a factor 2 for two

different locations during the same quench [55]. Ramesh et al. [9] also underlined the important coupling that occurs between the dynamics of the cooling fluid and the thermal dynamics of the part. Both influence heat exchange and a loss of accuracy occurs when one is determined without considering the other. Furthermore the chaotic nature of boiling limits a full analytic description of most of the boiling modes.

The lack of flexibility of the aforementioned correlations lead researchers to investigate Computational Fluid Dynamics (CFD) methods. CFD allows to reproduce and evaluate local phenomena that are difficult to estimate during tests. This gives another tool to better understand the overlying physics of each mode. It allows to free itself from all the experimental constraints and the inaccuracies of measurements linked to the inverse method. Once numerical models are validated they can even be used as a powerful experimental laboratory. They bring new insights, new possibilities, and offer prospects for coupling with emerging numerical optimisation methods.

1.3.1 Phase change simulations

Phase change problems require to simulate the mass, momentum and energy conservation. It also requires to handle multiphase flows with discontinuous quantities and conservation equations at the interfaces. Simulations rely on a discretisation space called mesh grid or mesh. Values are computed on a finite numbers of points (nodes) or volumes (cells) split around the simulation space. The equations to be solved are then discretised and linearised consistently with the mesh thanks to the discretisation scheme: Finite Difference Method (FDM), Finite Volume Method (FVM) or Finite Element Method (FEM).

- FDM: All the quantities are directly computed on the nodes and computed to respect the discretised formulation.
- FVM: Quantities are integrated on cells. Fluxes between cells are computed to respect integral equalities.
- FEM: Test functions are used to transform the volume integrals. Interpolation functions of chosen complexity are considered to discretise the quantities over the cells. Weights are computed to respect integral equalities for every arbitrary test function.

A schematic view of these differences is presented in Figure 1.17.

To tackle phase change problems the three conservation equations can be handled by Lagrangian or Eulerian approaches. The first one is the consideration of fluid particles that move with the mesh grid. The second one considers field quantities

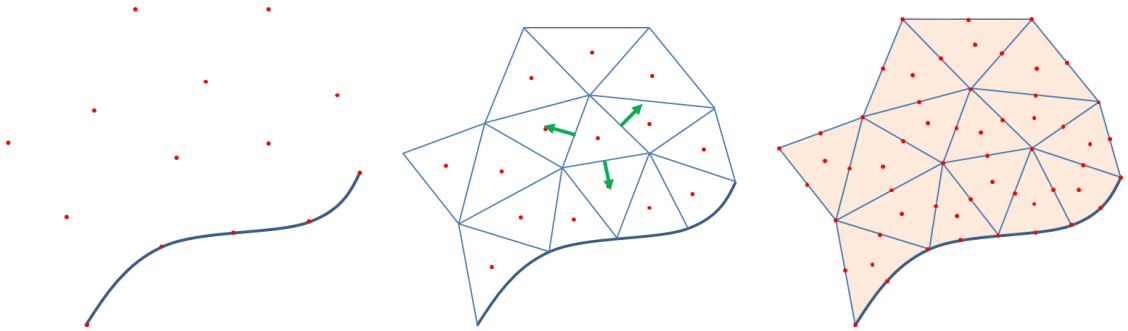

(a) Finite Difference Method. Quantities are computed on nodes.

(b) Finite Volume Method. Quantities are integrated in volumes and fluxes are computed between those volumes.

(c) Finite Element Method. Interpolation functions are used to discretise the quantities over the cells (here order 2 polynomials).

Figure 1.17: Schematic descriptions of the different numerical frameworks.

and the mesh is fixed during the resolution of the equation. Then multiphase flows require the identification of each phase. This can be handled with Volume of Fluid (VOF) methods by using a density function for each phase, or with Level Set (LS) methods by creating a distance function to the interface separating each phase. Every approach have advantages and issues discussed in the literature.

Pioneer works were done to simulate two-phase flows with phase change in 2D: Lee [64] developed a semi-implicit two-fluid phase change model with a sharp interface. A projection technique with iterative scheme was used to compute the velocity jump, and the mass transfer was computed thanks to a proportional law. This enabled him to simulate a steam-water jet impingement. Using the VOF method, this work was extended by Rattner et al. [65] for film condensation. The mass transfer rate previously chosen arbitrarily was assessed through enthalpy considerations. This model was embedded for a finite volume approach within the Open-FOAM library. Son et al. combined this second-order projection method with a Level Set method [66] to solve saturated 2D horizontal film boiling. Juric et al. [67] also simulated this problem with a single field formulation and a front tracking method implemented with finite differences. Welch et al. [68] did the same but with a Volume of Fluid based interface tracking method. Once again the projection method was used, and the reconstructed interface lead to the computation of temperature gradients from both sides. It enabled him to simulate 2D film boiling as shown in Figure 1.18. Kang et al. [70], Gibou et al. [71] and Tanguy et al. [72] implemented a Ghost Fluids Method to ease the introduction of interfacial terms within an Eulerian finite difference method. A similar approach was done by Esmaeeli et al. [73] who eliminated the iterative procedure with a predictor-corrector algorithm. Using

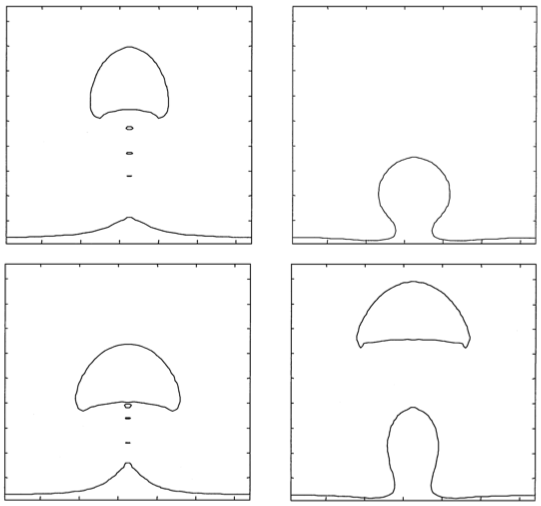

Figure 1.18: 2D Film boiling simulation with VOF method and an interface reconstruction. (from [68]).

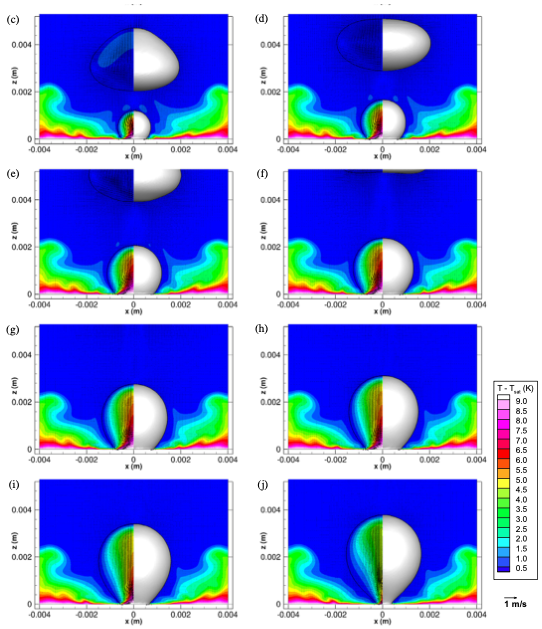

Figure 1.19: Simulation of a 3D bubble nucleation with LS method. (from [69]).

the interface tracking and projection methods with a sharp interface approach, Sato et al. [69] implemented a staggered finite-volume vaporisation solver and computed proper bubble nucleation and growth (see Figure 1.19).

More original methods were developed, like the coupled Level Set and Volume of Fluid method [74], aiming a better precision of the interface definition and of the mass change rate computation. The Arbitrary Lagrangian and Eulerian method was applied to simulate the vaporisation of a droplet [75]. At a larger scale, an extended vision of the VOF method, the four field, two-fluid model, was able to predict different set of data with boiling flows inside a pipe [76].

1.3.2 Quenching simulations

The behavior of the coolant is of secondary importance in quenching. The main interest lays in the thermal simulation inside the solid. However, we saw in previous sections that the latter was conditioned by the proper understanding of boiling phenomena. As the quenched part size can be a limiting factor of numerical simulations, a compromise has to be found. It is not feasible to simulate every single bubble of vapour in a 1 minute quench of a car cylinder head. Thus the simulation of hydrodynamics has to integrate models to conciliate an admissible computational cost and an acceptable precision on the heat transfer. Moreover, a choice has to

be made on the way to integrate the solid inside the computational domain. The fluid and solid domain can be completely separated, and two computations are done separately as in Figure 1.20a. Or the solid can be immersed inside the fluid domain and one computation is done for both parts as in Figure 1.20b. Both approaches are compared in Table 1.1.

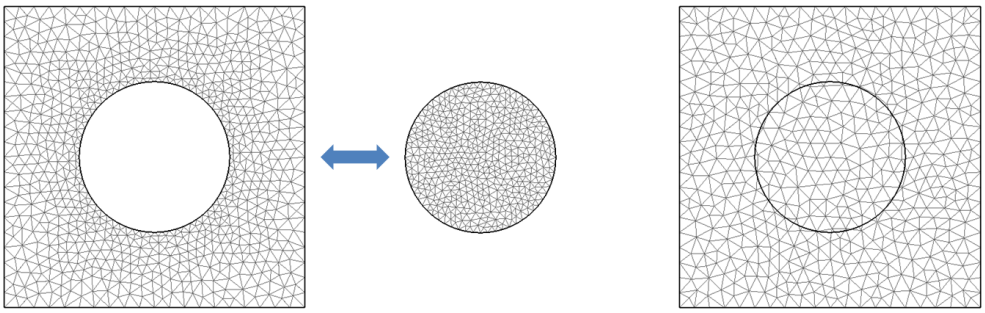

(a) Separated meshes with interface communication. *(b) Immersed solid.*

Figure 1.20: Example of separated and immersed domains.

Bristiel et al. [77] detailed how PSA researchers apply these numerical methods to concrete cases of hardening industrial parts [77]. They carry out simulations in two steps: first, they simulate the global behavior of the fluid and the part by simplifying the geometry of the part. They then derive the resulting heat exchange coefficients between the part and the fluid. Then they use them to redo a simulation on the part alone, this time with a much finer mesh and a more accurate geometry. They can thus optimise their processes, but also study the influence of chemical treatments on the mechanical strength of the parts. This allows them to reduce the number of experimental tests.

They rely on the work of Srinivasan et al. [13, 78] who developed a Finite Volume solver with an Eulerian approach. The phases are separated using VOF, and the solid domain is separated from the fluid one. The liquid vapour interface is not properly tracked and averaged quantities are considered regarding the vapour volume fraction. Phase change is computed by a proportional law regarding the local overheating of the fluid. Heat fluxes between the solid and the fluid are computed thanks to correlations fed with local quantities predicted by the solver. This enables to compute entire 3D quenches of complex part with reasonable meshes [55] (see Figure 1.21). Bo et al. [79] proposed the same approach and with additional models on the distribution of the vapour phase as a bubble mist.

Also using finite volume methods with VOF on an Eulerian framework, Ramezanzadeh et al. [32] integrated a convective term to sharpen the interface between vapour and liquid. The interface was tracked this way. A comparison with the averaged values approach is presented in Table 1.1. Computing the true heat transfer

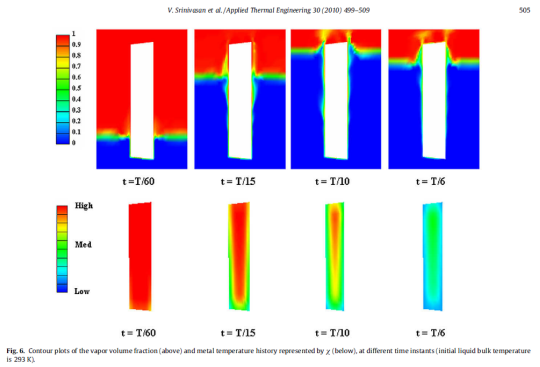

Figure 1.21: Simulation of the quench of a bar. The interface is not tracked but averaged quantities are considered. Correlations are used to estimate heat fluxes. (from [13]).

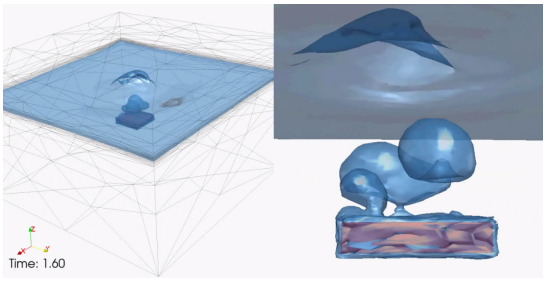

Figure 1.22: Simulation of the quench of a little brick. The interface is tracked using the LS method (from [80]).

at the solid fluid interface, they simulated in 2D the experiment presented in [55]. Once again the solid computational domain was separated from the fluid.

A LS approach can be found in the works of Khalloufi et al. [80, 81]. With an Eulerian framework based on a Finite Element solver, they simulated in 3D quenching processes for simple geometries in saturated conditions (see Figure 1.22).

	Pros	Cons
Separated domains	High control of the mesh Clean separation	Imposed conform mesh Interpolation between meshes
Immersed solid	Flexibility on the mesh Light implementation	Interface numerical challenges
Interface tracking	High descriptivity	High computational costs
Averaged quantities	Low computational costs	Relies on correlations

Table 1.1: Comparison of different approaches regarding the mesh and the multiphase model.

1.4 Contribution of the thesis

The present work aimed at pushing further numerical tools to simulate phase change problems and quenching. An innovative multiscale numerical framework was proposed. Its final goal was to provide a tool for industrials to better understand the physics of boiling and quenching. This works was indeed embedded inside the ANR industrial chair INFINITY gathering twelve industrial partners. The goal of the chair was to develop a software to have a first estimation of quenching in liquid coolants for arbitrary conditions and geometry.

All the numerical developments of this thesis relied on the finite element library CIMlib-CFD. This tool have been developed in the Centre de Mise en Forme des Matériaux (Cemef) laboratory in collaboration with industrial partners. It is a C++ Object Oriented Program that handles parallel computation. It aims at providing a set of components that can be organised to carry out simulations of material deformation, fluid dynamics, heat transfers, etc. [82, 83, 84, 85, 86]. The present works pursued previous works of the CFL team of Cemef and specifically to those of Mehdi Khalloufi [80].

The key control parameter in quenching is essentially the heat transfer between the solid and the fluid. For such application the behavior of the fluid is of second interest. However, we saw in this section the profound coupling between boiling phenomena and heat transfer. We aimed in this work at simulating the principal features of the liquid vapour mixture. In numerical simulations we focused our attention on the physics of the liquid vapour interface. Thus wetting phenomena were slightly tackled and the main mode that was studied was film boiling. Other modes were considered with analytical models and correlations.

The work of [80] lead to a first phase change model implemented inside the CIMlib-CFD library. However, this framework lacked of proper mass and energy conservation controls at the interface: the consideration of the density variation of a vaporising fluid particle was not implemented, and the energy bill at the interface was approximated with a model only valid for saturated conditions. We therefore proposed to extend this Finite Element numerical framework based on an implicit representation of the liquid vapour augmented by a remeshing algorithm. The liquid vapour interface was still tracked with the help of a Level Set description. A method was developed to better take into account interface heat fluxes at the interface. The mass conservation was also guaranteed with a work of a dedicated solver. This provided a tool to simulate the behavior of multifluid interfaces with phase change, temperature fluctuations and moderate convective effects. Validations were conducted through numerical 2D and 3D benchmarks of increasing complexity and comparisons were made with experiments.

In Chapter 2, the multiphase thermal framework is presented. The energy conservation equation is studied. Simplifications are made to only consider relevant

terms in the context of quenching. The Level Set method is presented along with the Continuous Surface Force approach to consider multiphase system in a stabilised way. A method to compute heat flux jumps at the liquid vapour interface dedicated to the framework is presented and validated in theoretical benchmarks. The coupling of this immersed volume approach and the thermal solver is tested with a first 2D benchmark.

In Chapter 3, the pseudo-compressible mechanical framework is presented. Mass and momentum conservation equations are studied and simplified in the context of quenching. A dedicated numerical solver is developed based on the former CIMlib-CFD incompressible Navier–Stokes solver to account for volume changes across the interface in the context of phase change. This new tool is tested and validated with a 2D benchmark and coupled with the Level Set method. This mechanical multiphase environment is studied and validated with 2D benchmarks.

In Chapter 4 the coupling with the mechanical and thermal solvers is presented. The interactions of this resulting phase change system with the numerical FEM framework and the remeshing algorithm are discussed. This new formulation is then tested and validated in 2D and 3D benchmarks.

In Chapter 5 a quenching experiment is presented. Little nickel balls of 1 cm diameter with different initial temperatures were quenched inside hot water that was pre-heated near saturation temperature. Videos of the experiment enabled to capture the vapour film behavior and the vapour bubbles dynamics. Hydrodynamical observations are compared with numerical simulation results.

In Chapter 6 the vertical film boiling case is discussed. A first analytical study is carried out to better understand the physics at play. Dominant terms and asymptotic behaviors are discussed. This understanding is then used to challenge and enriched the phase change solver in the context of film boiling. 3D real size numerical simulations are carried out and compared with experimental results.

In Chapter 7 a quenching model is presented. The phase change framework is enriched with a nucleation model to account for wetting phenomena at low temperatures. Correlations are studied and integrated in the model adapted to quenching. The combination of the boiling numerical simulation, the nucleation model and the interaction with a solid domain leads to a full quenching model. It relies on the descriptive capacities of the phase change framework. Two real size pool quenches are reproduced and numerical results are compared with the experiments. A study of an industrial jet impingement quenching is also carried out in Appendix D.

Chapter 2

Multiphase thermal framework

Contents

Résumé en Français

Ce chapitre présente le modèle thermique permettant la prise en compte du saut de flux de chaleur à l'interface liquide / vapeur. Tout d'abord, une analyse des ordres de grandeur des énergies en jeu aboutit à quelques simplifications. Premièrement, la température à l'interface peut être considérée constante, égale à la température de saturation du fluide à pression donnée. Deuxièmement, les variations de pression ont des effets non prépondérants en comparaison des variations d'énergie thermique, de même que les effets visqueux. Troisièmement, les effets de rayonnement peuvent être considérés comme surfaciques entre le solide et l'interface liquide / vapeur. Ces simplifications mènent à une modélisation physique des échanges d'énergies pour un système fluide diphasique avec changement de phase.

Le modèle est intégré dans un cadre numérique basé sur la méthode des Éléments Finis. Afin de représenter l'interface, une méthode Level Set régularisée est employée. Les forces et autres grandeurs surfaciques sont considérées volumiquement par l'emploi d'une fonction Dirac régularisée basée sur la fonction distance. Cette association d'ingrédients physiques et numériques mène à un système de deux équations de Convection–Diffusion sur la température et la fonction distance, dont la résolution est stabilisée par des méthodes numériques type SUPG et SCPG.

Le taux de vaporisation ou de condensation à l'interface liquide / vapeur est dicté par le bilan d'énergie à l'interface. Celui-ci fait intervenir le saut de flux de chaleur de part et d'autre de l'interface, qu'il faut donc calculer. Cette considération associée aux choix de représentation numérique de l'interface (dotée d'une épaisseur fictive) nécessite une méthode dédiée qui a été développée au cours de la thèse. Cette méthode est testée et validée sur trois cas test 2D. L'erreur analytique varie à l'ordre 1 avec la taille de maille et la dérivée seconde de la température normalement à l'interface.

Le modèle diphasique complété par ce calcul adapté du taux de vaporisation est évalué grâce au problème analytique de Stefan. Trois cas de figure sont étudiés avec notamment la considération d'un liquide non saturé qui généralise le problème de Stefan à ces cas dits "sous-refroidis". Le modèle réussit bien à représenter ce problème, avec une convergence à l'ordre 1 en taille de maille cohérente avec l'estimation analytique.

2.1 Introduction

Most of the time, the quenching liquid is below its saturation temperature. We saw in Section 1.2.2 that this difference of temperature called subcooling had a big impact on the heat transfer [26, 25, 87, 88, 27, 55, 62]. With a higher subcooling, the temperature of wetting (or Leidenfrost temperature T_{MHF}) is higher and heat transfers are globally enhanced. Especially during calefaction, conduction inside the liquid reduces vaporisation or even leads to condensation that decreases the vapour film thickness [57]. Moreover when forced convection is applied, more heat is extracted by warming up the liquid. All these observations justify to properly take subcooling into account to improve the model accuracy. This is mainly done with rigorous thermal and mass transfer models. The latter is especially a key point of phase change simulations.

As we saw in Section 1.2.1, the liquid is usually oversaturated close to the heater, meaning that the thermodynamical equilibrium is not reached. Moreover, differences of pressure due to hydrostatic pressure, inertia, or surface tension at the interface create spacial disparities of the equilibrium.

Considering the difference due to pressure variations, we considered the Clausius–Clapeyron law [19] that is a first approximation of the saturation pressure variation p_{sat} with the saturation temperature T_{sat}:

$$\frac{\partial p_{\mathrm{sat}}}{\partial T_{\mathrm{sat}}} = \frac{\mathcal{L}}{T_{\mathrm{sat}} [\![1/\rho]\!]} \tag{2.1}$$

where $\mathcal{L}$ is the latent heat of vaporisation, ρ is the density and $[\![x]\!] = x_V - x_L$ represents the jump of the quantity x between the vapour and the liquid phase. Considering small variations of pressure around atmospheric conditions ($p_{\mathrm{sat}} = 1.013\,\mathrm{bar}$ and $T_{\mathrm{sat}} = 100\,^{\circ}\mathrm{C}$ for water), the function $p - p_{\mathrm{sat}}$ can be approximated as linearly dependent of $T - T_{\mathrm{sat}}$. The coefficient is then given by Equation (2.1).

In the context of quenching, the parts are usually plunged in open pools of water or oil. Thus hydrostatic variations inside the pool are restricted to $\rho_{\mathrm{L}} g H$ where g stands for the gravitational field of earth and H is the depth of the pool. H is usually of the order of magnitude of 1 m. The associated hydrostatic pressure difference for water is then around 0.1 bar. Considering the coefficient given by Equation (2.1) ($0.03\,\mathrm{bar\,K^{-1}}$ for water at atmospheric pressure), the associated variation of the saturation temperature is around 3 K. Tabulated values for water at 1.1 bar give $T_{\mathrm{sat}} = 102\,^{\circ}\mathrm{C}$ [89], thus a variation of 2 K, which is close.

Considering pressure variations of the same order of magnitude due to surface tension effects leads to length scales of 10^{-5} m. This is out of the scope of this work. Considering pressure variations of the same order of magnitude due to inertial effects leads to velocities of $200\,\mathrm{m\,s^{-1}}$ in the vapour are and of $4\,\mathrm{m\,s^{-1}}$ in the liquid. This is at most the upper limit of the scope of this work. This is summed up in Table 2.1.

Studied effect	Hydrostatic pressure	Surface tension	Liquid inertial pressure	Vapour inertial pressure
Scaling law	$\Delta p \sim \rho_{\mathrm{L}} g L_{\mathrm{c}}$	$\Delta p \sim \gamma_0 / L_{\mathrm{c}}$	$\Delta p \sim \rho_{\mathrm{L}} u^2/2$	$\Delta p \sim \rho_{\mathrm{V}} u^2/2$
Parameter	L_{c}	L_{c}	u	u
Magnitude	$1\,\mathrm{m}$	$10^{-5}\,\mathrm{m}$	$4\,\mathrm{m\,s^{-1}}$	$200\,\mathrm{m\,s^{-1}}$

Table 2.1: Orders of magnitude of parameters associated to a pressure variation of $0.1\,\mathrm{bar}$ *for diverse mechanical effects.*

Variations of T_{sat} in quenching processes are limited to few kelvins. This is very small compared to the temperature variations encountered during quenching that can raise up to $1000\,^{\circ}\mathrm{C}$. Consequently, considering a constant saturation temperature in our work is a moderate assumption that is often taken in the literature. Based on this consideration, we properly wrote energy conservation of the two phase fluid system.

2.2 Energy conservation

2.2.1 Single phase formulation

We considered the general Eulerian form of the Navier–Stokes equations that describe the general behavior of a fluid in a gravity field. They stand for the equations of conservation of mass, momentum and energy and read:

$$\begin{cases} \dfrac{\partial \rho}{\partial t} + \vec{\nabla} \cdot (\rho \vec{u}) = 0 & (2.2) \\ \dfrac{\partial \rho \vec{u}}{\partial t} + \vec{\nabla} \cdot (\rho \vec{u} \otimes \vec{u}) = \vec{\nabla} \cdot \boldsymbol{\sigma} + \rho \vec{g} & (2.3) \\ \dfrac{\partial}{\partial t}\left(\rho e + \dfrac{\rho}{2} u^2\right) + \vec{\nabla} \cdot \left[\left(\rho e + \dfrac{\rho}{2} u^2\right) \vec{u}\right] = \vec{\nabla} \cdot (\boldsymbol{\sigma} \vec{u}) + \rho \vec{g} \cdot \vec{u} - \vec{\nabla} \cdot (\vec{q} + \vec{q_{\mathrm{R}}}) & (2.4) \end{cases}$$

where $\boldsymbol{\sigma}$ is the Cauchy stress tensor, e is the specific internal energy, $\vec{u}$ is the fluid velocity, $\vec{q}$ is the local conductive heat flux and $\vec{q_{\mathrm{R}}}$ is the local bill of radiation heat flux (emitted and received). The term $\rho u^2/2$ stands for the specific kinetic energy. In the present work we only worked with Newtonian fluids. The Cauchy stress tensor could then be written as the sum of the kinetic pressure tensor and the viscous stress tensor:

$$\boldsymbol{\sigma} = -p\mathbb{1} + \boldsymbol{\tau} \tag{2.5}$$

In this chapter, we focus on the energy conservation equation.

2.2.1.1 General form

First of all, we removed the specific kinetic energy from the energy conservation. To do so, we multiplied the momentum equation (2.3) by the velocity. With some mathematical manipulations, the kinetic energy conservation equation reads:

$$\rho \frac{\mathrm{D}}{\mathrm{D}t}\left[\frac{1}{2}u^2\right] = \left(\vec{\nabla}\cdot\boldsymbol{\sigma}\right)\cdot\vec{u} + \rho\vec{g}\cdot\vec{u} \tag{2.6}$$

with $\dfrac{\mathrm{D}*}{\mathrm{D}t} = \left(\dfrac{\partial *}{\partial t} + (u\cdot\nabla)*\right)$ the particle derivative. We subtracted this equation from the energy conservation equation (2.4). We also decomposed the Cauchy stress tensor. With some mathematical manipulations, the new form of the energy conservation equation reads:

$$\rho\frac{\mathrm{D}e}{\mathrm{D}t} = -p\vec{\nabla}\cdot\vec{u} + \boldsymbol{\tau} : \dot{\boldsymbol{\varepsilon}} - \vec{\nabla}\cdot(\vec{q} + \vec{q_{\mathrm{R}}}) \tag{2.7}$$

where $\dot{\boldsymbol{\varepsilon}} = (\vec{\nabla}\vec{u} + {}^{t}\vec{\nabla}\vec{u})/2$ is the strain rate tensor. This equation can be seen as a Lagrangian form of the internal energy conservation. For phase change processes, it is more common to work with enthalpies $h = e + p/\rho$. p is here the thermodynamic pressure that is confounded with the kinetic pressure using Stokes hypothesis. The enthalpy conservation equation reads:

$$\rho\frac{\mathrm{D}h}{\mathrm{D}t} = \frac{\mathrm{D}p}{\mathrm{D}t} + \boldsymbol{\tau} : \dot{\boldsymbol{\varepsilon}} - \vec{\nabla}\cdot(\vec{q} + \vec{q_{\mathrm{R}}}) \tag{2.8}$$

As we only considered monophasic systems, no phase change were considered. Thus we could write the enthalpy as a state function of temperature T and pressure P:

$$\mathrm{d}h = c_{\mathrm{p}}\,\mathrm{d}T + \frac{1-\alpha_{\mathrm{T}}T}{\rho}\,\mathrm{d}P \tag{2.9}$$

where:

$$c_{\mathrm{p}} = \left(\frac{\mathrm{d}h}{\mathrm{d}T}\right)_{|P} \tag{2.10}$$

is the specific heat capacity at constant pressure. The second term stands for the change of enthalpy due to pressure changes:

$$\frac{1-\alpha_{\mathrm{T}}T}{\rho} = \left(\frac{\mathrm{d}h}{\mathrm{d}P}\right)_{|T} \tag{2.11}$$

with $\alpha_{\mathrm{T}} = \dfrac{1}{V}\left(\dfrac{\mathrm{d}V}{\mathrm{d}T}\right)_{|P}$ the coefficient of cubic thermal expansion for a given volume V [90].

We could then write the energy conservation in terms of temperature variations:

$$\rho c_{\text{P}} \frac{\text{D}T}{\text{D}t} = (\alpha_{\text{T}} T) \frac{\text{D}p}{\text{D}t} + \boldsymbol{\tau} : \dot{\boldsymbol{\varepsilon}} - \vec{\nabla} \cdot (\vec{q} + \vec{q_{\text{R}}}) \tag{2.12}$$

Finaly, we rewrote the diffusion effects thanks to the Fourier Law $\vec{q} = -k\vec{\nabla}T$ with k the thermal conductivity:

$$\rho c_{\text{P}} \frac{\text{D}T}{\text{D}t} = (\alpha_{\text{T}} T) \frac{\text{D}p}{\text{D}t} + \boldsymbol{\tau} : \dot{\boldsymbol{\varepsilon}} + \vec{\nabla} \cdot k\vec{\nabla}T - \vec{\nabla} \cdot \vec{q_{\text{R}}} \tag{2.13}$$

2.2.1.2 Local Phenomena Analysis

Considering the term due to pressure variations, we assessed its order of magnitude by comparing $\rho c_{\text{P}} \Delta T$ with $(\alpha_{\text{T}} T)\, \Delta P$. We once again considered pressure variations of at most 0.1 bar. The cubic thermal expansion coefficient of water is around $\alpha_{\text{T}} \sim 10^{-4}\,\text{K}^{-1}$. For vapour, a first approximation using a perfect gas model lead to $\alpha_{\text{T}} \sim 1/T$: $(\alpha_{\text{T}} T)$ is at most equal to 1. Thus energetically speaking, a pressure variation of ΔP is equivalent to a temperature variation of $\alpha_{\text{T}} T\ \Delta P/(\rho c_{\text{P}})$. Taking values of ρc_{P} for water and water vapour at 100 °C [89], a 0.1 bar pressure variation leads to values gathered in Table 2.2 which are compared with characteristic values of temperature for quenching.

Regarding dissipative effects, we estimated their impact by a scaling law: $\boldsymbol{\tau} : \dot{\boldsymbol{\varepsilon}} \sim \eta u^2 / L_{\text{c}}^2$ where η is the dynamic viscosity. To be conservative, we considered the characteristic length of vapour films $L_{\text{c}} \sim 1\,\text{mm}$ and large velocity $u \sim 1\,\text{m}\,\text{s}^{-1}$. The equivalent temperature variation is then $\eta u^2/(\rho c_{\text{P}} L_{\text{c}}^2)$. Taking η for water and vapour at 100 °C [89], equivalent temperature variations are gathered in Table 2.2.

	Water	Vapour
Characteristic values	100 K	1000 K
Related to pressure variation of 0.1 bar	10^{-3} K	10 K
Related to dissipative effects	10^{-4} K	10^{-2} K

Table 2.2: Comparison of temperature variations due to variations of pressure with temperature characteristic values in the case of quenching.

We saw that both terms have a negligible impact on energy variations for quenching, and thus can be neglected.

Concerning radiative effects the Stefan–Boltzmann law predicts that it scales with T_w to the power 4. Thus these phenomenon are more dominant in high temperatures. A study of radiation phenomena for water and water vapour gave the following conclusions:

- The solid can be modeled as a grey body whose emissivity is very case-dependent.
- The vapour can be considered as transparent.
- The liquid absorbs all the radiation. The majority of the heat absorbed lies in a thin layer close to the liquid vapour interface.

Details of the local phenomena analysis on radiation effects are given in Appendix A. Consequently, the contribution of radiation can be reasonably considered to only play at the interface, and not inside each phase. It can be removed from the monophasic energy conservation equation. What remains are then only convective and diffusion terms:

$$\rho c_{\mathrm{p}} \left(\frac{\partial T}{\partial t} + \left(\vec{u} \cdot \vec{\nabla} \right) T \right) = \vec{\nabla} \cdot k \vec{\nabla} T \tag{2.14}$$

Regarding the variations of the material characteristics, characteristic values for water (resp. water vapour) at 25 °C and 100 °C (resp. 100 °C and 900 °C) of ρ, c_{p} and k as well as the diffusivity $D = k/\rho c_{\mathrm{p}}$ computed at atmospheric pressure are gathered in Table 2.3.

		ρ ($\mathrm{kg\,m^{-3}}$)	c_{p} ($\mathrm{J\,m^{-3}\,K^{-1}}$)	k ($\mathrm{W\,m^{-1}\,K^{-1}}$)	D ($\mathrm{m^2\,s^{-1}}$)
Liquid	25 °C	997	4181	0.606	1.45×10^{-7}
	100 °C	958	4215	0.677	1.68×10^{-7}
Vapour	100 °C	0.59	2080	0.024	1.95×10^{-5}
	900 °C	0.18	2400	0.12	2.7×10^{-4}

Table 2.3: Thermal properties of water and water vapour at extreme temperatures [89].

Values in the water are nearly constant and can be considered as such. This is less true in the vapour as large temperature differences lead to a factor 10 of the diffusivity. Values shall ideally be taken as functions of the temperature. For the sake of simplicity, we considered mean values of the vapour phase between T_{sat} and T_w in quenching simulations, except for the conductivity. The values of k for different temperatures are gathered in Appendix E.

2.2.2 Energy conservation at the interface

The energy conservation being written inside each phase, we considered energy terms at the interface between the vapour and the liquid phases. We discriminated the two vapour and liquid phases with the subscripts V and L. The jump of a quantity

x was expressed as $[\![x]\!]$, and $\overline{x}$ stood for the mean value. For instance, if x_V^+ is the value of x in the vapour close to the interface, and x_L^- the value of x in the liquid close to the interface:

$$\begin{cases} [\![x]\!] = x_V^+ - x_L^- & (2.15) \\ \overline{x} = \dfrac{x_V^+ + x_L^-}{2} & (2.16) \end{cases}$$

We also called $\vec{n}$ the unit normal vector of the interface, directed from the liquid phase to the vapour phase. Surface tension was considered. However, no wetting with the solid part was considered in the present work so this phenomenon was out of the scope of this work.

2.2.2.1 General form

The transition layer between liquid and gaseous states is a few Ångströms thick. It can be considered as sharp. Thus no volume terms exist at the interface. The energy conservation can be deduced from the consideration of a fluid particle that would cross this interface. If this particle moves at a speed $\vec{u}$ when crossing the interface moving at $\vec{u_{\mathrm{I}}}$, the relative velocity of this particle to the interface reads $\vec{u} - \vec{u_{\mathrm{I}}}$. We shall notice that this velocity is not necessarily continuous across the interface. This consideration allowed us to easily write the conservation of mass at the interface by balancing the mass fluxes:

$$[\![\rho \left(\vec{u} - \vec{u_{\mathrm{I}}}\right) \cdot \vec{n}]\!] = 0 \tag{2.17}$$

This quantity that is continuous at the interface is the mass transfer rate $\dot{m}$ in $\mathrm{kg\,m^{-2}\,s^{-1}}$. In the context of phase change, this is the mass of fluid that is being vaporised or condensed. We represented it by a vector $\vec{\dot{m}}$ described in Figure 2.1. When this vector points towards the vapour phase, this is vaporisation. When $\vec{\dot{m}}$ points towards the liquid phase, this is condensation. As for the monophasic formulation, we will need the contribution of the kinetic energy. Thus, we wrote the momentum conservation equation. The terms at play at the interface are:

- the momentum of the fluid particle crossing the interface $(\rho\vec{u})\left(\vec{u} - \vec{u_{\mathrm{I}}}\right) \cdot \vec{n}$
- the action of stresses from both sides of the interface $\boldsymbol{\sigma} \cdot \vec{n}$
- the action of surface tension at the interface $\gamma_0 \kappa \vec{n}$

The momentum conservation equation at the interface reads:

$$[\![(\rho\vec{u})\left(\vec{u} - \vec{u_{\mathrm{I}}}\right) \cdot \vec{n}]\!] = [\![\boldsymbol{\sigma} \cdot \vec{n}]\!] + \gamma_0 \kappa \vec{n} \tag{2.18}$$

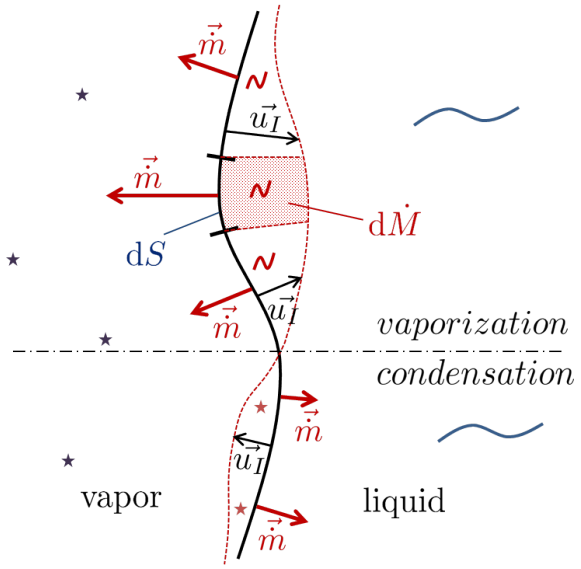

Figure 2.1: Schematic representation of the mass transfer rate vector. For vaporisation, the vector point towards the vapour. For condensation, it points towards the liquid.

Knowing that $\rho\left(\vec{u}-\vec{u_{\mathrm{I}}}\right)\cdot\vec{n}=\vec{\dot{m}}$ is continuous, the left-hand side can be factorised. On the other hand, multiplying the momentum jump equation by $\overline{\vec{u}}$ gives:

$$\frac{1}{2}\dot{m}[\![u^2]\!]=[\![\boldsymbol{\sigma}\cdot\vec{n}]\!]\cdot\overline{\vec{u}}+\gamma_0\kappa\vec{n}\cdot\overline{\vec{u}} \tag{2.19}$$

Regarding the energy conservation, the terms at play at the interface are:

- the energy flux of the fluid particle crossing the interface $\left(\rho e+\frac{\rho}{2}u^2\right)\left(\vec{u}-\vec{u_{\mathrm{I}}}\right)\cdot\overrightarrow{n}$
- the contributions of conductive and radiative heat fluxes from both sides of the interface $\left(\vec{q}+\vec{q_{\mathrm{R}}}\right)\cdot\vec{n}$
- the works of surface stresses from both sides of the interface $\boldsymbol{\sigma}\cdot\vec{u}$
- the works of surface tension at the interface $\gamma_0\kappa\vec{n}\cdot\vec{u_{\mathrm{I}}}$

The balance of all these terms at the interface leads to the following energy conservation equation:

$$\left[\!\!\left[\left(\rho e+\frac{\rho}{2}u^2\right)\left(\vec{u}-\vec{u_{\mathrm{I}}}\right)\cdot\vec{n}\right]\!\!\right]=[\![(\boldsymbol{\sigma}\cdot\vec{n})\cdot\vec{u}]\!]-[\![\left(\vec{q}+\vec{q_{\mathrm{R}}}\right)\cdot\vec{n}]\!]+\gamma_0\kappa\vec{n}\cdot\vec{u_{\mathrm{I}}} \tag{2.20}$$

The left hand side can also be factorised by $\dot{m}$. After replacing the kinetic energy part by its expression from the momentum jump equation, we got:

$$\dot{m}\,[\![e]\!]=\overline{\boldsymbol{\sigma}}\cdot[\![\vec{u}\cdot\vec{n}]\!]-[\![\left(\vec{q}+\vec{q_{\mathrm{R}}}\right)\cdot\vec{n}]\!]-\gamma_0\kappa\vec{n}\cdot\left(\overline{\vec{u}}-\vec{u_{\mathrm{I}}}\right) \tag{2.21}$$

As the fluid going through the interface undergoes a phase change process, the energy jump $[\![e]\!]$ is related to the phase change energy. The thermodynamics says that the energy jump of phase change written in terms of enthalpy $[\![h]\!]$ at a fixed pressure p is known, given by a linearised expression $\mathcal{L}+[\![c_\text{P}]\!](T-T_\text{sat})$ where $\mathcal{L}$ is the energy jump at that pressure p at the saturation temperature of the fluid $T = T_\text{sat}$.

Thus, by writing $e = h - \dfrac{p}{\rho}$, this leads to $[\![e]\!] = \mathcal{L} + [\![c_p]\!](T - T_{sat}) - \left[\!\left[\dfrac{p}{\rho}\right]\!\right]$. We also decomposed the Cauchy stress tensor: $\boldsymbol{\sigma} = -p\mathbb{1} + \boldsymbol{\tau}$ and rewrote the conductive heat flux with Fourier's law. After some algebraic considerations (see [19] for more details), we got the new energy jump equation form:

$$\dot{m}\left(\mathcal{L} + [\![c_\text{P}]\!](T - T_\text{sat}) + \overline{\left(\frac{1}{\rho}\right)}\left([\![p]\!] - \gamma_0\kappa\right)\right) = \overline{\boldsymbol{\tau}} \cdot [\![\vec{u}\cdot\vec{n}]\!] + [\![k\vec{\nabla}T\cdot\vec{n}]\!] - [\![\vec{q_\text{R}}\cdot\vec{n}]\!] \tag{2.22}$$

2.2.2.2 Local Phenomena Analysis

We saw above that dissipative works were negligible in regards to enthalpy variations. This is even more true in comparison with the enthalpy of vaporisation in the case of vapour and water, whose value is very large ($\mathcal{L} = 2.2564\,\text{J}\,\text{kg}^{-1}$ at atmospheric pressure). Similarly, pressure works are quite equivalent to the surface tension contribution and negligible in comparison with $\mathcal{L}$.

Concerning radiation, the contribution of the solid part is the only important term to consider in our system. It impacts the interface only from the vapour side, as water absorbs the majority of the electromagnetic waves: $-[\![\vec{q_\text{R}}\cdot\vec{n}]\!] = -\vec{q_\text{R}}\cdot\vec{n}$ (see Appendix A). We recall that $\vec{n}$ points towards the vapour phase. As $\vec{q_\text{R}}$ points towards the liquid phase, this term has a positive contribution to the energy jump as expected.

Moreover, we saw that the estimation of the thermodynamical equilibrium at the interface was a reasonable approximation. Thus at the interface $T \simeq T_\text{sat}$. Finally, the energy jump equation reads:

$$\dot{m}\mathcal{L} = [\![k\vec{\nabla}T\cdot\vec{n}]\!] - \vec{q_\text{R}}\cdot\vec{n} \tag{2.23}$$

If we remove the radiation contribution, this equations is also called the "Stefan condition".

To summarize:

- Radiation fluxes were considered to be localised at the interface and only from the vapour side.

- The influence of pressure variations on thermal energy variations was considered negligible (on each fluid as well as on the interface).
- Viscous dissipation was considered negligible in regards to thermal energy variations (on each fluid as well as on the interface).

2.3 Numerical framework for thermal analysis

The energy conservation equations being well posed, we needed to couple the monophasic formulation and the interface condition. Then this mathematical system must be integrated inside a numerical framework.

Several techniques exist to discriminate the different phases. Body fitted methods consist in separating the domain in subdomains with dedicated meshes. They are however not common in the case of gas liquid mixtures as it is rapidly tedious to keep track of all created subdomains. This is the reason why immersed methods suit better for phase change problems. Some methods allow to still follow the interface thanks to mesh deformation [75] or particle markers that enrich the mesh [67, 91, 92, 93]. Overall they allow the resolution of a single set of equations for the whole computational domain with variable material properties. These methods provide a rich and precise description of the interface but reveal limits for complex topologies that can appear in phase change systems. Consequently, implicit representations are preferred. The Volume Of Fluid method (VOF) [65, 68] consists in advecting a color function that represents the volume fraction of one phase (see Figure 2.2a). It allows mass conservation by construction but requires specific methods to deduce the interface which is not properly depicted. The other common option is the Level Set (LS) method. The interface is described by a distance function that is convected to keep track of its motion (see Figure 2.2b). The mass conservation is not so easily respected, and the method requires a fine enough mesh at the interface as well as quantitative error estimation. But it offers a better description of complex interfaces [66, 70, 72, 71, 94, 95, 96]. It is easy to implement in the Finite Element Method, allows to change rapidly the physical properties for each immersed structure and allows proper computation of normals and curvatures. These are the reasons why this latter method was chosen in the present work.

2.3.1 Level Set Method

We call $\Omega \subset \mathbb{R}^n$ the computational domain where n is the space dimension and Γ an interface between two sub-domains Ω_1 and Ω_2. The Level Set method consists

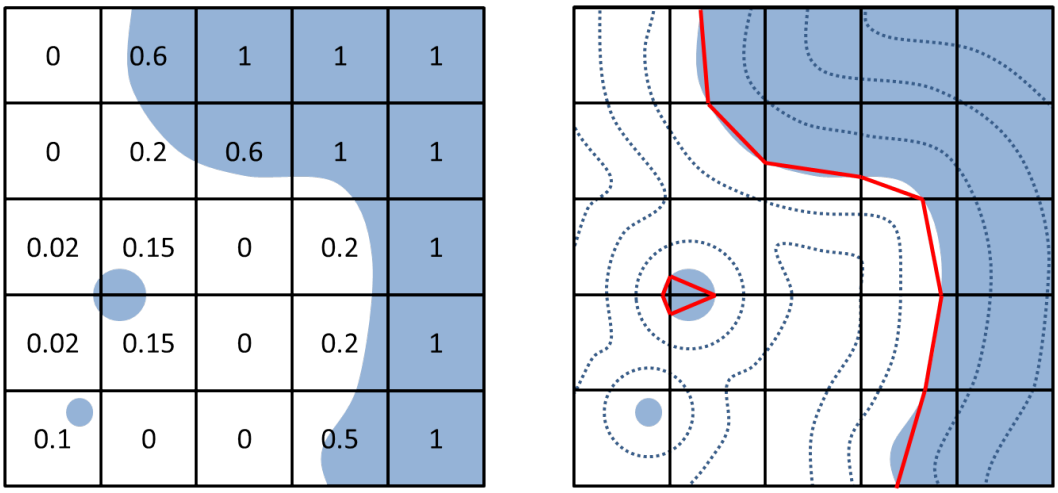

(a) Volume Of Fluid method. A volume fraction function identifies one phase from another. The interface can be reconstructed providing a sufficient mesh precision.

(b) Level Set method. A volume fraction function identifies one phase from another. The interface can be reconstructed providing a sufficient mesh precision.

Figure 2.2: Comparison between the VOF and the LS methods.

in considering a distance function $(\vec{x}, t) \longmapsto \alpha$ from the interface Γ:

$$\begin{cases} \alpha(\vec{x}, t) = d(\vec{x}, I) & \text{if } \vec{x} \in \Omega_1 \\ \alpha(\vec{x}, t) = -d(\vec{x}, I) & \text{if } \vec{x} \in \Omega_2 \\ \alpha(\vec{x}, t) = 0 & \text{if } \vec{x} \in \Gamma \end{cases} \tag{2.24}$$

where d stands for the signed Eulerian distance function operator.

The interface is therefore located on the zero values of this function. In the case of first order interpolation in tetrahedral meshes, the interface is shaped by a hyperplan simplex mesh (a set of segments in 2D and a set of triangles in 3D). Then the sign of this function allows to discriminate each phase and to attribute the associated material properties. In our case, Ω_1 stands for the vapour domain and Ω_2 stands for the liquid domain.

To keep track of the evolution of the interface in time, α must be updated accordingly. In the case of two passive fluids without phase change, the interface moves along with fluid particles. Thus α must respect the following convection equation:

$$\frac{\mathrm{D}\alpha}{\mathrm{D}t} = \frac{\partial \alpha}{\partial t} + (\vec{u} \cdot \vec{\nabla})\alpha = 0 \tag{2.25}$$

However, in the presence of phase change, the interface velocity relative to the fluid is not null. Thus, the interface velocity $\vec{u_{\mathrm{I}}}$ has to be taken into account:

$$\frac{\partial \alpha}{\partial t} + (\vec{u_{\mathrm{I}}} \cdot \vec{\nabla})\alpha = 0 \tag{2.26}$$

$\vec{u_{\mathrm{I}}}$ is a function of the fluid velocity and of the phase change mass transfer.

An important feature of this function is that it is easy to recover the normal $\vec{n}$ and the signed curvature κ_α of the interface thanks to spatial derivatives:

$$\begin{cases} \vec{n} = \dfrac{\vec{\nabla}\alpha}{\|\vec{\nabla}\alpha\|} & (2.27) \\ \kappa_\alpha = \vec{\nabla} \cdot \left(\dfrac{\vec{\nabla}\alpha}{\|\vec{\nabla}\alpha\|} \right) & (2.28) \end{cases}$$

Doing so, $\vec{n}$ points toward the vapour phase. κ_α is positive when the vapour phase is locally concave and the liquid phase convex, and inversely as shown in Figure 2.3.

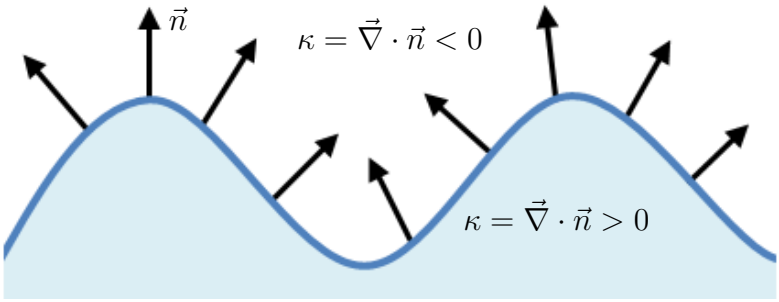

Figure 2.3: Description of the sign of the curvature. κ is positive when the vapour phase is locally concave and the liquid phase convex, and negative otherwise.

Another important feature is that if the distance property is respected, then anywhere in the domain $\|\vec{\nabla}\alpha\| = 1$. In practice, the velocity field is usually complex and the convection of α does not guarantee to maintain the distance property. As long as the interface Γ is properly convected this is not a big issue. However, if α is too distorted the resolution of the LS convection can be complicated. It can even lead to non negligible errors in the interface tracking [97].

This is the reason why the LS has to be reinitialised, meaning that the distance property must be recomputed without changing Γ. This reinitialisation is by itself a source of error on the mass conservation [98] and attention should be paid on the employed method. The frequency of reinitialisation is also an important parameter as the less the LS is reinitialised and the fewer error are made.

The CIMlib-CFD numerical framework gives the possibility to choose between three different approaches: a geometrical reinitialisation, an auto-reinitialisation and a reactive-convection reinitialisation. The first option to reinitialise the LS is to do it geometrically. The idea is simple: to find the cells crossed by Γ, to reconstruct Γ thanks to the values of α on the nodes close to Γ, and then to deduce from it the distance from Γ of all the nodes. Some methods have been developed to optimise this exploration [99, 100]. The second and third options rely on the resolution of the so-called "Hamilton–Jacobi" equation:

$$\frac{\mathrm{d}\alpha}{\mathrm{d}\tau} + s(\alpha)\left(\|\vec{\nabla}\alpha\| - 1\right) = 0 \tag{2.29}$$

where τ is a virtual time and s is the sign function. The steady state solution of this equation is the function α we are looking for. This equation is thus solved for a long enough time to get close to this steady state. The time depends on how far α is from the analytical distance function. This method has been upgraded to improve the mass conservation with the addition of a convective reactive term and its integration inside the LS convection equation explicitly [101] or implicitly [98]. A deep comparison of these approaches was out of the scope of this work and the geometrical method was chosen for its simplicity of use.

2.3.2 Smoothed interface approach

Working with immersed interfaces, the computation was done on one single domain. Thus material properties had to be different depending on the sub-domain. The LS was then used to discriminate the two phases. To do so, a Heaviside function $\alpha \longmapsto H_\alpha$ related to the interface Γ was considered. Its value is 0 on one domain, and 1 on the other. It was used as a flag to determine all the considered properties: the density ρ, the dynamic viscosity η, the specific heat capacity c_P and the thermal conductivity k:

$$\begin{cases} \rho = H_\alpha \rho_\mathrm{V} + (1 - H_\alpha)\rho_\mathrm{L} & (2.30) \\ \eta = H_\alpha \eta_\mathrm{V} + (1 - H_\alpha)\eta_\mathrm{L} & (2.31) \\ c_\mathrm{P} = H_\alpha \dfrac{(\rho c_\mathrm{P})_\mathrm{V}}{\rho} + (1 - H_\alpha)\dfrac{(\rho c_\mathrm{P})_\mathrm{L}}{\rho} & (2.32) \\ \dfrac{1}{k} = \dfrac{H_\alpha}{k_\mathrm{V}} + \dfrac{(1 - H_\alpha)}{k_\mathrm{L}} & (2.33) \end{cases}$$

Since ρ was mixed using an arithmetic law, this means that H_α was comparable to a volume fraction. c_P was then mixed accordingly, as it is a specific entity. For k, a geometric mixing law has been shown to improve the continuity of fluxes at the interface [102, 103].

However, the question of the interface had to be raised. The classical Heaviside function is a discontinuous function at the interface. This would create discontinuous properties inside the domain. For example, in the case of water and water vapour, the density would jump from around $1\,\mathrm{kg\,m^{-3}}$ to around $1000\,\mathrm{kg\,m^{-3}}$ between two mesh nodes. This is known to create stability problems. A solution is then to regularise the transition between the two phases. This was done by considering a smoothed Heaviside function with an interface thickness ε (represented in Figure 2.4a):

$$\begin{cases} H_\alpha = 1 & \text{if } \alpha > \varepsilon \\ H_\alpha = \dfrac{1}{2}\left(1 + \dfrac{\alpha}{\varepsilon} + \dfrac{1}{\pi}\sin\left(\dfrac{\pi\alpha}{\varepsilon}\right)\right) & \text{if } |\alpha| \leq \varepsilon \\ H_\alpha = 0 & \text{if } \alpha < -\varepsilon \end{cases} \tag{2.34}$$

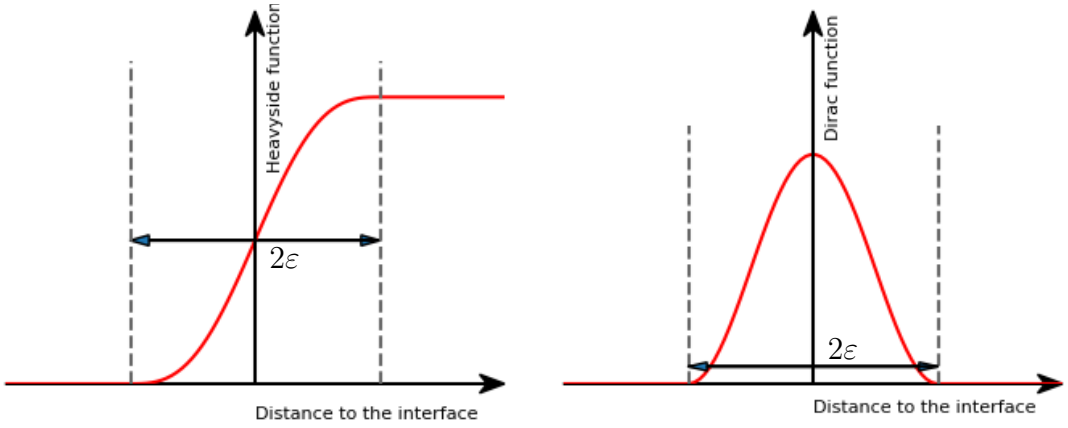

(a) Smoothed Heavyside function H_α. *(b) Smoothed Dirac function δ_α.*

Figure 2.4: Shapes of interfacial functions H_α and δ_α in the context of the smoothed interface and Continuous Surface Force approach. ε is the interface thickness.

2.3.3 Continuous Surface Force method

Immersed methods also need a designed solution to include surface terms such as surface tension and phase change. Sharp terms are also known to cause numerical instabilities. Working with smoothed interface, the natural choice was to use the Continuous Surface Force approach. The idea was to spread surface terms over the smoothed interface to turn them into volume terms with the help of the LS. Doing so, a proper monolithic formulation could be solved once to account for both phases as well as surface terms. This consideration had been shown to bring stability to multiphase flow solvers with a simple implementation thanks to pioneer works ([91,

104, 96]), even though it is at a price of some precision loss [105]. The results of preexisting implementation and improvements of this method was used [106].

Surface terms were turned into volume terms with the help of the smoothed Dirac function $\alpha \longmapsto \delta_\alpha$ (see Figure 2.4b). It is defined as the derivative of H_α with respect to α. Thus:

$$\begin{cases} \delta_\alpha = 0 & \text{if } |\alpha| > \varepsilon \\ \delta_\alpha = \dfrac{1}{2\varepsilon}\left(1 + \cos\left(\dfrac{\pi\alpha}{\varepsilon}\right)\right) & \text{if } |\alpha| \leq \varepsilon \end{cases} \tag{2.35}$$

δ_α being the derivative of H_α, this entails the following relationships:

$$\begin{cases} \vec{\nabla} H_\alpha = (\vec{\nabla}\alpha)\delta_\alpha & (2.36) \\ \dfrac{\partial H_\alpha}{\partial t}(\alpha) = \dfrac{\partial \alpha}{\partial t}\delta_\alpha & (2.37) \end{cases}$$

2.3.4 Phase Change model

The energy jump equation entails a heat flux jump that is not straightforward to implement. The common consideration of saturated conditions simplifies the problem. However, in subcooling conditions, the jump has to be properly computed. Two considerations are popular:

- To allow overheating and subcooling of the interface by computing the local mass transfer rate $\mathrm{d}\dot{M}$ through a proportional law, with a coefficient r empirically chosen:

  $$\mathrm{d}\dot{M} = r(T - T_{\text{sat}})\,\mathrm{d}V \tag{2.38}$$

  where T is the temperature field and T_{sat} the saturation temperature at atmospheric pressure.

  Lee et al. [64] were the first to implement this model, which is still used today (see for example [32]). An issue of this method is to correctly set the value of r. One option is the estimation of time constants of vaporisation and condensation with enthalpy considerations [79], extended with maximum values of mass transfer rate to avoid numerical instabilities [65]. Srinivasan et al. [13] linked r to geometrical considerations, even though an empirical parameter was still used.

- To consider the interface to always remain at the equilibrium thermodynamic saturation temperature, and to determine the mass transfer rate through a difference of heat flux:

  $$\mathcal{L}\,\mathrm{d}\dot{M} = [\![\vec{q}\cdot\vec{n}]\!]\,\mathrm{d}S \tag{2.39}$$

where $\mathcal{L}$ is the latent heat of vaporisation, $\vec{q}$ the heat flux, $\vec{n}$ the normal vector of the interface, $\mathrm{d}S$ the infinitesimal surface and $[\![x]\!]$ represents the jump of the quantity x across the interface.

A simplification is to only consider the heat flux from the vapour phase [81, 21, 107, 19], working or not in saturated conditions. Using the VOF method, Welch et al. [68] reconstructed the interface within a cell to determine the temperature gradients from both sides, while Sun et al. [108] considered a heat flux balance on the cells located on the interface and on the saturated cells directly close to the interface. Welch et al. [68] and Sato et al. [69] computed temperature gradients between interface and cell centers on cells that intersect the interface thanks to their sharp interface framework.

In the present work, the latter consideration was taken, that was believed to rely less on arbitrary coefficients. One difficulty of this modeling is however to properly compute temperature gradients from both sides of the interface. A possible approach is to capture every quantity straight at the interface while preserving discontinuities thanks to appropriated methods. In the context of Volume Of Fluid, the framework presented by Tanguy et al. [105] involving the Ghost Fluid method or by Sato et al. [69] with a dedicated Sharp Interface approach are examples of solutions.

In our case the combination of the Continuous Surface Force approach and the heat flux jump computation has to be consistent. To do so, a complete fictitious interface was considered for the phase change distribution and for the temperature profile (see Figure 2.5).

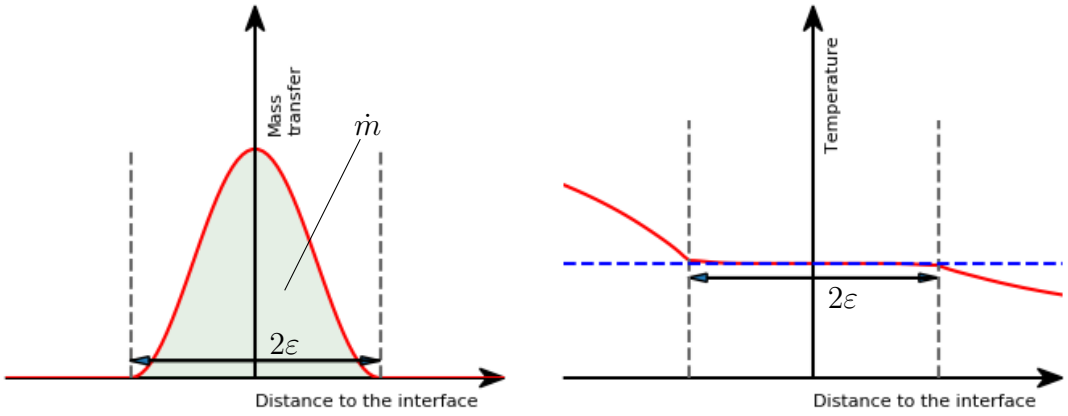

(a) Volume mass transfer rate distribution.

(b) Constant interface temperature model.

Figure 2.5: Interfacial temperature and mass transfer profiles in the context of smoothed interface and Continuous Surface Force approach.

Thus the jump was not computed on one straight surface that usually features the interface, but on the border of this thick interface. To the authors' knowledge, such consideration was new and demanded the design of a dedicated method that is presented hereafter.

The mass transfer term was then integrated in the energy conservation equation thanks to the Dirac function:

$$\rho c_p \left(\frac{\partial T}{\partial t} + \left(\vec{u} \cdot \vec{\nabla} \right) T \right) = \vec{\nabla} \cdot k \vec{\nabla} T - \left(\mathcal{L} \vec{\dot{m}} + \vec{q_R} \right) \cdot \vec{\nabla} \alpha \delta_\alpha \tag{2.40}$$

The scalar product of $\vec{\dot{m}}$ with $\vec{\nabla}\alpha$ and not $\vec{n}$ guarantees that the integral of the Dirac equals 1 over the interface even if $\|\vec{\nabla}\alpha\| \neq 1$. The radiation contribution is positive as $\vec{q_R}$ and $\vec{\nabla}\alpha$ are of opposite direction.

With such modeling of the phase change, the associated interface velocity $\vec{u_I}$ could be deduced. In absence of velocity field, the LS convection equation then reads:

$$\frac{\partial \alpha}{\partial t} - \frac{\vec{\dot{m}}}{\rho} \cdot \vec{\nabla} \alpha = 0 \tag{2.41}$$

A proper demonstration of this term is done in the next chapter. Moreover in appendix B, a demonstration is undertaken to prove that these formulations are equivalent to sharp interface formulations for $\varepsilon \to 0$.

2.3.5 Discretisation Scheme

The coupling between the energy conservation equations and the Level Set framework being set, we embedded this formulation inside a numerical framework. Most of the studies in the literature of phase change simulation are done with Eulerian formulations [64, 65, 66, 73, 19, 74, 76]. This is justified by the large deformations of liquid vapour interfaces that prevents a tracking of interface with nodes. The Arbitrary Lagrangien Eulerian approach can be a solution to overcome this difficulty [67, 75], but was not considered in this work.

Regarding discretisation schemes, Finite Difference are sometimes considered [70, 72, 71, 73]. However Finite Volume formulations are usually preferred [65, 66, 68, 19, 74] as it guarantee the mass conservation.

The Finite Element Method (FEM) is less common for the simulation of phase change systems [75]. It offers a better error predictability, a possibility to increase the order of elements for a better precision and allows mixed formulation. This is the reason why we worked with this formulation.

The considered equations to be solved can be represented by a single scalar transient convection-diffusion-reaction equation (CDR). Given a scalar variable φ,

the general formulation of the CDR equation over a spacial domain Ω for a time $t \in [t_i, t_f]$ reads:

$$\frac{\partial \varphi}{\partial t} + \left(\vec{u} \cdot \vec{\nabla}\right) \varphi - \vec{\nabla} \cdot (D\vec{\nabla}\varphi) + r\varphi = f \tag{2.42}$$

where D is a diffusion coefficient, r a reaction coefficient and f a source term.

When working with FEM, this "strong" formulation needs to be transformed into a "weak" formulation with the introduction of a test function φ:

$$\begin{cases} \text{Find } \varphi \in S_h \text{ such that } \forall w \in W_h : \\ \left\langle \dfrac{\partial \varphi}{\partial t} + \left(\vec{u} \cdot \vec{\nabla}\right) \varphi, w \right\rangle + \left\langle D\vec{\nabla}\varphi, \vec{\nabla} w \right\rangle + \langle r\varphi, w \rangle = \langle f, w \rangle \end{cases} \tag{2.43}$$

where S_h and W_h are standard finite element spaces. They usually stand for the discretised space of the physical spacial domain Ω considered. $\langle \varphi, \psi \rangle = \int_\Omega \varphi \cdot \psi \, \mathrm{d}\Omega$ is the standard scalar product in $L^2(\Omega)$. This products holds for scalars or vectors. More details on these mathematical aspects can be found in [80] on which this present work relied.

This type of problem had already been studied with FEM. The resolution of this equation as such is numerically limited by the action of the convective term [82, 109, 110]. Thus, stabilisation techniques had been developed, and especially the Streamline Upwind Petrov Galerkin (SUPG) stabilisation [111, 112] and the Shock Capturing Petrov Galerkin (SCPG) [113] stabilisation. These are two terms that are added to the weak formulation as scalars products of the residual of the equation $\mathcal{R}(\varphi)$ and of a function of φ. The residual $\mathcal{R}(\varphi)$ is the difference between the left-hand side and the right-hand side of the equation. Doing so, these terms are expected to vanish when the linear solver converge to the discrete solution as in this case $\mathcal{R}(\varphi) \to 0$. The stabilised weak formulation of the CDR equation then reads:

$$\begin{cases} \text{Find } \varphi \in S_h \text{ such that } \forall w \in W_h : \\ \left\langle \dfrac{\partial \varphi}{\partial t} + \left(\vec{u} \cdot \vec{\nabla}\right) \varphi, w \right\rangle + \left\langle D\vec{\nabla}\varphi, \vec{\nabla} w \right\rangle + \langle r\varphi, w \rangle \\ + \underbrace{\sum_K \left\langle \mathcal{R}(\varphi), \tau_{\text{SUPG}} \left(\vec{u} \cdot \vec{\nabla}\right) w \right\rangle_K}_{\text{streamline upwind}} + \underbrace{\sum_K \left\langle \mathcal{R}(\varphi), \tau_{\text{SCPG}} \left(\tilde{\vec{u}} \cdot \vec{\nabla}\right) w \right\rangle_K}_{\text{discontinuity capturing}} = \langle f, w \rangle \end{cases} \tag{2.44}$$

where K is the element index, $\tilde{\vec{u}}$ is an auxiliary vector, function of the gradient of φ. τ_{SCPG} and τ_{SCPG} are stabilisation coefficients usually dependent on numerical parameters like the mesh size, the Reynolds and Péclet number, etc. The SUPG term controls the oscillations in the direction of the velocity trajectories for convection dominated regimes. The SCPG term adds numerical diffusion in the neighborhood

of sharp gradients. More details on these methods, their benefits and on the way to compute τ_{SCPG}, τ_{SCPG} and $\tilde{\vec{u}}$ can be found in [82, 80, 109, 110, 111, 112, 113].

2.4 Heat Flux Jump Computation method

Working with a smoothed interface, the quantities that vary inside the interface lead to non physical values of the temperature gradients. To properly compute the heat flux jump across the interface, temperature gradients were considered from the borders of the interface. Doing so, a method had to be designed to capture this value and propagate it on all the nodes of the interface.

2.4.1 Description of the extension method

The propagation of the heat flux through the interface relies on a common technique explained by Aslam et al. [114]. The general idea of this technique is to extend on Ω a scalar quantity q_0 that lives on Ω_0 (generally Ω and Ω_0 form a partition of the computation space). The extension is done by following streamlines of a normalised vector field $\vec{n}$ through an interface Γ that separates the two domains Ω and Ω_0. In other words, the solution q equals q_0 on Ω_0, and on Ω, q is set constant on the streamlines of $\vec{n}$, its value being the value of q_0 on the intersection of Γ with the streamline. This corresponds to the resolution of the following system:

$$\begin{cases} q = q_0 & \text{on } \Omega_0 \quad (2.45) \\ \vec{n} \cdot \vec{\nabla} q = 0 & \text{on } \Omega \quad (2.46) \end{cases}$$

(2.45) is solved immediately, and is used as a Dirichlet condition on Γ for the resolution of (2.46). For frontiers of Ω that are at the vicinity of the calculation domain, a Neumann condition of null flux is used.

The second equation by itself is not numerically unconditionally stable, so a diffusion term is added:

$$\vec{n} \cdot \vec{\nabla} q - \vec{\nabla} \cdot (\lambda \vec{\nabla} q) = 0 \quad (2.47)$$

This choice is motivated by its simplicity of implementation. The value of λ should be as small as possible in Ω to limit its impact on the solution, but large enough to stabilise the solver. If h is the mesh size, a dimensional analysis leads to:

$$\frac{|\vec{n}| q}{h} \simeq \frac{\lambda q}{h^2} \quad (2.48)$$

As $\vec{n}$ is normalised, the condition reads $\lambda \simeq h$. λ was chosen at most of the same order of magnitude as h.

Before implementing this method for the heat flux jump computation, it was tested on two test cases: the extension of a scalar field that has a cylindrical symmetry on a disc, and the extension of a scalar field on a square with a sharp angle. For both cases, the field $\vec{n}$ is based on the gradient of the Level Set α (the signed distance function in respect to the interface that is positive inside Ω). As a result, $\vec{n}$ is normal to the interface.

2.4.2 Benchmarks

2.4.2.1 The disc case

The domain Ω is a disc of radius $R = 0.2$ centered on the origin of a 1×1 square domain (see Figure 2.6a). The source field q_0 is defined in the cylindrical coordinates system (r, θ) such as:

$$q_0(r, \theta) = -2r \tag{2.49}$$

$\vec{n}$ is defined as:

$$\vec{n}(r, \theta) = -\vec{e_r} \tag{2.50}$$

Thus $\vec{n}$ has a singularity at the origin.

The case was implemented on an unstructured mesh of triangles of characteristic size $h = 10^{-2}$ with $\lambda = 10^{-3}$. Results projected on the horizontal axis of the disc are plotted on Figure 2.6b.

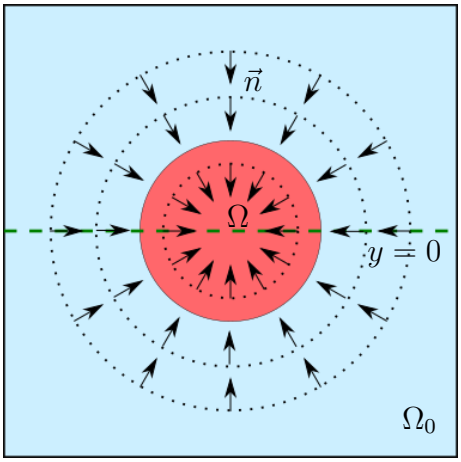

(a) Schematic description of the disc test case.

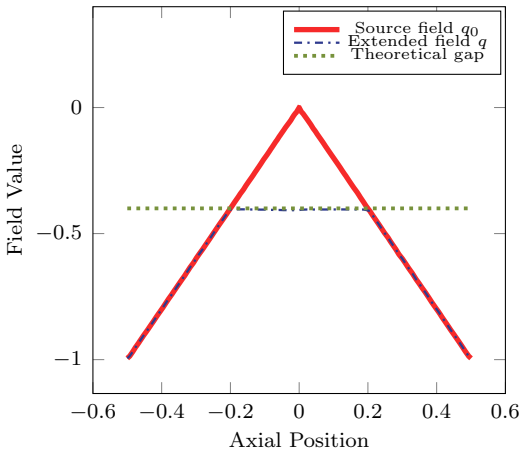

(b) Source and extended field values on the radial axis $y = 0$.

Figure 2.6: The disc test case: an initial radial scalar field is extended on a disc (the red zone) following the radial vector field (the black arrows). Results projected on the green dotted line are shown in (b).

The extension of q_0 over Ω is well computed, and the singularity of the vector field $\vec{n}$ does not cause issues to the solver. Errors can be controlled by refining the mesh.

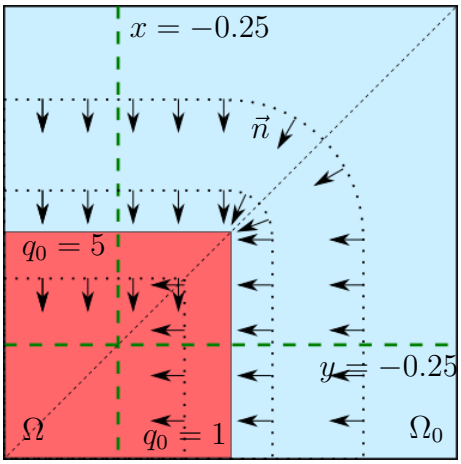

(a) Schematic description of the square test case.

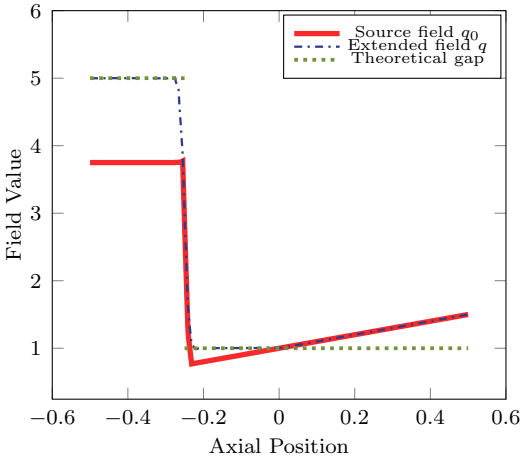

(b) Source and extended field values on the horizontal axis $y = -0.25$.

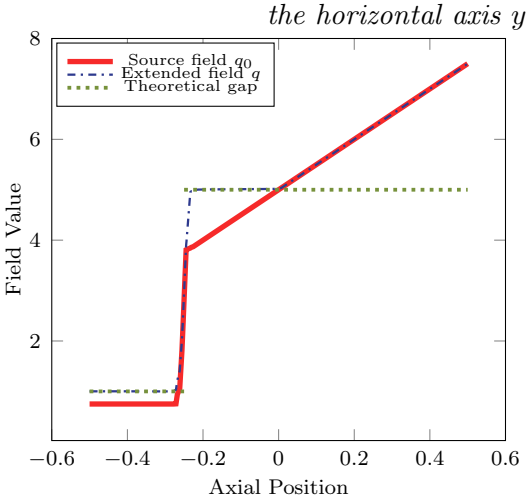

(c) Source and extended field values on the vertical axis $x = -0.25$

Figure 2.7: The square test case: an initial radial scalar field is extended on a square (the red zone) following a vector field normal to the square interface (the black arrows). Results projected on the horizontal and vertical green dotted lines are shown in (b) and (c).

2.4.2.2 The square case

The domain Ω is for this case a square of 0.5×0.5 placed on the lower-left corner of the resolution space, still being a 1×1 square (see Figure 2.7a). The upper-right corner of Ω is located on the (0,0) point. The source field q_0 is defined as the scalar product of the vector field $(-1-x)\vec{e_x} + (-5-5y)\vec{e_y}$ with $\vec{n}$, still defined as the gradient of the signed distance function of the square (positive inside the square). In the lower-right corner of the domain, $\vec{n} = (-1, 0)$ and q_0 is the plane $z = x + 1$. In the upper-left corner, $\vec{n} = (0, -1)$ and q_0 is the plane $z = y + 5$. The transition between the two planes is made smoothly in the upper-right corner, and is made through a discontinuity on the diagonal of Ω. q_0 is defined in order to have two different values on each face of Ω: 5 on the upper face, and 1 on the left face.

The case was implemented on an unstructured mesh of triangles of characteristic size $h = 1{\times}10^{-2}$ with $\lambda = 3{\times}10^{-3}$. Results projected on horizontal and vertical axes of the square are plotted on Figure 2.7b and Figure 2.7c.

The extension of q_0 over Ω is well computed. The transition of value near the singularity of the vector field $\vec{n}$ is properly treated. Errors can be controlled by refining the mesh.

2.4.3 Heat flux jump

2.4.3.1 Computation of jumps over a smooth interface

Back to the phase change problem, the idea was to apply this method on each side of the interface to access the values of the balance of heat fluxes on every point of the interface. The method was applied with the scalar field $\dfrac{\vec{\nabla}\alpha}{\|\vec{\nabla}\alpha\|} \cdot (k\vec{\nabla}T)$ to determine the heat fluxes on the vapour and on the liquid sides.

A first simple approach would be to choose Ω as the domain of the interface, and Ω_0 the union of the vapour and the liquid domains for both cases (it is useless to further project the heat flux from one phase on the whole domain of the other phase).

However, due to diffusion effects, the transition from T_{sat} on the interface to the temperature profile diffuses on a few elements. A "safety margin" was taken to make sure that the temperature profile is well established. This is the reason why the heat flux value to project was chosen at a distance equal to h from the isovalue $\alpha = \pm\varepsilon$. Moreover, to further reduce the influence of the diffusion term λ, the end of Ω was considered at a distance of $3h$ away from the isovalue $\alpha = \pm\varepsilon$. The Figure 2.8 summarises these considerations. Doing so, the heat flux jump is well defined and constant on the domain $\{\alpha \in [\varepsilon; \varepsilon]\}$.

As an illustration and test purpose, this method was implemented on a simple 2D test case: a 1×1 square with a vertical interface $x = 0$ at its center (see Figure 2.9a).

The field to project from the left side of the interface is $q_{0L} = 5000y(1 + x)$, and the associated domain Ω_L is located between the axes $x = -0.07$ and $x = 0.05$. The field to project from the right side of the interface is $q_{0R} = 10000y(1 + x)$, and the associated domain Ω_R is located between the axes $x = -0.05$ and $x = 0.07$. $\vec{n}_L$ and $\vec{n}_R$ are taken normal to the interface, but of opposite directions.

The case was implemented on an unstructured mesh of triangles of characteristic size $h = 10^{-2}$ with $\lambda = 10^{-3}$. Results projected on the central vertical axis and on

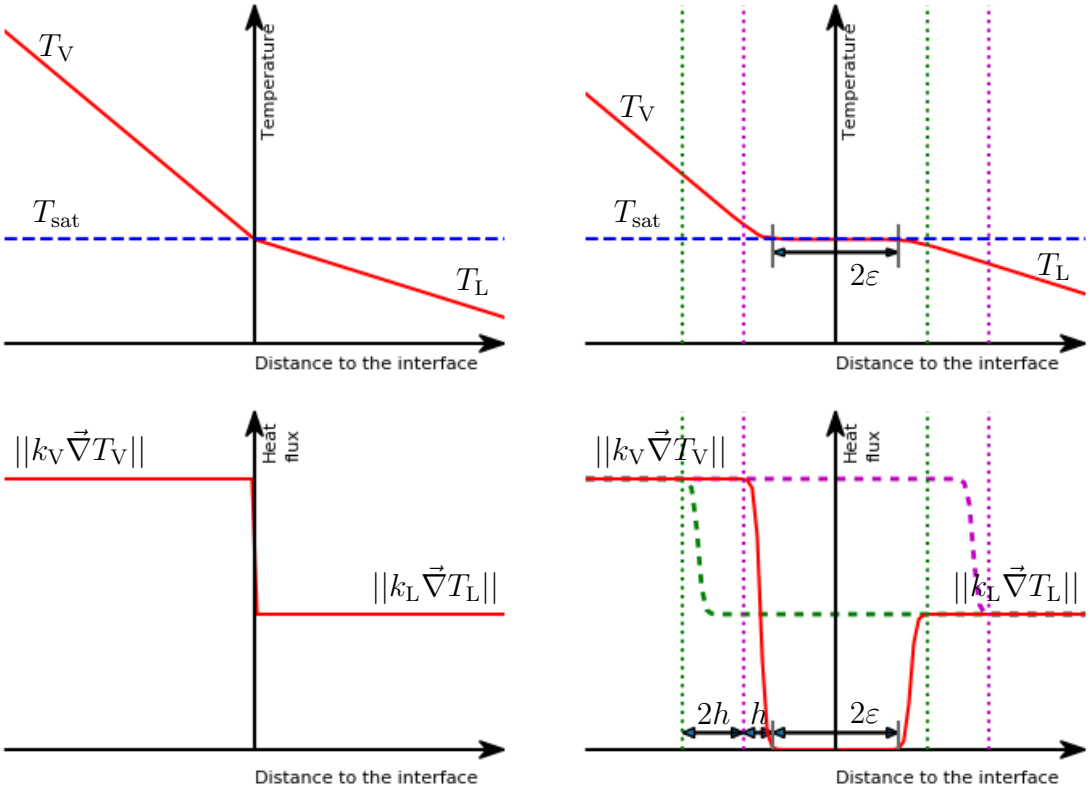

(a) Sharp interface configuration *(b) Smooth interface configuration*

Figure 2.8: Modeling of the interface temperature and heat flux profiles with a Continuous Surface Force approach. In order to well capture the heat flux jump, heat flux values are extended from a distance $\varepsilon + h$ of the interface center. The end of the extension domain is located at a distance $\varepsilon + 3h$ of the interface center to reduce diffusion impacts on the extended value.

the horizontal axis $y-0.25$ are plotted on Figure 2.9b and Figure 2.9c. The extension was well computed, and errors were in the order of magnitude of the mesh precision.

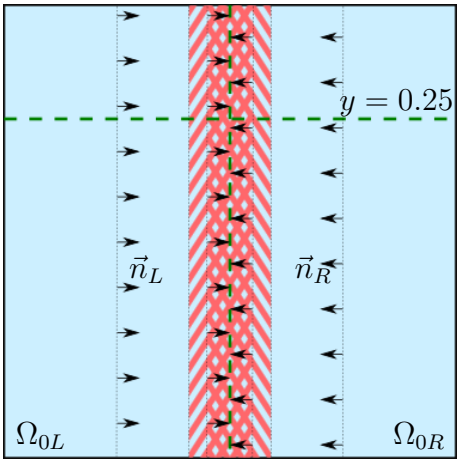

(a) Schematic description of the Interface Case

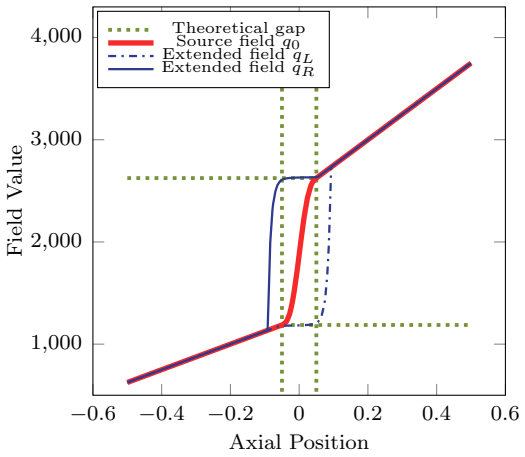

(b) Source and extended field values on the horizontal axis $y = 0.25$

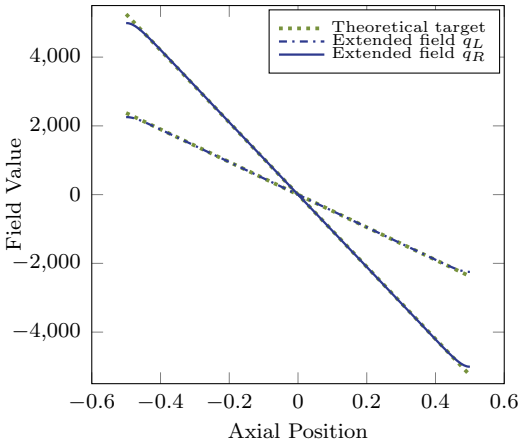

(c) Theoretical and extended field values on the centered vertical axis $x = 0$

Figure 2.9: The interface test case — an initial radial scalar field is extended from both sides of a thick interface (the red zone) following the normal vector field (the black arrows). Results projected on the horizontal and vertical green dotted line are shown in (2.9b) and (2.9c).

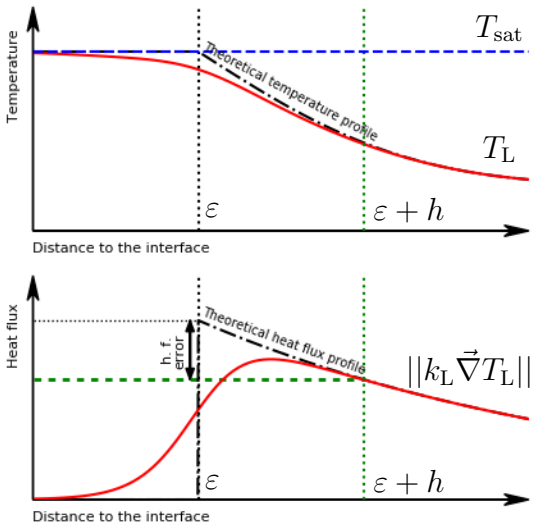

(a) Graphical illustration of the safety margin

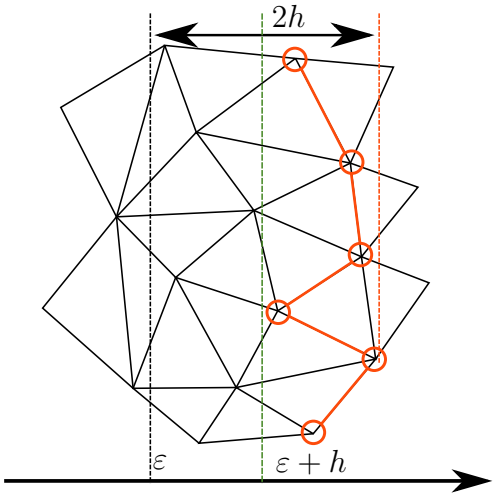

(b) Schematic description of the selection of reference points of the extension method

Figure 2.10: Description of the "safety margin" taken for the extension of the heat flux that avoids errors due to the continuity of the temperature gradient. Heat flux values are taken from points away of at least $\varepsilon + h$ from the interface. As the mesh in not structured, the effective distance varies from one point to another up to $\varepsilon + 2h$.

2.4.3.2 Precision of the method

As the extended heat flux is located one mesh size away h from the boundary of the interface, an error is made, which is proportional to h (see Figure 2.10a). Noting s the position of the boundary interface, and taking the distance function α, a linear approximation on q around s reads:

$$q(s+h) = q(s) + \frac{\partial q}{\partial \alpha}(s)h + o(h) \tag{2.51}$$

Extending q from the position $s + h$ instead of s thus leads to an error $\dfrac{\partial q}{\partial \alpha}(s)$. Furthermore, unstructured mesh had been used. The evaluation of points $\varepsilon + h$ away from the interface used as reference points for the extension method leads at most to a doubled "safety margin", as shown on Figure 2.10b.

Considering only conductive heat fluxes $q = \vec{q} \cdot \vec{\nabla}\alpha / \|\vec{\nabla}\alpha\| = -k\partial T/\partial\alpha$, this leads to a maximum error on $\dot{m}$:

$$|\Delta \dot{m}| \quad \propto \quad \frac{1}{\mathcal{L}} \sum_{L,V} k \left| \frac{\partial^2 T}{\partial \alpha^2} \right| 2h \tag{2.52}$$

This order 1 precision constrains the method to have fine meshes on the interface to handle large heat flux gradients. The presented mass transfer modeling was associated to a thermal equation and a Level Set convection equation. This coupling was applicable to solve diphasic and "static" (no fluid velocity) thermal systems with phase change. Thus only divergence free cases were tackled at first, meaning equal density between phases.

2.4.4 Stabilisation

We considered a purely diffusive system where all the phases had the same density ρ. In this configuration, equation (2.40) can be rewritten as follow:

$$\rho c_{\mathrm{p}} \frac{\partial T}{\partial t} = \vec{\nabla} \cdot \left(k \vec{\nabla} T \right) - \mathcal{L} \left(\dot{\vec{m}} \cdot \vec{\nabla} \alpha \right) \delta_\alpha \tag{2.53}$$

We recall that in the absence of velocity, the LS convection equation (2.41) reads:

$$\frac{\partial \alpha}{\partial t} - \frac{\dot{\vec{m}}}{\rho} \cdot \vec{\nabla} \alpha = 0 \tag{2.54}$$

In a perfect system there is an equivalence between the condition $T = T_{\mathrm{sat}}$ at the interface and the formulation of the source term $-\mathcal{L} \left(\dot{\vec{m}} \cdot \vec{\nabla} \alpha \right) \delta_\alpha$ in addition to the computation of the mass transfer thanks to the Heat Flux Jump Computation $\dot{\vec{m}} = \left[\!\left[k \vec{\nabla} T \cdot \dfrac{\vec{\nabla} \alpha}{\| \vec{\nabla} \alpha \|} \right]\!\right]$: formulated this way, the system theoretically maintains the interface temperature at T_{sat}.

The proposed system is theoretically consistent, as the formulation tends toward the sharp interface formulation for small ε. However, the conservation of T_{sat} is unfortunately not ensured as such. Among other reasons, overshooting effects appear. Moreover the conductivity jump leads to stronger diffusion effects on the liquid side that tends to cool down the interface.

To guaranty the efficiency of the method, a penalisation term in the form of a reactive term $A \delta_\alpha \left(T - T_{\mathrm{sat}} \right)$ was added, A being a sufficiently large parameter. In the present work, we took a value of $10^6 \, \mathrm{W \, K^{-1} \, m^{-2}}$, the order of magnitude of $\mathcal{L} \times 1 \, \mathrm{K}$. This formulation guarantees the conservation of T_{sat} on the interface.

$\vec{\dot{m}}$ being computed thanks to the heat flux jump, the final isochoric diphasic thermal system reads:

$$\begin{cases} \rho c_{\text{p}} \dfrac{\partial T}{\partial t} + A(T - T_{\text{sat}})\delta_\alpha = \vec{\nabla} \cdot \left(k \vec{\nabla} T \right) \\ \qquad\qquad\qquad\qquad -\mathcal{L} \left(\vec{\dot{m}} \cdot \vec{\nabla} \alpha \right) \delta_\alpha & (2.55) \\ \dfrac{\partial \alpha}{\partial t} - \dfrac{\vec{\dot{m}}}{\rho} \cdot \vec{\nabla} \alpha = 0 & (2.56) \\ \qquad \text{with:} \quad \mathcal{L}\vec{\dot{m}} = \left[\!\!\left[k \vec{\nabla} T \cdot \dfrac{\vec{\nabla} \alpha}{\| \vec{\nabla} \alpha \|} \right]\!\!\right] & (2.57) \end{cases}$$

2.5 Isochoric subcooled Stefan problem

The Stefan problem is a classical benchmark of phase change solvers [105, 115, 69, 116]. It is usually solved in saturated conditions in the liquid. This means that only the vapour characteristics are important and that no convection is at play. To test our heat flux jump computation method, we decided to modify this benchmark to include subcooling effects. It adds the influence of liquid side heat fluxes. Before integrating a dedicated mechanical solver, we considered an isochoric configuration. This means that no dilatation occurs at the interface and that all the system is mechanically at rest. However, volume heat capacity ρc_{p} were still considered different between the vapour and the liquid.

2.5.1 Reminders of the problem

The considered Stefan problem is a semi infinite domain (indexed by the coordinate $x \in [0, +\infty[$) filled with liquid at initial temperature T_∞, and touching a wall ($x = 0$) at temperature $T_w > T_{\text{sat}}$ (see Figure 2.11). At $t > 0$, the wall warms up the liquid and vaporisation occurs, creating a moving interface positioned by $s(t)$ that goes away from the wall. The boundary is set to T_{sat}.

The governing equations of this problem read:

$$\begin{cases} (\rho c_{\text{p}})_{\text{V}} \dfrac{\partial T}{\partial t} = k_{\text{V}} \dfrac{\partial^2 T}{\partial x^2} & \text{for } x \in [0, s(t)[& (2.58a) \\ (\rho c_{\text{p}})_{\text{L}} \dfrac{\partial T}{\partial t} = k_{\text{L}} \dfrac{\partial^2 T}{\partial x^2} & \text{for } x \in]s(t), +\infty[& (2.58b) \end{cases}$$

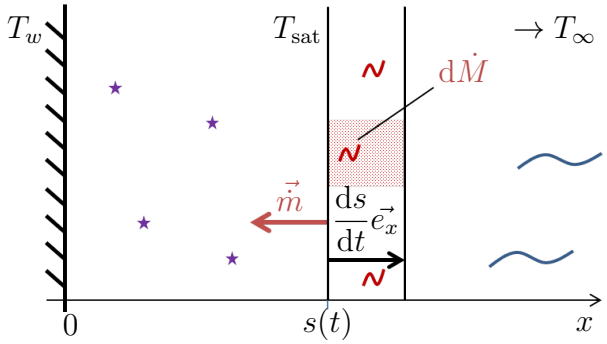

Figure 2.11: Description of the Stefan problem. The wall to the left is at T_w, and the liquid to the right is at T_∞ far from the interface. The heat flux from the wall provides heat to the interface by conduction. The liquid heats up and vaporises, but conduction in the liquid slows down the interface progress. As both phases have the same density, the mass transfer does not create any movement in the fluid.

With the boundary conditions:

$$\begin{cases} T(x, t=0) = T_\infty & \text{for } x > 0 & \text{(2.59a)} \\ T(x=0, t) = T_w & \text{for } t > 0 & \text{(2.59b)} \\ T(x=+\infty, t) = T_\infty & \text{for } t > 0 & \text{(2.59c)} \\ T(x=s(t), t) = T_{\text{sat}} & \text{for } t > 0 & \text{(2.59d)} \end{cases}$$

Moreover, the energy jump condition at the interface remaining at T_{sat} reads:

$$\mathcal{L}\dot{m} = \rho_{\text{V}}\mathcal{L}\frac{\mathrm{d}s}{\mathrm{d}t} = -k_{\text{V}}\frac{\partial T}{\partial x}_{|x=s(t)^-} + k_{\text{L}}\frac{\partial T}{\partial x}_{|x=s(t)^+} \tag{2.60}$$

A common solution is to impose an interface position s that varies as the square root of the time:

$$s = 2\chi\sqrt{D_{\text{V}}t} \tag{2.61}$$

where χ is a constant to identify.

Considering the new variable $\xi = \dfrac{x}{2\sqrt{D_{\text{V}}t}}$, a solution of (2.58a) reads $T(x,t) = F(\xi(x,t))$. Thus in each phase:

$$\frac{\partial T}{\partial t} = -\frac{x}{4t\sqrt{D_{\text{V}}t}}F'(\xi) \tag{2.62}$$

$$\frac{\partial^2 T}{\partial x^2} = \frac{1}{4D_{\text{V}}t}F''(\xi) \tag{2.63}$$

F is then solution of:

$$-\frac{x}{4t\sqrt{D_\mathrm{V}t}}F' = D_\mathrm{V}\frac{1}{4D_\mathrm{V}t}F'' \tag{2.64}$$

$$F'' + 2\xi F' = 0 \tag{2.65}$$

Integrating this equation:

$$F' = \lambda\,\mathrm{e}^{-\xi^2} \tag{2.66}$$

Back from the formulation in temperature:

$$T(x,t) = F(\xi) = A\int_0^\xi e^{-u^2}\,\mathrm{d}u + B = \frac{\sqrt{\pi}}{2}A\,\mathrm{erf}(\xi) + B \tag{2.67}$$

with erf the error function. The same reasoning can be done for the liquid side equation (2.58b).

The integration constants of both expressions are determined with the boundary conditions (2.59b), (2.59c) and (2.59d). The temperature field then reads:

$$T(x,t) = \begin{cases} T_w + \dfrac{T_\mathrm{sat} - T_w}{\mathrm{erf}\,(\chi)}\,\mathrm{erf}\left(\chi\dfrac{x}{s(t)}\right) & \text{for } x \in [0, s(t)] \\ T_\infty + \dfrac{T_\mathrm{sat} - T_\infty}{\mathrm{erfc}\left(\chi\sqrt{\dfrac{D_\mathrm{V}}{D_\mathrm{L}}}\right)}\,\mathrm{erfc}\left(\chi\dfrac{x}{s(t)}\sqrt{\dfrac{D_\mathrm{V}}{D_\mathrm{L}}}\right) & \text{for } x \in [s(t), +\infty[\end{cases} \tag{2.68}$$

where erfc $= 1-$erf is the complementary error function. We recall that $\lim\limits_{x\to+\infty}\mathrm{erf}(x) = 1$ and note that condition (2.59a) is also respected in the limit of small t.

The temperature gradient reads:

$$\frac{\partial T}{\partial x}(x,t) = \begin{cases} \dfrac{1}{\sqrt{\pi D_\mathrm{V}t}}\dfrac{T_\mathrm{sat} - T_w}{\mathrm{erf}\,(\chi)}\,\mathrm{e}^{-\left(\chi\frac{x}{s(t)}\right)^2} & \text{for } x \in]0, s(t)] \\ -\dfrac{1}{\sqrt{\pi D_\mathrm{L}t}}\dfrac{T_\mathrm{sat} - T_\infty}{\mathrm{erfc}\left(\chi\sqrt{\dfrac{D_\mathrm{V}}{D_\mathrm{L}}}\right)}\,\mathrm{e}^{-\left(\chi\frac{x}{s(t)}\sqrt{\frac{D_\mathrm{V}}{D_\mathrm{L}}}\right)^2} & \text{for } x \in]s(t), +\infty[\end{cases} \tag{2.69}$$

χ is evaluated thanks to the resolution of the energy equation at the interface (2.60). Thanks to the expression of the temperature gradient:

$$\rho_\mathrm{V}\mathcal{L}\chi\sqrt{D_\mathrm{V}} + \frac{k_\mathrm{V}(T_\mathrm{sat} - T_w)\,\mathrm{e}^{-\chi^2}}{\sqrt{\pi D_\mathrm{V}}\,\mathrm{erf}(\chi)} + \frac{k_\mathrm{L}(T_\mathrm{sat} - T_\infty)\,\mathrm{e}^{-\chi^2\frac{D_\mathrm{V}}{D_\mathrm{L}}}}{\sqrt{\pi D_\mathrm{L}}\,\mathrm{erfc}\left(\chi\sqrt{\dfrac{D_\mathrm{V}}{D_\mathrm{L}}}\right)} = 0 \tag{2.70}$$

This equation has to be solved numerically. In the present work, a Powell's conjugate direction method has been used for this purpose thanks to a Scilab code.

One can notice that the temperature gradient (and its derivative) at the interface tends toward the infinite as the time is close to zero. This entails an extra complexity for the computation of the Heat Flux Jump at the beginning of the simulation: it is interesting as it allows to test the performances of the Heat Flux Jump Computation feature and the error estimation (2.52).

All physical properties are those of a water and vapour mixture and summarised in table 2.4. Yet a divergence free test case is considered and the density of water is taken as the density of vapour (though ρc_p values are not changing).

	ρ ($\mathrm{kg\,m^{-3}}$)	ρc_p ($\mathrm{J\,m^{-3}\,K^{-1}}$)	k ($\mathrm{W\,m^{-1}\,K^{-1}}$)	$\mathcal{L}$ ($\mathrm{J\,kg^{-1}}$)
Vapour	5.97×10^{-1}	1.12×10^{3}	2.48×10^{-2}	2.26×10^{6}
Liquid		4.40×10^{6}	6.79×10^{-1}	

Table 2.4: Physical properties of the considered fluids for the isochoric Stefan problem.

2.5.2 Studied cases

2.5.2.1 Case 1: without subcooling

The first case solved was the classical Stefan problem with the liquid being at saturation temperature. The wall was 10 K above the saturation temperature, and $\chi = 0.067$.

The test case was computed for an unstructured 2D mesh of dimension 1×10^{-4} m by 5×10^{-4} m with 5 mesh sizes h (in m): 1×10^{-6}, 2×10^{-6}, 4×10^{-6}, 7×10^{-6} and 1×10^{-5}. The time step was set to 1×10^{-5} s. The interface thickness was set to $6h$ with an extension zone of $8h$.

The simulation started with an initial interface position of 2×10^{-5} m (identified as the border of the thick interface on the vapour side). The initial temperature profile was computed according to its analytical solution.

2.5.2.2 Case 2: with a small subcooling

The second case was similar to the first one, except that the water phase was not at saturation temperature anymore. An initial temperature for the water of $T_{\mathrm{sat}} - 1$ K was taken, and $\chi = 0.021$. The domain, mesh sizes, time step and other parameters were the same. The initial position of the interface was also 2×10^{-5} m.

2.5.2.3 Case 3: with a high subcooling

The robustness of the method was assessed in computing a more extreme Stefan Case for higher temperature: the wall was 900 K above the saturation temperature, the liquid was 10 K below, and $\chi = 0.101$. Furthermore, the remeshing methods (presented in Section 4.2.2) were applied to test the good behavior of the combined methods with a mesh refined around the interface.

The test case was computed for an unstructured non uniform 2D mesh of dimension 2×10^{-4} m by 2×10^{-3} m with 5000 nodes with an unstructured mesh whose mesh size h at the interface varies among 5 values (in m): 5×10^{-7}, 1×10^{-6}, 2×10^{-6}, 3×10^{-6} and 5×10^{-6}. The time step was still 1×10^{-5} s. The initial position of the interface was this time 1×10^{-4} m. The interface thickness was set to $6h$ with an extension zone of $8h$.

2.5.3 Results

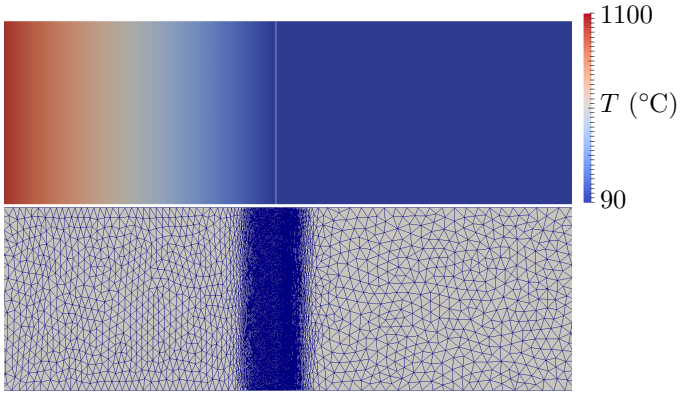

Figure 2.12: Temperature field and mesh of the Case 3 simulation for $h = 2\times10^{-6}$ m at time 0.1 s. The mesh is refined around the interface where temperature gradients and physical properties variations are important. Only the left side of the computational domain is plotted.

An example of temperature field values and mesh for the Case 3 is shown in Figure 2.12. The resmeshing algorithm is working properly. Results of interface position and mass transfer rate values versus time are plotted in Figures 2.14a and 2.15a for the Case 1, in Figures 2.14b and 2.15b for the Case 2, and in Figures 2.14c and 2.15c for the Case 3. Results of Case 1 are satisfactory, as errors on the position and mass transfer rate were small (less than 1 %) whatever the mesh size.

The influence of the mesh size appears for the second case, mostly at the first time steps of the simulation. This is explained by a higher heat flux gradient on

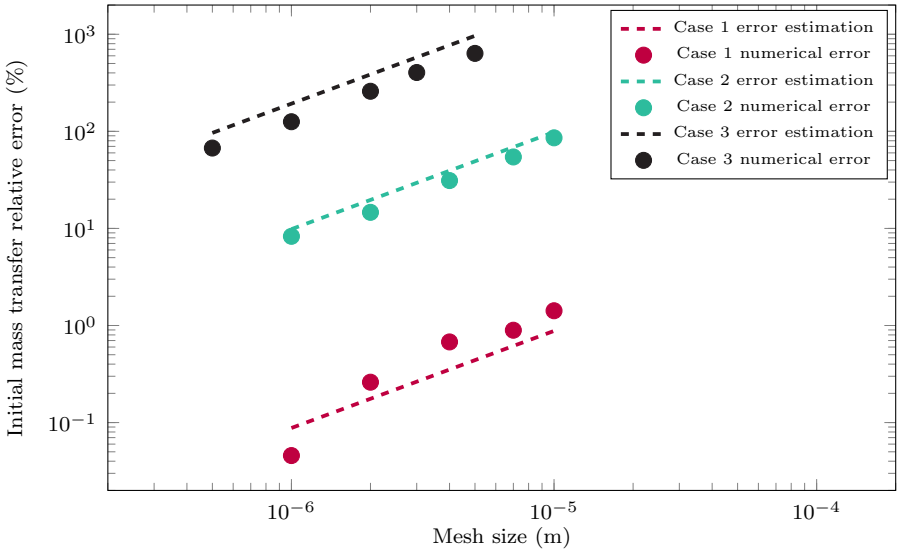

Figure 2.13: Relative error of the initial mass transfer rate value versus interface mesh size. Estimations of this error given by equation (2.52) are plotted in dashed lines.

the liquid size that increases the error on the mass transfer rate described by (2.52). Otherwise the case remains correctly described by the simulations.

Results for the Case 3 stresses even more this observation, as even smaller mesh sizes reveal non negligible errors due to the important thermal constraint at play at the first time steps of the simulation. As soon as the temperature gradient is lower, errors on the mass transfer rate quickly decrease.

2.5.4 Precision and accuracy order

A first estimation of the HFJC method accuracy given by equation (2.52) could be confirmed by plotting the errors of the three simulations on a $(h, \Delta\dot{m})$ graph. This is shown on Figure 2.13.

The lines represent the error estimation, thanks to the computation of $\dfrac{\partial^2 T}{\partial x^2}(s, t = t_0)$ given by the analytical solution. The error estimation correctly fits with the simulations results. This means that these errors are due to a too coarse grid, and can be controlled and reduced with the mesh size. An optimised approach to properly solve sub-cooled Stefan problems would be to control the mesh refinement according with the time.

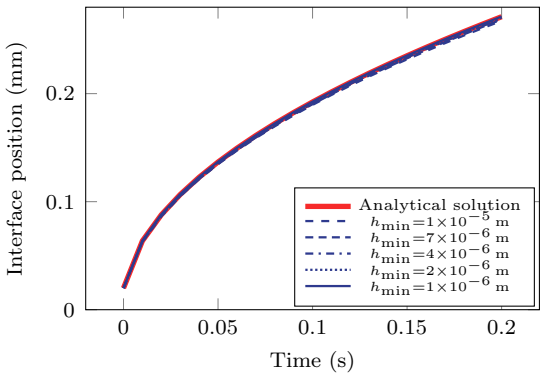

(a) Case 1

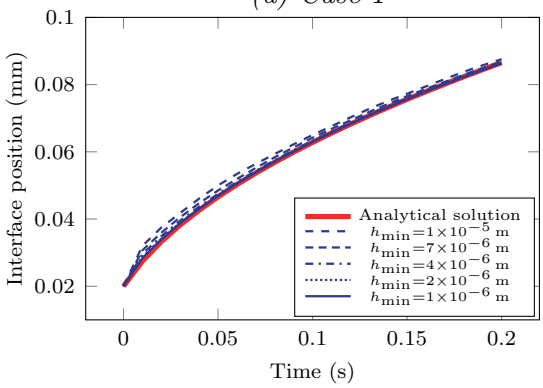

(b) Case 2

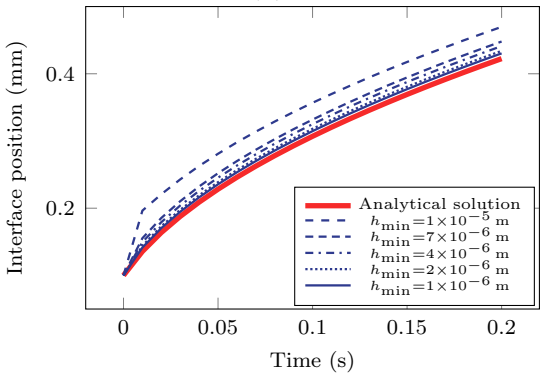

(c) Case 3

Figure 2.14: Analytic and simulated positions of the interface for different mesh sizes h

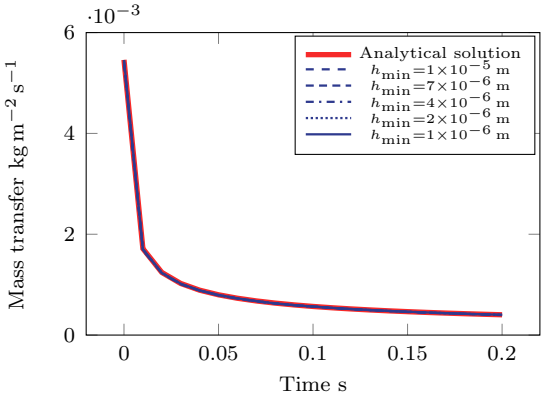

(a) Case 1

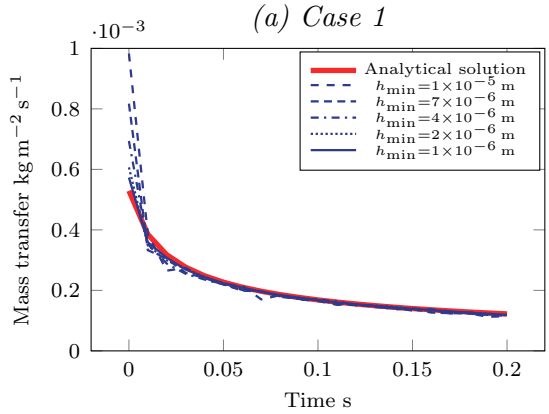

(b) Case 2

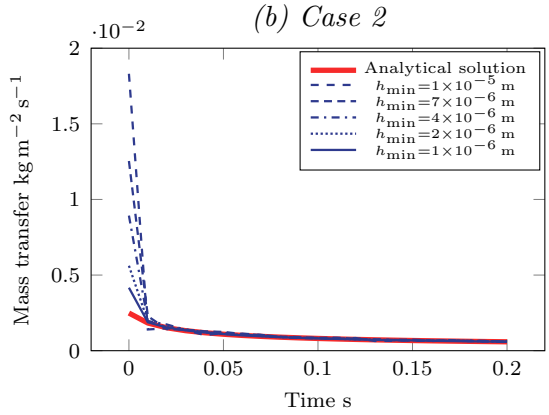

(c) Case 3

Figure 2.15: Analytic and simulated mass transfer rates for different mesh sizes h.

To further study the accuracy of the method, a convergence analysis with the mesh size h was done. The error is defined as:

$$\text{err} = \frac{1}{N} \sum_{i \in [\![1,N]\!]} [\![s^i_{\text{simu}} - s^i_{\text{an}}]\!] \tag{2.71}$$

where N is the number of sample steps among each iteration step, taken as 20. s^i_{simu} and s^i_{an} are the position of the simulated and analytic interface at sample step i.

Results for the three cases are plotted on Figure 2.16a, Figure 2.16b and Figure 2.16c.

For all cases, the convergence order is around 1 as predicted by (2.52): the accuracy of the HFJC method is controlled by the value of ε that should be small enough to properly compute heat fluxes. If this condition is validated, and providing that the mesh is properly refined and validates the Fourier condition far from the interface, the presented method can be applied to more complex cases.

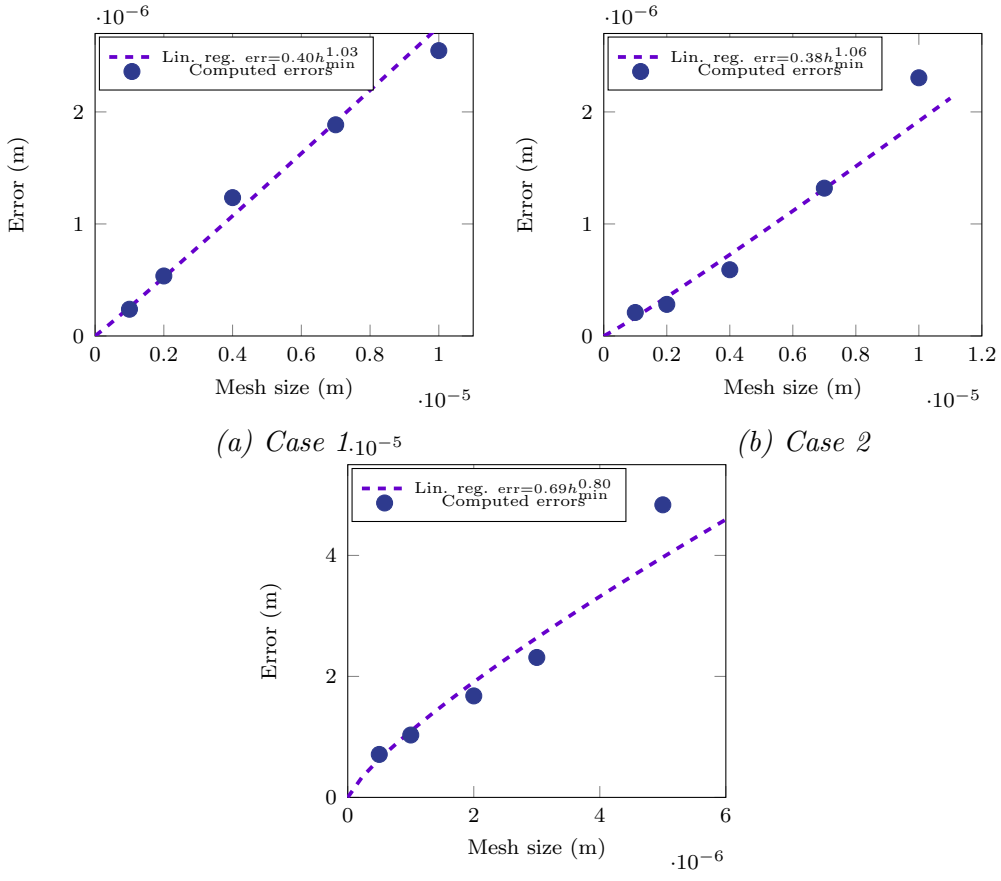

Figure 2.16: Space–time convergence analysis for the isochoric Stefan Benchmark.

2.6 Conclusions

- The energy equation was reduced to a convection diffusion reaction equation on the temperature with a source term to account for the latent heat of vaporisation.
- A reaction term was added to reinforce the saturation temperature at the interface.
- A Level Set Method was used to localise the liquid vapour interface.
- The numerical interface was smoothed by a thickness ε.
- A Heat Flux Jump Computation method designed for smooth interfaces was developed and tested on 3 benchmarks. We observed that its accuracy is proportional to the mesh size and to the derivative of the temperature gradient normal to the interface.
- The resulting isochoric phase change model was validated in three configurations of subcooled Stefan problems.

Chapter 3

Pseudo-compressible mechanical framework

Contents

Résumé en Français

Ce chapitre présente le modèle mécanique permettant la prise en compte du saut de vitesse à l'interface lié à la différence de densité entre les phases liquide et vapeur. Une analyse des ordres de grandeur des efforts en jeu nous permet de nous contenter d'une formulation incompressible dans chaque phase. Le cadre numérique existant basé sur une approche Virtual Multi-Scale est ainsi employé. À l'interface, les effets liés au changement de phase impliquent une discontinuité de vitesse découlant de la conservation de la masse, mais ont des effets modestes sur le saut de quantité de mouvement.

Ces conclusions couplées à la modélisation de l'interface présentée dans le chapitre précédent mènent à la mise en place d'une modélisation mécanique proche de celle d'un système diphasique sans changement de phase. La seule différence repose sur l'ajout de deux termes: un terme source dans l'équation de conservation de la masse qui représente le changement de densité du fluide qui change de phse, et un terme additionnel dans la vitesse de convection de la fonction Level Set. L'ajout du terme source nécessite la modification du solveur Navier–Stokes existant. Ce nouveau solveur est validé sur un cas 2D analytique avec une convergence à l'ordre 2 sur la taille de maille.

Le système complet est ensuite validé sur deux cas test 2D analytiques avec des taux de transfert de masse à l'interface constants. Tout d'abord, une interface plane est considérée avec différents rapports de masse volumique entre la phase liquide et la phase gazeuse (entre 2 et 2000). Le modèle est alors validé avec une convergence à l'ordre 2 en taille de maille quel que soit le rapport de masse volumique en considérant une taille d'interface constante. Cependant, la considération d'une taille d'interface fixée sur la taille de maille met en lumière une erreur systématique liée à la discrétisation de la fonction Dirac à l'interface. Celle-ci influence directement la précision du modèle. Une valeur de six éléments semble le minimum pour avoir une représentation correcte de l'interface et une erreur faible.

Le second cas test considéré est la croissance d'une bulle. Cette fois-ci le rapport de masse volumique est fixé à celui d'un mélange eau / vapeur d'eau (2000). Ce cas test met en lumière un biais du modèle qui apparait pour des épaisseurs d'interface trop importantes devant le rayon de courbure. Il peut être corrigé par l'ajout d'un terme du second ordre dans la vitesse de convection de la fonction Level Set. Ce faisant, un ordre de convergence proche de 2 en taille de maille est retrouvé.

3.1 Introduction

Boiling involve many hydrodynamical aspects that bring a lot of thermal convection. The velocity field has to be solved to account for theses phenomena. Attention has also to be paid at the interface, as phase change involves velocity jumps. As the vapour phase is usually much lighter than the liquid phase (ratio around 2000 for the liquid phase), vaporisation entails an important dilatation at the interface. This is numerically challenging, and requires a specific attention adapted to the framework. Usually, specific interfacial laws are added to the linear system to account for the velocity jump, and a projection technique is used. For example, several works solved this procedure with an iterative scheme to compute the velocity until it respects the mass conservation [64, 66, 68, 70, 67]. The interface was treated as a sharp frontier [64, 66, 68] or a smoothed one for Juric et al. [67]. Kang et al. [70] also implemented a Ghost Fluids Method to ease the introduction of interfacial terms such as the surface tension. This work was improved to eliminate the iteration procedure with a predictor-corrector algorithm [73] or combined with the Ghost Fluids Methods [72, 69, 71].

In the present work, the CSF approach provides an opportunity to regularise the mass transfer to reduce numerical instabilities. This approach does not suit methods with sharp interfaces, as the velocity field has a great impact on temperature gradients: the velocity at the interface would not properly represent the velocity from both sides, and it would involve non negligible errors on the heat flux jump computation. As thick interfaces were considered, what matters is the velocity at the borders of the interface. This is allowed by a regularised velocity jump. To the author's knowledge, the resolution of phase change problems with regularised velocity jumps in the context of FEM was something new that required a dedicated work.

3.2 Pseudo-compressible Navier-Stokes solver

3.2.1 Single phase formulation

The first question to arise is the consideration of density and viscosity variations inside the fluid. Considering the Mach number:

$$\mathrm{Ma} = \frac{u}{a} \tag{3.1}$$

as a is the speed of sound, its values are low. Considering a velocity of $1\,\mathrm{m\,s^{-1}}$ which is an upper bound of velocities encountered during boiling, orders of magnitude of Ma are around 10^{-2} in the vapour and 10^{-3} in the liquid. Pressure waves can clearly be neglected.

Regarding the variations of the material properties, characteristic values for water (resp. water vapour) at 25 °C and 100 °C (resp. 100 °C and 900 °C) of ρ and η as well as the kinematic viscosity $\nu = \eta/\rho$ computed at atmospheric pressure are gathered in Table 3.1.

		ρ (kg m^{-3})	η (Pa s)	ν (m^2 s^{-1})
Liquid	25 °C	997	8.9×10^{-4}	8.92×10^{-7}
	100 °C	958	2.8×10^{-4}	2.92×10^{-7}
Vapour	100 °C	0.59	1.2×10^{-5}	2.03×10^{-5}
	900 °C	0.18	4.5×10^{-5}	0.25×10^{-5}

Table 3.1: Mechanical properties of water and water vapour at extreme temperatures [89].

Variations of density in the water are not significant, but temperature inhomogeneities can still have an influence on the flow (what is usually called natural convection). To assess its influence, we computed the Grashof number, which assesses the impact of density variations due to temperature gradients:

$$\mathrm{Gr} = \frac{g\alpha_T L_c^3 \rho^2 \Delta T}{\eta^2} \tag{3.2}$$

In the liquid a characteristic length L_c of 1 m leads to a Gr of around 10^{11} which is important. Clearly natural convective terms are at play in the liquid side, even for a smaller quenching pool with a lower L_c. Thus a Boussinesq model — valid for small density ratios — was employed to assess this phenomena in Section 6.3.2.1.

For water vapour, variations of densities are higher. However orders of magnitude of density and characteristic length are much smaller than those of the liquid, leading to a much smaller Gr (around 10^2 for L_c of 1 mm). Moreover buoyancy on the vapour is dominant, meaning that natural convection inside the vapour can be neglected. This means that variations of the density should not have a direct impact on the hydrodynamics. However a smaller density means a higher volume for the same mass. This means that for the same amount of vapour, a warmer vapour leads to a thicker vapour film. As for thermal properties, values shall ideally be taken as functions of the temperature. For the sake of simplicity, we considered mean values of ρ_V between T_{sat} and T_w. Regarding the viscosity, changes are not large but still significant. Ideally the viscosity changes shall also be taken into account. The value of the viscosity will be discused further.

Consequently, the consideration of incompressible flows in both phase is acceptable, providing that a correction is done in the vapour side. This means that in each phase, the classical formulation of the incompressible Navier–Stokes equations can

be considered:

$$\begin{cases} \vec{\nabla} \cdot \vec{u} = 0 & (3.3) \\ \rho \left(\dfrac{\partial \vec{u}}{\partial t} + (\vec{u} \cdot \vec{\nabla}) \vec{u} \right) = -\vec{\nabla} p + \vec{\nabla} \cdot 2\eta \dot{\boldsymbol{\varepsilon}} + \rho \vec{g} & (3.4) \end{cases}$$

where $\dot{\boldsymbol{\varepsilon}}$ is the strain rate tensor coming from $\boldsymbol{\tau}$.

3.2.2 Interface conditions

The interface conditions (2.17) (2.18) coming from the mass and momentum conservation are recalled:

$$\begin{cases} [\![\rho \left(\vec{u} - \vec{u_{\mathrm{I}}} \right) \cdot \vec{n}]\!] = 0 & (3.5) \\ [\![(\rho \vec{u}) \left(\vec{u} - \vec{u_{\mathrm{I}}} \right) \cdot \vec{n}]\!] = [\![\boldsymbol{\sigma} \cdot \vec{n}]\!] + \gamma_0 \kappa \vec{n} & (3.6) \end{cases}$$

The first equation can be rewritten to express the interface velocity:

$$\vec{u_{\mathrm{I}}} \cdot \vec{n} = \frac{[\![\rho \vec{u} \cdot \vec{n}]\!]}{[\![\rho]\!]} \tag{3.7}$$

We also recall that we defined the mass transfer rate as $\dot{m} = \rho \left(\vec{u} - \vec{u_{\mathrm{I}}} \right) \cdot \vec{n}$. This definition coupled with (3.5) allows to express the normal velocity jump:

$$[\![\vec{u} \cdot \vec{n}]\!] = \left[\!\!\left[\frac{1}{\rho} \right]\!\!\right] \dot{m} \tag{3.8}$$

The Figure 3.1 describes this velocity jump. There are no constraints on the tangential part of the velocity that is usually considered to be continuous. We recall that the mass transfer rate vector is defined as $\vec{\dot{m}} = \dot{m} \vec{n}$. Then:

$$[\![\vec{u}]\!] = \left[\!\!\left[\frac{1}{\rho} \right]\!\!\right] \vec{\dot{m}} \tag{3.9}$$

Equation (3.9) clearly shows that a mass transfer implies a velocity jump at the interface providing that vapour and liquid densities are different.

Regarding the equation of momentum conservation (3.6), the left-hand side can be factorised by $\dot{m}$, the velocity jump can be replaced by (3.9) and the constraint tensor σ can be decomposed:

$$\left[\!\!\left[\frac{1}{\rho} \right]\!\!\right] \dot{m}^2 \vec{n} = -[\![p \vec{n}]\!] + [\![\boldsymbol{\tau} \vec{n}]\!] + \gamma_0 \kappa \vec{n} \tag{3.10}$$

This equation can be considered as such in the following numerical framework. However it is interesting to notice that only two terms are significant: the pressure jump and the surface tension force. The left-hand size stands for a change

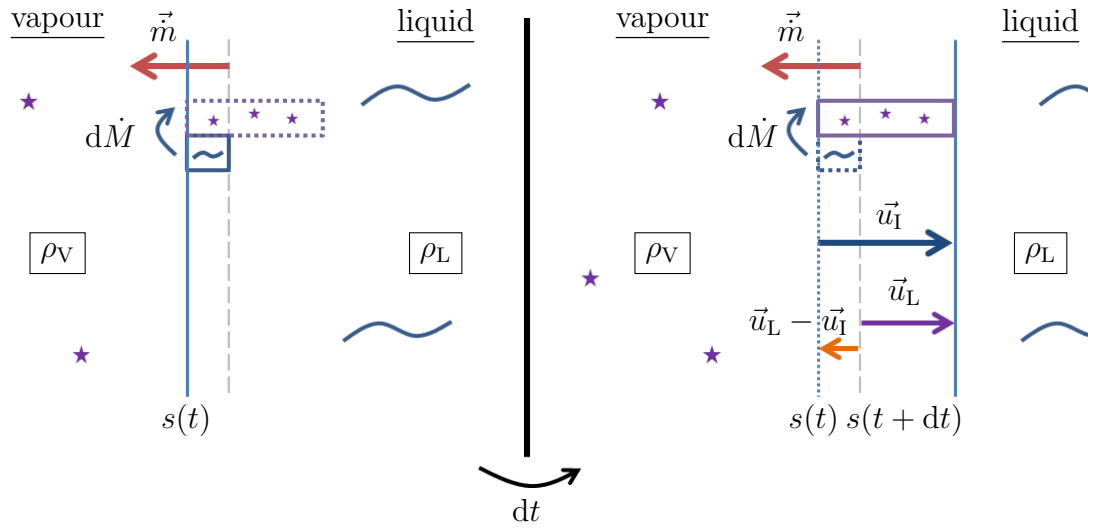

Figure 3.1: Representation of the velocity jump due to the density difference. In this graphic, the vapour phase is static. The extension of the fluid particle that vaporises pushes the liuqid back at a lower velocity than the interface.

of momentum across the interface: a fluid particle that is being vaporised gains in momentum. But the phase change must be very intense for this term to be significant regarding pressure variations [19]. Besides, viscous effects in the normal direction are also negligible. What comes out of these simplification is the usual Young–Laplace equation:

$$[\![p]\!] = \gamma_0 \kappa \tag{3.11}$$

3.2.3 Pseudo-compressible formulation

The integration of phase change effects at the interface demands a modification of the incompressible equations. Equation (3.9) indeed shows that it is impossible to consider a fully incompressible flow with phase change and two phase flows with different densities. The velocity jump was then treated in a monolitic approach: a source term s was added on the velocity divergence equation 3.3. This lead to a variation of the Navier–Stokes equations that was called the "Pseudo-Compressible Navier–Stokes equations":

$$\begin{cases} \vec{\nabla} \cdot \vec{u} = s & (3.12) \\ \rho \left(\dfrac{\partial \vec{u}}{\partial t} + (\vec{u} \cdot \vec{\nabla}) \vec{u} \right) = -\vec{\nabla} p + \vec{\nabla} \cdot 2\eta \dot{\vec{\varepsilon}} + \rho \vec{g} & (3.13) \end{cases}$$

In these equations, s has to be formulated in a way to guarantee the mass conservation described by Equation (3.9). The demonstration of the expression of s is done in Section 3.3.

3.2.4 Variational Multiscale Approach

The "pseudo-compressible" formulation needed to work on a dedicated solver to properly solve this new set of equations. To do so, we relied on existing FEM codes previously developed in the CIMlib-CFD library [117, 82, 118, 103]. These former formulations were dedicated to the multiphase incompressible Navier–Stokes problems.

The resolution of flow problems with FEM is well known to be a challenge. Convection dominated flows lead to strong oscillations in layers with large velocity variations [112]. Secondly an inappropriate combination of interpolation functions for velocity and pressure yields unstable schemes [119, 120, 121]. This is the Ladyzhenskaya–Babuška–Brezzi condition. The P1–P1 (linear interpolation on tetrahedron) interpolation scheme does not respect this condition. The first issue can be solved with stabilisation terms similarly to the SUPG and SCPG methods presented in Section 2.3.5. Regarding the second issue, a first solution is simply to enrich the interpolation scheme. However this increases significantly the computational cost.

A method that proved its efficiency to solve both challenges while keeping the P1–P1 interpolation is the Variational MultiScale (VMS) Approach. This is a mixed formulation approach that divides the variable space into two subscales: the coarse and fine scales. Every variable is then expressed with two components. The fine scales are solved in a approximated manner and the solution is injected in the coarse scales equations. The resulting equations are known to respect the Ladyzhenskaya–Babuška–Brezzi condition [84, 117, 82, 103].

The weak formulation of the stabilised VMS formulation reads:

$$\begin{cases} \text{Find } (\vec{u}_h, p_h) \in V_h \times P_h \text{ such that } \forall (\vec{v}_h, q_h) \in V_{h,0} \times P_h : \\ \left\langle \rho \left(\dfrac{\partial \vec{u}_h}{\partial t} + \left(\vec{u}_h \cdot \vec{\nabla} \right) \vec{u}_h \right), \vec{v}_h \right\rangle - \left\langle p_h, \vec{\nabla} \cdot \vec{v}_h \right\rangle + 2 \left\langle \eta \dot{\boldsymbol{\varepsilon}}(\vec{u}_h), \dot{\boldsymbol{\varepsilon}}(\vec{v}_h) \right\rangle \\ \underbrace{+ \sum_K \left\langle \tau_u \mathcal{R}_u, \rho \left(\vec{u}_h \cdot \vec{\nabla} \right) \vec{v}_h \right\rangle_K + \sum_K \left\langle \tau_p \mathcal{R}_p, \vec{\nabla} \cdot \vec{v}_h \right\rangle_K}_{\text{subspace enrichment}} = \langle f, \vec{v}_h \rangle \\ \left\langle \vec{\nabla} \cdot \vec{v}_h, q_h \right\rangle \underbrace{- \sum_K \left\langle \tau_p \mathcal{R}_p, \vec{\nabla} q_h \right\rangle_K}_{\text{subspace enrichment}} = 0 \end{cases} \tag{3.14}$$

where $\mathcal{R}_u$ (resp. $\mathcal{R}_p$) is the residual of the momentum conservation equation (resp. the mass conservation or velocity divergence equation). τ_u and τ_p are coefficients deduced from the fine scales equations. They are function of the mesh size and of local values of $\vec{u}_h$ on the element K. V_h and P_h are standard finite element spaces and $V_{h,0}$ is V_h but with a 0 value on boundary points with Dirichlet conditions. The temporal discretisation is done with a Backward Differentiation Formula, following the work of [122]. More details on the implementation of (2.44), and on the values of τ_u and τ_p can be found in [117, 82, 118, 103, 80]

This formulation is valid for the incompressible formulation. Considering the addition of the source term s_h in the velocity divergence equation, the second equation is slightly modified:

$$\left\langle \vec{\nabla} \cdot \vec{v}_h, q_h \right\rangle - \sum_K \left\langle \tau_p \mathcal{R}_p, \vec{\nabla} q_h \right\rangle_K = \underbrace{\langle s_h, q_h \rangle}_{\text{phase change contribution}} \tag{3.15}$$

The residual $\mathcal{R}_p$ also needs to be modified to take into account this change. Otherwise existing VMS parameters are not changed.

3.2.5 Pseudo-compressible square benchmark

We considered a first benchmark inspired by Hachem [117], whose first purpose was to study the behavior of the incompressible Navier–Stokes solver.

The target was to reproduce the following steady analytical solution on a $(0,1) \times (0,1)$ square:

$$\begin{cases} u_x = -5xy^4 + Ax^2 & \text{(3.16a)} \\ u_y = -0.5 + y^5 & \text{(3.16b)} \\ p = 0.5(y^5 - y^{10}) + 5\nu y^4 & \text{(3.16c)} \\ f_x = 5xy^8 + 10xy^3 + 60\nu xy^2 - 2\nu A - 15Ax^2y^4 + 2A^2x^3 & \text{(3.16d)} \\ f_y = 0 & \text{(3.16e)} \\ \varphi = 2Ax & \text{(3.16f)} \end{cases}$$

To do so, the values of f_x, f_y, φ and the boundary solutions were set as described on Figure 3.2. The pressure boundary conditions were set free.

Two convergence studies were done with two values of A: 0.01 and 0.1. Five mesh sizes were considered: 2×10^{-3}, 5×10^{-3}, 1×10^{-2}, 2×10^{-2} and 5×10^{-2}. ρ was set to 1, and η to 0.001. The simulation started with a zero velocity, and runned until time 20. The time step was set to 0.1. Results at time 20 were compared to the analytical solution. An example of the velocity and pressure fields is plotted in Figure 3.3.

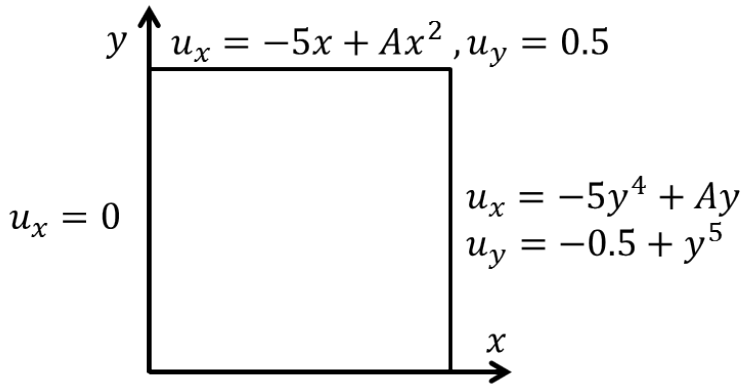

Figure 3.2: Dirichlet velocity boundary conditions for the Square Benchmark. The other velocity components are set with homogeneous Neumann boundary conditions.

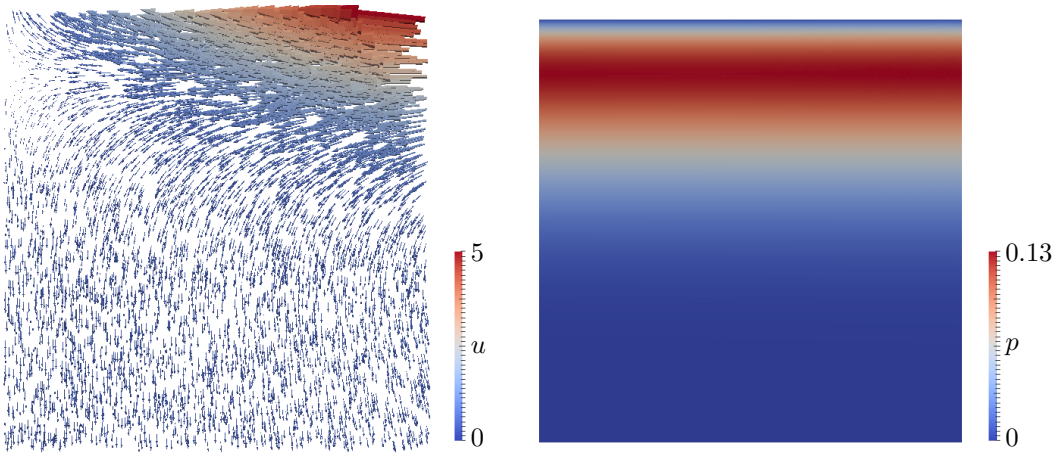

Figure 3.3: Final velocity and pressure fields for $A = 0.1$ and $h = 2{\times}10^{-3}$.

The error criteria based on the L2 norm was used:

$$\mathrm{err} = \sqrt{\frac{\int_\Omega (x_{\mathrm{simu}} - x_{\mathrm{an}})^2 \, \mathrm{d}S}{\int_\Omega (x_{\mathrm{an}})^2 \, \mathrm{d}S}} \tag{3.17}$$

where x stands for the velocity vector or the pressure. The time interval [0,20] was long enough to ensure the steady state, when differences between two time steps were in the order of magnitude of the machine precision (see Figure 3.4)

Results of the convergence study for both variables are plotted on Figure 3.5 for $A = 0.1$ and 3.6 for $A = 0.01$. The order of convergence for the case $A = 0.01$ is of the same order as the one of the incompressible formulation computed by Hachem [117], proving the good behavior of the solver for this case. For $A = 0.1$, the order

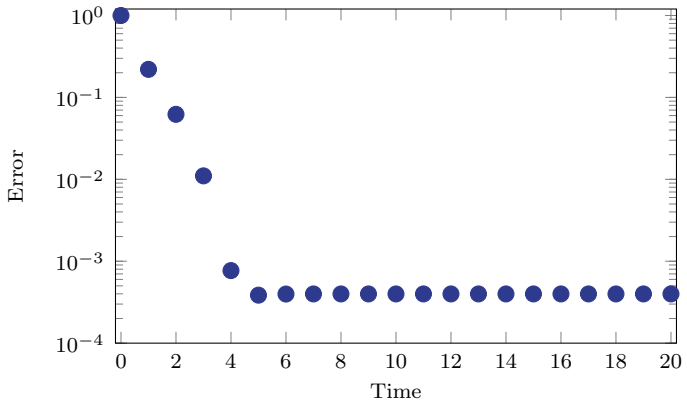

Figure 3.4: L2 norm error evolution for $A = 0.1$ and $h = 5{\times}10^{-3}$. The final time considered is high enough to guaranty the steady state regime on the final iteration.

of convergence is reduced (close to 1), showing a limit of the range of applicability of the formulation for larger source terms and velocities.

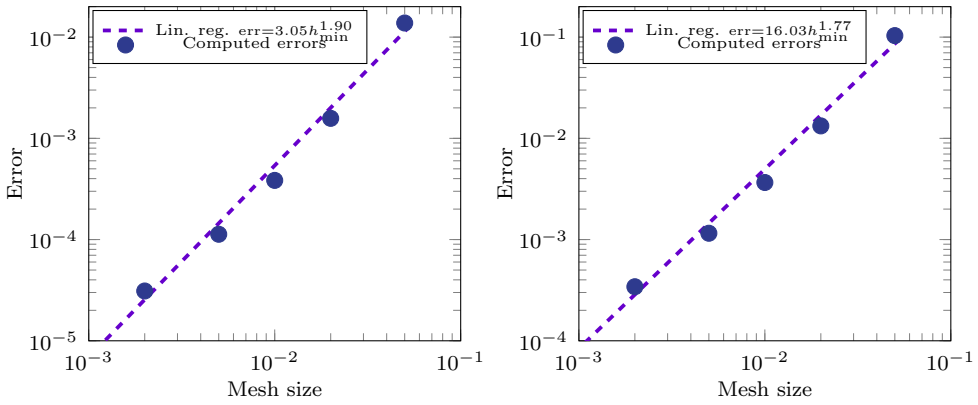

(a) Velocity L2 norm error *(b) Pressure L2 norm error*

Figure 3.5: Space convergence analysis for the Pseudo-compressible square benchmark with $A = 0.01$.

3.3 Multiphase formulation

3.3.1 Mass conservation

The regularised velocity jump leads to the emergence of a source term in the velocity divergence equation of the classical incompressible Navier–Stokes equations. This term was expressed following a phase change Dirac profile described in Section 2.3.4.

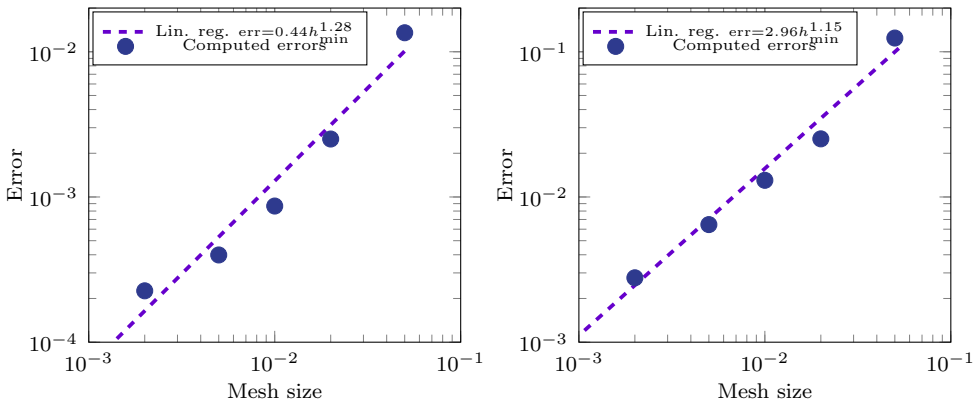

(a) Velocity L2 norm error *(b) Pressure L2 norm error*

Figure 3.6: Space convergence analysis for the Square Benchmark with $A = 0.1$.

Its formulation could be found by writing the mass conservation for each phase of the domain. Considering H_α as a volume fraction of vapour phase:

$$\frac{\partial \left[H_\alpha \rho_\mathrm{V}\right]}{\partial t} + \vec{\nabla} \cdot (H_\alpha \rho_\mathrm{V} \vec{u}) = \dot{\vec{m}} \cdot (\vec{\nabla}\alpha)\delta_\alpha \tag{3.18}$$

$$\frac{\partial \left[(1 - H_\alpha) \rho_\mathrm{L}\right]}{\partial t} + \vec{\nabla} \cdot ((1 - H_\alpha) \rho_\mathrm{L} \vec{u}) = -\dot{\vec{m}} \cdot (\vec{\nabla}\alpha)\delta_\alpha \tag{3.19}$$

The addition of equations (3.18) and (3.19) gives back the global conservation of mass (2.2) as expected.

At the interface, the thermodynamical equilibrium was assumed to be respected. In this context ρ_V and ρ_L are constant. Dividing (3.18) and (3.19) by ρ_V and ρ_L respectively and adding the results provides the wanted source term:

$$\vec{\nabla} \cdot \vec{u} = \left[\!\left[\frac{1}{\rho}\right]\!\right] \left(\dot{\vec{m}} \cdot \vec{\nabla}\alpha\right) \delta_\alpha \tag{3.20}$$

This is consistent with the velocity jump expressed by the sharp interface formulation (3.8), but it leads to a regularised velocity as shown in Figure 3.7b.

3.3.2 Convection of the interface

The first equation (3.18) can be rewritten to get a form of convection equation. Developing the divergence term and replacing the velocity divergence term by the expression of (3.20) leads to:

$$\frac{\partial H_\alpha}{\partial t} + \vec{u} \cdot \vec{\nabla} H_\alpha = \left(\frac{H_\alpha \rho_\mathrm{V} + (1 - H_\alpha)\rho_\mathrm{L}}{\rho_\mathrm{V} \rho_\mathrm{L}}\right) \left(\dot{\vec{m}} \cdot \vec{\nabla}\alpha\right) \delta_\alpha \tag{3.21}$$

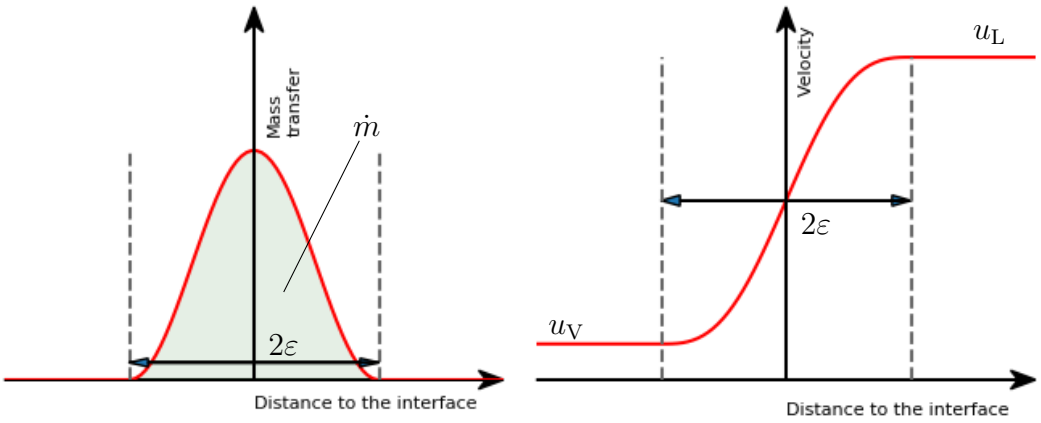

(a) Volume mass transfer rate distribution.

(b) Velocity jump.

Figure 3.7: Interfacial velocity and mass transfer profiles in the context of smoothed interface and Continuous Surface Force approach.

with $\rho = H_\alpha \rho_V + (1 - H_\alpha)\rho_L$ and thanks to the relationship between the derivatives of H_α and α given by equations (2.36) and (2.37):

$$\frac{\partial \alpha}{\partial t}\delta_\alpha + \vec{u} \cdot (\vec{\nabla}\alpha)\delta_\alpha = \left(\frac{\rho}{\rho_V \rho_L}\right)\left(\vec{\dot{m}} \cdot \vec{\nabla}\alpha\right)\delta_\alpha \tag{3.22}$$

This equation only lives at the interface, where δ_α is not null. The critical point with the LS method is to properly convect the 0 isovalue. This is the information that contains the interface position. The fact that the LS is not properly convected away from the interface does not create any errors on the mass conservation as α is reinitialised anyway. It is thus acceptable to solve this equation on the whole computational domain. As long as this equation is respected on the interface, the mass conservation is respected. We then simplified by δ_α to obtain the new LS convection equation:

$$\frac{\partial \alpha}{\partial t} + \left(\vec{u} - \frac{\rho}{\rho_V \rho_L}\vec{\dot{m}}\right) \cdot \vec{\nabla}\alpha = 0 \tag{3.23}$$

As expected, the convection velocity is the fluid velocity corrected by a term that accounts for the relative velocity of the interface to the fluid due to phase change. The coupling with the mass conservation equation (3.20) has however a second order bias. It fails to properly ensure mass conservation for a degenerated case when the radius of curvature is smaller than the interface thickness ε. This bias is most of the time not significant. But it can be important in some benchmarks as for the following Growing Bubble benchmark. This is the reason why a second

order correction term was added to the LS convection equation:

$$\frac{\partial \alpha}{\partial t} + \left(\vec{u} - \frac{\rho}{\rho_V \rho_L} \vec{\dot{m}} - \left[\!\left[\frac{1}{\rho} \right]\!\right] \vec{\dot{m}} \frac{\kappa_\alpha}{\|\vec{\nabla}\alpha\|} \int_{-\varepsilon}^{0} H_\alpha \, \mathrm{d}\alpha \right) \cdot \vec{\nabla}\alpha = 0 \tag{3.24}$$

The integral can be computed analytically knowing the analytical expression of H_α. As $\int_{-\varepsilon}^{0} H_\alpha \, \mathrm{d}\alpha$ is of the order of magnitude of ε, as long as $1/\kappa_\alpha >> \varepsilon$ the second order correction term is not significant. The origin of this second order bias and the demonstration of the way to correct it are detailed in Appendix C.

3.3.3 Coupled Level-Set Pseudo-compressible formulation

All these ingredients allowed us to build a mechanical multiphase monolithic solver with phase change. The only remaining effect to add was the surface tension $\vec{\gamma_\alpha}$. This term is only dependent on the interface geometry, and thus on α. In the context of the CFS approach, the surface tension contribution reads:

$$\vec{\gamma_\alpha} = \gamma_0 \kappa_\alpha \delta_\alpha \vec{n} = \gamma_0 \vec{\nabla} \cdot \left(\frac{\vec{\nabla}\alpha}{\|\vec{\nabla}\alpha\|} \right) \delta_\alpha \vec{\nabla}\alpha \tag{3.25}$$

We simply added this expression as a source term on the right-hand-side of (3.4) to include surface tension in the momentum conservation. However, if surface tension is implemented explicitly (meaning that it is considered as a constant term in the time discretisation) then the resolution is limited by the very constraining BZK condition:

$$\Delta t^{\mathrm{BZK}} < \sqrt{\frac{\overline{\rho} h^3}{2\pi\gamma_0}} \tag{3.26}$$

where Δt is the time step of simulation and h is the mesh size. BZK stands for the surnames of the original authors that first expressed this stability condition [94] This is the reason why semi-implicit techniques have been developed to overcome this difficulty [123, 124]. The idea is to extrapolate a prediction of the diffusion of velocity induced by surface tension at the interface. In addition to the explicit source term $\vec{\gamma_\alpha}$, the velocity term is then integrated implicitly in the time discretisation scheme. Denner et al. [125] explained that this new implicit term performs well as it includes dissipation of the surface energy of capillary waves with short wavelength. Details of the numerical implementation used for the present work can be found in [80].

Including this term in the momentum energy conservation, and coupling the pseudo-compressible Navier–Stokes equations with the LS convection equation leads

to the following system:

$$\begin{cases} \vec{\nabla}\cdot\vec{u} = \left[\!\left[\frac{1}{\rho}\right]\!\right]\left(\vec{\dot{m}}\cdot\vec{\nabla}\alpha\right)\delta_\alpha & (3.27) \\ \rho\left(\frac{\partial\vec{u}}{\partial t} + (\vec{u}\cdot\vec{\nabla})\vec{u}\right) = -\vec{\nabla}p + \vec{\nabla}\cdot 2\eta\dot{\vec{\varepsilon}} + \rho\vec{g} + \vec{\gamma_\alpha} & (3.28) \\ \frac{\partial\alpha}{\partial t} + \left(\vec{u} - \frac{\rho}{\rho_{\mathrm{V}}\rho_{\mathrm{L}}}\vec{\dot{m}} - \left[\!\left[\frac{1}{\rho}\right]\!\right]\vec{\dot{m}}\frac{\kappa_\alpha}{\|\vec{\nabla}\alpha\|}\int_{-\varepsilon}^{0} H_\alpha\,\mathrm{d}\alpha\right)\cdot\vec{\nabla}\alpha = 0 & (3.29) \end{cases}$$

3.4 2D Benchmarks

3.4.1 Moving interface

The first benchmark that we considered to challenge the diphasic framework was the convection of a straight line, meaning no theoretical influence of the surface tension term. The case was solved in 2D in a $1\,\mathrm{m}\times 1\,\mathrm{m}$ square domain. The set up of this "moving interface" benchmark is as follow: a vertical interface separates a vapour phase of small density on the left part from a liquid phase of high density on the right part. A mass transfer $\dot{m}$ is imposed from the vapour to the liquid phases. The fluids can only escape on the right side, leading to an interface displacement from left to right along with the liquid being pushed away due to the change of density. No slip boundary conditions are fixed on the left side, and free slip conditions are fixed on the top and bottom sides. Pressure conditions are set free. This is summarised up in Figure 3.8. A constant interface velocity of $u_{\mathrm{I}} = 2\times10^{-3}\,\mathrm{m\,s^{-1}}$ is imposed.

Different density ratios $\rho_{\mathrm{L}}/\rho_{\mathrm{V}}$ were considered ranging from 2 to 2000 by changing ρ_{V}. $\dot{m}$ was set accordingly to have the desired u_{I}. The interface starts at a position $0.4\,\mathrm{m}$ from the left side. The benchmark was computed with the fluid properties gathered in Table 3.2.

No reinitialisation was done for this benchmark, leading to a deformed Level Set. This enhanced the capability of the formulation to handle non reinitialised Level Set on simple configurations. The case was computed with four mesh sizes (in m): 5×10^{-3}, 1×10^{-2}, 2×10^{-2} and 5×10^{-2}. Four time steps were set accordingly to

	ρ ($\mathrm{kg\,m^{-3}}$)				η ($\mathrm{Pa\,s}$)	γ_0 ($\mathrm{J\,m^{-2}}$)
Ratio r	2000	200	20	2		
Vapour	5×10^{-1}	5	5×10^{1}	5×10^{2}	1.2×10^{-5}	6×10^{-2}
Liquid	10^3				2.8×10^{-4}	

Table 3.2: Physical properties of the considered fluids.

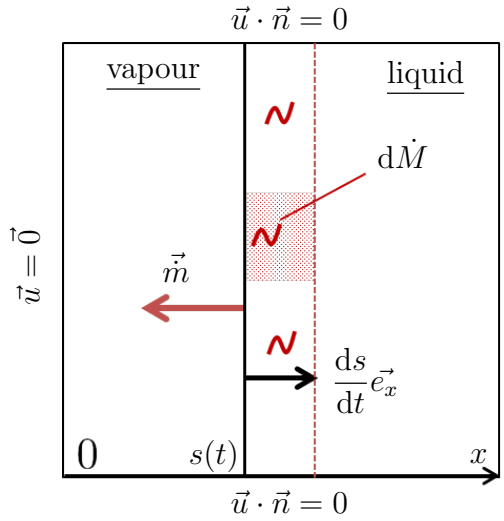

Figure 3.8: Description of the Moving Interface Benchmark. Dirichlet conditions are described in this figure. Boundary conditions for the velocity components and pressure that are not mentioned are set free.

maintain a constant CFL value of 0.2 related to the interface velocity $u_\mathrm{I} = \dot{m}/\rho_\mathrm{V}$. Two convergence studies were done. In the first one, the parameter ε was set constant to 0.1 m. In the second one, ε was set consistently with the mesh size h: $\varepsilon = 3h$. The considered error was computed following (2.71) but with $N = 10$ sample points.

3.4.1.1 Constant ε

Positions for every mesh size for the case $r = 2000$ are plotted on Figure 3.9, and convergence studies for every ratios are plotted in Figure 3.10.

Displacement of the interface is properly computed according to the analytical solution, validating the combination of the two solvers. This is true whatever the density ratio. The convergence is well observed, with an order of 2 whatever the density ratio. This is coherent with the results of the pseudo compressible square benchmark with $A = 0.01$.

3.4.1.2 Varying ε

The idea of the formulation is to reduce the interface size as much as possible, as the goal is to model a quasi sharp interface. The physical mixing length of a vapour liquid interface is of the order of magnitude of an Å, though this scale is rarely reached in practice. ε is then set according to the mesh size value. The same law as for the Stefan problem described in Section 2.5 was taken: $\varepsilon = 3h$.

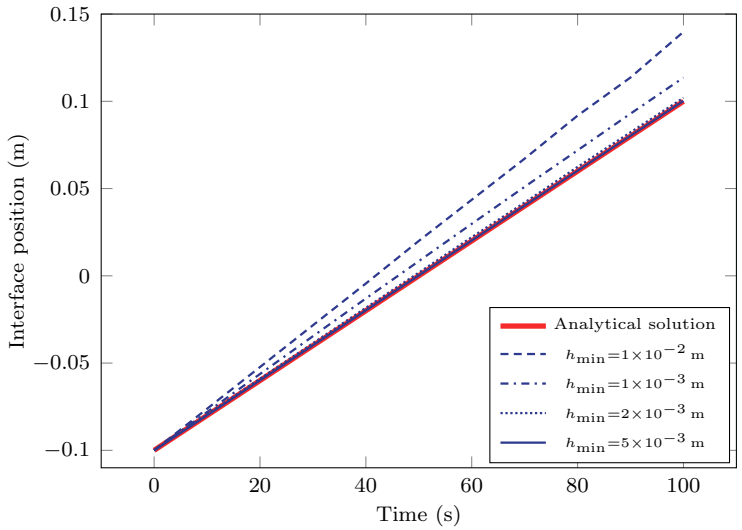

Figure 3.9: Interface position in the case $r = 2000$ for $\varepsilon = 0.1\,\mathrm{m}$ for the Moving Interface Benchmark.

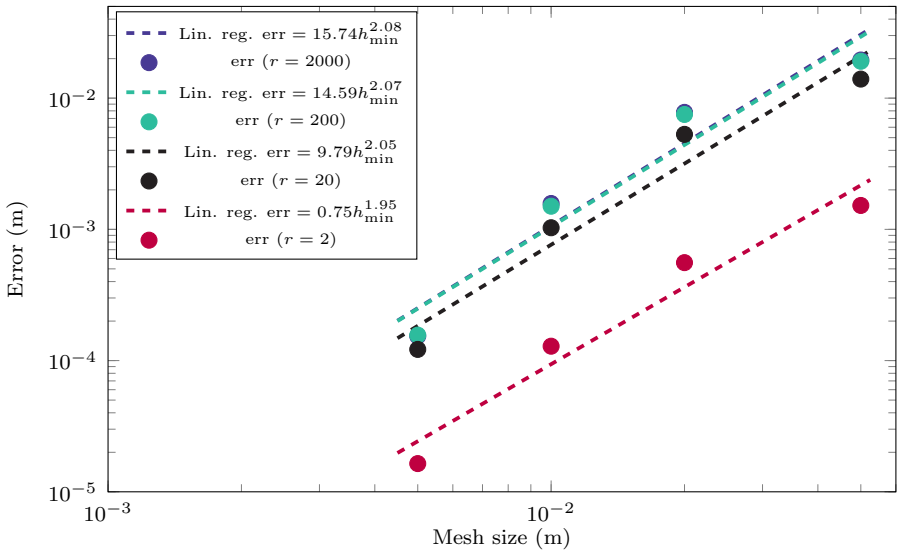

Figure 3.10: Space-time convergence analysis for the Moving Interface benchmark for $\varepsilon = 0.1\,\mathrm{m}$.

Doing so, two problems arose. Firstly, numerical instabilities described by [125] were not handled anymore and disturbed the interface. This is not surprising, as the BZK condition ($\Delta t_{\mathrm{BZK}} < \sqrt{(\rho_{\mathrm{V}} + \rho_{\mathrm{L}})h^3/4\pi\gamma_0}$) was exceeded by 2 orders of magnitudes, and the way the surface tension is handled does not fully control these

instability, according to [125]. But this problem can be handled by reducing the time step.

Secondly an error remained even with no surface tension or with a stabilisation by increasing both viscosities by a factor 100. No proper convergence was observed up to a certain mesh size and a residual error of around 1% remained. For example, interface positions for a ratio $r = 2000$ with higher viscosity are plotted Figure 3.11.

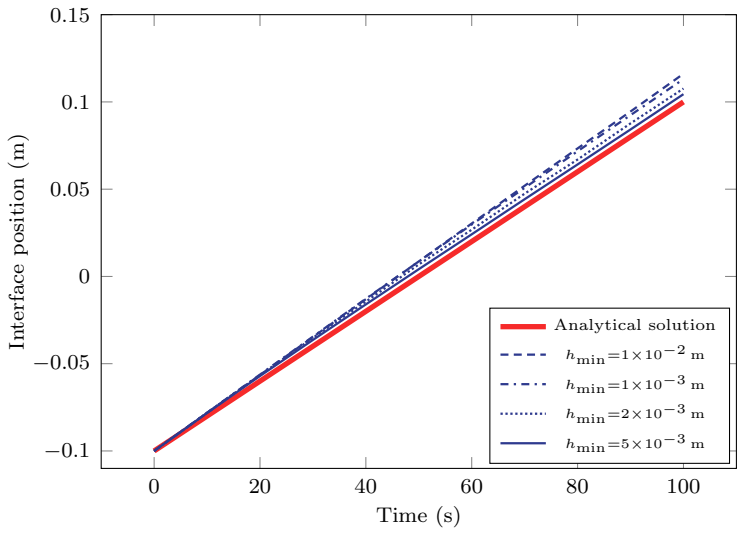

Figure 3.11: Interface position in the case $r = 2000$ for $\varepsilon = 3h$ for the Moving interface benchmark.

This can be explained by the discretisation of the Dirac function δ_α. Considering a ε proportional to h means that the δ_α function is discretised with the same number of point whatever the mesh size: 7 discretisation points for $\varepsilon = 3h$ (see Figure 3.12). However what is important is the capability of the function δ_α to have an integral of 1 over the interface. But this is not guaranteed with a fixed amount of sample points in an unstructured mesh.

To demonstrate this, a Python code was implemented to assess the order of magnitude of the error made by the discretisation on the integral computation in a 1D configuration. The idea was to recreate an approximation of an unstructured mesh for $\varepsilon = 3h$. We considered a constant mesh size h of 1 and seven reference sample points $\tilde{a}$, enriched with two extremity sample points at a distance $4h$ from the center to cover the entire function:

$$\tilde{a}_{i\in[\![0,8]\!]} = -(3+1)h + h\,i \tag{3.30}$$

A batch of 1000 groups of sample points were created thanks to the random function rd() from the numpy library of Python which generates a random real

between 0 and 1. Every sample point was randomly placed around a reference sample point at a maximum distance ζ. This is supposed to represent the non uniformity of the mesh. The bigger ζ, the more distorted the mesh is.

$$\{a_i\}_{j\in[\![1,1000]\!]} = \left\{\tilde{a}_i + \zeta\frac{\mathrm{rd}() - 0.5}{0.5}\right\} \tag{3.31}$$

An example of a resulting sampling is plotted in Figure 3.12.

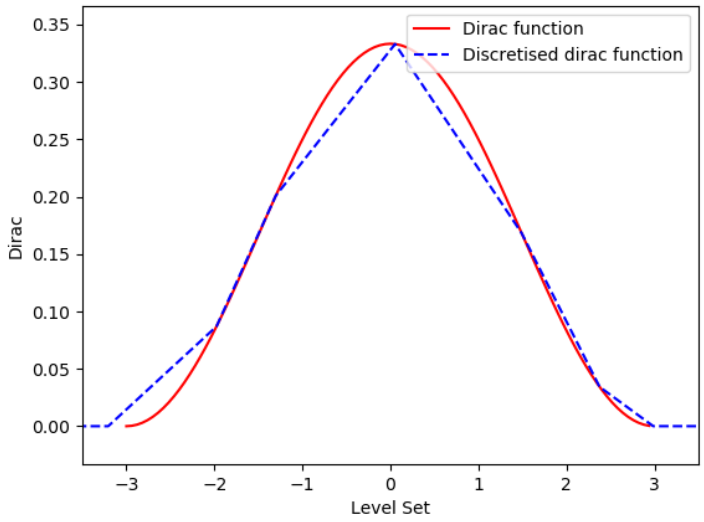

Figure 3.12: Example of discretisation of the Dirac function δ_α in 1D. A thousand similar discretisations are done in the same way using randomised positions around the reference points.

For different values of ζ, a thousand δ_α functions with randomised discritisation points were created. Integrals of these functions were then computed. Mean values of the error made are plotted in Figure 3.13. Tests were carried out with groups of points bigger than 1000 without changing the results. Thus, these results were assumed to represent well the discretisation error done with an unstructured mesh. The order of magnitude of the error is of the percent. This is the same as the one observed for the interface displacement with ε changing with h. This is a possible explanation to the fact that the formulation with a varying interface thickness does not properly converge in mesh size. A permanent residual error exists due to the sampling of the Dirac function: if the integral is not properly computed, the integrated velocity field resulting from the velocity divergence equation deviates from the analytical solution. Then, the convection velocity of the Level Set equation also deviates from the analytical solution due to the same error, leading to an error on the interface position.

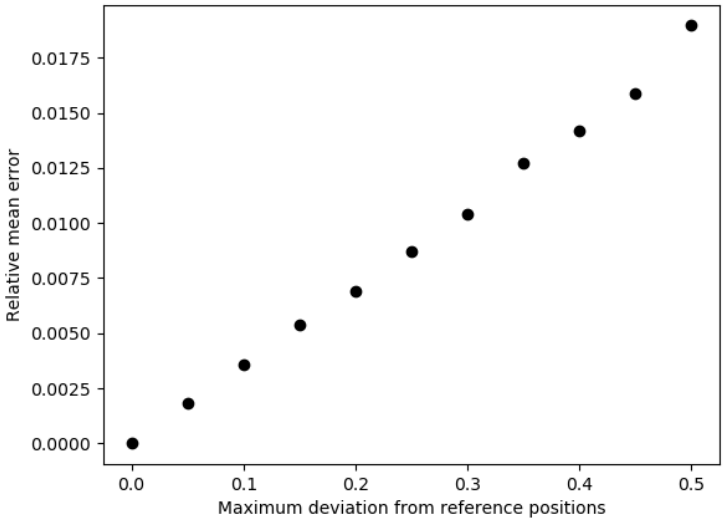

Figure 3.13: Influence of the value of ζ on the mean value of the integral absolute deviation of the discretised Dirac functions of every batch. The more scattered the discretisation points and the larger the deviation.

3.4.2 Growing Bubble

This 2D benchmark was considered to enhance the contribution of the surface tension term. Inside a square domain of $0.008\,\mathrm{m} \times 0.008\,\mathrm{m}$, a circular bubble of low density grows with a constant mass transfer inside a fluid of higher density, as shown in Figure 3.14. This fluid is pushed away outside of the domain, whose boundary conditions are of homogeneous Neumann type (see Figure C.1).

A constant mass transfer of $0.1\,\mathrm{kg\,m^{-2}\,s^{-1}}$ from the vapour phase towards the liquid phase was set. The initial radius of the bubble was set to $0.001\,\mathrm{m}$. Inside the bubble, a small zone was set at 0 velocity to prevent the derivation of the bubble. The benchmark was computed for the fluid properties gathered in Table 3.3.

This time, the Level Set was reinitialised to avoid important distortions of the distance property. The reinitialisation is done every 0.001 s, thus 10 times during the simulation. This is high enough to ensure that the Level Set is not too deformed,

	Density ρ $(\mathrm{kg\,m^{-3}})$	Viscosity η $(\mathrm{Pa\,s})$	Surface Tension γ_0 $(\mathrm{J\,m^{-2}})$
Vapour	1	1.78×10^{-5}	7×10^{-2}
Liquid	10^3	10^{-3}	

Table 3.3: Physical properties of the considered fluids.

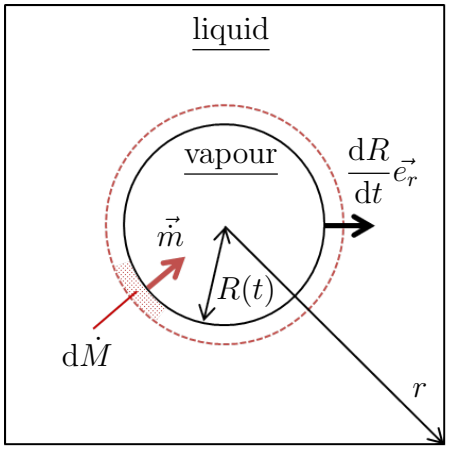

Figure 3.14: Description of the Growing Bubble Benchmark. A constant mass transfer is set to feed the bubble whose radius increases linearly.

but low enough to avoid any systematic error due to the DRT method detailed in [99].

The case was computed with four mesh sizes: (in m): 2×10^{-5}, 5×10^{-5}, 1×10^{-4} and 2×10^{-4}. Four different time steps were set accordingly to maintain a constant CFL value of 0.025 related to the interface velocity $\dot{m}/\rho_{\mathrm{V}}$. With these parameters, the BZK condition was roughly respected. Two studies were done: in the first one, the parameter ε was set constant to $2\times10^{-4}\,\mathrm{m}$. In the second one, ε was set consistently with the mesh size h: $\varepsilon = 3h$.

The considered error was based on the radius R, among $N = 10$ sample points:

$$\mathrm{err} = \frac{1}{N} \sum_{i\in[\![1,N]\!]} \left| R^i_{\mathrm{simu}} - R^i_{\mathrm{an}} \right| \tag{3.32}$$

We first studied the case with a constant ε with and without the second order correction, in order to enhance the effect of this term. The configuration without the correction term showed a residual error on the radius even with the smallest values of time step and mesh size. This error vanished with the addition of the correction (see Figure 3.15).

Results of the convergence study with the correction term are shown in Figure 3.16. Now, a proper convergence is observed. An order of convergence close to 2 is coherent with the former results of the moving interface.

Regarding the convergence study for the varying ε, radius for different time step and mesh size are plotted in Figure 3.17.

The error is not very significant for small h and Δt, but there is still a lack of convergence due to the Dirac discretisation. The order of magnitude of the error is

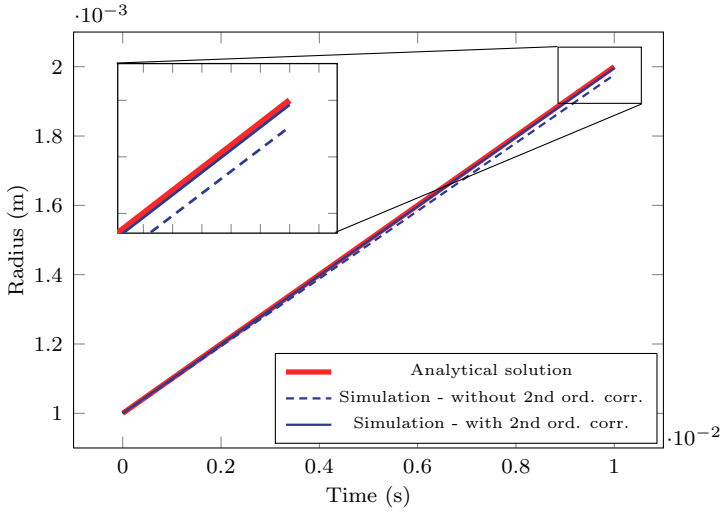

Figure 3.15: Impact of the 2nd order correction term on the LS convection velocity the Growing Bubble benchmark for $\varepsilon = 2{\times}10^{-4}$ m.

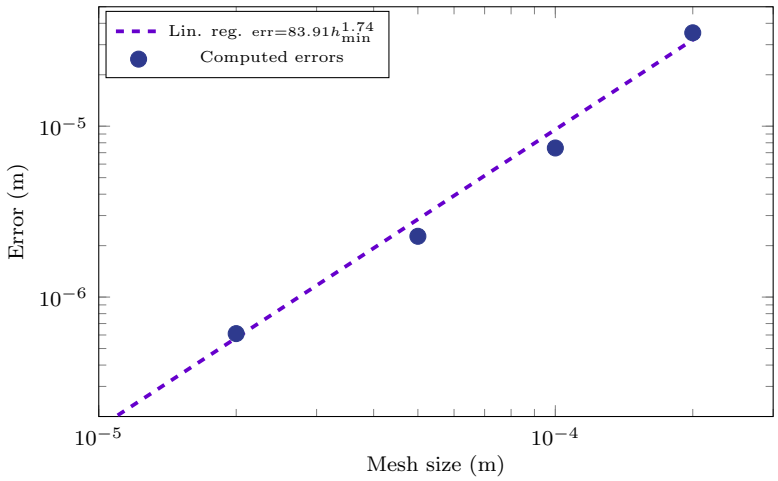

Figure 3.16: Space-time convergence analysis for the Growing Bubble benchmark for $\varepsilon = 2{\times}10^{-4}$ m.

again the same as the one estimated thanks to our Python code, explaining the non convergence of the scheme for a varying ε. This is however an error of relative small importance for more complex cases, and that can be reduced by raising the number of discretisation points to describe δ_α.

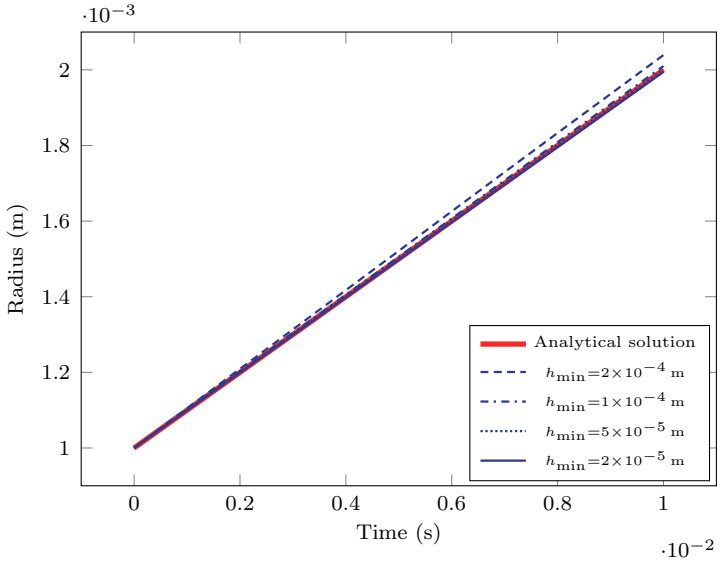

Figure 3.17: Radius for different mesh sizes and time steps for the growing bubble benchmark for $\varepsilon = 3h$.

3.5 Conclusions

- The mass and momentum conservation equations were adapted in the context of a multiphase system with phase change to account for the interfacial velocity jump. A source term appears in the velocity divergence equation.
- A dedicated pseudo-compressible Navier–Stokes solver was extended from a preexisting incompressible Navier–Stokes solver to account for the source term in the velocity divergence equation. It was tested and validated with a 2D single phase benchmark
- The coupling of the pseudo-compressible solver with the adapted Level Set convection equation leads to a mechanical diphasic model with phase change. This model was tested and validated in two 2D benchmarks: the moving interface and the growing bubbles.
- A second order term appears in the Level Set velocity equation if the curvature radius is of the same order of magnitude as ε.
- A systematic error is present due to the discretisation of the Dirac function. A sufficient number of discretisation points are required for the velocity jump to be properly computed.

Chapter 4

Complete phase change solver

Contents

Résumé en Français

Ce chapitre présente le modèle de changement de phase complet regroupant les modèles mécanique et thermique. Un couplage faible est mis en place avec la résolution successive de chaque équation. En particulier, le taux surfacique de transfert de masse est calculé par le saut de flux de chaleur du modèle thermique. Sa valeur est ensuite réinjectée dans l'équation de conservation de la masse et dans l'équation de convection de la Level Set. Afin d'optimiser le coût de calcul de l'ensemble, un maillage adaptatif issu de la librairie de calcul CIMLib-CFD est utilisé afin de raffiner le maillage uniquement autour de l'interface. C'est en effet là où les besoins en précision de maillage sont les plus importants.

Le modèle de changement de phase est validé sur deux cas test 2D analytiques représentant des situations simples de vaporisation. Le premier est le cas de Stefan compressible, similaire à celui étudié au Chapitre 2 mais avec deux phases aux densités différentes. Une seule configuration "sous-refroidie" est étudiée. La convergence à l'ordre 1 en taille de maille est bien observée. Le second cas est le cas de Scriven. Il s'agit de la croissance d'une bulle de vapeur dans un liquide sur-saturé. Ce cas est plus complexe à simuler car il rajoute les effets de tension de surface, et il met en place un système plus instable: une erreur sur la position de l'interface tend à s'accroître, contrairement à la configuration du cas de Stefan. De fait, le modèle proposé ne permet pas de surmonter cette difficulté nouvelle, et seule une correction *ad hoc* permet d'obtenir la convergence en taille de maille. Cette observation intéressante n'est pas pénalisante, car seules des configurations avec des liquides non sur-saturés sont concernées par le cadre de l'étude.

Un cas test de la littérature est finalement étudié: le film de vapeur horizontal. Il s'agit de l'étude du développement d'un film de vapeur sur une plaque dont la température est fixée. Le film est initialisé avec une perturbation dont la longueur d'onde est calculée selon la théorie de l'instabilité de Rayleigh–Taylor. Ce cas test est étudié en 2D et en 3D. Dans les deux cas, l'hydrodynamique, la forme de l'interface liquide vapeur ainsi que le flux calculé sont proches des résultats de la littérature. Une étude qualitative est aussi réalisée pour des cas "sous-refroidis" avec un comportement qui est proche de celui attendu.

4.1 Introduction

On the one hand, a multiphase thermal model with phase change was developed and validated for a 1D benchmark. On the other hand a mechanical multiphase monolithic model with phase change was developed and validated for 2D benchmark. A complete phase change solver was then built upon those two models. The full set of equations and assumptions is recalled in this section. The full solving procedure is presented as well as the remeshing algorithm to optimise the computation cost. 2D benchmarks and 3D benchmarks were investigated.

4.2 Eulerian framework

4.2.1 Coupled Navier–Stokes, Thermal and Level Set solvers

Combining the pseudo-compressible framework with the thermal solver leads to the following full phase change system:

$$
\begin{cases}
\text{Mass conservation:} \\
\underbrace{\vec{\nabla}\cdot\vec{u}}_{\text{Particle deformation}} = \underbrace{\left[\!\left[\frac{1}{\rho}\right]\!\right]\left(\dot{\vec{m}}\cdot\vec{\nabla}\alpha\right)\delta_\alpha}_{\text{Phase change velocity jump}} & (4.1) \\
\text{Momentum conservation:} \\
\underbrace{\rho\left(\frac{\partial\vec{u}}{\partial t}+(\vec{u}\cdot\vec{\nabla})\vec{u}\right)}_{\text{Momentum particle variation}} = \underbrace{-\vec{\nabla}p}_{\text{Pressure works}} + \underbrace{\vec{\nabla}\cdot 2\eta\dot{\vec{\varepsilon}}}_{\text{Viscous works}} + \underbrace{\rho\vec{g}}_{\text{Gravity}} + \underbrace{\gamma_0\kappa_\alpha\delta_\alpha\vec{\nabla}\alpha}_{\text{Surface tension}} & (4.2) \\
\text{Energy conservation:} \\
\underbrace{\rho c_{\mathrm{p}}\left(\frac{\partial T}{\partial t}+\left(\vec{u}\cdot\vec{\nabla}\right)T\right)}_{\text{Energy particle variation}} + \underbrace{A(T-T_{\mathrm{sat}})\delta_\alpha}_{T_{\mathrm{sat}}\text{ stabilisation}} = \underbrace{\vec{\nabla}\cdot k\vec{\nabla}T}_{\text{Conduction}} - \underbrace{\left(\mathcal{L}\dot{\vec{m}}+\vec{q_{\mathrm{R}}}\right)\cdot\vec{\nabla}\alpha\delta_\alpha}_{\text{Interface source term}} & (4.3) \\
\text{Level Set convection:} \\
\frac{\partial\alpha}{\partial t}+\left(\underbrace{\vec{u}-\frac{\rho}{\rho_{\mathrm{V}}\rho_{\mathrm{L}}}\dot{\vec{m}}}_{\text{Interface velocity}} - \underbrace{\left[\!\left[\frac{1}{\rho}\right]\!\right]\dot{\vec{m}}\frac{\kappa_\alpha}{\|\vec{\nabla}\alpha\|}\int_{-\varepsilon}^{0}H_\alpha\,\mathrm{d}\alpha}_{\text{2nd order correcton}}\right)\cdot\vec{\nabla}\alpha=0 & (4.4) \\
\text{Energy conservation at the interface:} \\
\underbrace{\mathcal{L}\left(\dot{\vec{m}}\cdot\vec{\nabla}\alpha\right)}_{\text{Phase change enthalpy}} = \underbrace{\left[\!\left[k\vec{\nabla}T\cdot\vec{\nabla}\alpha\right]\!\right]}_{\text{Conductive fluxes jump}} - \underbrace{\vec{q_{\mathrm{R}}}\cdot\vec{\nabla}\alpha}_{\text{Radiation}} & (4.5)
\end{cases}
$$

We recall the assumptions taken:

- The thermodynamical equilibrium at atmospheric pressure was considered at the interface.
- The flow was considered incompressible inside each fluid domain except at the interface.
- Radiation fluxes were considered to be localised at the interface and only from the vapour side.
- The influence of pressure variations on thermal energy variations was considered negligible (on each fluid as well as on the interface).
- Viscous dissipation was considered negligible in regards to thermal energy variations (on each fluid as well as on the interface).

We considered a weak coupling meaning that each equation is solved one after the other. The Figure 4.1 explains the algorithm procedure.

4.2.2 FEM framework and remeshing techniques

We recall that the whole system was embedded inside a FEM framework. The mechanical part of the model was implemented using a VMS approach detailed in Section 3.2.4. The thermal part and the Level Set model were solved using a SUPG–SCPG approach for Convection–Diffusion–Reaction equations detailed in Section 2.3.5.

To reduce the computational time, an extra feature was added to this environment. A remeshing algorithm was used to focus the computation on nodes of interest. For example, it allows to have a liquid vapour interface described with a fine mesh and at the same time a moderate amount of mesh nodes.

An automatic mesh adaptation procedure was used for unstructured meshes with a constrain set on the maximum number of elements. To do so, a metric based on parameters of interest was designed. A metric is a symmetric positive definite tensor that represents a local base and modifies the distance computation from the Euclidean space. It can be used as a weighting tool to give importance to selected directions of the space. This direction is boosted during the remeshing at the expense of other directions. For example, in 2D, the metric associated to a distance $h_{\min}$ in the first coordinate and $h_{\max}$ in the second coordinate reads.

$$\boldsymbol{M} = \begin{pmatrix} 1/h_{\min}^2 & 0 \\ 0 & 1/h_{\max}^2 \end{pmatrix} \tag{4.6}$$

The remeshing procedure associated to this metric provides an anisotropic mesh shown in Figure 4.2. This approach is optimised for the computation of systems that

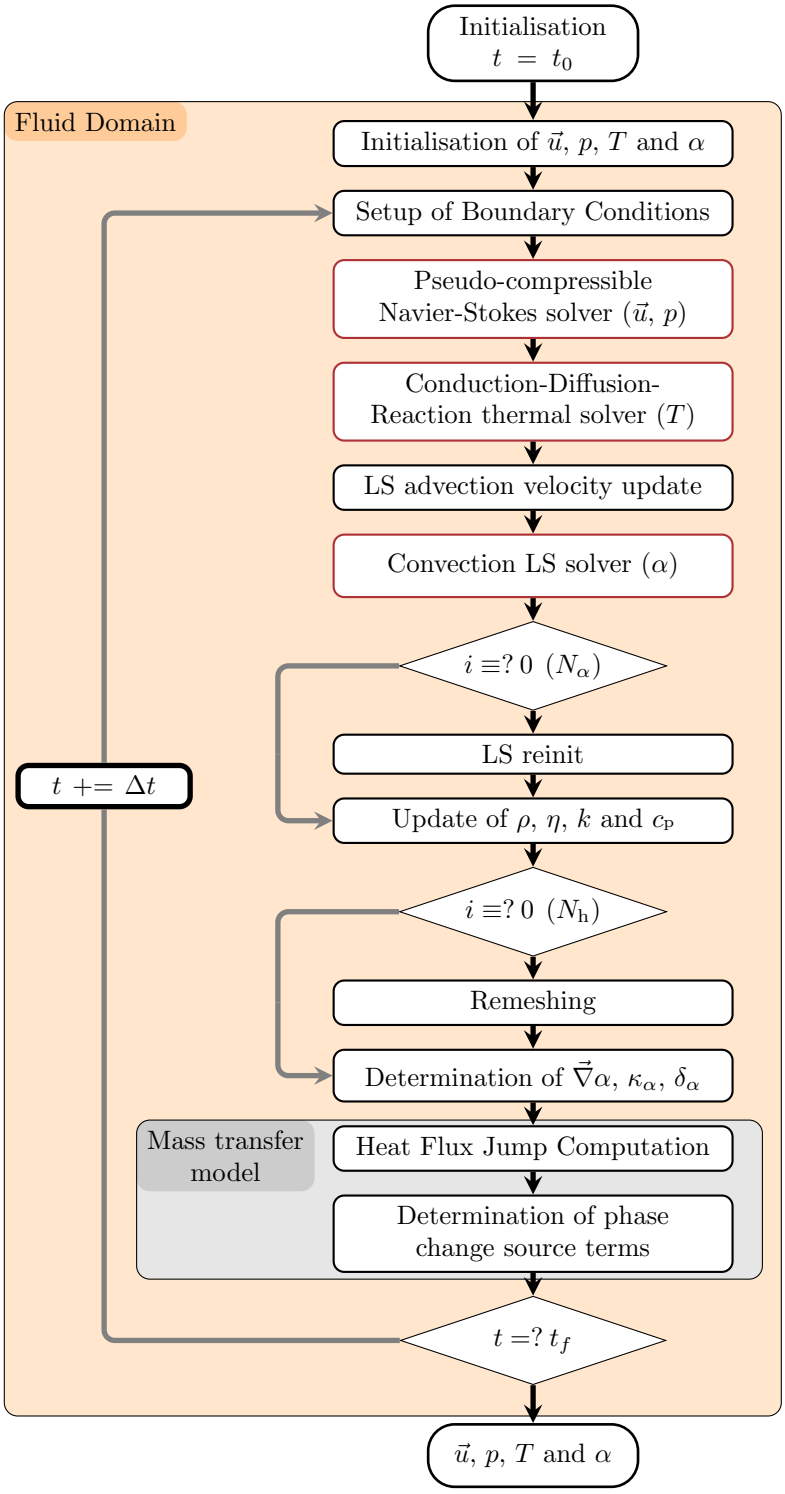

Figure 4.1: Solving procedure of the phase change solver.

require precision along the selected directions. Details on the adaptation technique, the construction of the metric and the error estimator are given in [126, 83]. The numerical methods used to solve partial differential equations on this mesh were therefore modified adequately to take into account the anisotropy of the elements [83].

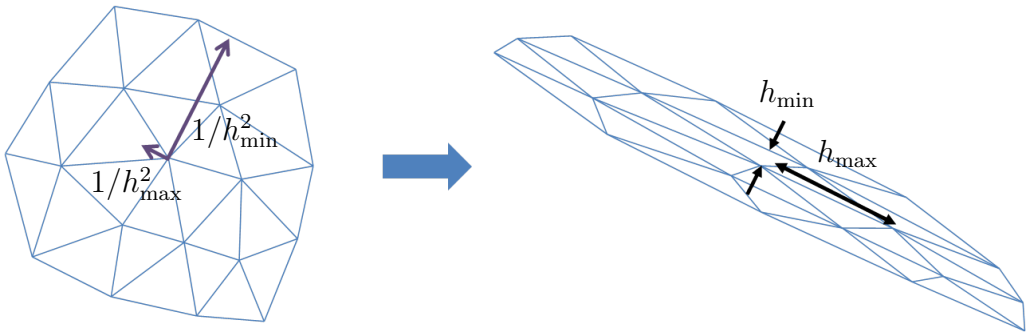

Figure 4.2: Principle of the anisotropic remeshing. The two vector represent the local base of the metric. The main axis is favored with a finer mesh while the weak axis leads to a coarse mesh in its direction.

In the context of phase change, quantities close to and at the interface are of high importance. The interface is the domain that is affected by most of the possible numerical instabilities. Moreover the thinner the interface the more descriptive the model. This is the reason why the metric was designed to accentuate a fine mesh at the interface. A constrain was set on the mesh size h_{min} normal to the interface as in Figure 4.3. This approach allowed to control and reduce the interface thickness ε.

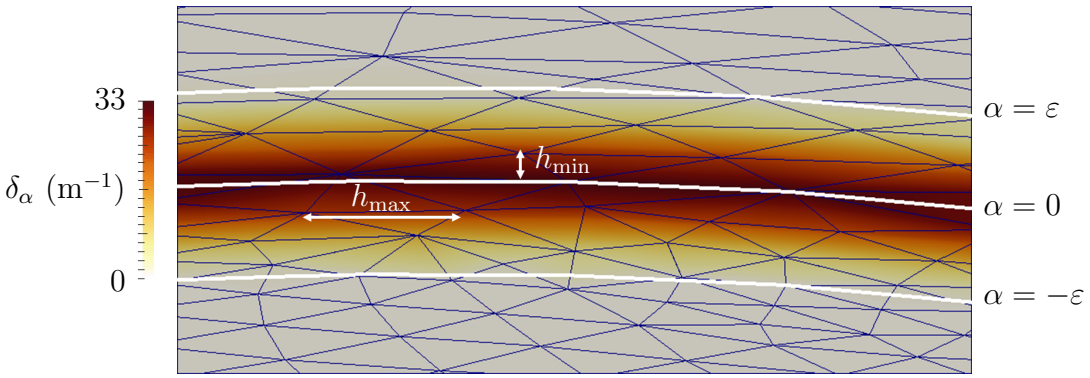

Figure 4.3: Visualisation of the mesh at the interface. The mesh size normal to the interface is correctly set to h_{min}, while the other dimension is set to h_{max}. The dirac function is also plotted, for the case $\varepsilon = 0.3\,\text{m}$.

4.3 2D benchmarks

4.3.1 Subcooled compressible Stefan Benchmark

4.3.1.1 Equations

In this new formulation, the vaporizing molecules push back the liquid as their density changes (see Figure 4.4). The equation in the vapour phase is unchanged as the vapour is still static. However in the liquid phase, a convective term appears. The new equation reads:

$$\frac{\partial T}{\partial t} + u_L \frac{\partial T}{\partial x} = D_{\mathrm{L}} \frac{\partial^2 T}{\partial x^2} \tag{4.7}$$

The velocity u_L is spatially constant, and determined thanks to the velocity jump at the interface:

$$u_L = \left[\!\left[\frac{1}{\rho}\right]\!\right] \dot{m} = \left[\!\left[\frac{1}{\rho}\right]\!\right] \rho_{\mathrm{V}} \frac{\mathrm{d}s}{\mathrm{d}t} \tag{4.8}$$

Boundary conditions (2.59a)–(2.59d) do not change. The interface displacement is still proportional to the square root of the time:

$$s(t) = 2\chi\sqrt{D_{\mathrm{V}} t} \tag{4.9}$$

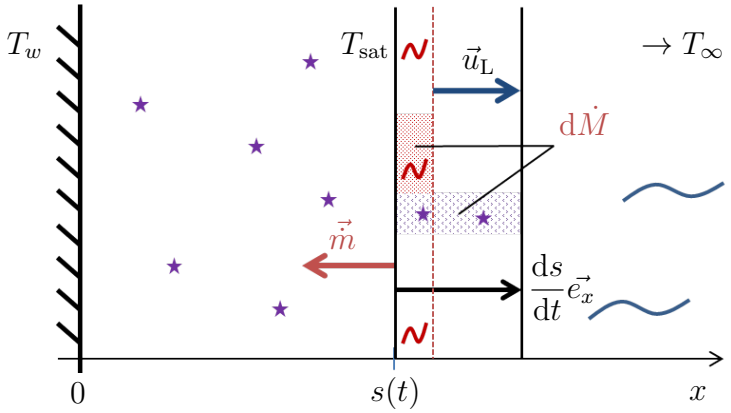

Figure 4.4: Description of the compressible Stefan problem. The wall to the left is at T_w, and the liquid to the right is at T_∞ far from the interface. The heat flux from the wall gives energy to the interface by conduction. The liquid heats up and vaporises, but conduction in the liquid slows down the interface progress. As the liquid is more dense, its vaporisation creates a volume. The vapour is blocked by the wall and pushes the liquid back.

A simple change of variable allows to transform equation (4.7) back to a diffusion equation. Defining $\tilde{T}$ such that $T(x,t) = \tilde{T}(x - \int_0^t u_L(\tau)\,\mathrm{d}\tau, t)$:

$$\frac{\partial \tilde{T}}{\partial t} = D_\mathrm{L} \frac{\partial^2 \tilde{T}}{\partial x^2} \tag{4.10}$$

Following the same steps as in Section 2.5.1, $\tilde{T}$ is of the form $A\,\mathrm{erf}(x/2\sqrt{D_\mathrm{L} t}) + B$. Thus in the liquid phase:

$$T = A\,\mathrm{erf}\left(\frac{x - \int_0^t u_L(\tau)\,\mathrm{d}\tau}{2\sqrt{D_\mathrm{L} t}}\right) + B \tag{4.11}$$

Moreover with the relation 4.8:

$$\int_0^t u_L(\tau)\,\mathrm{d}\tau = \left[\!\left[\frac{1}{\rho}\right]\!\right] \rho_\mathrm{V} \int_0^t \frac{\mathrm{d}s}{\mathrm{d}t}\,\mathrm{d}\tau = \left(1 - \frac{\rho_\mathrm{V}}{\rho_\mathrm{L}}\right) [\![s]\!]_0^t = \left(1 - \frac{\rho_\mathrm{V}}{\rho_\mathrm{L}}\right) s(t) \tag{4.12}$$

Finding A and B with the boundary conditions, the solution of this new version of the Stefan benchmark then reads:

$$T(x,t) = \begin{cases} T_w + \dfrac{T_\mathrm{sat} - T_w}{\mathrm{erf}\,(\chi)}\,\mathrm{erf}\left(\chi \dfrac{x}{s(t)}\right) & \text{for } x \in [0, s(t)] \\ T_\infty + \dfrac{T_\mathrm{sat} - T_\infty}{\mathrm{erfc}\left(\chi \dfrac{\rho_\mathrm{V}}{\rho_\mathrm{L}} \sqrt{\dfrac{D_\mathrm{V}}{D_\mathrm{L}}}\right)}\,\mathrm{erfc}\left(\chi \dfrac{x - \left(1 - \dfrac{\rho_\mathrm{V}}{\rho_\mathrm{L}}\right) s(t)}{s(t)} \sqrt{\dfrac{D_\mathrm{V}}{D_\mathrm{L}}}\right) & \text{for } x \in [s(t), +\infty[\end{cases} \tag{4.13}$$

The temperature gradient reads:

$$\frac{\partial T}{\partial x}(x,t) = \begin{cases} \dfrac{1}{\sqrt{\pi D_\mathrm{V} t}} \dfrac{T_\mathrm{sat} - T_w}{\mathrm{erf}\,(\chi)}\,\mathrm{e}^{-\left(\chi \frac{x}{s(t)}\right)^2} & \text{for } x \in]0, s(t)] \\ -\dfrac{1}{\sqrt{\pi D_\mathrm{L} t}} \dfrac{T_\mathrm{sat} - T_\infty}{\mathrm{erfc}\left(\chi \dfrac{\rho_\mathrm{V}}{\rho_\mathrm{L}} \sqrt{\dfrac{D_\mathrm{V}}{D_\mathrm{L}}}\right)}\,\mathrm{e}^{-\left(\chi \frac{x - \left(1 - \frac{\rho_\mathrm{V}}{\rho_\mathrm{L}}\right) s(t)}{s(t)} \sqrt{\frac{D_\mathrm{V}}{D_\mathrm{L}}}\right)^2} & \text{for } x \in]s(t), +\infty[\end{cases} \tag{4.14}$$

χ is evaluated thanks to the resolution of the energy equation at the interface (2.60). Thanks to the expression of the temperature gradient:

$$\rho_{\mathrm{V}}\mathcal{L}\chi\sqrt{D_{\mathrm{V}}} + \frac{k_{\mathrm{V}}(T_{\mathrm{sat}} - T_w)\,\mathrm{e}^{-\chi^2}}{\sqrt{\pi D_{\mathrm{V}}}\,\mathrm{erf}(\chi)} + \frac{k_{\mathrm{L}}(T_{sat} - T_\infty)\,\mathrm{e}^{-\chi^2\frac{\rho_{\mathrm{V}}^2}{\rho_{\mathrm{L}}^2}\frac{D_{\mathrm{V}}}{D_{\mathrm{L}}}}}{\sqrt{\pi D_{\mathrm{L}}}\,\mathrm{erfc}\left(\chi\frac{\rho_{\mathrm{V}}}{\rho_{\mathrm{L}}}\sqrt{\frac{D_{\mathrm{V}}}{D_{\mathrm{L}}}}\right)} = 0 \tag{4.15}$$

This equation has once again to be solved numerically. In the present work, a Scilab code was used for this purpose.

4.3.1.2 Case studied

Only one configuration was tested: $T_w = T_{\mathrm{sat}} + 10\,\mathrm{K}$, $T_\infty = T_{\mathrm{sat}} - 1\,\mathrm{K}$. Then $\chi = 2.52\times10^{-2}$. The interface was still initialised at $1\times10^{-4}\,\mathrm{m}$. The physical properties of the fluids are given in Table 4.1.

The test case was computed for an unstructured non uniform 2D mesh of dimension $2\times10^{-4}\,\mathrm{m}$ by $2\times10^{-3}\,\mathrm{m}$ with a maximum of 10 000 nodes with an unstructured mesh whose mesh size h at the interface varied among 5 values (in m): 1×10^{-6}, 2×10^{-6}, 4×10^{-6}, 7×10^{-6} and 1×10^{-5}. Five different time steps were set accordingly to maintain a constant CFL value of 0.2 related to the initial interface velocity $\dot{m}(t = t_0)/\rho_{\mathrm{V}}$. The interface thickness was set to $3h$ with an extension zone of size $4h$.

Results of interface position and mass transfer rate values versus time are plotted in Figure 4.5 and 4.6.

The convergence was considered regarding the error on the interface position, computed with (2.71) with $N = 100$ sample points. The convergence is plotted in Figure 4.7.

The convergence is well observed, with an order 1 that is coherent with the prediction of (2.52). The computed errors are above the order of magnitude of the one caused by the discretisation of the Dirac. This explains why it does not disturb the convergence. This may appear for smaller time steps and mesh sizes.

	ρ ($\mathrm{kg\,m^{-3}}$)	c_{P} ($\mathrm{J\,kg^{-1}\,K^{-1}}$)	k ($\mathrm{W\,m^{-1}\,K^{-1}}$)	η ($\mathrm{Pa\,s}$)	$\mathcal{L}$ ($\mathrm{J\,kg^{-1}}$)
Vapour	5.97×10^{-1}	2.030×10^{3}	2.48×10^{-2}	1.20×10^{-5}	2.26×10^{6}
Liquid	9.584×10^{2}	4.216×10^{3}	6.76×10^{-1}	2.8×10^{-4}	

Table 4.1: Physical properties of the considered fluids for the compressible subcooled Stefan benchmark.

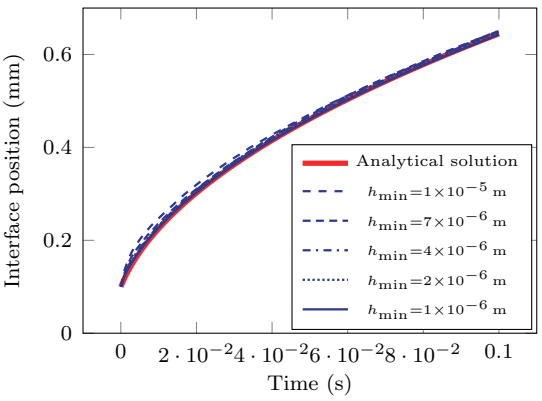

Figure 4.5: Position of the interface for different mesh sizes and time steps for the compressible Stefan problem benchmark.

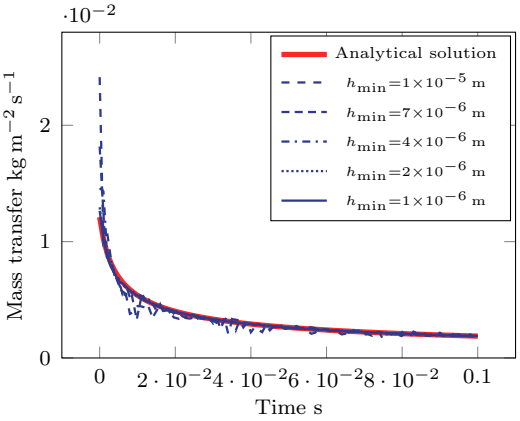

Figure 4.6: Mass transfer for different mesh sizes and time steps for the compressible Stefan problem benchmark.

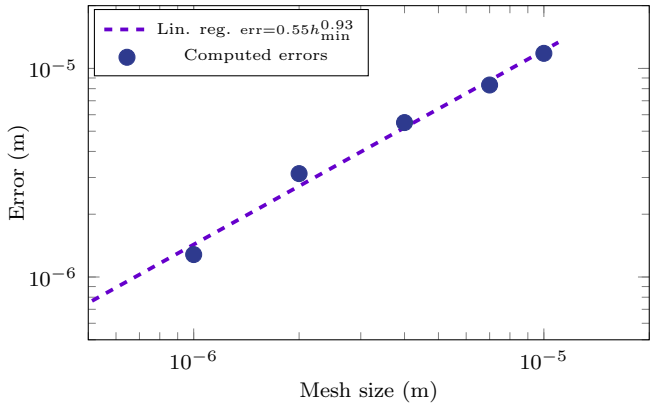

Figure 4.7: Space-time convergence analysis for the compressible Stefan problem benchmark.

4.3.2 Scriven benchmark

The last analytical benchmark considered was the so-called "Scriven problem". This benchmark adds to the Stefan problem two major difficulties. The first one is related to the curvature of the interface and especially Surface Tension effects. The second one is the unstable nature of this test case, that makes it difficult to solve. This difference lies on the oversaturated state of the liquid. For the Stefan test case, a small error on the interface position leads to a stabilizing $\dot{m}$ (see Figure 4.8a). For example, if the interface is a little above the analytical solution, this leads to a higher heat flux on the liquid side, meaning a reduction of $\dot{m}$: the interface slows down to recover the analytical solution. In the Scriven benchmark, a small error on the radius leads to an amplifying error on $\dot{m}$ (see Figure 4.8b).

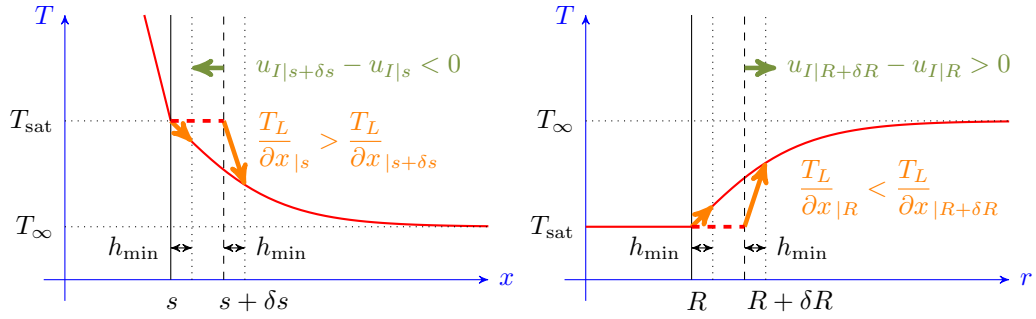

(a) Stefan configuration *(b) Scriven configuration*

Figure 4.8: Stability of the Stefan and the Scriven solution to an error on the interface position. For the Sefan problem, a positive error δs on the interface leads to a larger temperature gradient. This leads to a reduced interface velocity according to (2.60) that diminishes the error. For the Scriven problem, a positive error δR on the radius also leads to a larger temperature gradient but the sign is inversed. This leads to a larger interface velocity according to (4.30) that amplifies the error.

4.3.2.1 Global description

We considered a 2D version of the problem. This is a cylindrical vapour "bubble" at saturation temperature T_{sat} that grows inside an infinite oversaturated liquid domain. The bubble initially starts with a null radius. The liquid initially starts with a uniform temperature $T_\infty > T_{\text{sat}}$. The liquid vapour interface remains at T_{sat} (thermodynamic equilibrium). The bubble starts to evolve at a time $t = 0$. Its radius $R(t)$ grows with time as the heat from the supersaturated liquid vaporises at its surrounding. The bubble is not subject to any other effects. It is then immobile and the problem has a cylindrical symmetry: all the physical unknowns are only function of the cylindrical coordinate r and of the time t. Both phases are incompressible. The geometric configuration is similar to the one of the Growing bubble benchmark described in section 3.4.2 (see Figure 4.9).

The case is characterised by an adimensional number, the Jakob number defined as:

$$\text{Ja} = \frac{\rho_{\text{L}} c_{\text{pL}} (T_\infty - T_{\text{sat}})}{\rho_{\text{V}} \mathcal{L}} \tag{4.16}$$

and a relative density ratio coefficient:

$$\epsilon = \left(1 - \frac{\rho_{\text{V}}}{\rho_{\text{L}}}\right) \tag{4.17}$$

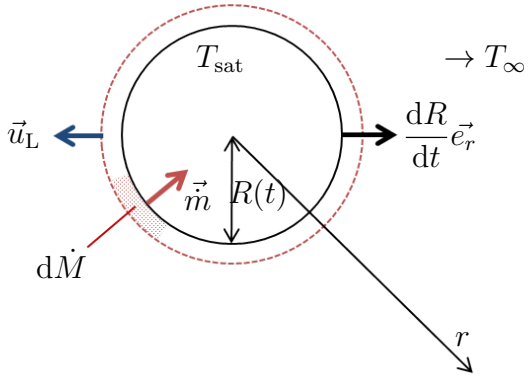

Figure 4.9: Description of the Scriven problem. A bubble is initialised inside a superheated liquid. The heat from the liquid vaporises the liquid close to the bubble. This feeds with vapour the bubble that grows.

The boundary conditions can be summed up as:

$$\begin{cases} T(r, t=0) = T_\infty & \text{for } r > 0 \quad (4.18) \\ T(r \leq R, t) = T_{\text{sat}} & \text{for } t > 0 \quad (4.19) \\ T(r = +\infty, t) = T_\infty & \text{for } t > 0 \quad (4.20) \end{cases}$$

4.3.2.2 Conservation equations

The following sections are dedicated to the demonstration of the analytical solution of this benchmark. Volumes and surfaces are considered similarly as this is a 2D case.

Mass conservation inside the liquid We consider conservation of mass on a liquid ring with inner radius $R_1 > R$ and outer radius R_2:

- Input mass flux: $\rho_{\text{L}} u(R_1, t) 2\pi R_1 \, \mathrm{d}t$
- Output mass flux: $\rho_{\text{L}} u(R_2, t) 2\pi R_2 \, \mathrm{d}t$

The liquid being incompressible, the mass of liquid in the ring is constant at any time, leading to a velocity that is only time dependent:

$$ru(r, t) = K(t) = Ru(R, t) \quad (4.21)$$

Mass conservation at the interface We consider the surface mass of liquid that vaporise per time unit $\dot{m}(t)$. The mass of vapour created over $\mathrm{d}t$ then reads

$2\pi R\dot{m}\,\mathrm{d}t$. We equalise the equivalent volume by the additional volume of the bubble between t and $t+\mathrm{d}t$:

$$2\pi R\dot{m}\,\mathrm{d}t = \rho_\mathrm{V}\pi(R(t+\mathrm{d}t)^2 - R(t)^2) \tag{4.22}$$

Hence:

$$\frac{2R\dot{m}}{\rho_\mathrm{V}} = \frac{\mathrm{d}R^2}{\mathrm{d}t} = 2R\frac{\mathrm{d}R}{\mathrm{d}t} = 2R\dot{R} \tag{4.23}$$

We get the first relationship between the dynamics of growth of the bubble and the mass transfer rate:

$$\dot{R} = \frac{\dot{m}}{\rho_\mathrm{V}} \tag{4.24}$$

Moreover, the expansion of the vaporizing particles pushes the surrounding liquid away. We consider the volume $\mathrm{d}V$ of liquid flowing through a circle of radius $r > R(t+\mathrm{d}t)$ between t and $t+\mathrm{d}t$:

$$\mathrm{d}V = u(t)2\pi r\,\mathrm{d}t \tag{4.25}$$

It corresponds to the volume of fluid expelled by the dilatation. If $\mathrm{d}M = 2\pi R\dot{m}\,\mathrm{d}t$ is the instant vaporised mass, it occupied in t a volume of liquid $\mathrm{d}M/\rho_\mathrm{L}$ and it occupies in $t+\mathrm{d}t$ a volume of vapour $\mathrm{d}M/\rho_\mathrm{V}$. This excess volume is as much liquid to evacuate. Hence:

$$u(t)2\pi r\,\mathrm{d}t = 2\pi R\dot{m}\,\mathrm{d}t\left(\frac{1}{\rho_\mathrm{V}} - \frac{1}{\rho_\mathrm{L}}\right) \tag{4.26}$$

Thus:

$$u(t)r = R\dot{m}\left(\frac{1}{\rho_\mathrm{V}} - \frac{1}{\rho_\mathrm{L}}\right) = R\dot{R}\epsilon \tag{4.27}$$

Energy conservation in the liquid We only consider thermal energies variations, i.e. $\Delta e = \rho c_\mathrm{p}\Delta T$. Moreover, only the convective and diffusive effects are taken into account in the liquid. The convective-diffusive equation in the liquid reads:

$$\rho_\mathrm{L}c_{\mathrm{p}\mathrm{L}}\left(\frac{\partial T}{\partial t} + (\vec{u}\cdot\vec{\nabla})T\right) = \vec{\nabla}\cdot(k_\mathrm{L}\vec{\nabla}T) \tag{4.28}$$

Considering constant parameters and writing the liquid diffusivity $D_\mathrm{L} = k_\mathrm{L}/(\rho_\mathrm{L}c_{\mathrm{p}\mathrm{L}})$, this equation in cylindrical coordinate reads:

$$\frac{\partial T}{\partial t} + u\frac{\partial T}{\partial r} = D_\mathrm{L}\left(\frac{\partial^2 T}{\partial r} + \frac{1}{r}\frac{\partial T}{\partial r}\right) \tag{4.29}$$

Energy conservation at the interface As the vapour is at saturation temperature, no heat flux exists inside the vapour phase. All the heat given by diffusion from the liquid to the interface is used to vaporise the liquid:

$$\mathcal{L}\dot{m} = k_{\mathrm{L}} \frac{\partial T}{\partial r}_{|r=R} \tag{4.30}$$

4.3.2.3 Resolution of the equation

In the same idea as for the Stefan problem, we assume that the radius R vary as the square root of the time:

$$R = 2\beta\sqrt{D_{\mathrm{L}}t} \tag{4.31}$$

where β is a constant to identify. This consideration entails:

$$\dot{R} = \beta\sqrt{\frac{D_{\mathrm{L}}}{t}} \tag{4.32}$$

$$u(r,t) = \frac{2\epsilon\beta^2 D_{\mathrm{L}}}{r} \tag{4.33}$$

The energy conservation equation can be rewritten:

$$\frac{\partial T}{\partial t} + \frac{2\epsilon\beta^2 D_{\mathrm{L}}}{r}\frac{\partial T}{\partial r} = D_{\mathrm{L}}\left(\frac{\partial T^2}{\partial r^2} + \frac{1}{r}\frac{\partial T}{\partial r}\right) \tag{4.34}$$

Considering the new variable $\xi = \dfrac{r}{2\sqrt{D_{\mathrm{L}}t}}$, we look for a solution of the form $T(r,t) = F(\xi(r,t))$:

$$\frac{\partial T}{\partial t} = -\frac{r}{4t\sqrt{D_{\mathrm{L}}t}}F'(\xi) \tag{4.35}$$

$$\frac{\partial T}{\partial r} = \frac{1}{2\sqrt{D_{\mathrm{L}}t}}F'(\xi) \tag{4.36}$$

$$\frac{\partial^2 T}{\partial r^2} = \frac{1}{4D_{\mathrm{L}}t}F''(\xi) \tag{4.37}$$

F is then solution of:

$$-\frac{r}{4t\sqrt{D_{\mathrm{L}}t}}F' + \frac{2\epsilon\beta^2 D_{\mathrm{L}}}{r}\frac{1}{2\sqrt{D_{\mathrm{L}}t}}F' = D_{\mathrm{L}}\left(\frac{1}{4D_{\mathrm{L}}t}F'' + \frac{1}{2r\sqrt{D_{\mathrm{L}}t}}F'\right) \tag{4.38}$$

$$-\frac{r}{\sqrt{D_{\mathrm{L}}t}}F' + \frac{4\epsilon\beta^2 D_{\mathrm{L}}t}{r\sqrt{D_{\mathrm{L}}t}}F' = F'' + \frac{2D_{\mathrm{L}}t}{r\sqrt{D_{\mathrm{L}}t}}F' \tag{4.39}$$

$$-2\frac{r}{2\sqrt{D_{\mathrm{L}}t}}F' + 2\epsilon\beta^2\frac{2\sqrt{D_{\mathrm{L}}t}}{r}F' = F'' + \frac{2\sqrt{D_{\mathrm{L}}t}}{r}F' \tag{4.40}$$

$$F'' = -2\xi F' + \frac{2\epsilon\beta^2}{\xi}F' - \frac{1}{\xi}F' \tag{4.41}$$

Integrating this equation:

$$F' = \lambda\,\mathrm{e}^{-\xi^2+(2\epsilon\beta^2-1)\ln(\xi)} = \lambda\xi^{2\epsilon\beta^2-1}\,\mathrm{e}^{-\xi^2} \tag{4.42}$$

Back from the formulation in temperature:

$$T(x,t) = F(\xi) = A\int_{\xi}^{\infty}\frac{x^{2\epsilon\beta^2}}{x\,\mathrm{e}^{x^2}}\,\mathrm{d}x + B \tag{4.43}$$

The integration constants are determined with the boundary conditions. At $r \to \infty$ or equivalently $\xi \to \infty$), $T \to T_\infty$. At the interface $r = R = 2\beta\sqrt{D_{\mathrm{L}}t}$ so $\xi = \beta$, $T = T_{\mathrm{sat}}$. The temperature hence reads:

$$T = T_\infty - \frac{T_\infty - T_{\mathrm{sat}}}{\int_\beta^\infty \frac{x^{2\epsilon\beta^2}}{x\,\mathrm{e}^{x^2}}\,\mathrm{d}x}\int_{\frac{r}{2\sqrt{D_{\mathrm{L}}t}}}^{\infty}\frac{x^{2\epsilon\beta^2}}{x\,\mathrm{e}^{x^2}}\,\mathrm{d}x \tag{4.44}$$

β is determined with the condition of energy conservation at the interface (4.30):

$$\mathcal{L}\dot{m} = \mathcal{L}\rho_{\mathrm{V}}\dot{R} = k_{\mathrm{L}}\frac{\partial T}{\partial r}_{|r=R} \tag{4.45}$$

$$\mathcal{L}\rho_{\mathrm{V}}\beta\sqrt{\frac{D_{\mathrm{L}}}{t}} = k_{\mathrm{L}}\frac{T_\infty - T_{\mathrm{sat}}}{2\sqrt{D_{\mathrm{L}}t}\int_\beta^\infty \frac{x^{2\epsilon\beta^2}}{x\,\mathrm{e}^{x^2}}\,\mathrm{d}x}\frac{\beta^{2\epsilon\beta^2}}{\beta\,\mathrm{e}^{\beta^2}} \tag{4.46}$$

β is then solution of:

$$2\mathcal{L}\rho_{\mathrm{V}}\beta D_{\mathrm{L}} = k_{\mathrm{L}}\frac{T_\infty - T_{\mathrm{sat}}}{\int_\beta^\infty \frac{x^{2\epsilon\beta^2}}{x\,\mathrm{e}^{x^2}}\,\mathrm{d}x}\frac{\beta^{2\epsilon\beta^2}}{\beta\,\mathrm{e}^{\beta^2}} \tag{4.47}$$

$$\frac{\rho_{\mathrm{L}}c_{\mathrm{pL}}(T_\infty - T_{\mathrm{sat}})}{\rho_{\mathrm{V}}\mathcal{L}} = \frac{2\beta^2\,\mathrm{e}^{\beta^2}}{\beta^{2\epsilon\beta^2}}\int_\beta^\infty \frac{x^{2\epsilon\beta^2}}{x\,\mathrm{e}^{x^2}}\,\mathrm{d}x \tag{4.48}$$

$$\mathrm{Ja} = \frac{2\beta^2\,\mathrm{e}^{\beta^2}}{\beta^{2\epsilon\beta^2}}\int_\beta^\infty \frac{x^{2\epsilon\beta^2}}{x\,\mathrm{e}^{x^2}}\,\mathrm{d}x \tag{4.49}$$

This equation has to be solved numerically to find the value of β. The temperature solution can be rewritten:

$$T = T_\infty - (T_\infty - T_{\mathrm{sat}})\frac{2\beta^2\,\mathrm{e}^{\beta^2}}{\mathrm{Ja}\beta^{2\epsilon\beta^2}}\int_{\frac{r}{2\sqrt{D_{\mathrm{L}}t}}}^{\infty}\frac{x^{2\epsilon\beta^2}}{x\,\mathrm{e}^{x^2}}\,\mathrm{d}x \tag{4.50}$$

4.3.2.4 Case Studied

The case was considered for Ja = 10 leading to a value of $\beta = 8.266$. Physical parameters taken into account are gathered in Table 4.2.

As pretty small mesh sizes were considered, the remeshing algorithm was used. It ensured the mesh properties described by Figure 4.10, where $h_{\min}$ is changed for the space convergence analysis, $h_{\text{ext}} = 3h_{\min}$ and $h_\infty = 10h_{\min}$

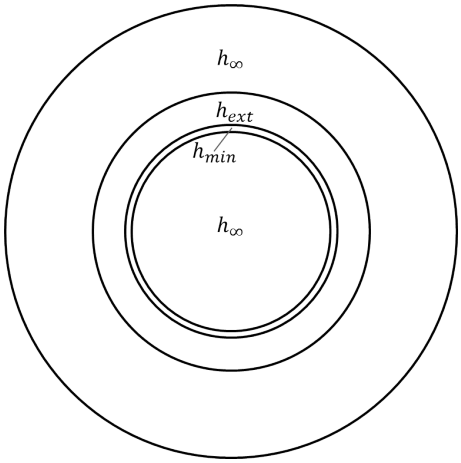

Figure 4.10: Spatial distribution of the mesh size for the Scriven problem.

The test case was computed for an unstructured non uniform 2D mesh of dimension $6{\times}10^{-3}$ m by $6{\times}10^{-3}$ m with a maximum of 5000 nodes with an unstructured mesh whose mesh size $h_{\min}$ at the interface was set to 5 different values (in m): $2{\times}10^{-6}$, $5{\times}10^{-6}$, $1{\times}10^{-5}$, $2{\times}10^{-5}$ and $5{\times}10^{-5}$. Five different time steps were set accordingly to maintain a constant CFL value of 0.15 related to the initial interface velocity $\dot{m}(t = t_0)/\rho_{\text{V}}$. The radius was initialised at 0.001 m, that corresponds to an initial time of $t_0 = 0.0246$ s. The simulation ran from t_0 to $4t_0$, so that the analytical radius varied from 0.001 m to 0.002 m.

The interface thickness was set to $3h_{\min}$ with an extension zone of size $4h_{\min}$. As the thickness influences a lot the temperature gradients, an offset was implemented. Instead of considering the physical interface at $r = R$ to be represented by the 0 isovalue of the LS, it is represented by the isovalue $\alpha = -\varepsilon$. This way, the

	ρ (kg m^{-3})	c_{p} (J kg^{-1} K^{-1})	k (W m^{-1} K^{-1})	η (Pa s)	$\mathcal{L}$ (J kg^{-1})	γ_0 (J m^{-2})
Vapour	0.59	2034	0.26	$1.23{\times}10^{-2}$	$2.257{\times}10^{6}$	0.059
Liquid	958	4216	0.6	$2.82{\times}10^{-4}$		

Table 4.2: Physical properties of the considered fluids for the Scriven benchmark.

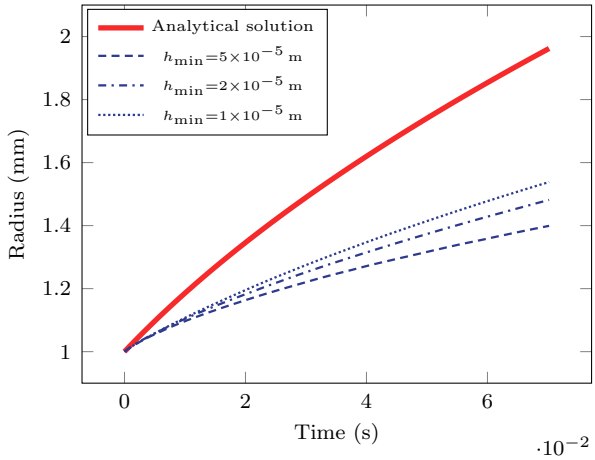

Figure 4.11: Radius versus time for the Scriven Problem for h_{min} varying from 1×10^{-5} to 5×10^{-5} m with the original framework.

temperature gradient discontinuity is placed accordingly to the analytical solution. However this modification entailed the need of a correction term on the mass transfer rate:

$$\dot{m}_{corrected} = \frac{r(\alpha = 0) + \varepsilon}{r(\alpha = 0)} \dot{m}_{computed} \tag{4.51}$$

Results of interface position and mass transfer rate values versus time are plotted in Figures 4.11 for the three coarser mesh sizes.

The conclusion is immediate: the simulation fails at converging to the analytical solution. A proposed explanation is that the temperature gradient on the liquid side is impacted by the temperature profile inside the interface, fixed at T_{sat}. As the energy conservation equation is solved on the whole domain, convection and diffusion effects might be at play at the interface between the liquid side and the interface. As for the Stefan problem, this benchmark is very sensitive to any little error on the temperature gradient, and a small perturbation can lead to such large errors. The difference with the Stefan model is that this latter has a stabilisation configuration, that allow modest errors on the heat fluxes (see Figure 4.8). This means that this current implementation fails at solving the 2D Scriven test case.

To confirm this analysis, the code was modified to remove the potential perturbation effects at the interface. Instead of enforcing T_{sat} at the interface thanks to the reaction term, a Dirichlet condition was set at the interface with the analytical solution extended for $r < R$. The mathematical expression of $T(r, t)$ indeed even stands for the vapour domain though it has no physical meaning. This way, diffusion and convection effects do not disturb the gradient temperature. Otherwise we considered the same configuration with other parameters unchanged. Results of in-

terface position and mass transfer rate values versus time are plotted in Figure 4.12 and 4.13.

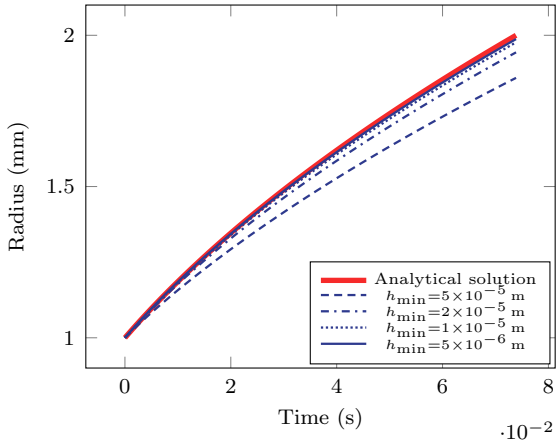

Figure 4.12: Radius for different mesh sizes and time steps for the Scriven problem benchmark with semi-analytic boundary conditions.

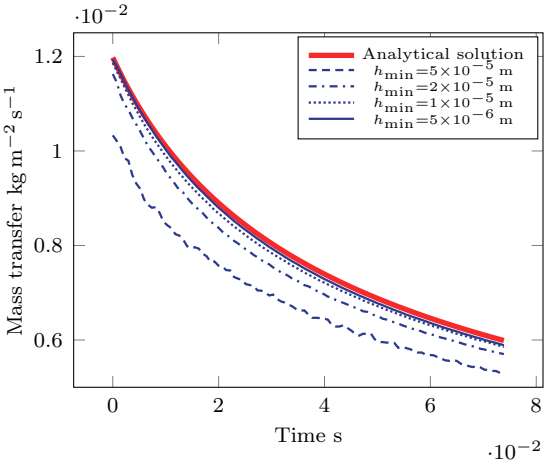

Figure 4.13: Mass transfer for different mesh sizes and time steps for the Scriven problem benchmark with semi-analytic boundary conditions.

The convergence was considered regarding the error on the interface position, computed with 3.32 with $N = 100$ sample points. The convergence is plotted in Figure 4.14.

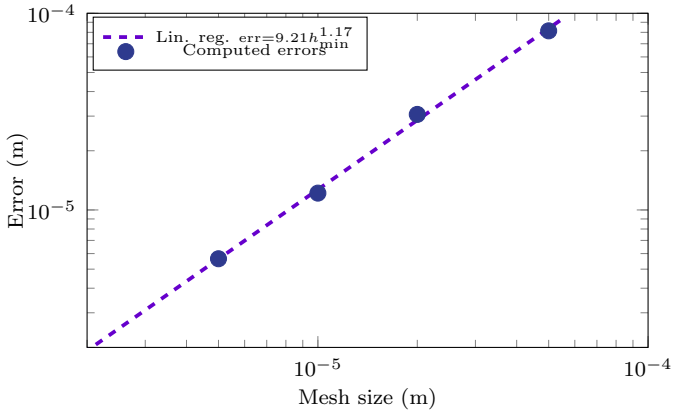

Figure 4.14: Space-time convergence analysis in mesh sizes and time steps for the Scriven problem benchmark with semi-analytic boundary conditions.

This time, the convergence is observed. The order of convergence around 1 is once again coherent with the prediction of (2.52). This also shows that the error made by the discretisation of the Dirac is not on play yet, and confirms the influence

of volume terms on the gradient computation at the interface. Apart from this issue, the entire framework was properly running. To solve this issue, a future step would be to implement a method similar to the Ghost Fluid presented by [105]. In the framework of Finite Elements, the eXtended Finite Element Method combined with Discontinuous Galerkin Method presented by [127, 128] (among others) is a path to explore. However in the context of quenching, oversaturation is usually limited as shown in Section 2.1, and is not the driver of vaporisation. Thus the present formulation is considered acceptable for our application.

4.4 Horizontal film boiling

We considered the saturated film boiling test case as it is a classical benchmark to validate phase change models at saturation conditions in 2D [68, 129, 80] and 3D [73]. It consists of a horizontal plane solid heated at a constant temperature T_w superior to the saturation temperature T_{sat} of the fluid above. The liquid is uniformly at T_{sat} and vaporises due to the heat flux from the heater. As the liquid vapour interface is assumed to remain at T_{sat}, the liquid never touches the solid and a permanent vapour film is maintained. As shown in Figure 4.15, the interface was initialised with a mean thickness $\overline{e} = 5\,\text{mm}$ and a perturbation of amplitude $A = 2\,\text{mm}$ and of wavelength λ_{RT}, the most unstable wavelength of the Rayleigh Taylor (RT) instabilities:

$$\lambda_{\text{RT}} = \begin{cases} 2\pi\sqrt{3}\lambda_{\text{RTc}} \text{ in 2D} \\ 2\pi\sqrt{6}\lambda_{\text{RTc}} \text{ in 3D} \end{cases} \tag{4.52}$$

with λ_{RTc} being the inverse of the critical wave number of the RT instabilities:

$$\lambda_{\text{RTc}} = \sqrt{\frac{\gamma_0}{(\rho_{\text{L}} - \rho_{\text{V}})g}} \tag{4.53}$$

Temperature was fixed on the heater with no slip conditions. Adiabatic and slip boundary conditions were set on vertical faces. Zero gauge pressure with free output velocity was set on the top. The temperature was initially set to T_{sat} at the interface. A linear profile was set in the vapour layer from T_w and T_{sat}. The fluids properties are gathered in Table 4.3.

A comparison was done between the obtained spatial mean heat flux q_w and experimental data [18, 58] through the assessment of the Nusselt Number (Nu) computed with λ_{RTc}:

$$\text{Nu} = \frac{\lambda_{\text{RTc}} h_{\text{HTC}}}{k_{\text{V}}} = \frac{\lambda_{\text{RTc}} q_w}{k_{\text{V}} \Delta T_w} \tag{4.54}$$

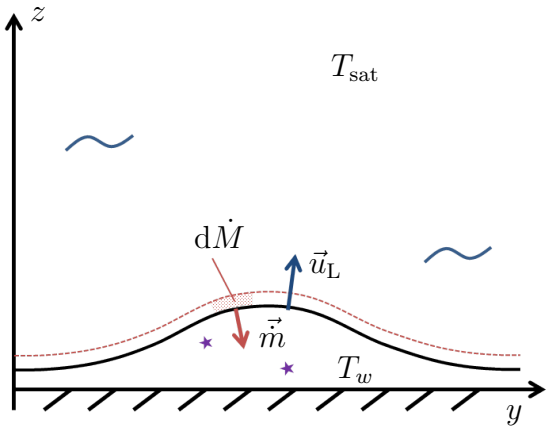

Figure 4.15: Description of the horizontal film boiling benchmark. The liquid vapour interface is initialised with a small perturbation of wavelength λ_{RT}.

The computed Nusselt numbers are plotted in Figure 4.18 and compared with the correlations of Berenson (Nu_B) [18] and Klimenko (Nu_K) [58]:

$$\mathrm{Nu}_B = 0.425(\mathrm{Gr}\,\mathrm{Pr}\,/\mathrm{Ja})^{1/4} \tag{4.55}$$

$$\mathrm{Nu}_K = 0.1691(\mathrm{Gr}\,\mathrm{Pr}\,/\mathrm{Ja})^{1/3} \tag{4.56}$$

where the Grashof number $\mathrm{Gr} = \rho_{\text{V}}(\rho_{\text{L}}-\rho_{\text{V}})g\lambda_{\text{RTc}}/\eta_{\text{V}}^2$ is the ratio of buoyancy effects over viscous effects, the Prandtl number $\mathrm{Pr} = \eta_{\text{V}}c_{\text{pV}}/k_{\text{V}}$ is the ratio of kinematic viscosity over thermal diffusivity, and the Jakob number $\mathrm{Ja} = c_{\text{pV}}\Delta T_w/\mathcal{L}$ is the ratio of sensible heat over latent heat of vaporisation.

	ρ ($\mathrm{kg\,m^{-3}}$)	η (Pa s)	c_{p} ($\mathrm{W\,m^{-1}\,K^{-1}}$)	k ($\mathrm{J\,kg^{-1}\,K^{-1}}$)	$\mathcal{L}$ ($\mathrm{J\,kg^{-1}}$)	γ_0 ($\mathrm{J\,m^{-2}}$)
Liquid	200	0.1	400	40	10 000	0.1
Vapour	5	0.005	200	1		

Table 4.3: Properties of the liquid and vapour phases for the horizontal film boiling benchmark.

4.4.1 2D saturated formulation

First, the case was solved on a 2D domain of 8 cm by 40 cm, and runned on a 10 000 nodes with an unstructured mesh whose mesh size was refined at the interface up to 10^{-4} m. Two solid overheating values ΔT_w were considered: 5 K and 10 K.

If z is the vertical component and y the horizontal component ($y = 0$ being the vertical central axis of the computational domain), the initial interface was defined as:

$$z = \overline{e} + A \cos\left(\frac{2\pi}{\lambda_{\mathrm{RT}}} y\right) \tag{4.57}$$

The interface and temperature profiles are plotted at different time steps for an overheating of 5 K in Figure 4.16. The typical mushroom shape observed by [80, 129] is well reproduced here: the filament following the first bubble does not break up thanks to the 2D configuration of the case.

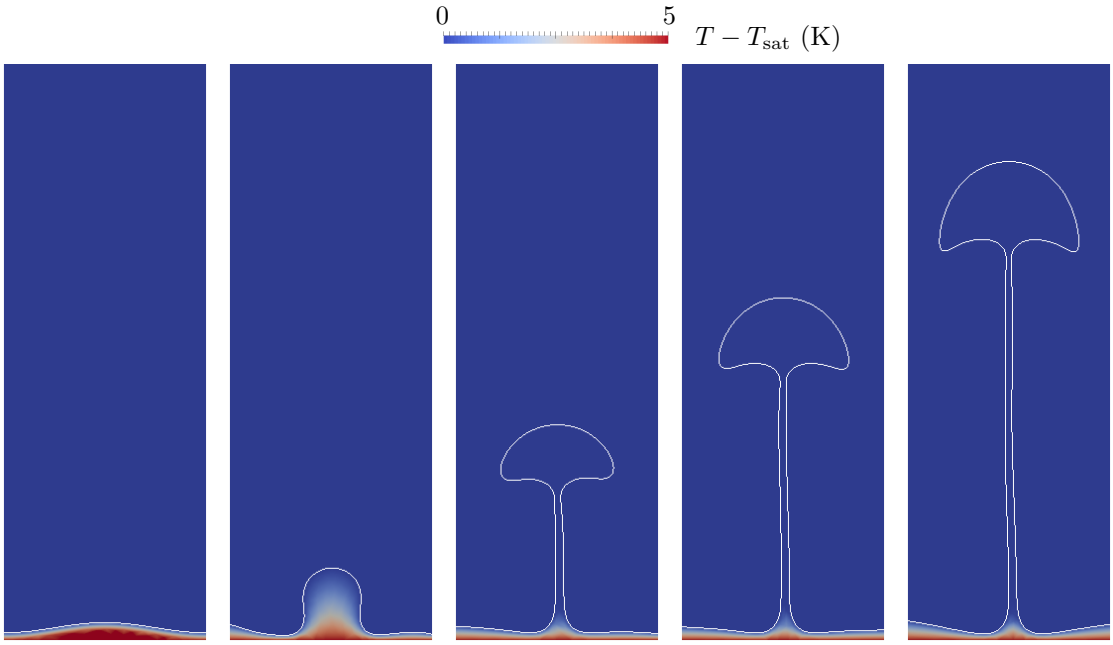

(a) 0 s *(b)* 0.25 s *(c)* 0.5 s *(d)* 0.75 s *(e)* 1 s

Figure 4.16: Temperature and interface of the 2D computation of the 5 K *horizontal film boiling.*

The mesh is plotted at different time steps for an overheating of 5 K in Figure 4.17. The remeshing algorithm works properly as the mesh is refined at the interface to the desired mesh size. The interpolation succeeds well in transporting the different fields from the old meshes to the new ones, and the interface is well captured.

Comparison of the computed Nusselt with results of Klimenko and Berenson were plotted in Figure 4.18. Results are close to those obtained by [129, 80], that is a Nusselt that tends closely to the correlation of Klimenko. This shows the relevance of our model for such boiling modes.

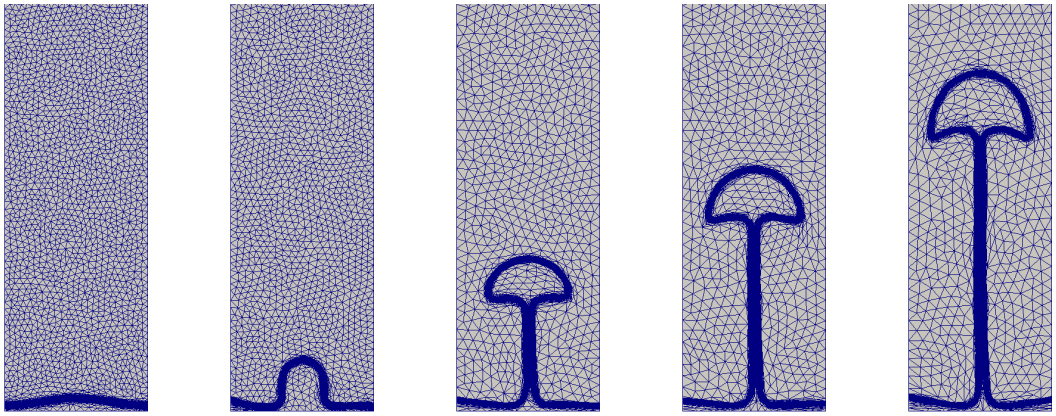

(a) 0 s *(b)* 0.25 s *(c)* 0.5 s *(d)* 0.75 s *(e)* 1 s

Figure 4.17: Mesh of the 2D computation of the 5 K *horizontal film boiling.*

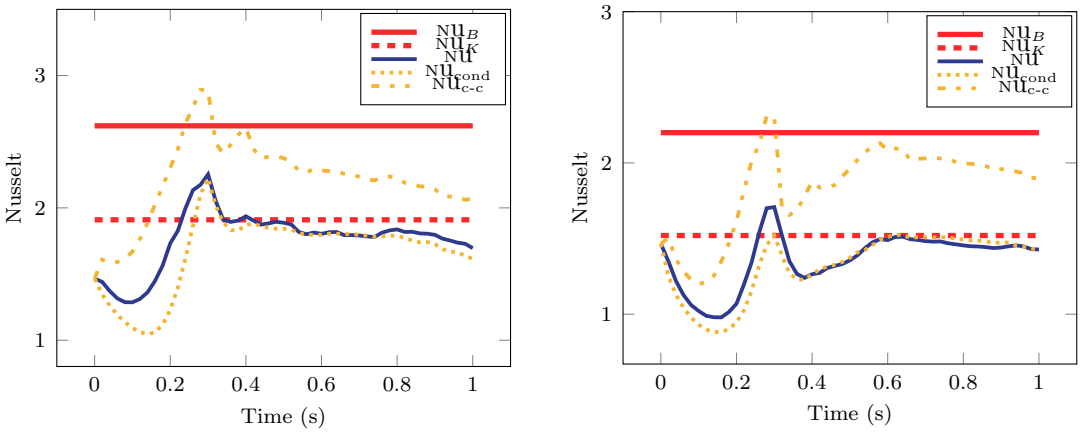

(a) 5 K *(b)* 10 K

Figure 4.18: Comparison of the computed Nusselt with results of [18, 58].

4.4.2 3D saturated formulation

Secondly, the case was solved on a 3D domain of 12 cm by 12 cm by 30 cm, and runned on a 200 000 nodes with an unstructured mesh whose mesh size was refined at the interface up to 10^{-3} m. Only an overheating of 10 K of ΔT_w was considered.

If z is the vertical component and (x,y) the horizontal components ($(x = 0, y = 0)$ being the vertical central axis of the computational domain), the initial interface was defined as:

$$z = \overline{e} + \frac{A}{2}\left[\cos\left(\frac{2\pi}{\lambda_{\mathrm{RT}}}x\right) + \cos\left(\frac{2\pi}{\lambda_{\mathrm{RT}}}y\right)\right] \tag{4.58}$$

In this configuration $\lambda_{\mathrm{RT}} = 11$ cm.

A cross section view of the interface and of the temperature profile are described in Figure 4.19. The mesh is also plotted at different time steps in Figure 4.20.

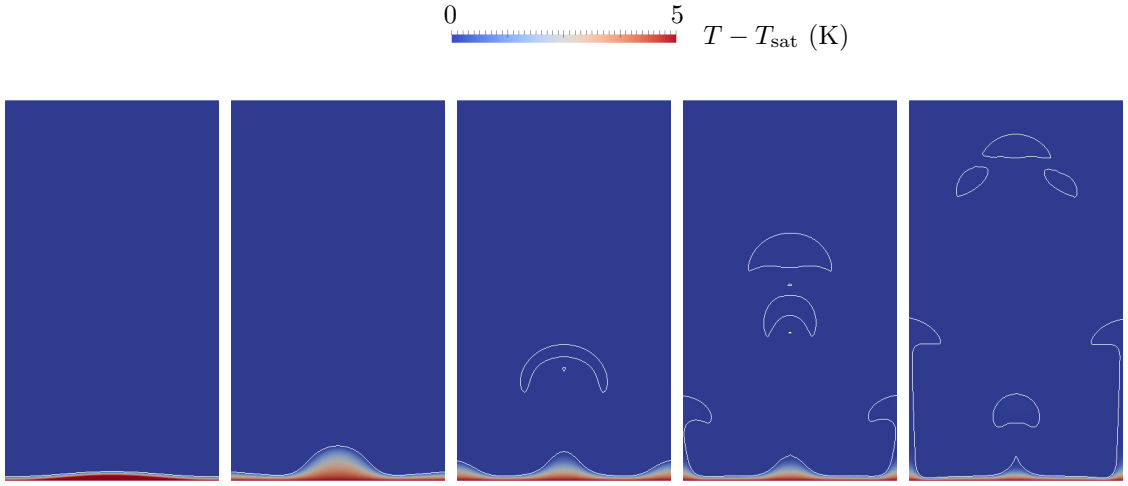

(a) 0 s *(b)* 0.25 s *(c)* 0.5 s *(d)* 0.75 s *(e)* 1 s

Figure 4.19: Cross section view of the temperature field of the 3D computation of the 5 K *horizontal film boiling.*

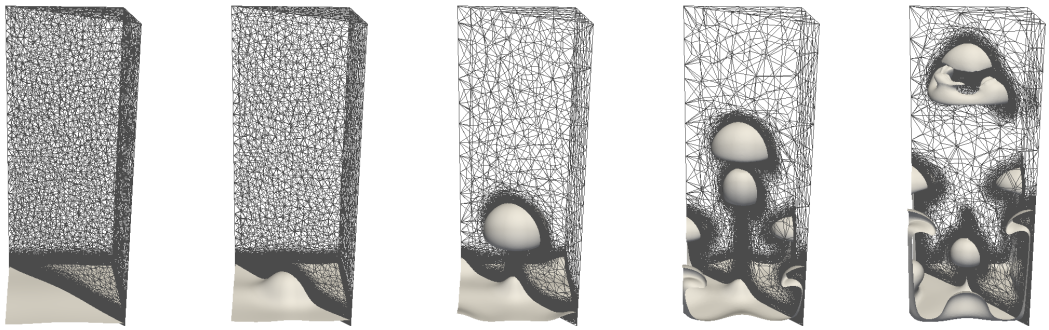

(a) 0 s *(b)* 0.25 s *(c)* 0.5 s *(d)* 0.75 s *(e)* 1 s

Figure 4.20: Mesh and interface of the 3D computation of the 5 K *horizontal film boiling.*

This time, the 3D nature of the bench leads the bubble to break up as capillary forces are too strong on the filament, which is consistent with the physics. In the current configuration, the bubbles were expected to have a radius around $R \simeq \lambda/2$ [18, 130] which is roughly the case if we consider the fist bubble cap in Figure 4.19c and 4.19d. Furthermore, following the study of [131] the corresponding radius is correlated to a specific bubble shape: an axisymmetric bubble with a skirt that

tends to form a flat cap. This is exactly what we observed in the simulation before the second bubble interacts with the first one. The mushroom type bubble that began to form at the edge of the domain are purely numerical bias due to the boundary conditions and the rectangular shape of the domain. Regarding the mesh, the remeshing algorithm also works properly in 3D as the mesh is refined at the interface.

Comparison of the computed Nusselt with results of Klimenko and Berenson are plotted in Figure 4.21. The mean Nusselt is a little lower than in 2D. This is due to the fact that the formation of a bubble entails a temporary large film thickness. The mushroom type bubble prevents such event. As heat fluxes are globally done by conduction (as shown below), a large thickness leads to a lower heat flux. Around 1 s, the influence of mushroom type bubbles at the boundary increase the heat flux. As these bubble are only due to slip conditions on the walls, no conclusion can be drawn here. Symmetric conditions would be required for a further analysis of this case in permanent regime. As such, the model is coherent with physical expectations.

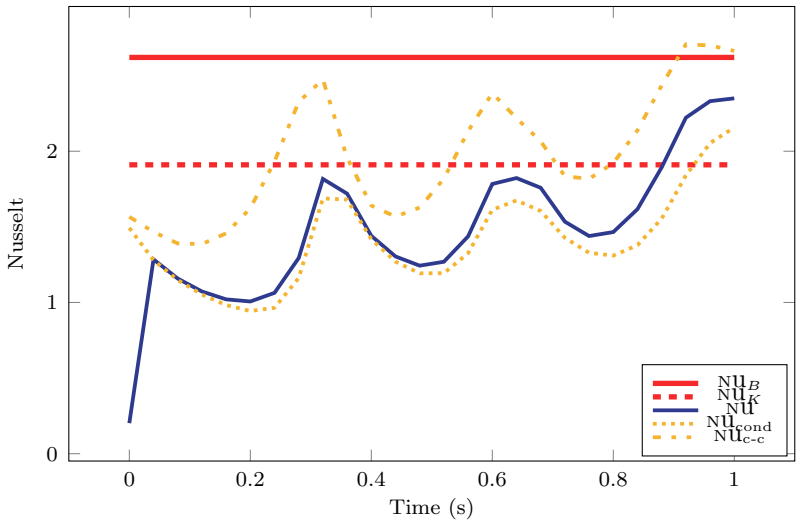

Figure 4.21: Comparison of the computed Nusselt in 3D with results of [18, 58].

4.4.3 Heat flux a posteriori estimation

A first analysis of the nature of heat flux was done with the estimation of mean conductive and convective effects. Considering a quasi-static condition, the local heat flux reads:

$$q_w = \frac{k_{\mathrm{V}} \Delta T_w}{e} \tag{4.59}$$

Thus the corresponding spatial averaged Nusselt over a surface S in pure conduction reads:

$$\mathrm{Nu}_{\mathrm{cond}} = \frac{1}{S}\int_S \frac{\lambda_{\mathrm{RT}} q_w}{k_{\mathrm{V}}\Delta T_w}\,\mathrm{d}S = \lambda_{\mathrm{RT}}\frac{1}{S}\int_S \frac{1}{e}\,\mathrm{d}S \tag{4.60}$$

Then, a possible estimation of convective effects is given by the Péclet number that is the ratio of convective effects to conductive effects.

$$\mathrm{Pe} = \frac{\rho_{\mathrm{V}} c_{\mathrm{PV}} e\vec{\overline{u}}}{k_{\mathrm{V}}} \tag{4.61}$$

where $\overline{u}$ is the mean velocity inside the vapour film. With a Poiseuille flow estimation, it can be estimated from the solid surface thanks to the gradient of the tangential velocity component $\vec{u}_t$:

$$\overline{u} = \left|\frac{\partial \vec{u}_t}{\partial \vec{n}}\right|_{\vec{x}\in w} \tag{4.62}$$

The corresponding spatial averaged Nusselt of conducto-convective estimation reads:

$$\mathrm{Nu}_{\text{c-c}} = \frac{1}{S}\int_S (1+\mathrm{Pe})\mathrm{Nu}_{\mathrm{cond}}\,\mathrm{d}S \tag{4.63}$$

These two estimations of Nusselt were computed for 2D and 3D cases and compared the simulation (see Figure 4.18 and 4.21). What can be deduced is that the major part of heat fluxes is done by conduction. The contribution of convection (difference between the computed Nusselt and the conduction Nu) is here overestimated by more than a factor of four. This means that the conducto-convective estimation is not relevant for this configuration.

4.4.4 Subcooled configuration

For demonstration purposes, we considered a subcooled version of the 2D horizontal film boiling case. We considered it to study the reaction of the full heat flux jump computation method within a more realistic case, though only qualitative observations were made. The case set up (domain size, mesh, etc.) was similar to the one presented in Section 4.4.1 for the saturated 2D film boiling. The only change was that the liquid layer was initialised with a temperature profile that was linear on a layer e_∞:

$$T_{\mathrm{L0}}(\alpha<0) = \max\left(T_{\mathrm{sat}} + \Delta T_\infty \frac{\alpha+\varepsilon}{e_\infty}, T_\infty\right) \tag{4.64}$$

One overheating ΔT_w of 5 K was considered with three subcoolings ΔT_∞: 1 K, 2 K and 5 K. The phases distribution profiles at different time steps for all configurations are described in Figure 4.22,4.23,4.24 and 4.25. We can see that a very

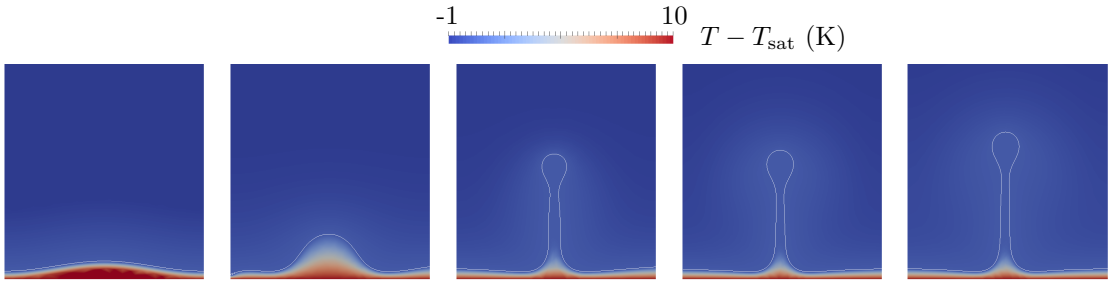

(a) 0 s *(b)* 0.25 s *(c)* 0.5 s *(d)* 0.75 s *(e)* 1 s

Figure 4.22: Phase distribution and temperature of the 2D computation of the 1 K *horizontal film boiling with* 1 K *subcooling.*

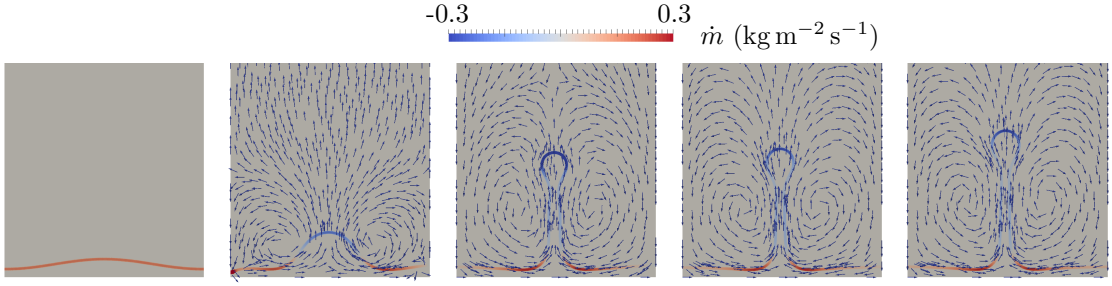

(a) 0 s *(b)* 0.25 s *(c)* 0.5 s *(d)* 0.75 s *(e)* 1 s

Figure 4.23: Mass transfer and velocity trajectories of the 2D computation of the 1 K *horizontal film boiling with* 1 K *subcooling.*

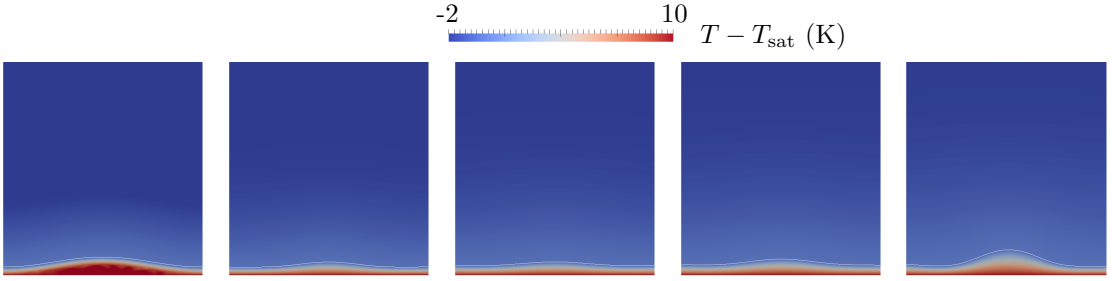

(a) 0 s *(b)* 0.25 s *(c)* 0.5 s *(d)* 0.75 s *(e)* 1 s

Figure 4.24: Phase distribution and temperature of the 2D computation of the 2 K *horizontal film boiling with* 1 K *subcooling.*

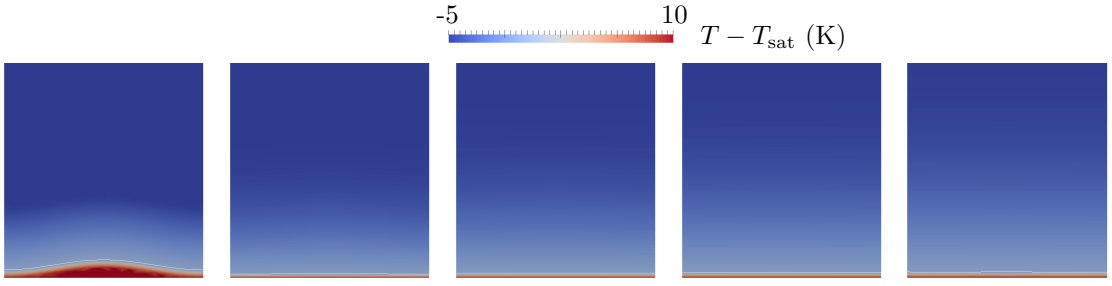

(a) 0 s *(b)* 0.25 s *(c)* 0.5 s *(d)* 0.75 s *(e)* 1 s

Figure 4.25: Phase distribution and temperature of the 2D computation of the 5 K *horizontal film boiling with* 1 K *subcooling.*

small subcooling has already a critical impact on the flow. It restrains strongly the development of the instability and reduces the film thickness. The development of the mushroom shape bubble is stopped when the vapour phase moves too far into the liquid phase. Condensation occurs at the top of this bubble and a recirculation is observed from the bottom of the bubble with vaporisation that feeds the bubble. For the highest subcooling, the bubble does not even develop. This behavior is coherent with experimental analysis and supports the fact that the heat flux jump was properly implemented.

4.5 Conclusions

- The two phase thermal and pseudo-compressible solvers were coupled to obtain a full phase change model.
- The framework was enriched with a remeshing algorithm to refine the mesh at the liquid vapour interface.
- The model was tested in two analytical benchmarks: the subcooled compressible Stefan problem, and the Scriven problem. It appeared that the model is validated for non oversaturated conditions but needs further developments for oversaturated conditions.
- The model was tested on more realistic cases such as the horizontal film boiling test case. It successfully modeled the development of the Rayleigh–Taylor instability in presence of phase change with a satisfactory simulation of the heat transfer.
- For relatively viscous fluids, the major heat transfer mode in the vapour film is done by conduction.

Chapter 5

Experimental quenching of a small nickel sphere

Contents

Résumé en Français

Ce chapitre présente l'étude de la trempe de petites sphères en mode de caléfaction. Une approche expérimentale est menée, et les résultats sont confrontés à ceux de la simulation permis par notre modèle de vaporisation. Les sphères considérées sont des billes de nickel de 1 cm de diamètre, chauffées à des températures allant de 300 °C à 900 °C. Elles sont plongées dans un bain d'eau dont la température varie entre 95 °C et 98 °C. La durée de vie du film de vapeur est mesurée. De plus, un système de caméra rapide est mis en place afin de visualiser le profil du film de vapeur.

En reliant la durée de vie du film de vapeur avec la température de trempe, on remonte à une estimation des valeurs instantanées de la température de la sphère et du flux de chaleur dégagé par celle-ci. Cela est permis par la considération d'une température homogène au sein de la sphère, ainsi que d'un modèle de flux de chaleur inspiré par la littérature. Les clichés pris par la caméré rapide sont traités par un code Matlab pour bien cerner l'interface liquide / vapeur. Ainsi, l'épaisseur moyenne du film sur trois secondes ainsi que la taille moyenne des bulles de vapeur et leur fréquence de libération sont mesurées. On observe alors que le film est plus épais aux plus hautes températures de sphère et de bain, ce qui est cohérent avec ce que prédirait un modèle de conduction pure. La taille des bulles suit la même tendance, ce qui confirme bien qu'un bain plus froid récupère plus de chaleur, limitant la vaporisation au profit du réchauffement du liquide. La fréquence de libération des bulles est cependant constante, et donc indépendante du débit de vapeur libéré ou de la taille des bulles. Enfin, les flux de chaleur mesurés montrent que l'énergie libérée par la sphère est principalement utilisée pour réchauffer le bain, notamment pour d'importants "sous-refroidissements".

Les performances du modèle de vaporisation sont évaluées via la comparaison aux résultats expérimentaux pour six régimes thermiques différents, la température de la sphère étant constante pour chaque régime. La viscosité de la vapeur est cependant augmentée pour des raisons de stabilité numérique. Les profils hydrodynamiques simulés sont fidèles aux résultats expérimentaux à hautes températures. Aux basses températures, les transferts thermiques entre l'interface et l'eau sont sous-estimés, ce qui met en lumière des transferts thermiques liés à des petites échelles qui peuvent être corrigés par la considération d'un modèle convectif.

5.1 Introduction

The majority of industrial processes involving boiling imply water. This is consequently the most studied medium when studying boiling. However the large density ratio, the low viscosity of both media and the very large latent heat of vaporisation make it very hard to simulate. Boiling with water is very chaotic, turbulent and involves many scales whatever the mode. Without any model to simulate solid–liquid contact, the only mode that is for the moment possible to simulate is the film boiling mode.

The performance of our numerical framework should be challenged on real boiling test cases with water. The diversity of the mechanisms involved in boiling lead us to first reduce the scope of our work to a first simple benchmark. The reason behind this approach is to avoid to tackle the full complexity of boiling at first and recover some fundamental features to be validated. Consequently, a choice was done to experimentally study the quenching of a small nickel sphere of 1 cm diameter. Such small scale enables a better precision on the interface description. It also helps to maintain the film boiling mode with the help of capillary forces. Moreover, the spherical geometry does not present any sharp edges that offer preferencial wetting points. High pool temperature were also considered to improve the vapour film lifetime. Such small scale with nickel allows no strong temperatures gradients inside the sphere. Consequently the approximation of a homogeneous temperature is consistent and avoids the thermal complexity in the solid (the Biot number is at most of around 0.2). The other advantages of nickel is that it is not subject to phase transformation on those temperature ranges. Finally, this choice was motivated by more practical reasons as such small scales involve lower energies and thus an easier implementation.

The quenching of small spheres have already been studied in the literature, and some conclusions are already known. Dhir et al. [54] studied the quenching of 19 and 24 mm spheres of various materials. They showed that the larger the subcooling, the higher the Leidenfrost temperature T_{MHF}. This latter was measured between 200 and 300 °C for low subcooling below 10 K ($T_\infty > 90\,°\mathrm{C}$). The associated heat fluxes before the vapour film collapse was around $5{\times}10^4\,\mathrm{W\,m^{-2}}$, and was also improved with the subcooling. They showed that the flux varied with a power 3/4 of the temperature in the absence of subcooling and forced convection. Radiation effects were shown to represent at most 10 % of the total heat flux. Finally they observed that the Leidenfrost temperature T_{MHF} was sensitive to the surface condition that was modified by oxidation during the heating. Jouhara et al. [24] had the same conclusions with the study of different shapes of copper parts. Larger sphere diameters lead to higher heat fluxes. They observed transient wetting phenomena with high frequency at the top of the spheres during film boiling. In both studies the film boiling was turbulent for low subcooling, with mean vapour thicknesses of around

0.1 mm at T_{MHF}. Both authors confirmed that the temperature was mostly homogeneous, and that the temperature variation was proportional to the heat fluxes. This was also shown by [132].

The aim of this Section is to reproduce our own sphere quenching experiments with different pool temperatures. This was done with the help of a four-month intern. We recovered the main features of such systems and studied the relevance of our model and numerical code to simulate them.

5.2 Experimental apparatus

5.2.1 System components

The test sample consisted of a nickel sphere of 1 cm diameter. Thermal properties of nickel used in this Section are given in Table 5.1. It was heated in an oven (see Figure 5.1a) with a temperature control ranging from 100 °C to 900 °C. A pyrometer was used to double check its temperature. With the help of pliers, the sphere was moved by hand from the oven to a water pool at atmospheric pressure. It was a tank 30 cm long, 15 cm wide and 20 cm deep made of glass so that the sphere was visible from the side (see Figure 5.1b). The water was warmed with the help of an immersed heater. The sphere was held by an aluminium base with four contact points. It was positioned at mid-height of the pool (see Figure 5.1c). The tank was almost completely filled so that the free surface of the pool did not impact the hydrodynamics around the sphere. The temperature of the bath was controled with a thermocouple positioned at one corner of the pool oposit from the heater. Temperatures of 95 °C and 98 °C are considered. A schematic description of the whole set up is presented in Figure 5.2.

A camera set up was used with a Nikon camera 1 J5, and a 1 NIKKOR VR 10–30 mm lens. It was placed in front of the sphere at the same height. Opposit of the camera, a lighting system was set up to create a contrast. This way, the vapour film was easily identified from the liquid phase. Two types of shootings were used: a normal mode with real time images. And a high-speed camera mode with 400 pictures per seconds over 3 seconds.

ρ ($\mathrm{kg\,m^{-3}}$)	ρc_{p} ($\mathrm{J\,m^{-3}\,K^{-1}}$)	k ($\mathrm{W\,m^{-1}\,K^{-1}}$)
8470	444	90

Table 5.1: Physical properties taken for the nickel sphere.

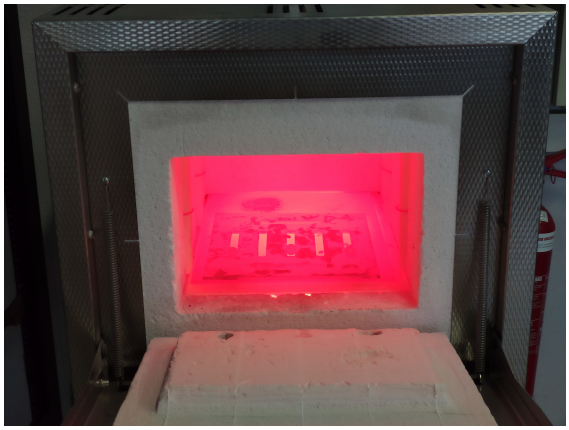

(a) The oven at 900 K. We can glimpse the shape of one small nickel ball at the center.

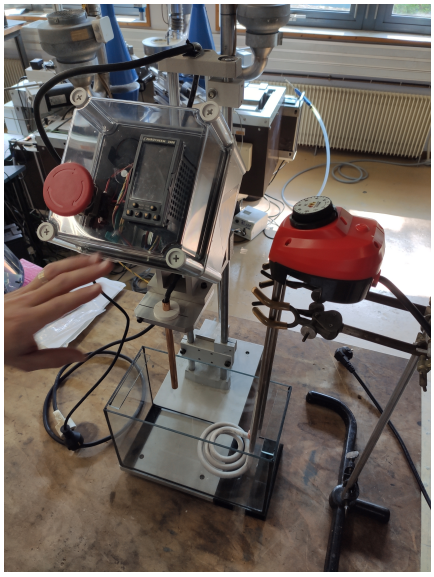

(b) Picture of the quenching bath. The immersed heater is on the rigth of the bath. The thermocouple is not shown here, but was placed oposit to the heater. The rod is the set up of another ongoing experiment.

(c) Picture of the sphere from the camera viewpoint. The focus was set to have the sphere on the plane of sharpness.

Figure 5.1: Pictures of the experimental test bench.

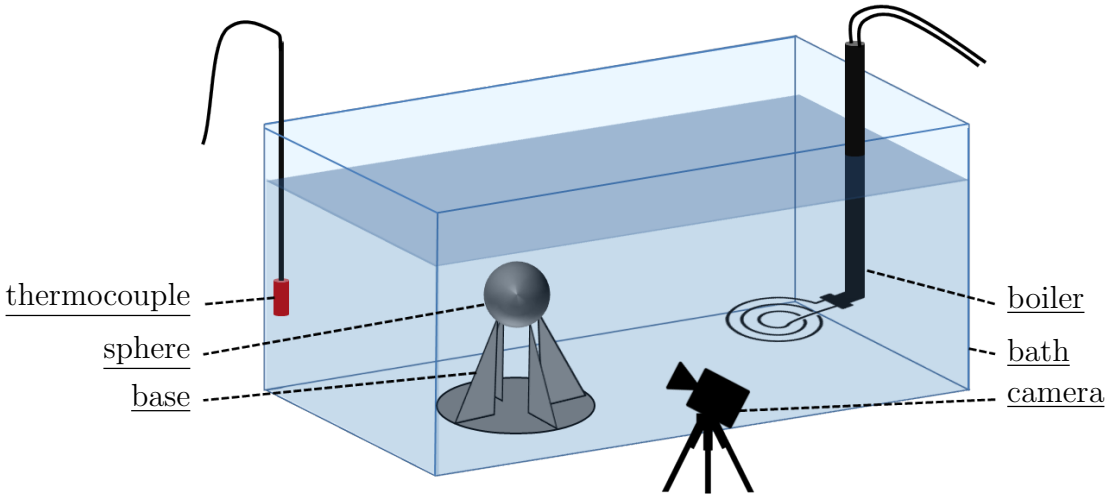

Figure 5.2: Pictures of the experimental test bench.

5.2.2 Experimental protocol

In order to have the most reproducible tests possible, we paid attention to keep the heating times and temperatures under control. Once we had succeeded in obtaining reproducible tests we could carry out trials by varying the temperature of the oven and the temperature of the water.

First the oven was switched on. Once the desired temperature was reached, the sphere was moved inside. During the heating time the thermal plunger was switched on until the water started to boil. Once the sphere had reached the prescribed temperature, the boiler was turned off and the water cooled down naturally to the desired temperature. Then the temperature of the sphere was checked with the pyrometre, and the sphere was quickly moved into the pool with the help of pliers. The chronometre started when the sphere was plunged and stopped when nucleate boiling started. Camera shootings were done as frequently as possible until boiling stopped. A last shooting was done after the end of boiling to recover a picture of the sphere that was used as a calibration for the post treatment. The resulting videos were then analysed using Matlab. The focus was set to have the sphere on the plane of sharpness. A balance had to be found regarding the distance of the camera from the sphere. It should be close enough to have a good accuracy, but far enough to capture the entire bubbles. These measures were only done during the calefaction mode.

5.3 Experimental method

5.3.1 Measurements strategy

5.3.1.1 Estimation of the cooling curve

As no thermocouple was available to assess the instantaneous temperature of the sphere, an estimation of this temperature was done from the measurements of the quenching time. This estimation was based on two assumptions. The first is that the sphere temperature is uniform. This hypothesis can be validated by computing the diffusion time τ_c inside the sphere associated to half of its diametre $\mathcal{D}/2$:

$$\tau_c = \frac{\mathcal{D}^2}{4D_S} \tag{5.1}$$

with D_S the diffusivity of the sphere. This leads to a characteristic time $\tau_c = 1\,s$, which is small in regards to the experimental quenching times (from 10 s to 50 s). Another way to assess this assumption is to consider the Biot number. In our configuration, it is around 10^{-2}, meaning a strong influence of conductive effects in the solid. It is thus acceptable to consider the temperature inside the sphere as homogeneous. This also allowed us to write the following energy conservation bill on the entire sphere:

$$q\mathcal{S}_S = \rho_S c_{PS} \mathcal{V}_S \dot{T}_S \tag{5.2}$$

with $\dot{T}_S = \mathrm{d}T_S/\,\mathrm{d}t$ the cooling rate of the sphere, $\mathcal{S}_S$ its surface and $\mathcal{V}_S$ its volume. The second hypothesis is that the cooling rate is only a function of the sphere temperature, of the pool temperature and of the physical constant properties of the different phases. This entails that the previous states of the sphere do not influence its current behavior. In other words, the long transient phenomenon is assumed not to impact the sphere cooling. Mathematically speaking, this hypothesis leads to the existence of a monotone function f that links the cooling rate $\dot{T}_S$ and the current state:

$$\dot{T}_S = f(T_S, T_\infty) \tag{5.3}$$

If we know this function f, we can integrate this equation to recover the current temperature in function of time t. The following strategy explains how to recover this function.

General theory Following this hypothesis, we can write:

$$\frac{\mathrm{d}T_S}{f(T_S, T_\infty)} = \mathrm{d}t \tag{5.4}$$

Integrating this equation, there is a bijective function F that only depends on T_∞ (and on material properties) and that respects the following equality for every couple (t_1,T_{S1}) and (t_2,T_{S2})

$$F(T_{S1}) - F(T_{S2}) = t_1 - t_2 \tag{5.5}$$

In other words at a given time t and for every couple (t_1,T_{S1}) encountered by the cooling curve $T_S(t)$, the temperature T_S reads:

$$T_S = F^{-1}\left(F(T_{S1}) + (t - t_1)\right) \tag{5.6}$$

This property entails the existence of a master cooling curve: given a pool temperature, all cooling curves are linked together and follow the same path. For example, let us consider two cooling curves of initial temperature T_{S1} and T_{S2} shown in Figure 5.3. If we define the two associated cooling functions $g_1(t)$ and $g_2(\tilde{t})$ and if we define t_2 such that $g_1(t_2) = T_{S2}$, then thanks to (5.6):

$$g_1(t) = F^{-1}\left(F(T_{S2}) + (t - t_2)\right) \tag{5.7}$$

$$g_2(\tilde{t}) = F^{-1}\left(F(T_{S2}) + (\tilde{t} - 0)\right) \tag{5.8}$$

If we synchronise the two cooling times t and $\tilde{t}$ such that $\tilde{t} = 0$ when $t = t_2$, or in other words $\tilde{t} = t - t_2$, then we have $g_1(t) = g_2(t - t_2)$: the two cooling curves overlap in a same master curve.

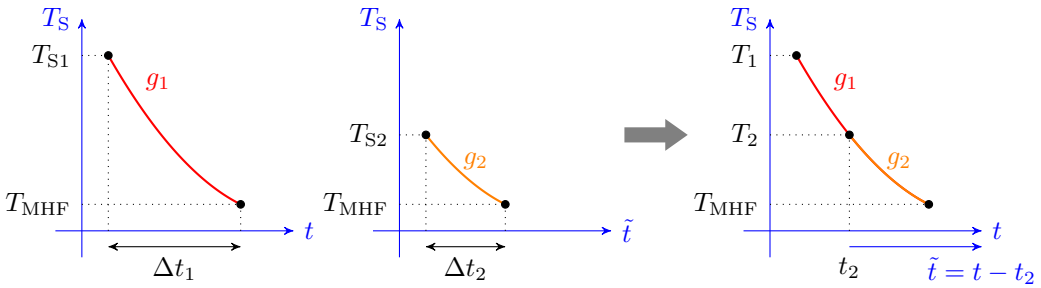

Figure 5.3: Graphical view of the master cooling curve. If the cooling rate is only a function of the temperature, then the two cooling curves of two different initial temperatures overlap on the same master curve.

This curve is the same as the one obtained by plotting the initial temperature of the sphere T_{Si} versus the total cooling time Δt as shown in Figure 5.4. It can be easily estimated by several quenching tests with different initial temperatures. If we find the function $T_{Si} = h(\Delta t)$, then the cooling curve g_1 of a given couple $(\Delta t_1,T_{S1})$ reads:

$$g_1(t) = h(\Delta t_1 - t) \tag{5.9}$$

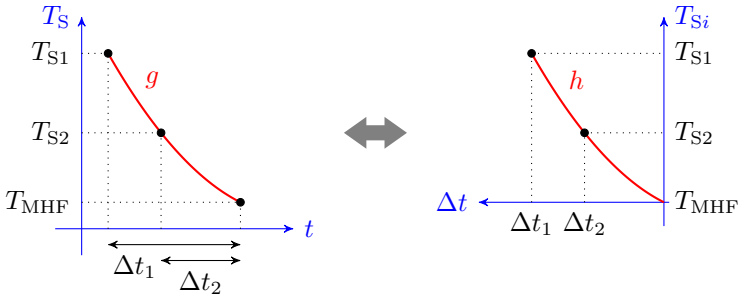

Figure 5.4: Graphical view of the cooling curve and cooling time graph equivalency. The master cooling curve presented in Figure 5.3 can be obtained by plotting the initial temperature versus the cooling time.

And:

$$\dot{T_S} = g_1'(t) = -h'(\Delta t_1 - t) \tag{5.10}$$

Thus, if we can find a relationship between h and h' for any Δt_1, we can recover the function f.

To sum up:

- A certain number of quenching tests at different initial sphere temperatures T_{Si} are done for a given pool temperature.
- For each experiment, the quenching time Δt it measured.
- This leads to an estimation of the function $T_{Si} = h(\Delta t)$, and thus to h'.
- A relationship $h' = F(h)$ is deduced.
- Thanks to (5.9) and (5.10), this leads to $\dot{T_S} = -F(T_S)$.

Application in the case of a sphere Dhir et al. [54] developed a Boundary Layer model of a vapor film around of a sphere with subcooling. This lead to a relationship between the cooling rate and the overheating from which they recovered a 3/4 order power law. They challenged this model with experimental results with good agreement. This result motivated us to write:

$$\dot{T_S} \sim -A(T_S - T_{sat})^{3/4} \tag{5.11}$$

With this consideration, the problem can be simplified to finding the proportionality coefficient A. We note $\Delta T_S = T_S - T_{sat}$. Integrating (5.11) between T_S and T_{MHF}:

$$\Delta T_S = \left((T_{MHF} - T_{sat})^{1/4} + A(t_f - t)/4\right)^4 \tag{5.12}$$

Thus, the function $T_{Si} = h(\Delta t)$ reads:

$$T_{Si} = h(\Delta t) = \left((T_{\mathrm{MHF}} - T_{\mathrm{sat}})^{1/4} + A\Delta t/4\right)^4 + T_{\mathrm{sat}} \tag{5.13}$$

Values of T_{MHF} and A are then recovered iteratively to minimise the interpolation error with experimental values. Thanks to (5.2), the estimated cooling curve allowed us to recover an estimation of the heat flux noted $q_{\dot{T_{\mathrm{S}}}}$.

5.3.1.2 Measurement of thermo-hydrodynamic quantities

The camera set up allowed to observe the hydrodynamics of vapour. More precisely three quantities were measured: the vapour film thickness at mid height of the sphere e_{exp}, the volume of vapour bubbles that just detached from the vapour film $\mathcal{V}_{\mathrm{exp}}$ and the frequency of creation of bubbles f_{exp}. To do so, we used a fast camera to capture 1200 frames in 3 s at different time steps of the experiments.

Images of the vapour film around a hot metallic sphere in water were captured with a Nikon camera at 60fps. The post treatment of those images has been made with a Matlab code. The camera pictures were binarised to recover matrices of 0 and 1 using the *imbinarize* Matlab function. A very high contrast was required for this application. It was set up so that the liquid phase was identified with 0 (black pixels) whereas the vapour and solid phase were identified with 1 (white pixels). A correction was also implemented to fill holes inside the vapour bubbles that were due to light reflection effects. To do so, the *imfill* Matlab function was used. This is explained in Figure 5.5.

Once these preliminary steps were completed, the pixel size was converted to a physical length. It was done thanks to the pictures of the last video sequence. Indeed, in these last snapshots, boiling is over and only the sphere remains with no vapour around. The scale could be computed with the measurement of the sphere diameter which was known. The number of pixels of the sphere was counted, and from this we deduced the length of one pixel d_{p}.

These pictures were analysed in different ways to recover the desired quantities. Though the pictures only offered a 2D view of the experiment, the analysis was based on the assumption that the problem was axisymmetric. Thus 3D estimations were extracted from this post-treatment. Moreover, thanks to the estimation of the cooling curve explained in last section, we could recover an estimation of the cooling rate $\dot{T}_{\mathrm{S}}$. This was done thanks to the measurement of the difference of time between the snapshot and the time of collapse of the vapour film.

Vapour film thickness The height of the sphere equator was obtained thanks to the snapshots of the sphere without boiling. At this height, the sphere and the vapour film on both sides are gathered in one horizontal line of white pixels (see

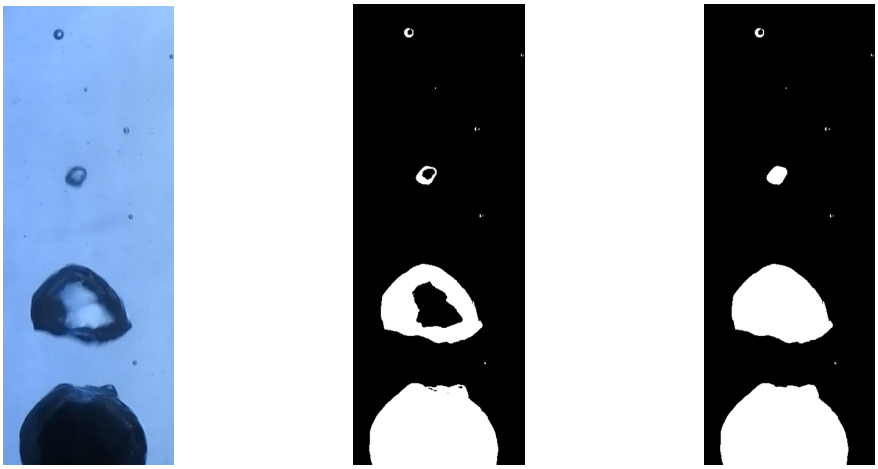

(a) Raw picture. *(b) Binarised picture.* *(c) Post-treated binarised picture.*

Figure 5.5: Example of the binarisation of an experimental picture from high speed camera. The liquid phase is identified with black pixels whereas the vapour and solid phases are in white. Reflection and refraction effects lead to misidentification of the vapour phase at the centers of bubbles that can be corrected with a filling function.

Figure 5.6). Thus the length of this line at this height corresponds to the sum of the diameter of the sphere and of two vapour film thicknesses (see Figure 5.6). Thanks to this consideration and to the value of a pixel size d_p, the current vapour film thickness was measured. This was done for all 1200 pictures of every shot. The mean value was then computed as an estimation of e_exp.

Vapour bubble volume The binarised picture provided a cross section of the bubbles. Under the assumption that the bubbles are axisymmetric, the revolution of this cross section defines the bubble volumes. Thus, we considered that each pixel line is a cylinder whose diameter is the length of the line corrected by d_p and whose height is d_p. The sum of the infinitesimal cylinders associated to one bubble is an estimation of its volume. This approximation is described in Figure 5.7.

This computation was done for all 1200 pictures of every shot. The pictures were cropped to get rid of the volume of the sphere. Moreover the maximum computed volume was saved to only consider the biggest bubble. However, the volume recovered was not constant. Firstly, the bubble development leads to an increasing of the volume before its detachment from the vapour film. Secondly condensation effects cause the bubble to shrink while raising. This leads to a volume variation represented in Figure 5.8. The volume of the sphere was then taken as the mean value of all the peaks of this quasi-periodic function. A Fast Fourier Transform

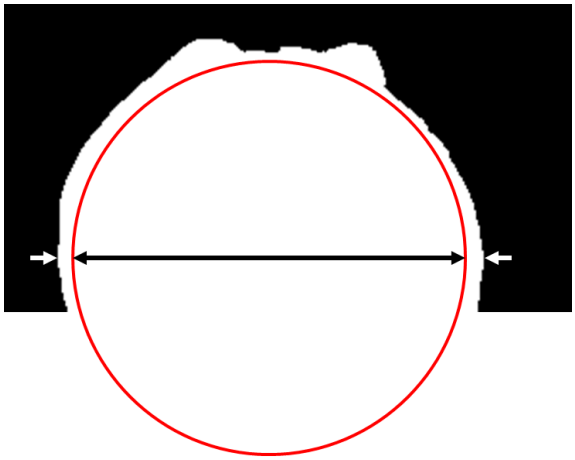

Figure 5.6: Measurement of the vapour film thickness. The length of the line of white pixels at the height of the sphere equator is measured. This corresponds to the sum of the diameter of the sphere and of two vapour film thicknesses.

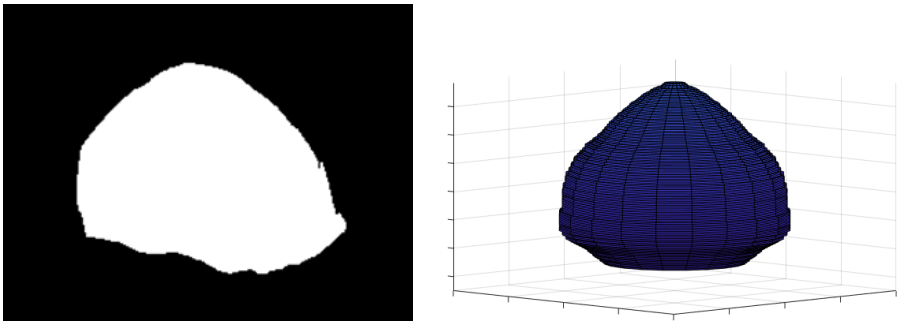

(a) Binarised picture. *(b) Axisymmetric model.*

Figure 5.7: Axisymmetric 3D model of a vapour bubble recovered from a 2D binarised picture. The length of each line of white pixel is considered to be an infinitesimal cylinder. The sum of these cylinder represents an estimation of the bubble volume.

analysis using the associated Matlab function allowed to recover the amplitude of each frequency (see Figure 5.8). The addition of the amplitude of the first peak of non zero frequency with the constant value of the signal lead to the estimation of the vapour bubble volume $\mathcal{V}_{\text{exp}}$.

The period of the volume measurement signal is directly linked with the detachment frequency. The first non zero frequency was identified as the detachment frequency f_{exp}.

Vapour bubble detachment frequency This procedure has however to be tempered by a phenomenon that occurred at high sphere temperature and at low sub-

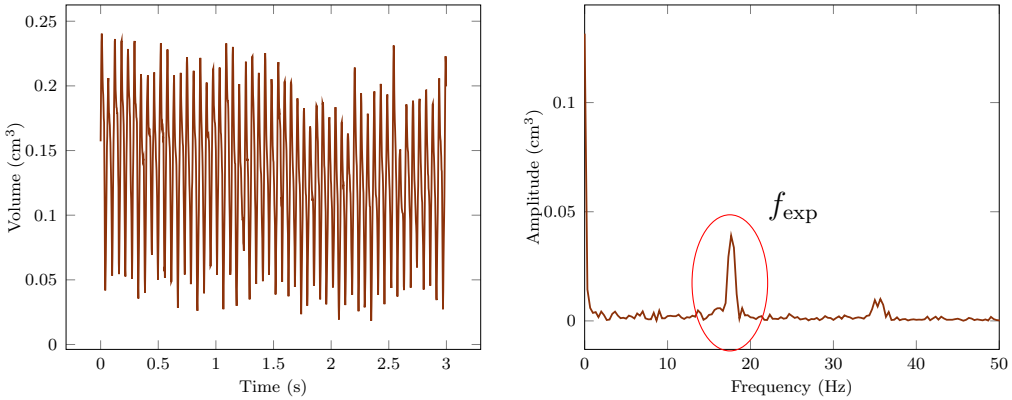

(a) Vapour bubble volume *(b) Volume frequency spectrum*

Figure 5.8: Measurement of vapour bubble volume and detachment frequency over a high-frequency snapshot. The measurement of a bubble varies in regards to the time due to the bubble formation process and to condensation. However this variation is periodic. The period of this signal leads to the measurement of the detachment frequency. The addition of the amplitude of this frequency with the constant value of the signal leads to the bubble volume.

cooling, when the vaporisation was strong. In this context, the bubbles were so large that some merged with the previous one. This lead to the measurements of doubled bubble volumes along with half detachment frequencies. These pathological cases were solved by a hand correction.

Equivalent heat fluxes The measurement of the vapour film thickness allowed to recover an estimation of the heat fluxes at the surface of the sphere. Considering pure conduction inside the vapour film, the associated heat flux reads:

$$q_e = \frac{k_{\text{S}} \Delta T_{\text{S}}}{e_{\text{exp}}} \tag{5.14}$$

with k_{S} the thermal conductivity of the sphere. This estimation is based on the assumption that the vapour film thickness at the equator of the sphere is a reliable value for the global vapour film thickness around the sphere. The vapour film model of [54] predicts a thickness that is close to be constant in the south hemisphere of the sphere. However, the area of detachment of the bubbles undergoes a lot of perturbations and might deviate from this estimation.

The measurement of the vapour bubble volumes and detachment frequencies allowed us to estimate the energy used to vaporise the liquid. We define an equivalent heat flux:

$$q_{f\mathcal{V}} = \frac{\rho_{\text{V}} f_{\text{exp}} \mathcal{V}_{\text{exp}} \mathcal{L}}{\mathcal{S}_{\text{S}}} \tag{5.15}$$

with ρ_V, $\mathcal{S}_S$ respectively the density and the surface of the sphere, and $\mathcal{L}$ the latent heat of vaporisation of water. This estimation has to be considered carefully, as this neglects potential important condensation effects over the vapour film and during the development of the bubble.

5.3.1.3 Measurement uncertainties

Regarding the pool temperature, the thermocouple was placed at one corner of the bath. Thus the pool temperature inhomogeneities were not captured. Moreover, at high temperature, the temperature of the bath decreased by a little more than $1\,\mathrm{K/\,min}$. Thus an uncertainty of around $1\,\mathrm{K}$ on the pool temperature was considered.

Several uncertainties are to be noticed regarding the sphere temperature:

- Temperatures within the oven were not homogeneous. Discrepancies of around $50\,\mathrm{K}$ at most were measured. Thus the oven temperature was not a reliable information. At the same time, the precision of the pyrometre measurement was linked with the distance from the sphere. At high temperature, it was not possible to get very close as it could have damaged the system. We estimated that measurement of T_{Si} was reliable within $\pm 10\,\mathrm{K}$.

- The displacement of the sphere from the oven to the pool was also a source of temperature loss. Convective effects predicted by the Whitaker correlation [133] are negligible in our system. However, radiation effects can have a more significant impact at higher temperature. Considering the associated radiative heat flux q_R, the associated temperature drop is around:

$$\dot{T_S} = \frac{q_R \mathcal{S}_S}{\rho_S c_{PS} \mathcal{V}_S} \tag{5.16}$$

  at the highest temperature ($900\,^\circ\mathrm{C}$) a black body model leads to a cooling rate of $10\,\mathrm{K\,s^{-1}}$. The displacement of the sphere took around $5\,\mathrm{s}$, leading to a potential overestimation of $50\,\mathrm{K}$. However the real emissivity of the nickel should be lower than 1. Another $10\,\mathrm{K}$ uncertainty was then considered to be conservative.

- A $1\,\mathrm{K}$ difference in the temperature pool leads to a difference of around $10\,\mathrm{K}$ for the value of T_{MHF}. As this latter is used to determine the temperature of the sphere, this adds another uncertainty.

- Conduction effects at the contact points with the aluminium base were considered negligible. The ratio of the diameter of the spikes to the diameter of the sphere was indeed very low. However, its presence could facilitate the wetting and thus increase T_{MHF}.

- The spheres used for the experiments underwent oxydation when they were heated in the oven. This could be another potential source of error for the estimation of T_{MHF}. However it is difficult to quantify.

Regarding the camera system, the measurement uncertainty is linked to the set up resolution. A pixel was shown to represent a distance d_{p} of around 0.05 mm. This is around 10 % of the experimental values of film thickness, which is not negligible. This should not impact a lot the estimation of the bubble volumes. However, an uncertainty appears in the fact that the bubble are not really spherical. This deviation is not easy to quantify, but we estimated that it could easily lead to an estimated 30 % error. Moreover, the edges of the biggest bubbles sometimes got truncated by the window frame. Such high uncertainty is then supposed to correctly take into account this other biais which only appears at high overheating for the biggest bubbles. The frequency measurement is considered to be reliable as the data were each time very close to be periodical, leading to a distinct amplitude peak at a localised frequency on the Fourier transform. The uncertainty is mostly due to the thickness of the peak overlaping a small interval of frequences of around 0.3 Hz.

A mention has to be made on experiments at very low initial temperatures. We tried to estimate directly T_{MHF} with such tries, by considering the limit initial temperature at which the vapour film did not appear. It seemed however that hydrodynamical effects had important impact on the vapour film stability. This latter broke at higher temperature than the estimated one, and no conclusion could be drawn from these measures.

5.3.2 Experimental results

5.3.2.1 Cooling curve estimation

We estimated the cooling curve with around twenty experimental points with initial temperatures $T_{\mathrm{S}i}$ ranging from 300 °C to 900 °C. Two water pool temperatures T_∞ were considered: 95 °C and 98 °C leading to a subcooling of 5 K and 2 K respectively. The initial sphere temperatures $T_{\mathrm{S}i}$ versus the associated measured cooling times Δt_{ref} at a given water pool temperature are plotted in Figure 5.9. We recall the interpolation function (5.13) we aimed for:

$$T_{\mathrm{S}i} = \left((T_{\mathrm{MHF}} - T_{\mathrm{sat}})^{1/4} + A\Delta t/4\right)^4 + T_{\mathrm{sat}} \tag{5.17}$$

Values of A and T_{MHF} had been found iteratively to best fit the two experimental curves. The fitting curve are also plotted in Figure 5.9. The associated values of A and T_{MHF} are gathered in Table 5.2.

Values of T_{MHF} are consistent with the literature [54]. Variations of T_{MHF} are usually around 10 K per Kelvin of subcooling, which is once again consistent with

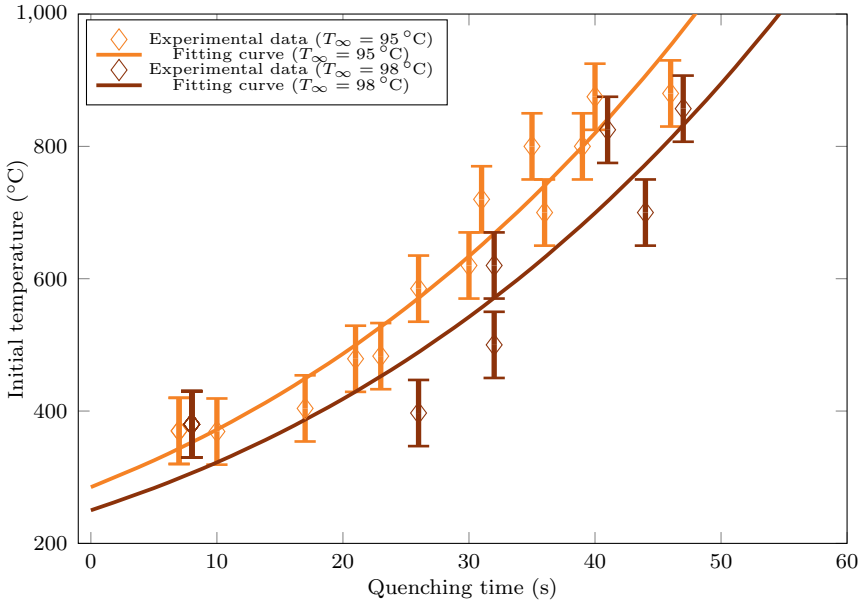

Figure 5.9: Experimental measurements of initial sphere temperature versus quenching time for two pool temperatures. The fitting curves base on the Boundary Model are also plotted.

	T_{MHF} (°C)	A ($\mathrm{K}^{1/4}\,\mathrm{s}^{-1}$)
$T_\infty = 95\,^\circ$C	285	0.1492
$T_\infty = 98\,^\circ$C	250	0.1448

Table 5.2: Exeprimental estimations of the Leidenfrost Temperature and cooling rate coefficient.

our estimation [56, 25]. Values of A are also in the same order of magnitude as in [54] whose correlation leads to a value of $0.18\,\mathrm{K}^{1/4}\,\mathrm{s}^{-1}$.

Overall the experimental points follow consistently the trend of our cooling rate model. The dispertion of the data is assumed to be mainly due to the uncertainties on the pool temperature. A 1 K error is enough to make the quenching last a few seconds more. This is all the more significant for a 98 °C pool as it is less easy to ensure a uniform temperature in the pool at values close to the saturation temperature. The mean behavior should be close to what is predicted by the trend. However this uncertainty can also appear on every quenching experiment. We shall thus keep this scattering in mind for the rest of the analysis. The associated estimated temperature and cooling rate are strongly affected by the deviation due to the pool temperature uncertainty.

The order of magnitude of associated heat fluxes is around $1\times10^5\,\mathrm{W\,m^{-2}}$, which is consistent with the order of magnitude of heat fluxes in calefaction for large overheating. We also noticed that the cooling rate is improved by the subcooling, which is consistent with observations of the literature [54, 24]. But this improvement is not really significant, as there is only a few percents difference between the two cooling rates (see Figure 5.10). The largest impact is the raise in T_{MHF}.

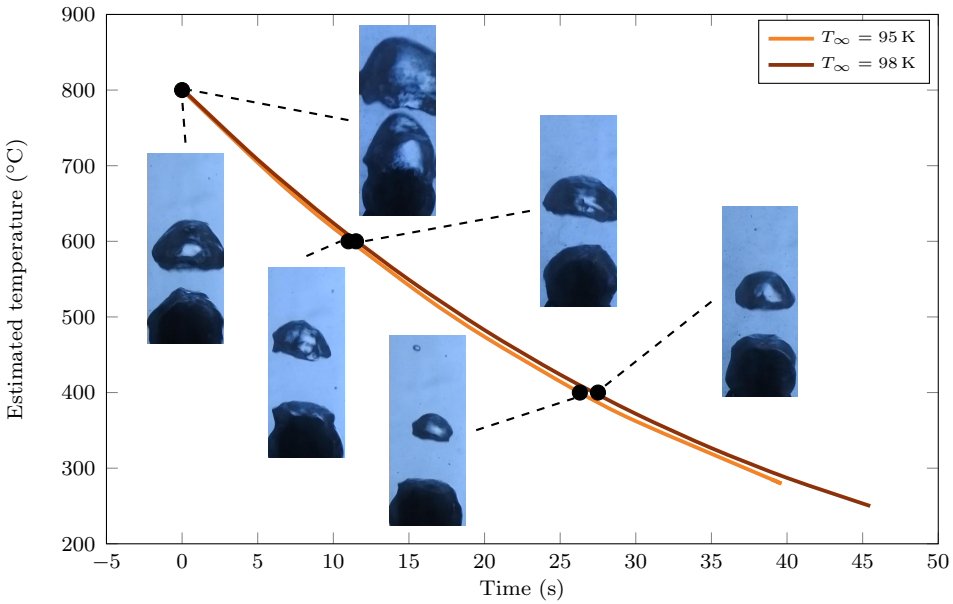

Figure 5.10: Representation of the experimental cooling curves for two pool temperatures. The cooling curves are close from each other, but the Leidenfrost temperature is significantly different. Pictures of some bubble regimes are plotted at the associated points. As expected, the hotter the sphere and the larger the bubbles. The colder the pool and the smaller the bubbles.

5.3.2.2 Qualitative comments on the camera observations

Experiments were done with the camera set up at the same two temperatures of 95 °C and 98 °C.

First of all the different boiling modes were observed over a quench, with a dominant calefaction mode, as expected. The Figure 5.11 describes a quench at different times and estimated temperatures for an initial temperature of around 830 °C with a pool temperature of around 98 °C. At first, a lot of vapour is created, with huge bubbles that can even coalesce with the previous. The interface is very unstable and wavy. The amount of vapour created gets smaller with time. Bubbles condensate when rising, and even vanish very quickly after their creation at the end

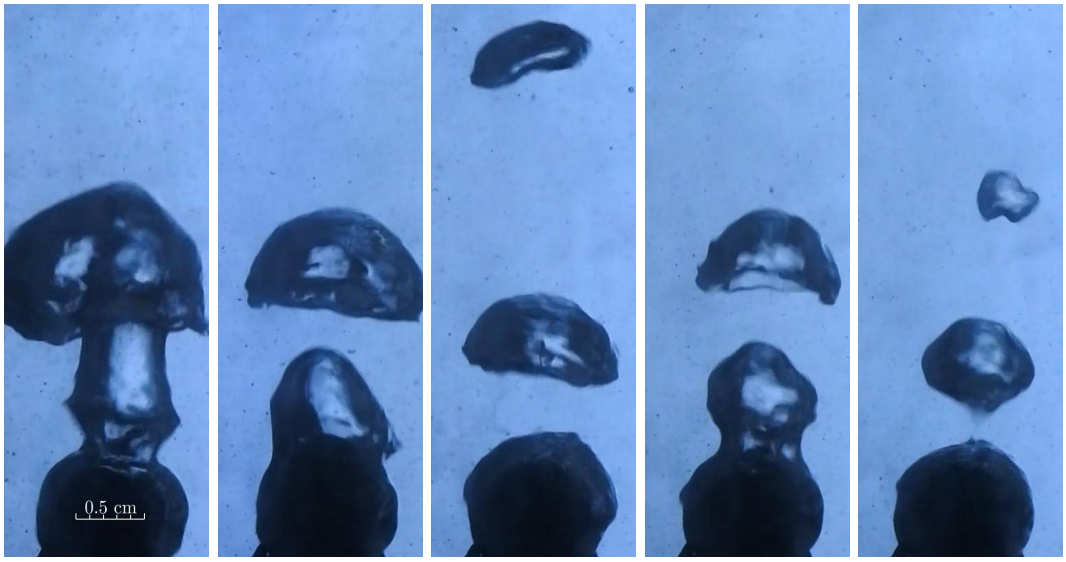

(a) 800 °C *(b)* 700 °C *(c)* 600 °C *(d)* 500 °C *(e)* 450 °C

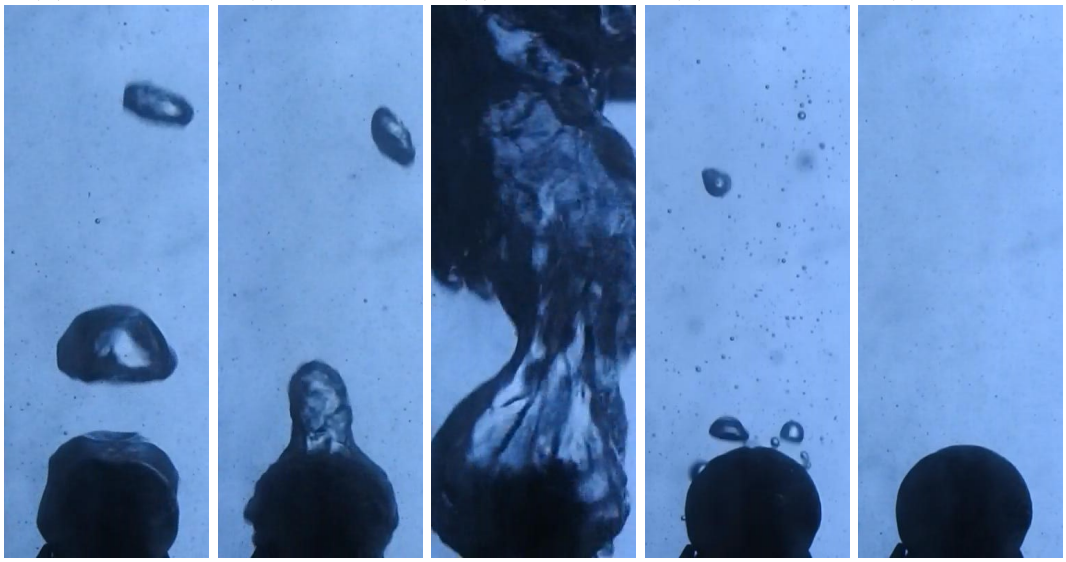

(f) 400 °C *(g)* 300 °C *(h)* 200 °C *(i)* 110 °C *(j)* 98 °C

Figure 5.11: Snapchot at different times of the quenching of a sphere with a 98 °C *pool temperature. Temperatures are estimated thanks to the cooling curve estimation, except for nucleation boiling where they are postulated for illustration purposes. (a) At the begining of the quench, a lot of vapour is created, with bubbles that coalesce with the previous ones. The interface is very unstable and wavy. (b), (c), (d), (e), (f) Then the vapour created reduces with time. Bubbles condensate when rising. The interface remains unstable and wavy with a similar behavior. (g) At some points, the creation of bubble slows and stops down until wetting starts. (h) Then a violent nucleate boiling starts with a large quantity of vapour created in a short amount of time. (i) Partial nucleate boiling ends the cooling of the sphere. (j) Finally boiling stops and the sphere coolds down with natural convection to the temperature of the bath.*

of the quench. For this initial temperature, this states lasted around 40 s. At some points, the creation of bubble slows down and stops until wetting starts. Depending on the quenches, wetting occurred in one shot or after few iterations. However no general law was observed for these conditions. After this transition boiling mode a violent nucleate boiling starts with a large quantity of vapour created in a short amount of time. This stage lasts few seconds before a short partial nucleate boiling mode ends the cooling of the sphere.

From the observation of the vapour film and vapour bubble, the vapour velocity was estimated to be around $1\,\mathrm{m\,s^{-1}}$. Considering the diameter of the sphere as a reference length, this leads to a Reynolds number of around 500. Flows inside the vapour are thus close to be laminar. However this does not prevent the liquid vapour interface to be wavy with phase velocities that also reached values around $1\,\mathrm{m\,s^{-1}}$. Normal velocities of the liquid vapour interface were assumed to be similar to the normal development rate of waves. It was measured around $0.02\,\mathrm{m\,s^{-1}}$ over a characteristic distance of 0.4 mm (order of magnitude of the wave amplitude). This leads to a Reynolds number in the liquid phase of around 100. The liquid phase is also mainly in a laminar regime, but seems to undergo important local recirculations close to the interface due to the vapour waves. This is expected to create a lot of convection inside the liquid and thus improved heat fluxes. The existence of these small scale interface perturbations also demonstrates that the surface tension is not the main factor of the interface behavior.

It was difficult to precisely estimate whether transient wetting phenomena were frequent. The amplitude of the waves being larger than the measured mean vapour film thickness, such liquid solid contacts are probable.

The vapour bubbles shape are associated to very large Galilei number ($\sim 10^4$) and moderate Eötvös numbers (~ 1), which is linked with asymetric bubbles that can evolve into doughnut-like or toroidal shaped bubble (see [131] for more details). This is what is observed mostly for large bubble at high overheating when two bubbles interact together (see Figure 5.11a). However, condensation process might influence a lot their shapes, as the bubble profiles turn into cap while decreasing in volume (see Figure 5.11f). This is all the more true in large subcooling conditions.

5.3.2.3 Quantitative results

Five quenches were carried out with the camera set up on, leading to five batches of measurements. Measurements of the vapour film thickness at mid height of the sphere e_{exp}, of the volume of vapour bubbles that just detached from the vapour film $\mathcal{V}_{\mathrm{exp}}$ and of the frequency of creation of bubbles f_{exp} are plotted in Figure 5.12, Figure 5.13 and Figure 5.14 respectively.

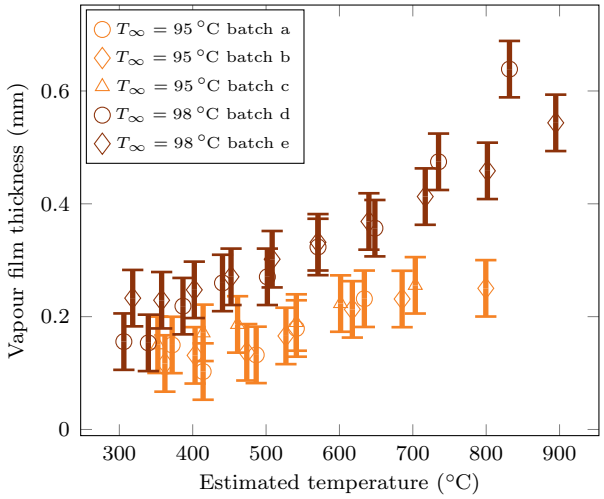

Figure 5.12: Experimental measurements of vapour film thicknesses at the equator of the sphere for liquid temperatures of $T_\infty = 95\,°C$ *and* $T_\infty = 98\,°C$.

The vapour film thickness e_{exp} is decreasing with temperature. The liquid side heat flux might not vary much, as the water pool behaves as a heat sink. For the vapour film to remain stable, the heat fluxes inside the vapour should also not vary too much. The decreasing temperature difference within the film must be compensated by a decrease in the film thickness. This argument also explains that a higher subcooling leads to a thinner vapour film.

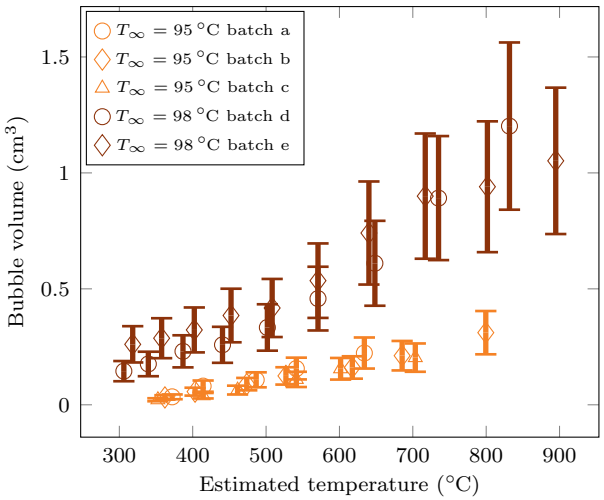

Figure 5.13: Experimental measurements of vapour bubble volumes for liquid temperatures of $T_\infty = 95\,°C$ *and* $T_\infty = 98\,°C$.

The volume of vapour bubbles $\mathcal{V}_{\text{exp}}$ is also decreasing with the sphere temperature. It can be explained by the fact that the lower the overheating, the more dominant the subcoolings effects. These latter entail a stronger condensation of bubble that reduce their size the moment they develop.

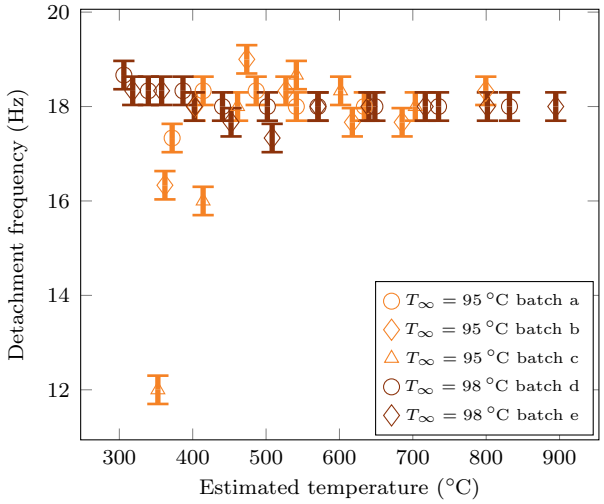

Figure 5.14: Experimental measurements of the vapour bubbles detachment frequency from the sphere for liquid temperatures of $T_\infty = 95\,°C$ *and* $T_\infty = 98\,°C$.

The frequency of detachment of bubbles f_{exp} is very stable. Associated with the observation on their volume, this means that the vapour flow rate decreases with a lower sphere temperature. This is consistent as the lower the overheating and the lower the energy available to vaporise the liquid, thus to a lower vapour volume rate. However it could be allowed by a constant volume and a decreasing frequency. This preferential mode of vapour evacuation is instructive as it implies that the detachment of bubbles is not constrained by the flow rate. This implies that the evacuation of vapour at the top of the sphere does not impact the low parts of the vapour film. More precisely it does not impact the rising of vapour inside the vapor film. One assumption is that viscous stress is the leading limitator of the vapour removal.

Estimations of heat fluxes Estimations from the vapour film thickness q_e and from the vapour creation $q_{f\mathcal{V}}$ are plotted in Figure 5.15 and compared with the estimation from the cooling rate model $q_{\dot{T_S}}$. The model based on the film thickness leads to an overestimated heat flux at lower overheating and larger subcooling. This can be understood as follows: the southern hemisphere of the sphere is cooled with a slower rate due to vapour entrapment. On the northern hemisphere of the

sphere, vapour convection leads to a larger volume of vapour that also degrades the heat transfers. This would entail that the heat transfers recovered by the vapour film thickness on the side is an upper bound of the fluxes. However this explanation does not consider wetting effects that improve the heat fluxes. These phenomena are assumed to be more frequent for more wavy interfaces, which is the case for a higher overheating and a low subcooling. This would explain why the conduction model underestimates the heat flux at high overheating for $T_\infty = 98\,°\mathrm{C}$. This would also explain why the heat flux is not correlated with the mean vapour film thickness (at least at the equator). A deeper analysis of the camera snapshots with an estimation of the full vapour film would help answer this question.

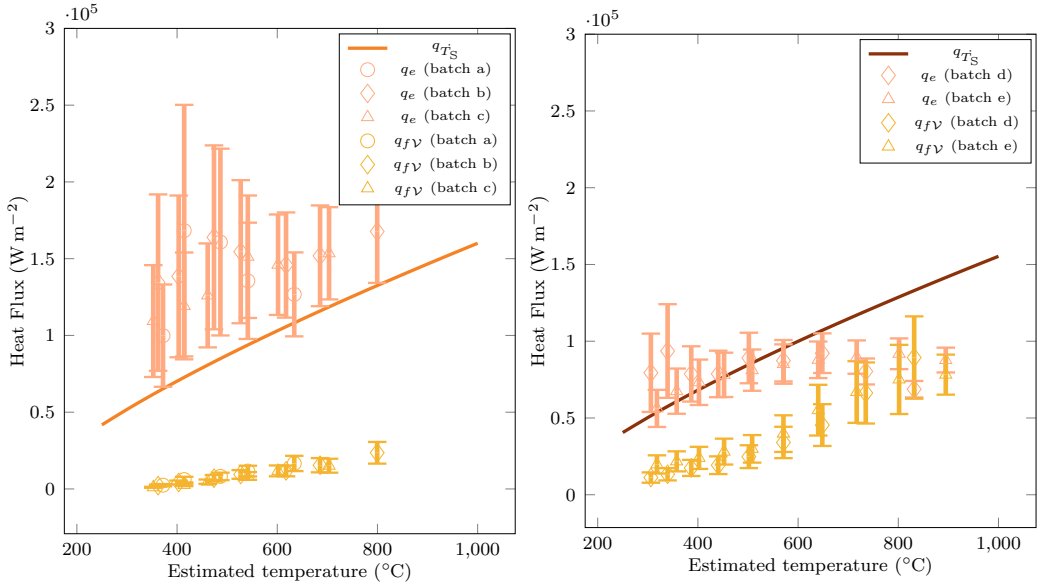

(a) $T_\infty = 95\,°\mathrm{C}$ *(b)* $T_\infty = 98\,°\mathrm{C}$

Figure 5.15: Comparison of experimental heat fluxes from the cooling rate estimation $q_{\dot{T}_S}$, the vapour film thickness q_e and the vaporisation $q_{f\mathcal{V}}$. q_e overestimates the heat fluxes for $T_\infty = 95\,°\mathrm{C}$ and at lower overheating for $T_\infty = 98\,°\mathrm{C}$. The energy budget to vaporise the liquid $q_{f\mathcal{V}}$ is negligible for the $T_\infty = 95\,°\mathrm{C}$.

Regarding the estimation of heat fluxes to vaporise the liquid, this value is only significant at very high temperature and low subcooling. This is consistent with the theory as the hotter the water and the less heat is evacuated inside it to heat it up. This informs us that the ratio of the energy used to vaporise over the energy to heat up the liquid is generally important: even for such a moderate subcooling as 5 K there is ten times more energy that is evacuated inside the liquid. This is assumed to be made possible thanks to the strong local convection in place in the liquid near the liquid vapour interface that evacuates a lot of heat inside the liquid. This point will be discussed further.

First perspectives on the experiment These results are considered interesting and shall be seen as a general description of the film boiling mode for the quenching of small spheres. A better control of the parameters (mostly the temperature) would allow to go deeper in the analysis and reduce the uncertainties regarding the estimated temperature. This is especially true in the pool where more thermocouples would provide a better picture of the temperature field. The experiment could be extended to more temperatures with other subcoolings.

An improvement of the camera would also allow to have more information on the hydrodynamics. First, two angles would provide a 3D picture of the bubbles and considerably reduce the error on the volume estimation. Secondly, this would allow a better assessment of the global film thickness through the integration of the thickness on the whole surface. Finally, a zoom on the liquid vapour interface would more precisely capture the vapour film waves.

5.4 Comparison with numerical simulations

We first challenged our phase change model to evaluate its relevance in this first real-world problem. We simulated the film boiling around a sphere at a fixed temperature. Thus the thermal effects in the sphere is not considered to simplify the configuration. This is acceptable since the time of the quenching experiment is large regarding the hydrodynamic time. Six working points were considered with sphere temperatures T_S set to 400 °C, 600 °C and 800 °C, and pool temperature T_∞ set to 95 °C and 98 °C. We compared the simulation results through the general behavior of the liquid vapour interface, and through the computation of the simulated vapour film mean thickness at the equator of the sphere, the vapour bubble volume and detachment frequency as well as the heat flux.

5.4.1 Simulation strategy

We ran the simulations on a domain of 50 mm by 50 mm by 75 mm (see Figure 5.16). The sphere was placed at the center of the domain with its center at height 25 mm from the bottom. 2×10^5 nodes were considered, with a minimum mesh size $h_{\min} = 0.2$ mm imposed at the liquid vapour interface. This distance is the order of magnitude of the smallest mean vapour film thickness, that could be a potentiel source of error. This will be discussed later. 1 s were simulated for each configuration, which was assumed to be long enough for the hydrodynamic steady state to be reached as its characteristic time is smaller.

One of the most important parameter to monitor is the vapour film thickness. To avoid errors due to the smoothed interface approach we considered an offset for the numerical interface in the same idea as for the Scriven benchmark modeling

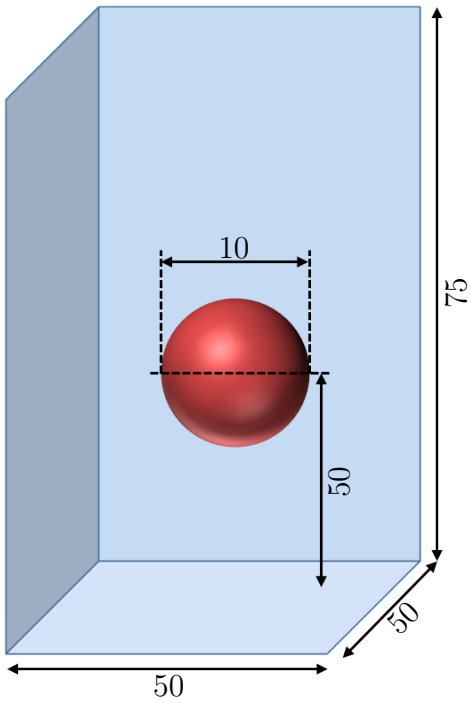

Figure 5.16: Schematic description of the computation domain for the sphere quenching. Values of lengths are given in mm.

(Section 4.3.2.4). The physical interface is considered to be at the isovalue $\alpha = \varepsilon$. The density and viscosity used for the mechanical solver had been set according to this interface with a P0 mixing: any element within $h_{\min}$ from the isovalue $\alpha = \varepsilon$ was set with constant values of ρ and η following a volume weighting of liquid and vapor values. This modification of the presented model was shown not to break the mass conservation of the phase change formulation. As the whole interface between $\alpha = -\varepsilon$ and $\alpha = \varepsilon$ was imposed at T_{sat}, this consideration lead to a proper film vapour with a temperature gradient between T_{S} and T_{sat}.

The vapour phase was initially set to T_{sat} and the water at T_{∞}. Regarding boundary conditions, the temperature was fixed at T_{S} on the sphere and at T_{∞} on the other domain frontiers. No slip conditions were set on all mesh borders except on the top where zero gauge pressure with free output velocity was set. The remeshing algorithm was called every five steps, and the Level Set function is reinitialised every two steps.

Values of vapour conductivity were taken accordingly to the Table E.1 from values of [89]. Values of other properties at $(T_{\text{sat}} + T_{\text{S}})/2$ are considered for the vapour phases, and at T_{sat} for the liquid phase. This is summed up in Table 5.3.

Attention should be paid on the value of the vapour viscosity. Many tests were carried to try to simulate this benchmark with the physical parameters mentioned above. However, such configuration did not guarantee a convergence of the linear resolution of the mechanical system. Tests were done with different time steps without succeeding in resolving this issue. Regarding the mesh, it was difficult to make it thinner without getting an oversized number of elements. One explanation of this difficulty is that our Reynolds number is underestimated, and that violent hydrodynamics might be at play at the liquid vapour interface. The combination of this stiff physics with the constraint of important material property gaps (a factor 2000 for the density and a factor 10 for the viscosity) seemed to lead to an ill-conditioned matrix. A deeper analysis of this effect would be required. A finer mesh would probably help to better understand this issue but this was not in the scope of this work.

We decided to resolved this issue with an augmented viscosity in the vapour. This kind of 0D turbulence model makes the flow more laminar and cuts of the small instabilities of the interface. We iteratively raised the value of η_V up to a factor 50. This lower limit allowed the convergence of mechanical solver. This simple approach could be improved with the help of recent models and techniques to take into account turbulence in two phase flows (see for example [134, 135]).

	ρ ($\mathrm{kg\,m^{-3}}$)	η ($\mathrm{Pa\,s}$)	c_p ($\mathrm{W\,m^{-1}\,K^{-1}}$)	k ($\mathrm{J\,kg^{-1}\,K^{-1}}$)	$\mathcal{L}$ ($\mathrm{J\,kg^{-1}}$)	γ_0 ($\mathrm{J\,m^{-2}}$)
Liquid	958	5×10^{-3}	4216	0.679	2.265×10^{6}	0.06
Vapour	0.4 0.42 0.46	1×10^{-3}	2030	$f(T_S)$		

Table 5.3: Properties of the liquid, vapour and solid phases for the 3D brick quenching simulation.

Radiative effects were also considered in the energy conservation equation of the liquid vapour interface with the simplification presented in Chapter 2. However, as the emissivity of the sphere ε_w was difficult to measure, two extreme cases were considered with $\varepsilon_w = 0$ (no radiation) and $\varepsilon_w = 1$ (black body) to assess the influence of radiation.

5.4.2 Results and comparison

5.4.2.1 First application of the model

A first batch of six simulations were carried with these parameters without radiation $\varepsilon_w = 0$. Two qualitative comparisons with experimental results are presented in Figures 5.17 to 5.18. Different pictures are considered over the period of formation of a vapour bubble $\tau_{\mathrm{exp}} = 1/f_{\mathrm{exp}}$. The associated sphere and pool temperatures

are ($T_\infty = 98\,°C$, $T_w = 800\,°C$) and ($T_\infty = 95\,°C$, $T_w = 600\,°C$). We can see that the main features are respected for the configuration with high overheating and low subcooling. However, the production of vapour is greatly overestimated in the second configuration. This conclusion is supported by the comparison of the bubble shapes for all configurations (see Figure 5.19).

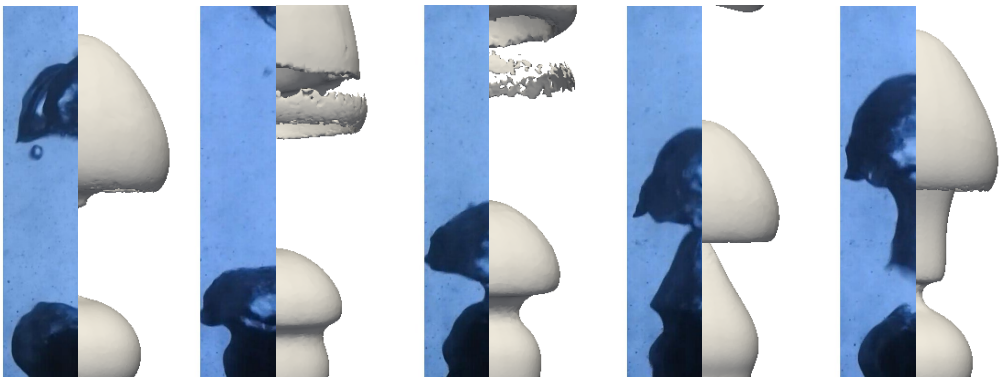

(a) t_0 *(b)* $t_0+1/4\tau_{exp}$ *(c)* $t_0+1/2\tau_{exp}$ *(d)* $t_0+3/4\tau_{exp}$ *(e)* $t_0+\tau_{exp}$

Figure 5.17: Comparison of experimental bubble profile with the simulation for $T_S = 800\,°C$, $T_\infty = 98\,°C$.

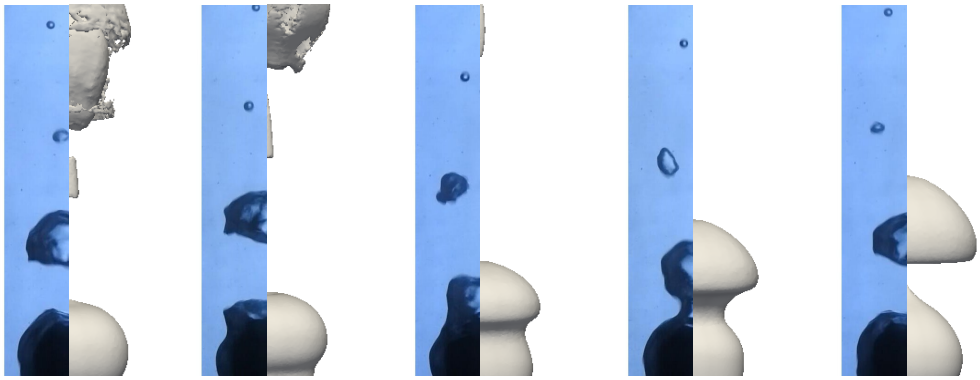

(a) t_0 *(b)* $t_0+1/4\tau_{exp}$ *(c)* $t_0+1/2\tau_{exp}$ *(d)* $t_0+3/4\tau_{exp}$ *(e)* $t_0+\tau_{exp}$

Figure 5.18: Comparison of experimental bubble profile with the simulation for $T_S = 600\,°C$, $T_\infty = 95\,°C$.

The predictions of the simulation regarding the vapour film mean thicknesses at the equator, the bubble volume and detachment frequency and the surface heat fluxes are compared with experimental results in Figure 5.20, 5.21, 5.22 and 5.23. We can see that the mean thickness is overestimated by a factor 1.5 in the $T_\infty = 98\,°C$ configuration, and by a factor 2 in the $T_\infty = 95\,°C$ configuration. This is assumed to be due to the augmented viscosity in the vapour film that prevents the existence of thin vapour layers for a given vapour flow. The coarse mesh size in the liquid vapour could be a supplementary factor of error. However the film thickness undergoes large

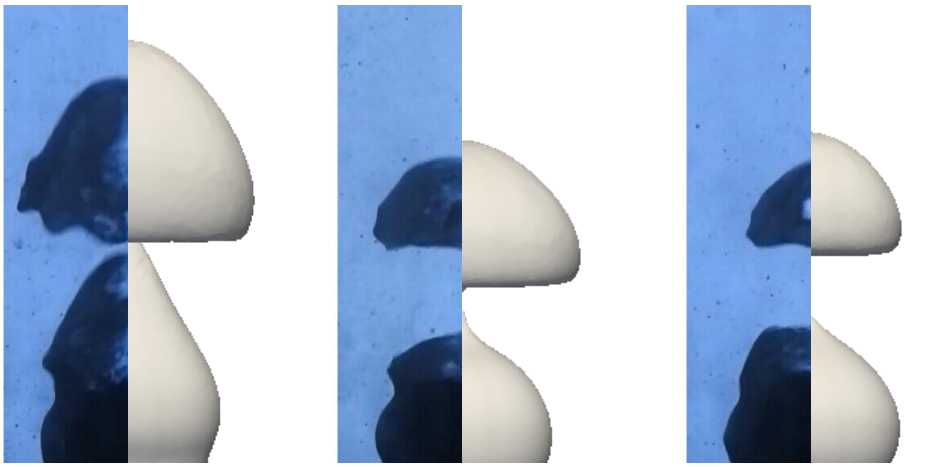

(a) $T_S = 800\,°C$, $T_\infty = 98\,°C$ *(b)* $T_S = 600\,°C$, $T_\infty = 98\,°C$ *(c)* $T_S = 400\,°C$, $T_\infty = 98\,°C$

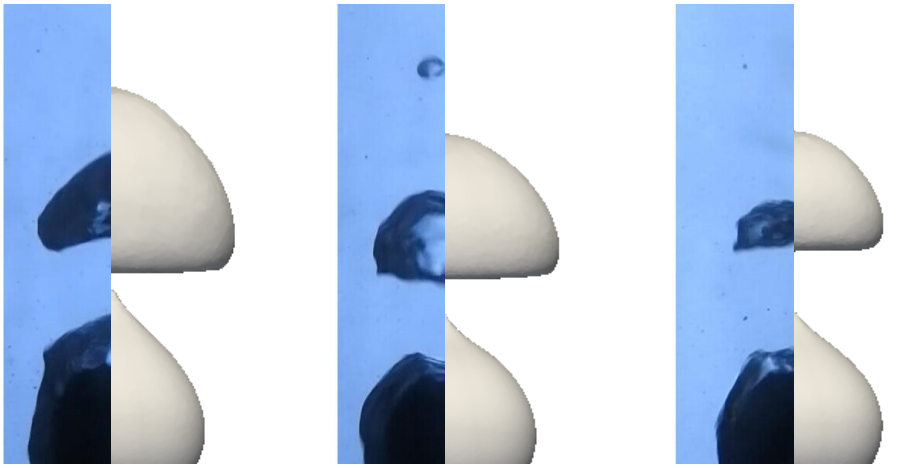

(d) $T_S = 800\,°C$, $T_\infty = 95\,°C$ *(e)* $T_S = 600\,°C$, $T_\infty = 95\,°C$ *(f)* $T_S = 400\,°C$, $T_\infty = 95\,°C$

Figure 5.19: Comparison of the simulated and experimental bubble profiles for different temperature configurations.

variations in sizes one order of magnitude above the mesh size. Thus this latter might not be the dominant error factor. Future tests with a finer mesh size should be done to confirm this conclusion. Regarding the bubble volumes, they are overestimated by the simulation except in conditions of high overheating and low subcooling. This is assumed to be due to an underestimation of liquid sides heat fluxes which allow a larger vaporisation. This argument also explains the overestimation of the vapour thickness. The frequency of detachment of bubbles is however better respected. This confirms that the volume of vapour is not the criteria of detachment of bubbles. It also shows that the detachment is not impacted by the vapour viscosity, and that it

is controlled by the liquid flow. Finaly, heat fluxes are underestimated by a factor two, which is consistent with the overestimation of the film thickness.

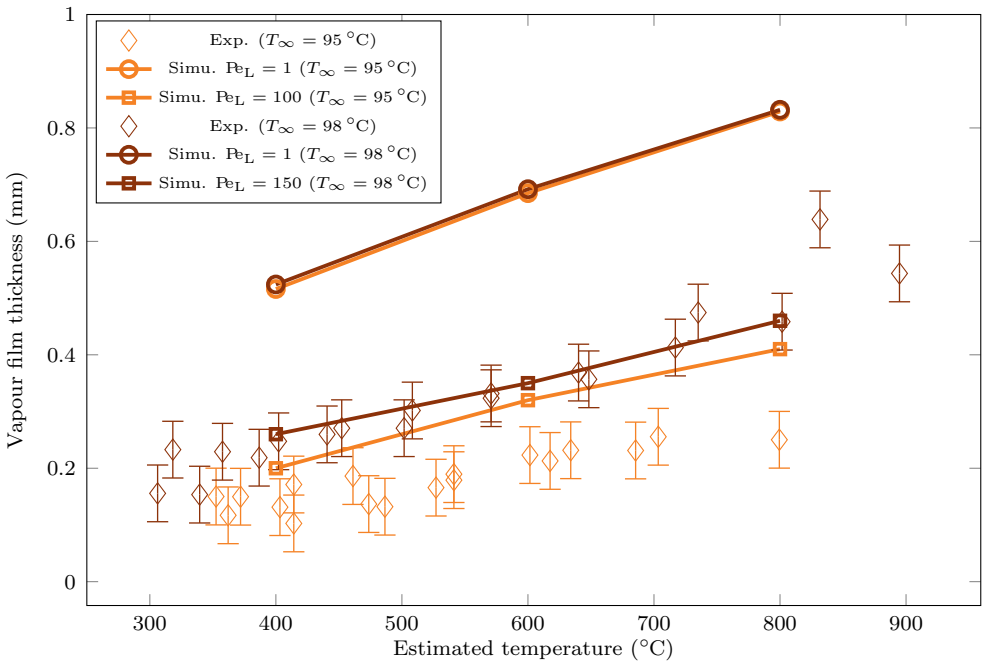

Figure 5.20: Comparison of experimental and simulated vapour film thicknesses at the equator of the sphere for liquid temperatures of $T_\infty = 95\,°C$ and $T_\infty = 98\,°C$.

5.4.2.2 Radiative effects

To assess the influence of radiative effects, we considered the worst case scenario of a black body model ($\varepsilon_w = 1$). We expect the influence of radiation to be dominant in the high overheating configuration, as the Stefan Bolzman law predicts heat fluxes that are only significant at this temperature range. To confirm this, the two extreme configurations were simulated: $T_S = 800\,°C$, $T_\infty = 98\,°C$ and $T_S = 400\,°C$, $T_\infty = 95\,°C$. The comparison criteria for the two emissivities are gathered in Table 5.4.

	e (mm)		$\mathcal{V}$ (cm^3)		f (Hz)		q_w ($W\,m^{-2}$)	
ε_w	0	1	0	1	0	1	0	1
$T_S = 800\,°C$, $T_\infty = 98\,°C$	0.83	1.3	1.5	2.75	17	17	81 800	137 940
$T_S = 400\,°C$, $T_\infty = 95\,°C$	0.52	0.59	0.5	0.69	15	17	34 000	42 800

Table 5.4: Comparison of the sphere quenching simulations without radiation and with a black body model.

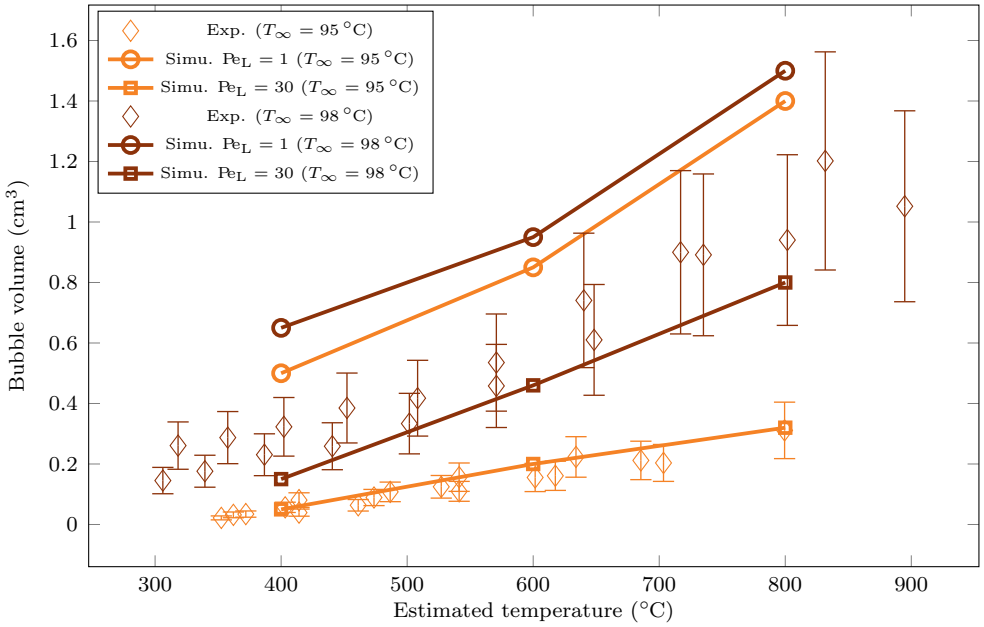

Figure 5.21: Comparison of experimental and simulated vapour bubble volumes for liquid temperatures of $T_\infty = 95\,°C$ and $T_\infty = 98\,°C$.

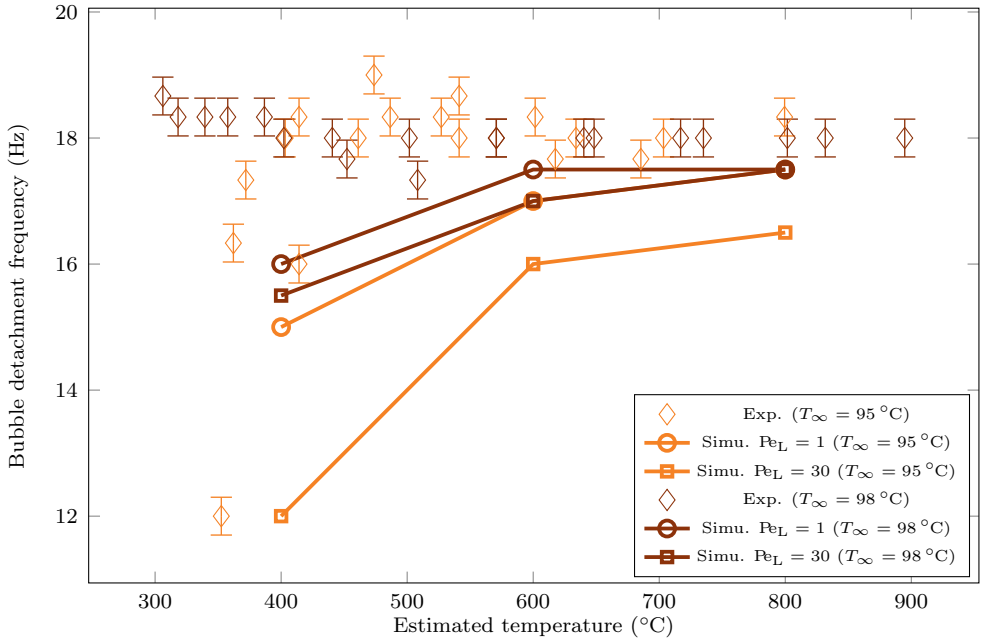

Figure 5.22: Comparison of experimental and simulated vapour bubble detachment frequency for liquid temperatures of $T_\infty = 95\,°C$ and $T_\infty = 98\,°C$.

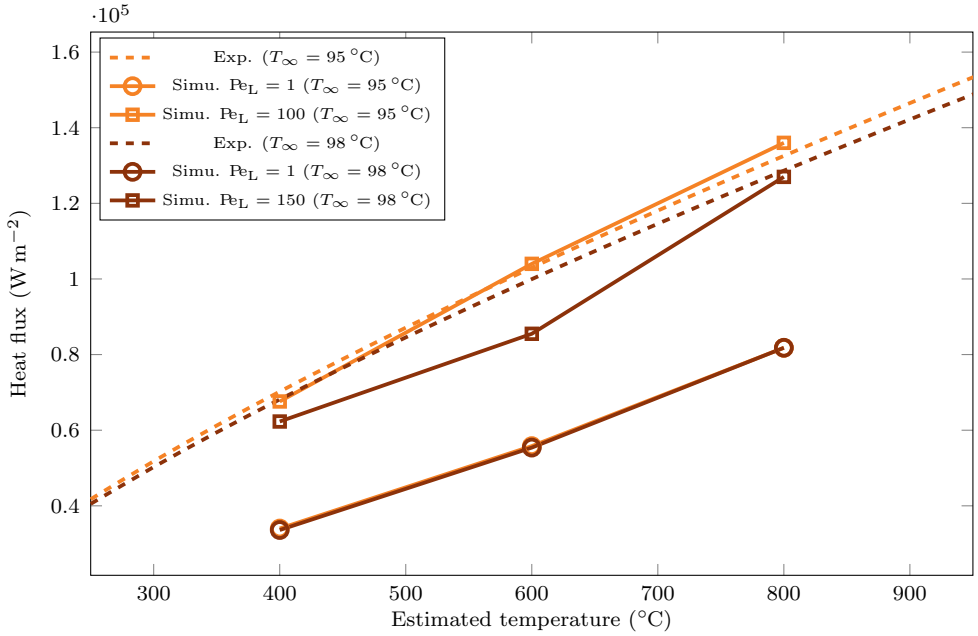

Figure 5.23: Comparison of experimental and simulated heat fluxes for liquid temperatures of $T_\infty = 95\,°\mathrm{C}$ and $T_\infty = 98\,°\mathrm{C}$.

As expected, radiation effects are more significant at large overheating. The vapour production is increased, with larger vapour film and bigger bubbles. The heat flux is almost doubled. At lower overheating the parameters are little changed, though the heat flux is increased by 25%. We should keep in mind that this comparison is made with a black body model, which is a very conservative approach. In the reality, the radiative fluxes might be at least twice smaller or even less. Thus the resulting influence of radiation is even less significant at low subcooling. We also notice that the frequency is unchanged, which once again confirms the independence of the vapour detachment on the vapour flow.

From these observations, we can conclude that radiative effects are not explaining the differences between the simulation and the experiment. The deviation from experimental heat fluxes is still significant at high subcooling, and the vapour production is still overestimated.

5.4.2.3 Modification of the liquid conductivity at the interface

An augmented vapour viscosity induces a more laminar regime in the vapour film with straight velocity trajectories. This cancels the interfacial perturbations that are assumed to be the cause of an improved convection and thus improved heat fluxes on the liquid side close to the interface. This underestimation would be the cause of the non simulation of small thermal scales inside the liquid. These effects

would explain the differences between the simulation and the experiment, especially at larger subcooling where the simulations predict a larger vapour creation that is not reduced by condensation.

To compensate the canceling of this convection close to the interface, a first model consists in evaluating this convection, and to deduce an equivalent thermal conductivity k_{Leq}. The model of an equivalent conductivity entails the assumption of a proportional relationship between the convective effects and the subcooling. This conductivity is then used when computing the heat flux jump at the interface.

In a similar way to Section 4.4.3 for the definition of the Péclet number, a first estimation of convective heat fluxes reads:

$$q_{\mathrm{eq}} \sim \rho_{\mathrm{L}} c_{\mathrm{pL}} u_n \Delta T_\infty \tag{5.18}$$

where u_n is the normal velocity of the liquid close to the interface. This is equivalent to the replacement of a particle of temperature T_{sat} with a particle T_∞ a at rate given by u_n. If this phenomenon occurs on a thickness δ_{c}, then the equivalent conductivity of this flux reads:

$$k_{\mathrm{Leq}} \sim \rho_{\mathrm{L}} c_{\mathrm{pL}} u_n \delta_{\mathrm{c}} \tag{5.19}$$

We defined the associated Péclet number Pe_{L} as the ratio of k_{Leq} to k_{L}:

$$\mathrm{Pe}_{\mathrm{L}} = \frac{k_{\mathrm{Leq}}}{k_{\mathrm{L}}} = \frac{\rho_{\mathrm{L}} c_{\mathrm{pL}} u_n \delta_{\mathrm{c}}}{k_{\mathrm{L}}} \tag{5.20}$$

In our context the normal velocity of the liquid close to the interface observed in the experiment was $u_n = 0.02\,\mathrm{m\,s^{-1}}$. δ_{c} is estimated with the vapour film waves maximum amplitude whose order of magnitude was $\delta_{\mathrm{c}} = 0.4\,\mathrm{mm}$. This leads to a value of around $k_{\mathrm{Leq}} = 30\,\mathrm{W\,m^{-1}\,K^{-1}}$ and to $\mathrm{Pe}_{\mathrm{L}} = 45$.

To confirm this value, an influence study on the heat flux was done for varying Pe_{L} at the highest overheating ($T_{\mathrm{S}} = 800\,^\circ\mathrm{C}$) for the two subcooling configurations. Results are plotted in Figure 5.24.

We can see that a augmented k_{Leq} improves a lot the heat fluxes. This is consistent as it reduces the vaporisation and thus lead to a thinner film. The value of $\mathrm{Pe}_{\mathrm{L}} = 100$ (resp. $\mathrm{Pe}_{\mathrm{L}} = 150$) seems to be the best approximation of convective effects inside the liquid for $T_\infty = 95\,^\circ\mathrm{C}$ (resp. $T_\infty = 98\,^\circ\mathrm{C}$). This means that Pe_{L} is case dependant which would be consistent with the model of the liquid recirculation: the vapour film waves are indeed affected by the subcooling. To study the influence of the overheating on k_{Leq}, we launched the six test cases for the two values of Pe_{L} mentioned above. The resulting heat fluxes and interface thicknesses are plotted in Figure 5.20 and Figure 5.23. We observe that there is a lower bound on the interface thickness that the model cannot overcome. This might be due to the resolution of the mesh. However the heat fluxes are still properly corrected. This confirms that

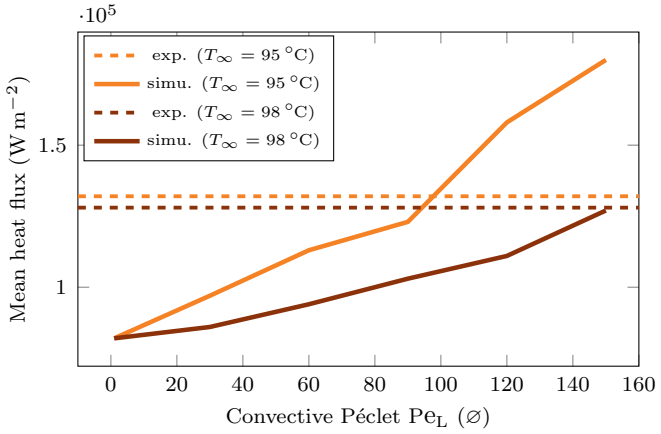

Figure 5.24: Study of the influence of Pe_L *on the vapour heat flux for* $T_\infty = 95\,°C$ *and* $T_\infty = 98\,°C$.

(a) $\mathrm{Pe}_L = 1$ *(b)* $\mathrm{Pe}_L = 30$ *(c)* $\mathrm{Pe}_L = 60$ *(d)* $\mathrm{Pe}_L = 90$ *(e)* $\mathrm{Pe}_L = 120$ *(f)* $\mathrm{Pe}_L = 150$

Figure 5.25: Comparison of the liquid vapour interface behavior for different values of convective conductivities.

the information of the interface thickness at the equator is not sufficient to describe the system and that a complete modelling is necessary.

Snapshots of the interface for $T_S = 800\,°C$ and $T_\infty = 95\,°C$ are plotted in Figure 5.25 for different values of Pe_L. We see that the vapour film is still wavy, meaning that the convective model does not cancel the hydrodynamics inside the vapour. However it cancels out the creation of bubbles. One explanation of this effect is that convective effects in the liquid are weaker around the bubbles than over the vapour film. Moreover, the liquid at the top of the sphere is heated up which reduces the effect of liquid convection. Consenquently, Pe_L seems also to be spatially dependant.

We tried to estimate the value of Pe_L that would match the convective effects during the rising of bubbles. We simulated the sphere quenching case with few different values of Pe_L and compared the results with the experiments through the comparison of the detached bubble. The order of magnitude that lead to the more promising result was for $\mathrm{Pe}_L = 30$ leading to $k_{Leq} = 20\,\mathrm{W\,m^{-1}\,K^{-1}}$. Two qualitative comparisons with experimental on the interface behavior during the formation of a vapour bubble are presented in Figures 5.26 to 5.27. The associated sphere and

pool temperatures are ($T_\infty = 98\,°C$, $T_S = 800\,°C$) and ($T_\infty = 95\,°C$, $T_S = 600\,°C$). This shows the capacity of the solver to predict the bubble evolution providing that the liquid side heat fluxes are properly computed. This is confirmed with the comparison of the bubble shapes of all test cases (see Figure 5.28), and with the comparison of the bubble volumes (see Figure 5.21). Regarding the other parameters of comparisons, we observe that this modifies the frequency of detachment of bubbles at low overheating (see Figure 5.22). This can be explained by a strong condensation at the top of the bubble that prevent them to grow.

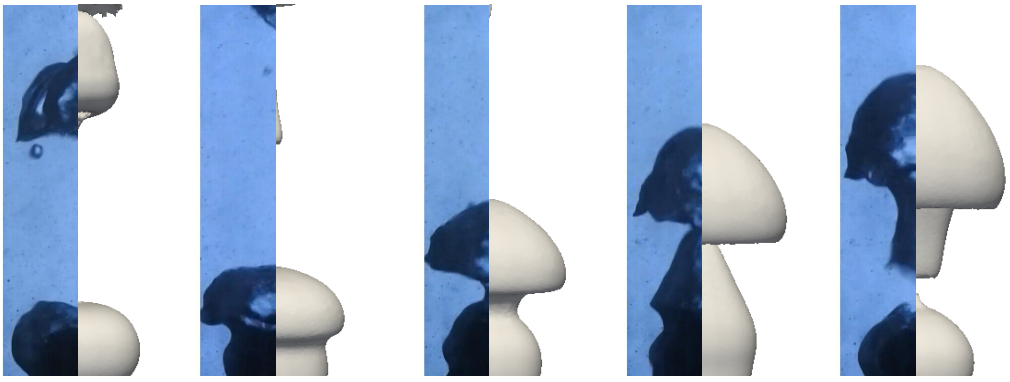

(a) t_0 (b) $t_0+1/4\tau_{exp}$ (c) $t_0+1/2\tau_{exp}$ (d) $t_0+3/4\tau_{exp}$ (e) $t_0+\tau_{exp}$

Figure 5.26: Comparison of experimental bubble profile with the simulation for $T_S = 800\,°C$, $T_\infty = 98\,°C$ *with the convective conductivity model for* $Pe_L = 30$.

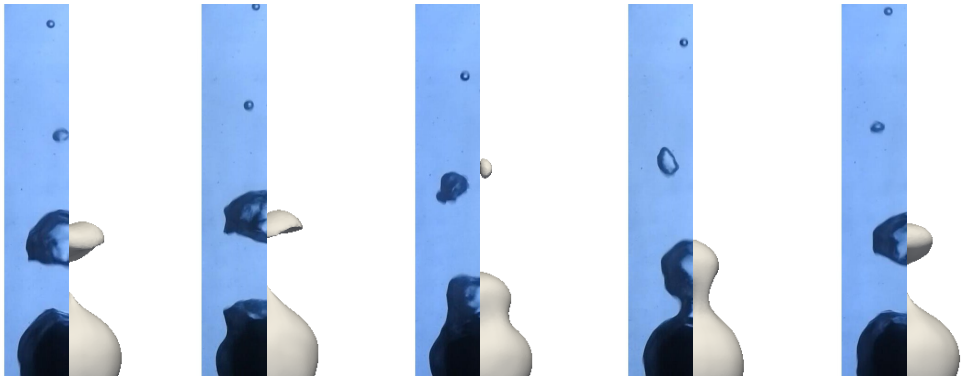

(a) t_0 (b) $t_0+1/4\tau_{exp}$ (c) $t_0+1/2\tau_{exp}$ (d) $t_0+3/4\tau_{exp}$ (e) $t_0+\tau_{exp}$

Figure 5.27: Comparison of experimental bubble profile with the simulation for $T_S = 600\,°C$, $T_\infty = 95\,°C$ *with the convective conductivity model for* $Pe_L = 30$.

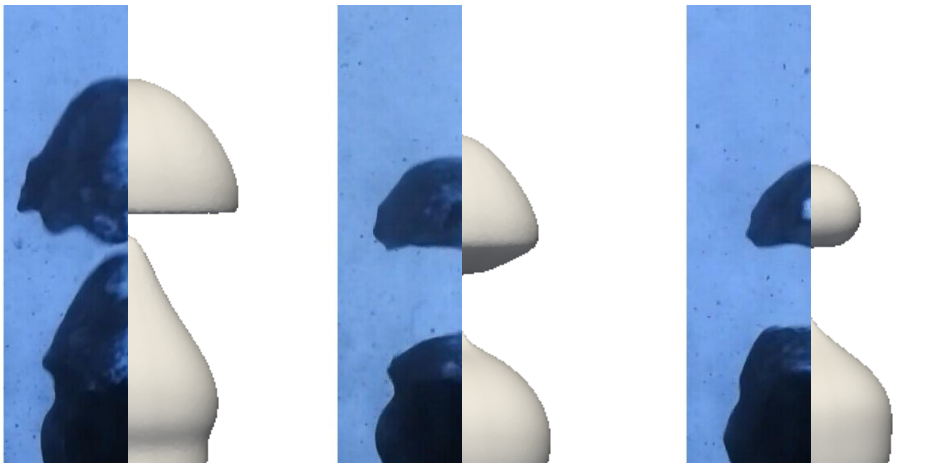

(a) $T_S = 800\,°\mathrm{C}$, $T_\infty = 98\,°\mathrm{C}$ *(b)* $T_S = 600\,°\mathrm{C}$, $T_\infty = 98\,°\mathrm{C}$ *(c)* $T_S = 400\,°\mathrm{C}$, $T_\infty = 98\,°\mathrm{C}$

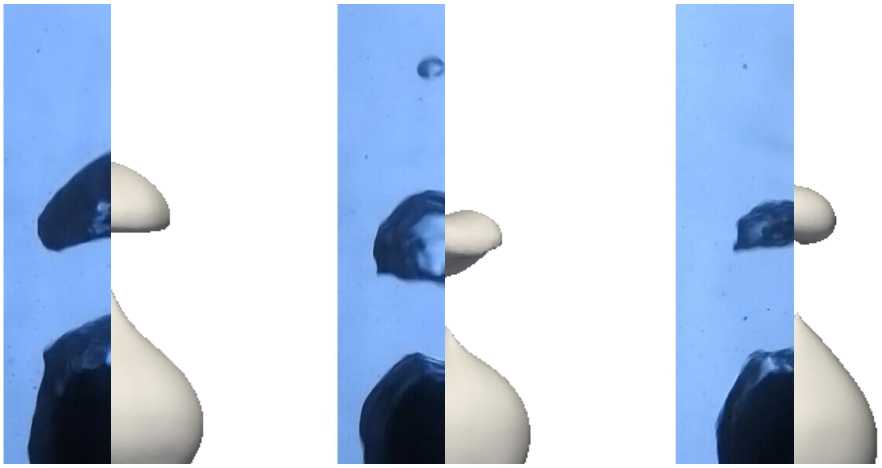

(d) $T_S = 800\,°\mathrm{C}$, $T_\infty = 95\,°\mathrm{C}$ *(e)* $T_S = 600\,°\mathrm{C}$, $T_\infty = 95\,°\mathrm{C}$ *(f)* $T_S = 400\,°\mathrm{C}$, $T_\infty = 95\,°\mathrm{C}$

Figure 5.28: Comparison of the simulated and experimental bubble profiles for different temperature configurations with the convective conductivity model for $\mathrm{Pe}_L = 30$.

5.5 First feedbacks on the model

The current approach with augmented viscosity succeeds better for configurations with important vaporisation. This is consistent as characteristic lengths in the vapour are larger, leading to less viscosity-driven flows.

The mode of convective conductivity in the liquid near the interface allows to recover some features of the flow, but is not universal. Moreover, no thermal steady state was reached in the simulation. This could change the values of k_{Leq} we measured. Further studies of this benchmark with finer meshes would be interesting. In

the present work, we decided to tackle another benchmark to deepen our comprehension of this convective phenomenon with a very documented configuration: the Vertical Film Boiling benchmark, as presented in the next Chapter.

5.6 Conclusions

- A quenching experiment with small nickel sphere had been proposed. Film boiling was the focus of the experiment.
- The cooling rate and instant temperature were assessed through the quenching time of spheres of different initial temperatures. The cooling rate was shown to respect a power law of coefficient 3/4 in respect to the overheating, which is consistent with the literature.
- Vapour film thickness, vapour bubble volume and detachment frequencies were measured thanks to a camera set up. Subcooling was shown to improve the condensation, reduce the vapour film thickness and increase the Leidenfrost temperature. However the heat fluxes were not improved significantly.
- The experiment provided a general description of the film boiling mode during the quenching of small spheres. The experiment could be improved with a better control on the temperature and a more advanced camera set up to provide 3D information.
- The vapour viscosity was augmented to allow the phase change framework to run properly. This vision predicted better the system features at low subcooling.
- This model did not allow to simulate local phenomenan that were expected to improve the liquid side heat fluxes. A model of convective conductivity was proposed to correct this biais and shown promising results.
- Radiation was shown to only matter significantly at high overheating.

Chapter 6

Study of vertical film boiling

Contents

Résumé en Français

Ce chapitre présente l'étude de la caléfaction sur une plaque verticale, réalisée en deux parties. Dans un premier temps, une première analyse qualitative est réalisée sur la base de deux articles de la littérature. Dans un deuxième temps, le cas est traité par simulation numérique grâce au modèle de vaporisation.

Les articles en question sont ceux de Vijaykumar et al. [57, 61]. Les auteurs ont mis en place une expérience dans laquelle un bloc de cuivre est inséré à travers l'une des cloisons verticales d'un bac parallélépipédique rempli d'eau. La surface apparente est une plaque verticale rectangulaire de 6.3 cm de largeur et de 10.3 cm de hauteur. Elle est chauffée à une température contrôlée afin d'assurer le mode de caléfaction dans le fluide. La température du bain est aussi contrôlée. Des thermocouples et des caméras permettent de récupérer divers paramètres comme le flux de chaleur ou le profil du film de vapeur. Ce dernier est majoritairement perturbé par des ondes d'interface provoquées par le cisaillement au sein de la phase vapeur et qui remontent verticalement le long de la plaque. Leur amplitude, leur longueur d'onde et leur vitesse de phase sont plus importantes pour de plus grandes températures de plaque et de bain. Si une plus grande température de plaque augmente le flux de chaleur, il en est de même pour la température de l'eau mais avec un facteur significativement plus important. Le flux de chaleur est majoritairement conductif au sein de la vapeur. Côté liquide, des effets convectifs liés à des petites échelles de gradient thermique mènent à un transfert de chaleur très intense.

Concernant l'étude par simulation numérique, la configuration dans un bain à 100 °C (régime saturé) est d'abord étudiée pour les trois températures de plaque de l'article. La viscosité augmentée de la vapeur rend les perturbations plus larges et plus plates. Cependant, les ordres de grandeur des transferts thermiques simulés sont proches de ceux mesurés expérimentalement. Ensuite, une étude par un modèle de Boussinesq permet d'écarter les effets de convection naturelle pour expliquer les transferts thermiques importants dans la phase liquide. Enfin, le modèle est appliqué pour six régimes thermiques différents avec différentes températures de bain. La considération du modèle convectif permet à nouveau de corriger les effets convectifs proches de l'interface qui ne sont pas simulés. L'ordre de grandeur du nombre de Péclet équivalent est le même que pour le chapitre précédent, ce qui laisse à penser que ces effets dépendent peu de la configuration géométrique et thermique.

6.1 Introduction

We saw in the previous section that the present numerical formulation required an augmented viscosity in the vapour phase to properly run without too much computational cost. The work on the sphere quenching experiments enhanced the fact that this impacted the vapour profile and degraded the heat transfer in subcooled conditions. Work has then to be done to correct this bias. The lack of additional data from this experiment motivated us to study another benchmark. As the present code aims at the modeling of industrial quenching, a larger scale is preferred for the correction to be more consistent with further simulations.

To focus on this question, we challenged the capacity of the numerical model with the vertical film boiling test case. This is a vertical heater at fixed temperature that is plunged into water. Thus no consideration of cooling inside the solid has to be taken. The length scale is larger compared to the previous benchmark but remains moderate. We first studied some mechanisms behind this test case. This gave us some insights and scales of magnitude of the physics involved to improve our correction of the phase change model.

We studied the experimental case of Vijaykumar et al. [61, 57]. This choice was motivated by the following reasons: (i) their experiments reproduce film boiling, which is the mode tackled by our framework, (ii) the paper shows numerous useful details on hydrodynamics and thermics, (iii) subcooling effects were studied. Their work is a continuation to the work of Bui et al. [136] who provided results in saturated conditions.

In the following, the findings of the two papers are summarized, the aim being to recover the principal physical features of the experiments. These findings, combined with our analysis have then been implemented to enrich our simulation strategy, and the results are compared with experimental results in the final part of this chapter.

6.2 Study of experimental results from the literature

6.2.1 The test bench

The experimental setup described by the Figure 6.1 is a cavity of height 40 cm and of horizontal surface approximately 100 cm^2, in which a copper block was placed mid height of one of the wall. The part of the block facing the interior of the cavity is a vertical surface of width $L = 6.3$ cm and height $H = 10.3$ cm. The block was heated by a variable AC power supply and was maintained at a fixed temperature between 250 °C and 400 °C on its surface thanks to a control device. The block having a volume of approximately 1 l, the time to cool it down by 1 K with a heat flux of 10^5 W m^{-2} (maximum value observed by the bench) would be around 6 s. This time is long enough to be able to ensure a temperature control with a precison below

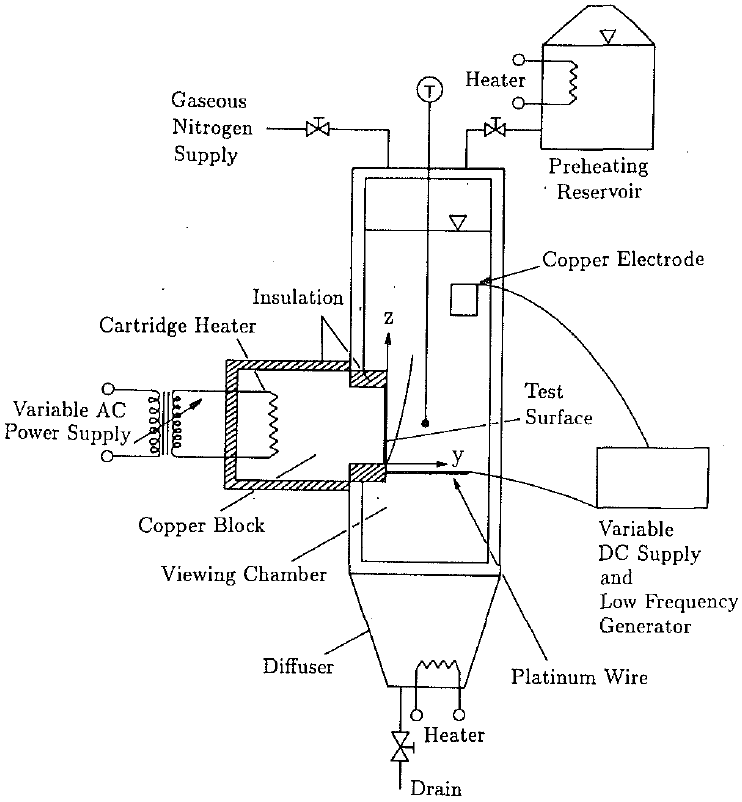

Figure 6.1: Complete description of the bench (scheme extracted from [61]). A copper heater is integrated in a chamber that is filled with preheated water.

1 K, this being confirmed by [57]. The cavity was filled with water at temperatures ranging from 85 °C to 100 °C. A platinum wire was placed normally to the copper plate and a difference of potential was measured at different heights, allowing to recover the local vapour film thickness. Hydrogen bubbles were also released in front of the copper surface to measure the water velocity stream. A front camera allowed to visualize the general behavior of the film as well as to track the hydrogen bubbles. Along with this apparatus, the temperature and heat flux at the surface of the heater were measured thanks to the temperature distribution measured inside the copper block. A holographic interferometry system was set up to recover the isotherms inside the liquid phase, allowing to recover the liquid side heat flux.

6.2.2 Estimation of vapour film characteristics

Before analysing the results and conclusions of Vijaykumar et al. [61, 57], we can shortly try to draw the main characteristics of the experiments. As the heater is warmer than the saturation temperature of the fluid, vaporization is expected to

occur. Conditions are set to create calefaction, so a vapour film is expected to be created. Water vapour being a thousand time lighter than water, buoyancy effects are expected to drive the vapour upwards. Thus, the vapour created at the bottom of the heater is expected to feed the upwards vapour film. In saturated conditions, the vapour film is then expected to grow from the bottom to the top. However, as vapour is a poor conductor, the vaporization rate is expected to decrease when increasing the film thickness. Thus the vapour film thickness is expected to plateau. With subcooling, the conduction in water is expected to recover some heat and thus reduce the vaporization rate, or even inverse the heat flux balance at the liquid vapour interface. This can cancel vaporization or even create condensation, thus stopping the film thickening.

A first complete model of vertical film boiling can be proposed, considering a steady state boundary layer (BL) flow. The saturated case is presented for example by Brennen [12], and illustrated by Figure 6.2a. The local film thickness varying with the vertical coordinate z is noted $e(z)$. An integrated vertical velocity $\vec{\overline{u}}(z)$ is considered, along with a conduction model through the vapour: $q_w = k_\mathrm{V}\Delta T_w/e$, where $\Delta T_w = T_w - T_\mathrm{sat}$ is the overheating. Moreover, the liquid is at saturation temperature so all the heat is used to vaporize the liquid, and the vapour heating is neglected: $q_w = \mathcal{L}\dot{m}$. Doing so, the mass balance reads:

$$\frac{\mathrm{d}\rho_\mathrm{V} e\overline{u}}{\mathrm{d}z} = \frac{k_\mathrm{V}\Delta T_w}{e\mathcal{L}} \tag{6.1}$$

Neglecting the momentum variation and considering the equilibrium of the buoyancy and the shear stresses, the force balance reads:

$$\eta_\mathrm{V}\frac{\overline{u}}{e} = (\rho_\mathrm{L} - \rho_\mathrm{V})ge \tag{6.2}$$

Solving the resulting differential equation leads to a film profile that scales in a power 1/4 with the vertical coordinate:

$$e = \left(\frac{4\eta_\mathrm{V} k_\mathrm{V}\Delta T_w}{3\rho_\mathrm{V}(\rho_\mathrm{L} - \rho_\mathrm{L})g\mathcal{L}}z\right)^{1/4} \tag{6.3}$$

The mean vapour velocity $\overline{u}$ can then be recovered and scales in a power 2 with the thickness of the vapour film.

We can also integrate this heat flux over a height H. It allows to recover an estimation of the vertical film boiling heat flux in saturated conditions:

$$q_{w\mathrm{S}} = \left(\frac{4}{3}\right)^{3/4}\left(\frac{\rho_\mathrm{V}(\rho_\mathrm{L} - \rho_\mathrm{L})g\mathcal{L}k_\mathrm{V}^3\Delta T_w^3}{\eta_\mathrm{V} H}\right)^{1/4} \tag{6.4}$$

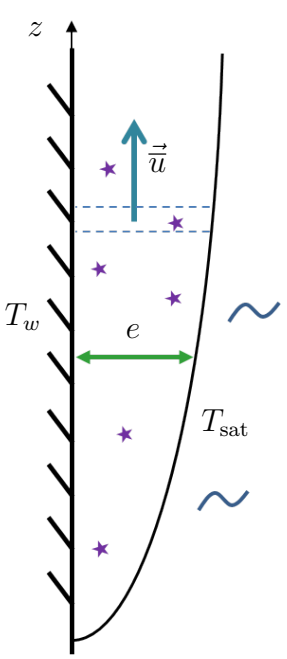

(a) Description of the Boundary Layer vapour film. Buoyancy effects make the vapour rise. It is limited by internal viscous forces. The layer thickness increases as vaporisation feeds the vapour film.

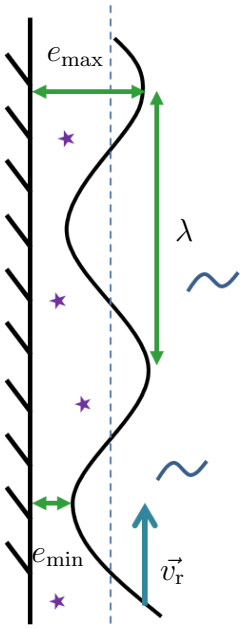

(b) General description of the vertical film waves. Waves are assumed to be periodic with a wavelength λ and a phase velocity $\vec{v_r}$. Zones of minimum amplitudes e_{min} are the "valleys" and areas of maximum amplitude e_{max} are the peaks.

Figure 6.2: Diagrams of the laminar and wavy vapour films.

We recover a power 3/4 on the overheating, that is consistent with the correlations presented in Section 1.2.3.5.

To account for subcooling effects, a first simple consideration is the addition of a constant liquid side flux q_∞ to the energy balance at the interface. The new mass balance equation then reads:

$$\frac{\mathrm{d}\rho_{\mathrm{V}} e\overline{u}}{\mathrm{d}z} = \frac{1}{\mathcal{L}}\left[\frac{k_{\mathrm{V}}\Delta T_w}{e} - q_\infty\right] \tag{6.5}$$

The resulting non linear differential equation is not trivial to solve, but can be approximated using a function that scales with $z^{1/4}$ for low values of z where $k_{\mathrm{V}}\Delta T/e >> q_\infty$, and as a linear function of q_∞ for high values of z where $e \sim k_{\mathrm{V}}\Delta T/q_\infty$. The main point is then to estimate q_∞, and will be discussed further.

Computing values of the film thickness predicted by the BL model (6.3) at mid height and at the top of the heater for $\Delta T_w = 200\,^{\circ}\mathrm{C}$ and $\Delta T_w = 300\,^{\circ}\mathrm{C}$ leads to

values gathered in Table 6.1. This also leads to velocities inside the vapour layer of order $\simeq 10\,\mathrm{m\,s^{-1}}$.

	e (mm) from BL model (6.4)		$e_{\max}/2$ (mm) from [61]
	$z = 50\,\mathrm{mm}$	$z = 103\,\mathrm{mm}$	(saturation)
ΔT_w=200 °C	0.12	0.15	5.2
ΔT_w=300 °C	0.14	0.17	6.8

Table 6.1: Film vapour thickness comparison between the Boundary Layer model and experimental values from [61].

We now consider the results of Vijaykumar et al. [61, 57]. Their first conclusion is that whatever the configuration (in the range of their experimental setup), the film is always wavy as shown in Figure 6.3. They named valleys the areas of minimum thickness, and peaks the areas of maximum thickness. The laminar representation does not match these experimental observations.

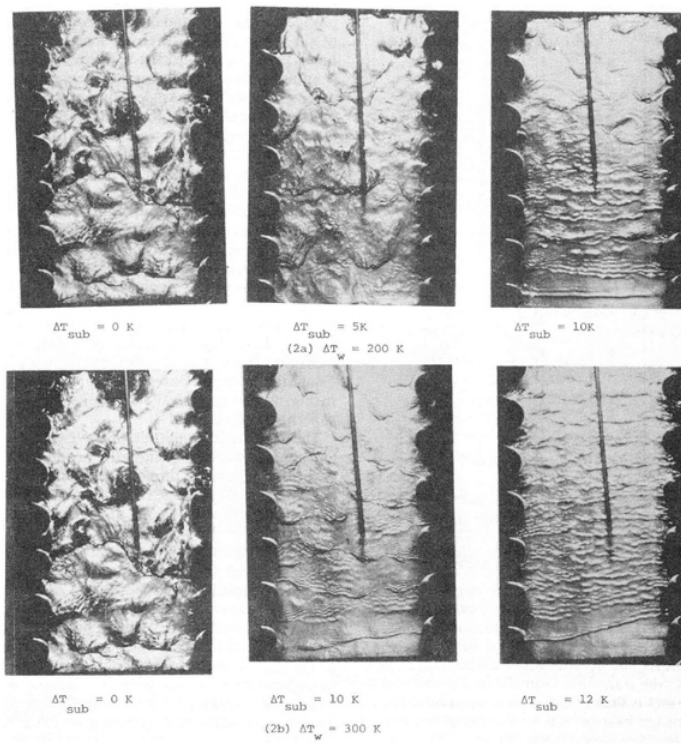

Figure 6.3: Frontal views of the vapour film at different temperature conditions (pictures extracted from [61]). For low subcooling waves are not organised and have forms of bulges. For high subcooling, wave fronts appear and amplitudes are smaller.

A better global description of the film was proposed by the authors through three parameters: the wavelength λ, the vertical phase velocity or rising velocity v_r and the maximum thickness e_{max}. We added another parameter: the minimum thickness e_{min}. Theses parameters are described in Figure 6.2b. Figure 6.4 confirms this description as waves are close to be periodic for low or high subcooling and seem not to vary with the height. The phase velocity is spatially and temporally constant as shown in Figure 6.4a. However the profiles did not always exhibit simple sinusoidal shapes, as shown in Figure 6.4b where large and flat valleys can be observed. Another important point is that on the valleys, the liquid vapour interface was very close to the wall, with minimum thicknesses much lower that maximum thicknesses.

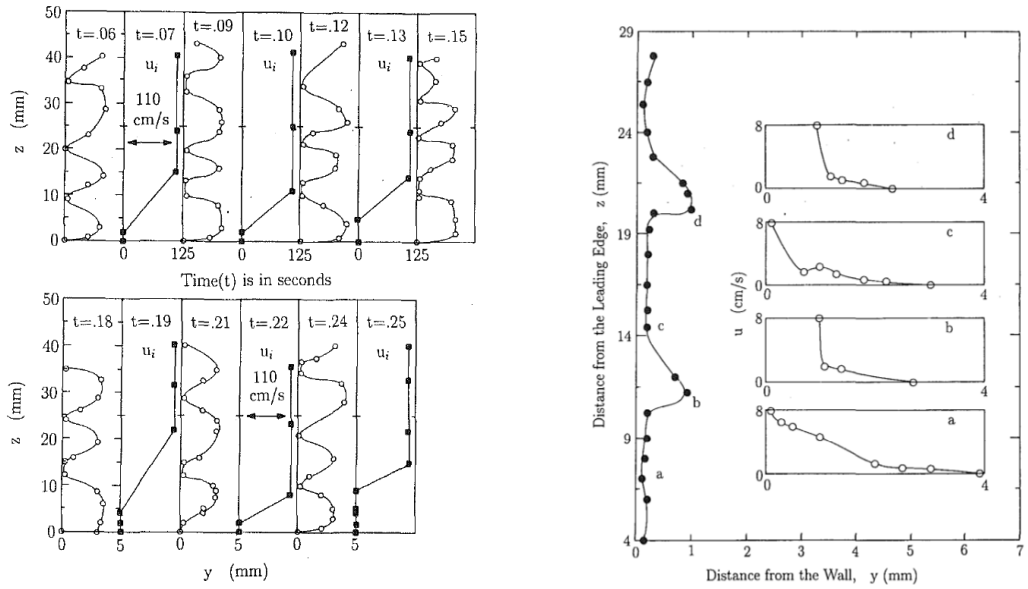

(a) Wave profile and phase velocity over time for ΔT_w=200 K and ΔT_∞=1.5 K.

(b) Wave profile and tangent liquid velocity profiles for ΔT_w=207 K and ΔT_∞=6.7 K

Figure 6.4: Experimental observations of the hydrodynamics of the vapour film extracted from [61, 57]. Waves are close to be periodic. The shear stress created by the vapour waves leads to a momentum diffusion inside the liquid.

In the range of the experiments, authors found that λ was around $2-20$ mm, e_{max} around $0.3-10$ mm and v_r around $0.01-3\,m\,s^{-1}$. In particular, the experimental values obtained for the saturated case are compared with the BL model in Table 6.1, and are two order of magnitude larger. We can conclude that the instabilities that create the waves on the interface increase the mean film thickness. This conclusion is confirmed in [137].

The only area where the boundary profile holds is at the bottom of the heater. Vijaykumar et al. [61] observed that this is the main area of generation of vapour that rises upwards before shaping itself in waves. The BL model can still be somehow relevant as it allows a first order solution on which more developed theories have been based. For example, [136, 137] proposed a model in which valleys are modeled with a BL.

Important features

- In vertical film boiling, the vapour film is always wavy. The wave parameters as the amplitude, wavelength and phase velocity are not changing much with the height.
- A model with a Boundary Layer approach allows to draft a first estimation of heat fluxes inside the film. However kinematic parameters are not predicted by this model as such.

6.2.3 Effect of subcooling: experimental results and interpretations

We recall that the subcooling is defined as the difference between the saturation temperature of the fluid and the temperature of the fluid far from the interface: $\Delta T_\infty = T_{\text{sat}} - T_\infty$. Vijaykumar et al. [61] observed that the influence of the subcooling is important regarding the film's hydrodynamics. The larger the subcooling, the smaller the waves' amplitude and wavelength, and the slower their rising velocity. Experimental values of velocities, wavelengths and wave amplitudes versus subcooling are plotted in Figure 6.5. From the saturated case to the 10–15 K subcooling configurations, all quantities are reduced by one order of magnitude. This shows how sensitive these quantities are to subcooling.

We can explain this tendency by the action of heat transfer from the liquid side q_∞. At saturation or for very low subcooling, all the heat removed from the heater is used for vaporization. Large amounts of vapour are created due to the intense heat transfer, leading to long and large bulges. Whereas for higher subcooling, a significant part of the heat is used to warm up the liquid. This reduces the amount of vapour to evacuate upwards, as well as the size of the bulges. Also, as the size of vapour layer is correlated with its rising velocity (see for example the work of Landel et al. [138]), smaller bulges have smaller rising velocities.

Vijaykumar et al. [61] showed that two different hydrodynamic regimes exist depending on the degree of subcooling. They first named a "3D" regime at saturation or for very low subcooling, shown on the left-hand-side of Figure 6.3, and also a "2D" regime for higher degrees of subcooling, shown on the right-hand-side

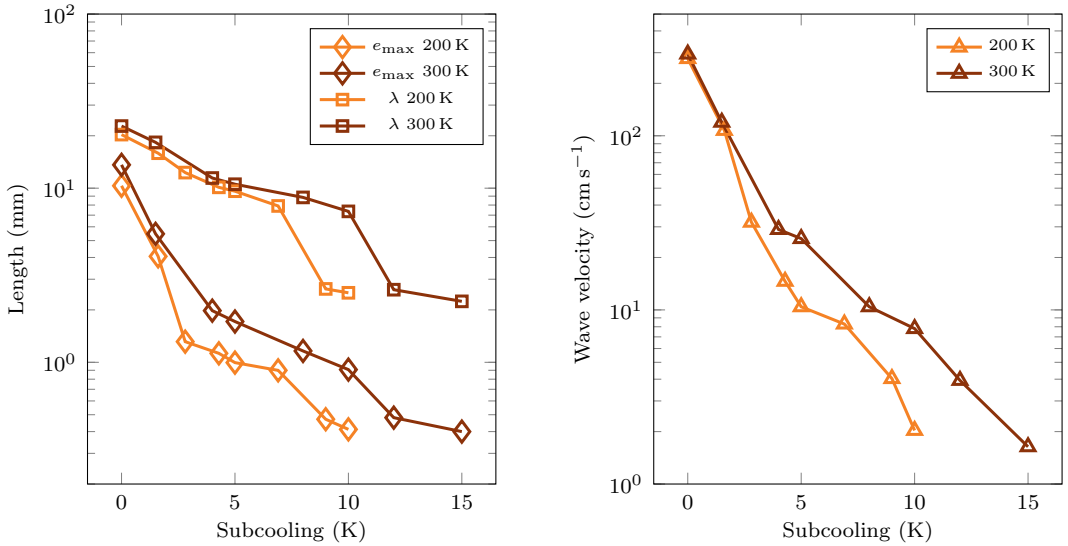

(a) Wave maximum amplitude and wavelength

(b) Wave rising velocity.

Figure 6.5: Hydrodynamic results of Vijaykumar et al. [61].

of Figure 6.3. In the 3D regime, waves are distributed over the heater with shapes of dunes of large amplitude and wavelength, and their distribution along the surface is quite random. The 2D regime is composed by regular waves of smaller amplitude and wavelength, and the wave front is horizontal.

The 2D waves are located a few centimeters above the bottom of the heater after reaching a steady regime, while their amplitude, wavelength and phase velocity do not change while rising upwards. The authors proposed that a vaporization–condensation cycle is then reached. Basically, this regime was explained as follows. At the valley, where the liquid is a little warmed up and close to the wall, the balance of energy at the interface is positive, leading to vaporization. However, at the peaks, the gradient inside the vapour is smaller. Furthermore, the isotherms in the liquid are narrowed, as the vapour penetrates the liquid domain, leading to a higher liquid side heat flux. The balance of energy at the interface then becomes negative, leading to condensation. This mechanisms is summarized in Figure 6.6a. The condition of appearance of the steady regime is the balance of flux between the heat flux from the heater q_w, and the liquid side heat flux q_∞. No vapour should indeed be created to maintain constant proportions of the waves, provided that the vapour velocity inside the film does not change.

Besides, from the available pictures of [61, 57], it seems that the value of e_{min} does not change much regarding the subcooling and the overheating, and are measured to be around 0.1 mm. As e_{max} decreases, the difference between e_{max} and e_{min} is reduced

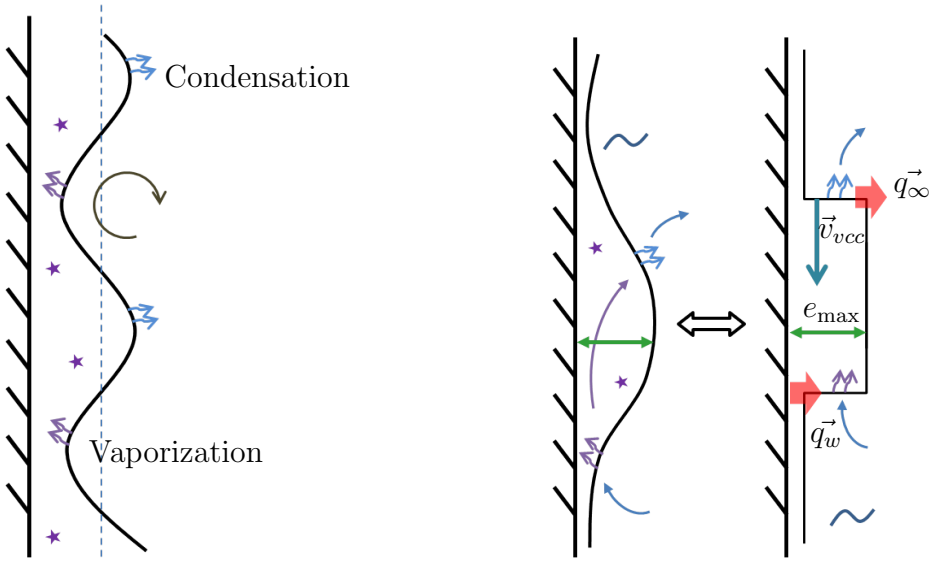

(a) Description of the vaporization–condensation cycle. The liquid vaporise in the valleys of the wave, where heat fluxes inside the vapour are very intense. Vapour condenses at the top of the bulges where vapour heat fluxes are moderate.

(b) Model of the vaporization–condensation cycle on a bulge. It is assumed that all the fluid particles vaporise and condensate in the vertical direction.

Figure 6.6: Schematic description and model of the vaporization–condensation cycle.

with the subcooling: the film got thinner and flatter. From these conclusions, we can set forth the hypothesis that the Boundary Layer model is more relevant for high enough subcooling, providing that this latter parameter is taken into account.

Important features

- Subcooling strongly reduces the wavelength and the amplitude of the vapour waves. It also reduces the phase velocity.

- At low subcooling, waves are 3D and organised in bulges. At high subcooling, waves are 2D and organised in horizontal oscillations. This 2D regime seems to be close to a boundary layer regime.

- At high subcooling, waves experience a vaporisation/condensation cycle.

6.2.4 Interfacial dynamics as a rising vapour bulge

We tried to assess the mechanisms at play in the wave formation and dynamics that are assumed to be responsible for high convection inside the liquid. Possible contributions are gravitational forces, surface tension forces, shear stresses, inertial effects and phase change in subcooling. As the Mach number is globally low (less than 10^{-2} if computed with v_r), pressure waves and compressibility effects due to phase change are assumed to be negligible.

We consider in this analysis only stabilised waves ahead of the bottom of the heater. In this configuration the net generation of vapour is negligible. The only phase change effect at play is the vaporisation–condensation cycle at large subcooling. It can be a potential phenomenon that acts against the rising of vapour bulges. If condensation occurs on the upper part of bulges, and vaporization on the lower part, this creates a phase velocity $\vec{v}_{vcc}$ opposed to $\vec{v_\mathrm{r}}$. A model is proposed to estimate the magnitude of $\vec{v}_{vcc}$, as shown in Figure 6.6b. We consider that all the heat is first converted into vapour, and then released into the liquid through condensation. This assumption yields on a perfect heat exchange that is conditioned by the fact that the steady state is reached and that locally, we have $q_w = q_\infty$. The amount of heat over a bulge of width L is $q_w L\lambda$. Then it is equal to the vaporisation rate $\mathcal{L}\dot{m}Le_\mathrm{max}$. With the relation $v_{vcc} = \dot{m}/\rho_\mathrm{L}$, the considered velocity reads:

$$v_{vcc} = \frac{q_w \lambda}{\rho_\mathrm{L} \mathcal{L} e_\mathrm{max}} \tag{6.6}$$

The influence of the vaporisation–condensation cycle can be assessed by computing the order of magnitude of v_{vcc} with values of $\vec{v_\mathrm{r}}$. For heat fluxes q_w of around $10^4\,\mathrm{W\,m^{-2}}$ and a ratio λ/e_max of around 10, the order of magnitude of v_{vcc} is then $10^{-4}\,\mathrm{m\,s^{-1}}$, which is two orders of magnitude lower than the minimum experimental values of $\vec{v_\mathrm{r}}$ measured by Vijaykumar et al [61]. We can conclude that the contribution of the vaporization–condensation cycle does not impact the liquid velocity as such. It can however affect more the vapour velocity as the vapour velocity resulting from this phase change scales in $\dot{m}/\rho_\mathrm{V}$.

Considering the wavelength, a first approach is to compare experimental wavelengths with theoretical values from the linear theory. Sherman calculated a wavelength λ_KH using linear stability analysis for the Kelvin Helmoltz instability theory with a finite film thickness. Surface tension was not taken into account[139]. This lead to a complex dispersion relation that needed to be solved numerically. We did this computation with the data of the experiment of Vijaykumar et al. [57]. It is plotted in Figure 6.7 along with the results of [61].

The model of Sherman [139] succeeds for the saturated case as well as for high subcoolings. This means that the mechanism of formation of the wave and thus the wavelength values might be mostly driven by the shear stress at the interface

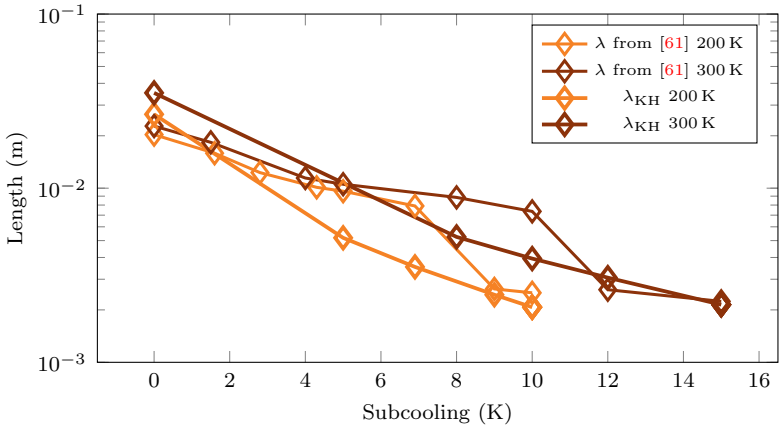

Figure 6.7: Comparision of experimental wavelengths λ [61] with the most dangerous wavelengths λ_{KH} in regards to the Kelvin–Helmholtz instability theories of [139].

from the vapour side. Jouhara et al. [24] confirm that ripples are due to Kelvin–Helmholtz instabilities, and that it is mostly relevant for high enough subcooling, where the interface is stabilized. Authors also mentioned that ripples are key features to consider for a proper modeling of heat transfers. This observation also leads to the conclusion that surface tensions effects do not seem to be dominant.

Regarding the mechanisms that control the phase velocity, we compared the drag stress τ acting on the vapour bulge from the liquid side with the equivalent stress related to buoyancy σ_{B}. The order of magnitude of the drag force was taken from the estimation of Vijaykumar et al. [61]:

$$\tau \sim 0.55 \rho_{\mathrm{L}} v_{\mathrm{r}}^2 \mathrm{Re}^{-0.65} \tag{6.7}$$

that is valid at least for the range of values of the experiments, with the Reynolds number being computed for v_{r} and $e_{\max}$.

The main force acting on the vapour film with a positive work is the buoyancy due to hydrostatic pressure inside the liquid phase, whose value for a 3D bulge of wavelength λ can be approximated as $(\rho_{\mathrm{L}} - \rho_{\mathrm{V}}) g \pi \lambda^2 e_{\max}/8$. For a 2D bulge of width l, this reads $(\rho_{\mathrm{L}} - \rho_{\mathrm{V}}) g l \lambda e_{\max}/2$. The equivalent surface force acting on the bulge to make it rise can be approximated in both configuration by: $(\rho_{\mathrm{L}} - \rho_{\mathrm{V}}) g e_{\max}/2$. In the same idea as for the friction coefficient, a buoyancy coefficient can be build:

$$\sigma_{\mathrm{B}} = \frac{(\rho_{\mathrm{L}} - \rho_{\mathrm{V}}) g e_{\max}}{2} \tag{6.8}$$

The two terms are compared in Figure 6.8. Though the formula is only providing an order of magnitude, it seems that buoyancy is mainly dominant over the liquid drag. Thus another effect is limiting the wave rising. The only possibility seems to

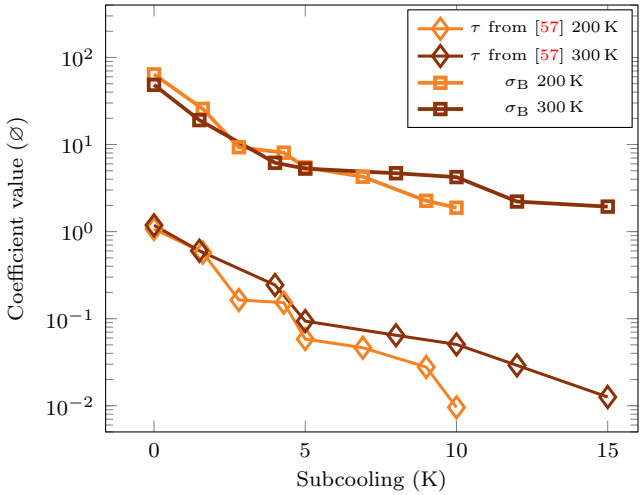

Figure 6.8: Comparison of shear stresses τ computed from the correlation of [57] with the equivalent stress of buoyancy forces σ_B.

be shear stress inside the vapour or inertial effects inside the liquid. This is all the more true in subcooled configurations where the flat film is closer to a Boundary Layer. We can conclude that the vapour film does not drag the liquid with it. Liquid particles close to the interface are supposedly moved by the vapour waves as a floater moves over the waves of a free surface. This entails a convection movement that is consistent with our analysis.

This conclusion agrees well with the observation of Vijaykumar et al. [61] who stressed the recirculation of water around the vapour waves. The recirculation is visible in Figure 6.9a, where streamlines follow the vapour profile. The Figure 6.9b shows normal velocity that demonstrates the circular motion of water near the vapour film. It provides large convection inside the liquid with circular liquid velocity cells. Jouhara et al. [24] confirm that ripples are key features to consider for a proper modeling of heat transfers inside the liquid.

Important features

- In a regime of stabilised vapour waves, the vaporisation condensation cycle does not affect the liquid velocity. But it improves the vapour velocity inside the film.

- The characteristic dimension of wavelengths is determined by Kelvin–Helmholtz instabilities computed for a finite vapour layer.

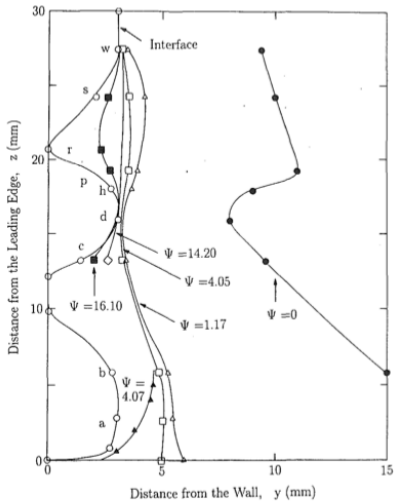

(a) Velocity trajectories in the liquid phase. Recirculations in the liquid are similar to those of a float on a free surface.

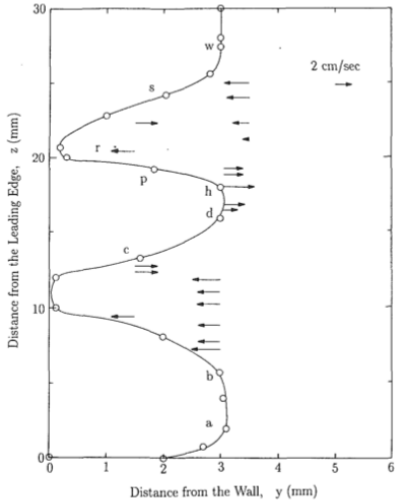

(b) Magnitude of the normal velocity component of liquid particles. This highlights the recirculation effects at play at the interface.

Figure 6.9: Experimental observations for ΔT_w=203 K and ΔT_∞=1.8 K extracted from [61, 57].

- Drag forces from the liquid side are not the major restrictors of the rising of vapour. Shear stresses inside the vapour film might be dominant at least at high subcooling.

- The vapour film does not drive the liquid upwards but creates a lot of convection at the interface and maybe some turbulence at higher subcooling.

6.2.5 Heat transfers deduced from experiments

Vijaykumar et al. [57] measured the value of q_w for overheatings of 150 °C, 200 °C and 300 °C, and for subcooling ranging from 0 to 15 °C. Experimental values measured at height $z = 50$ mm are plotted in Figure 6.10. What they concluded is that the hotter the heater, the lower the increase in heat flux. This is coherent with the order 3/4 of the boundary layer theory. This influence is amplified with a higher subcooling. Moreover, the higher the subcooling, the higher the heat flux. The heat flux $q_w(\Delta T_w, \Delta T_\infty)$ can be approximated with a good regression coefficient by the following linear law:

$$q_w(\mathrm{W\,m^{-2}}) = 8173 + 180\Delta T_w + 3904\Delta T_\infty \tag{6.9}$$

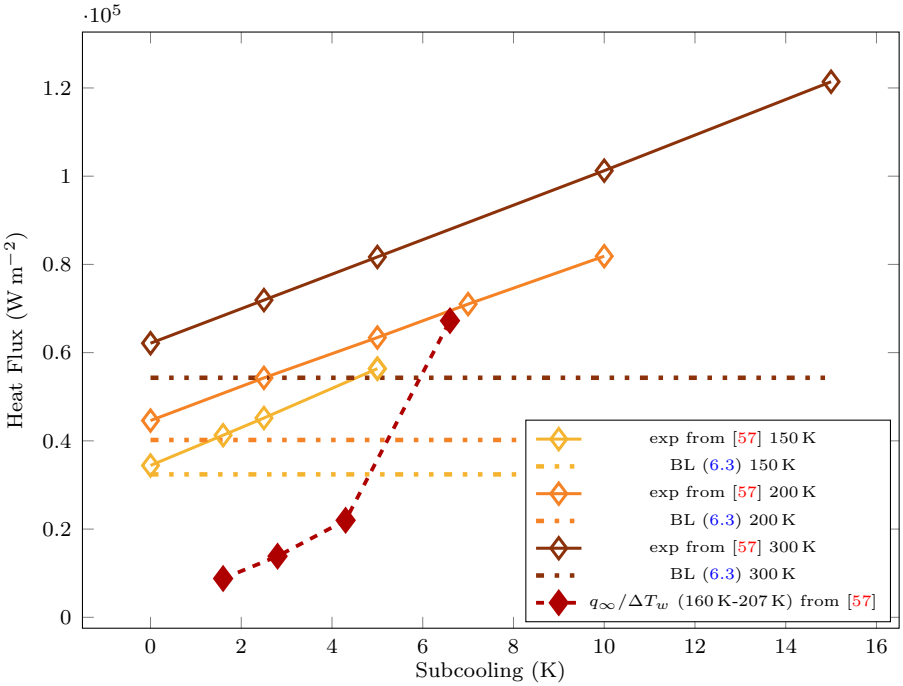

Figure 6.10: Heat fluxes measured by [57] compared with the heat fluxes predicted by the saturated Boundary Layer (BL) theory. Liquid side heat fluxes are also plotted to compare the portion of heat evacuated in the liquid.

Experimental values from [57] at height $z = 50\,\text{mm}$ are compared with the BL theory estimation and plotted in Figure 6.10. As expected, this model underestimates the heat flux and especially with subcooling. In practice, the wavy behavior of the vapour film adds a lot of convection to the system and create areas with a very locally thin vapor film. This appears to highly contribute to the heat transfer, as the conductive heat scales inversely with the vapour film thickness.

We previously speculated that for the steady regime to exist, the heat must be exclusively transferred into the liquid phase. Vijaykumar et al. [57] showed that q_∞ does not change much spatially. With that in mind the balance of flux between the heater and the liquid can be estimated by comparing experimental local q_w values with the mean value of q_∞ obtained over the heater for $\Delta T_w = 160\,\text{K}$–$200\,\text{K}$ (see Table 2 of [57]). The height $z = 50\,\text{mm}$ is assumed to be large enough to be located in the steady state part, where the conduction/convection system is in place. This comparison is plotted in Figure 6.10 and shows that the liquid side heat flux balances more with the wall heat flux at higher subcooling. This is coherent with the former conclusion that the steady regime mainly exists at high subcooling even though this conclusion is drawn from only one experimental point.

Important features

- Wall heat flux increases with the overheating and the subcooling. However the more heat, the less efficient the heat transfer. This is enhanced by subcooling.
- At high subcooling, heat transfer in the liquid tends to balance the wall heat flux.
- The wall heat transfer is not varying much with the height.

6.2.6 Heat transfer inside the vapour film: experiments and interpretations

The first question is to determine the principal mode of heat transfer inside the vapour film. Bui et al. [136] showed that for this temperature range, radiation was negligible. Vijaykumar et al. [57] estimated the conductive heat flux by integrating the formulation $k_V \Delta T_w / e$ over the heater with experimental values of e. These values are plotted in Figure 6.11 and compared with integrated measures of q_w. The estimated heat transfer from the local vapour film thickness is 25 % lower than the measured one, meaning an improvement inside the vapour film due to convective effects.

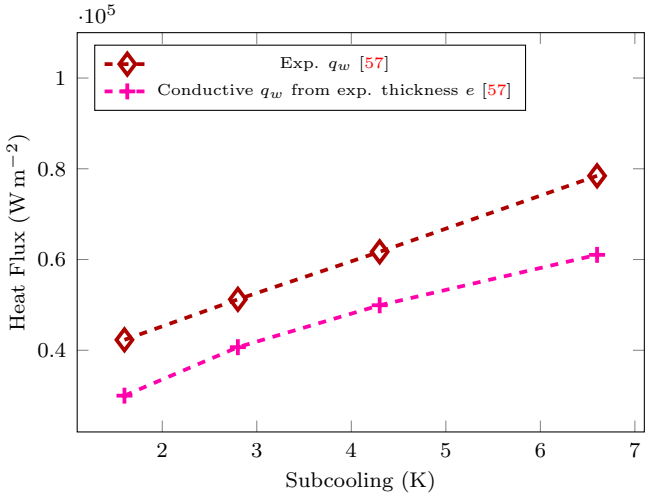

Figure 6.11: Estimated heat flux from conduction theory compared with experimental values (160 K–207 K) from [57]. The difference with the conduction estimation might be due to convective effects inside the vapour and radiation.

Otherwise, the difference between all the convection approaches and the experimental values may be due to moderate convective effects inside the vapour layer linked with the wavy nature of the interface. Jouhara et al. [24] mentioned that

at low subcooling, the very unstable nature of the film generates large convection inside the vapour film as well as solid–liquid contact that enhance significantly the heat transfer. For example, in the saturated condition for $\Delta T_w = 200\,\mathrm{K}$ with only conductive heat fluxes $k_\mathrm{V}\Delta T_w/e$, the equivalent mean film thickness e associated to the experimental value of $4.4{\times}10^4\,\mathrm{W\,m^{-2}}$ is around $10^{-4}\,\mathrm{m}$. Regarding the wavy profile of the film with $e_\mathrm{max} \simeq 10^{-2}\,\mathrm{m}$, this entails the existence of areas of great proximity between the liquid and the solid if not wetting.

Continuing with the question of the heat distribution, the heat used for vaporisation can be assessed by determining the volume of a vapour that is evacuated. Considering the width L of the plate and the sinusoidal profile:

$$e = e_\mathrm{min} + \frac{(e_\mathrm{max} - e_\mathrm{min})}{2}\left[1 + \cos\left(\frac{2\pi}{\lambda}(z - v_\mathrm{r}t)\right)\right] \tag{6.10}$$

the volume of a 2D vapour bulge reads:

$$\mathcal{V} = L\int_{z=0}^{z=\lambda} e(z,t)\,\mathrm{d}z = \frac{L(e_\mathrm{max} + e_\mathrm{min})\lambda}{2} \tag{6.11}$$

Thus, for $e_\mathrm{max} >> e_\mathrm{min}$ the energy extracted from the heater by a vapour bulge is:

$$\mathcal{E}_T = \frac{\rho_\mathrm{V} L e_\mathrm{max}\lambda\mathcal{L}}{2} \tag{6.12}$$

Considering that there is a bulge escaping from the top of the heater every $\tau_\mathrm{c} = \lambda/v_\mathrm{r}$, and scaling by the heater surface HL, the surface heat flux due to vapour creation reads:

$$q_\mathrm{Vc} = \frac{\rho_\mathrm{V} v_\mathrm{r} e_\mathrm{max}\mathcal{L}}{2H} \tag{6.13}$$

Values of q_Vc computed with the experimental results of [57] are plotted in Figure 6.12 and compared with local and mean experimental values of [57]. First of all, the higher the subcooling, and the less heat is used to create vapour, thus the more heat is transferred to warm up the liquid.

In saturated conditions, all the heat is almost fully converted through phase change. The rest of the heat is used to warm up the vapour. The latent heat of vaporization of the fluid $\mathcal{L}$ is one order of magnitude higher than $c_{\mathrm{p}\mathrm{V}}\Delta T_w$, and most of the vapour does not reach the solid temperature. Thus, considering the equality between the wall heat flux and the surface energy used to vaporise the vapour is a reasonable approximation: the flux from vapour creation should be very close to experimental values. However (6.13) overestimates the flux: e_max is an upper bound of the mean film thickness, and waves are 3D at low subcooling. Furthermore, Bui et al. [136] shew that bubble are leaving at 2/3 of the height of the heater in saturated cases, meaning a larger energy convected by vapour bubbles. Using inverse

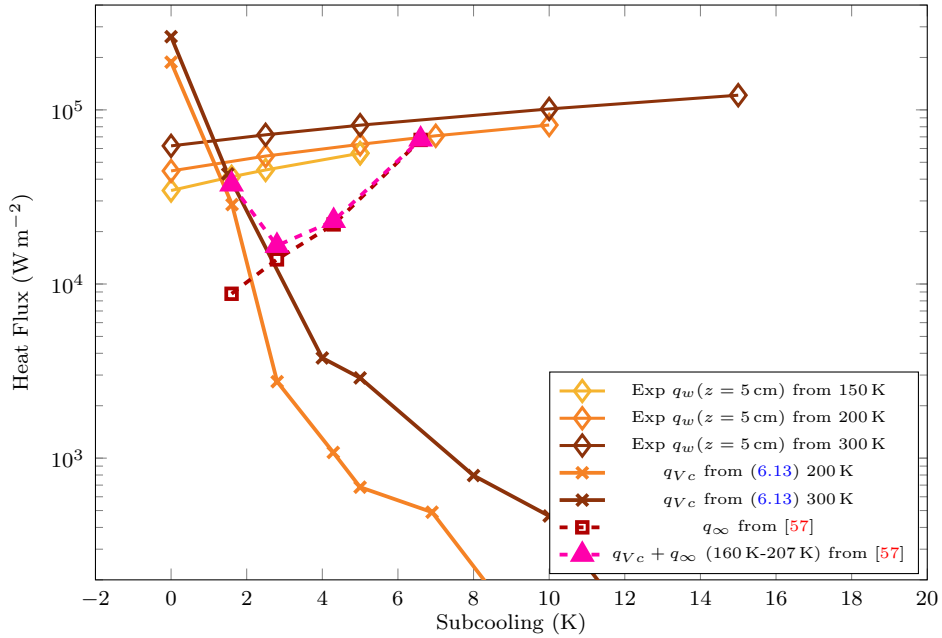

Figure 6.12: Estimation of the energy distribution. A portion of the heat flux should vaporise the liquid (q_{Vc}) while the other part should be used to warm up the liquid (q_∞). The addition of these two terms should balance measured heat fluxes, which is roughly the case.

computation, and finding the wave amplitude of a 2D shape (with $e_{\max} >> e_{\min}$) associated with the vapour mass flux that would match the equivalent heat flux leads to $e_{\max} = 2.7\,\text{mm}$ for $\Delta T_w = 200\,\text{K}$ and $e_{\max} = 2.9\,\text{mm}$ for $\Delta T_w = 300\,\text{K}$ in saturated conditions.

In subcooling conditions, if the assumption that vapour rises along with waves is relevant (some vapour might rise along the thin parts of the vapour film as claimed by Greitzer et al. [137]) then little energy is used for vapour creation, and the main factor of heat extraction is liquid warming up. We can add the value of estimated q_{Vc} with liquid side heat fluxes q_∞ from [57]. This leads to the same conclusion, as shown in Figure 6.12. If the steady state 2D regime is reached, meaning that q_w balances q_∞, then the energy supplied to create vapour comes from the few centimeters of the bottom before the steady state regime. Another conclusion is that while increasing the subcooling, the improvement of the heat transfer is simply due to conduction in the liquid. We can notice that the predicted heat flux from this addition is underestimated for around $\Delta T_\infty = 3\,\text{K}$. It may be due to an underestimation of internal vapour mass fluxes, or to an underestimation of experimental measurements.

Important features

- Heat transfer in the vapour film is done by conduction within 25% error. The rest shall be convective effects.
- Most of the heat transfer is concentrated around the thinner parts of the film, in the valley between the vapour bulges. Theses layers are at least two orders of magnitude thinner than the wave amplitude.
- In very low subcooling, most of the heat is used to vaporise the liquid. In higher subcooling, most of the heat is used to warm up the liquid.

6.2.7 Heat transfer in the liquid: experiments and interpretations

We saw in Section 3.2.1 that the Grashof number in the liquid is in general large, meaning important free convection dominance inside the liquid. We can estimate with scaling laws the associated convective velocity by balancing the buoyancy force due to thermal dilatation with inertial terms:

$$\rho_{\mathrm{L}} g \alpha_{\mathrm{TL}} \Delta T_{\infty} \sim \frac{\rho_{\mathrm{L}} u_{\mathrm{c}}^2}{L_{\mathrm{c}}} \tag{6.14}$$

This leads to a convection velocity of around

$$u_{\mathrm{c}} \sim \sqrt{L_{\mathrm{c}} g \alpha_{\mathrm{TL}} \Delta T_{\infty}} \tag{6.15}$$

Taking L_{c} as 0.1 m for a subcooling of 6.6 K, this leads to a velocity of $0.05\,\mathrm{m\,s^{-1}}$. At this order of magnitude, the velocity is organised in a Boundary Layer close to the hot surface (here the vapour liquid surface). We can combine this estimation of velocity with a BL analysis to recover the characteristic length of the boundary layer:

$$\delta \sim L_{\mathrm{c}} \mathrm{Re}^{-1/2} \tag{6.16}$$

This leads to a thickness of 0.5 mm, which leads to a conduction heat flux of $9000\,\mathrm{W\,m^{-2}}$ if the momentum BL is also the thermal BL. Compared to the experimental value of $67\,000\,\mathrm{W\,m^{-2}}$ of [57], this is negligible. The natural convection does not seem to be the main effect that improves the heat transfer between the liquid and the fluid. We notice that the diffusive thermal layer associated to such liquid side heat flux is around $k_{\mathrm{L}} \Delta T_{\infty} / \vec{q_{\infty}} \sim 6{\times}10^{-5}$ mm. This is very tiny, and thermal effects near the liquid vapour interface in the liquid are very sharp.

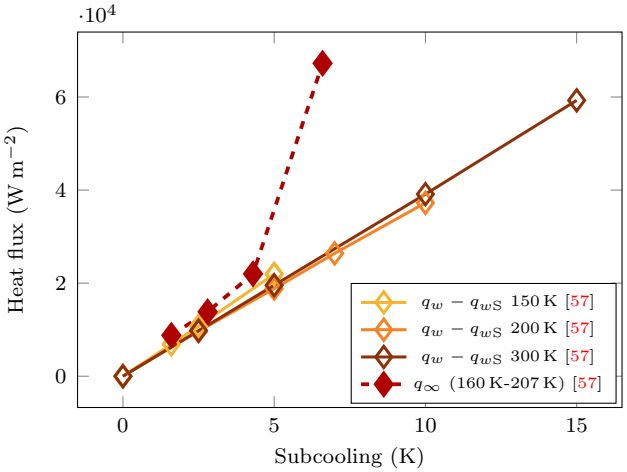

Figure 6.13: Visualisation of the difference between the total heat flux and the heat flux at saturation measured by [61]. These values are compared with the measured liquid side heat flux q_∞. The larger the subcooling and the larger the proportion of heat dedicated to warm up the liquid.

The global influence of subcooling on the heat flux can be assessed considering the difference of flux between subcooled and saturated conditions. At a given overheating ΔT_w, the difference $q_w - q_w(\Delta T_\infty = 0) = q_w - q_{wS}$ represents the part of heat flux added thanks to subcooling. This value is plotted in Figure 6.13.

All the curves at different overheating present a similar trend. It seems that the influence of subcooling could be a simple additive term from the saturated case $q_w(\Delta T_\infty = 0)$. This would corresponds to an additive contribution of the vaporization flux at saturation for a given overheating, and a conductive-convective flux to warm up the liquid independently of the overheating. On the liquid side, it can be modeled as a layer of liquid of constant thickness 0.2 mm with a temperature gradient scaling with ΔT_∞.

This analysis can be challenged with the values of liquid side heat fluxes obtained experimentally [57]. If the only influence of subcooling is the heating of a layer of fluid that is colder, then the liquid side heat flux should scale with ΔT_∞. This is the case for low subcooling, but quickly this appears to be wrong, especially for the last point at $\Delta T_w = 160$ K and $\Delta T_\infty = 6.6$ K. Besides, this seems to be correlated with the transition from 3D to 2D regime when the vaporization–condensation regime takes the lead.

This is confirmed by the tendency highlighted by Figure 6.12. The subcooling heat flux is progressively dominant in regards to the energy used for vaporisation. At some point, it can even get into the transition film boiling mode for higher subcooling, meaning that the creation of vapour is not maintained enough. It lead

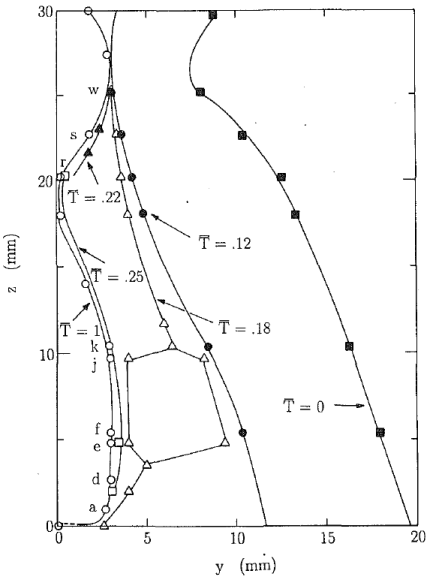

Figure 6.14: Isotherms extracted from [57] for ΔT_w=160 K and ΔT_∞=1.6 K. Thermal layers are very tiny that lead to intense heat fluxes.

Meduri et al. [62] to design an assessment of the Minimum Heat Flux point: a point at which all the heat is used to warm up the liquid, and vapour is fully condensed.

The improvement of the liquid side heat transfer suggests that the convection created by the vapour waves increases with the subcooling. The contraction of the streamlines on the peaks and a dilatation of the streamlines on the valleys observed by Vijaykumar et al. [61] and shown in Figure 6.9a is a marker of this convection. It leads to very stiff temperature gradients in the liquid, as shown in Figure 6.14. The strong increase of q_∞ shows that this effect is improved in higher subcooling. However, if we compute the Péclet number with the wave amplitude $e_{\max}$ (believed to be the main driver of convection in the liquid) and with the normal velocity computed by Vijaykumar et al. [57] u_n (scaling as around $10^{-2}\,\mathrm{m\,s^{-1}}$), we get a value that decrease from around 1000 to 100 with the subcooling from 1.6 to 6.6 K. This stresses the fact that convection is less dominant at higher subcooling, which is contradictory with experimental measurements of q_∞. This is a paradoxical point that we do not fully understand. One hypothesis that is coherent with conclusions of Section 6.2.6 is that the experimental liquid side heat fluxes are underestimated at low subcooling. This is plausible as the hydrodynamics is intense and may make the measurements harder.

Important features

- The effect of natural convection is negligible compared to the order of magnitude of heat transfer in the liquid.
- An additive law between the saturated case and the effect of subcooling seems to exist globally. However, the heat transfer in the liquid is strongly improved for higher subcooling at the expense of the creation of vapour.
- Strong convective effects close to the liquid vapour side are present and improved in higher subcooling.

6.2.8 Main conclusions

We summarize the main conclusions of this first study:

- The vapour film is always wavy. At low subcooling, waves are 3D and organised in bulges. At high subcooling, waves are 2D, smoothed, and organised in horizontal oscillations. It gets closer to a Boundary Layer form.
- The main term conditioning the film wavelength is the shear stress inside the vapour layer. The rising velocity and thickness are conditioned by buoyancy versus internal shear stress and maybe liquid inertia in low subcooling, and buoyancy versus internal shear stress in higher subcooling. All of this is obviously controlled by the amount of heat provided by the heater and by the amount of heat absorbed by the liquid.
- The wall heat flux increases with the overheating and the subcooling. However the more heat, the less efficient the heat transfer as the ratio $q_w/\Delta T_w$ decreases. This is enhanced by subcooling. At high subcooling, heat fluxes in the liquid tend to the wall heat flux.
- In the range of the experimental data, subcooling can be considered as an additive term regarding the saturated case. In practice, the higher the subcooling, the less vapour is created, and the more the liquid is being heated as the film enters a vaporisation condensation cycle.
- The heat transfer inside the vapour is close to being conductive, whereas the liquid side heat transfer is highly convective. The liquid is not dragged by the vapour film, and natural convection is not dominant. But local recirculations and turbulence may be at play very close to the liquid vapour interface.
- Most of the heat transfer is concentrated around the thinner parts of the film, in the valley between the vapour bulges. Theses layer are at least two orders of magnitude thinner than the wave amplitude.

6.3 Numerical simulation

The analysis of the experimental observations draw two main difficulties. First of all, the great discrepancy in the characteristic film thicknesses. Larger wave amplitude scale up to 10^{-2} m in saturated cases whereas areas where the heat flux is important show very thin vapour films (at most 10^{-4} m). This means that to properly simulate the film, such tiny length scale should be taken into account in a hydrodynamic system two orders of magnitude larger. Furthermore, all the vapour system evolves in a liquid pool which is one order of magnitude higher. In the liquid phases, diffusive thermal layers associated to high subcooling heat fluxes are also associated to small lengths (also around 10^{-4} m). This gap in characteristic scale is very restrictive for the simulations, even with remeshing techniques. Secondly, the hydrodynamics is very non deterministic with a lot of recirculations in the liquid and a wavy behavior of the vapour film with small characteristic times.

These observations confirm the conclusion of the previous chapter that the simulations of all the scales of film boiling remains a big challenge. The direct simulation of all the physical effects at play in 3D would require an important amount of computational resources with lot of elements, small time steps and a very stable numerical scheme. As this was out of the scope of this work, we pursued with our 0D modelling consisting in using an augmented viscosity in the vapour as shown in the previous chapter. The idea is again to determine how to compensate this approach to preserve the value of interest which is the mean heat flux. We studied two asymptotic scenarios: the saturated case, and the high subcooled case.

In both studies, the influence of radiation heat fluxes was neglected. Depending on the nature of the surface, radiation can count up to 15% of the wall heat flux (case for of a black body), but metal surfaces generally have moderate emissivities. For these range of temperatures, it was shown to have a moderate impact on the thermics of the system (see Section 5.4.2.2 as well as the conclusions of [136]).

6.3.1 The saturated configuration

6.3.1.1 Modeling approach

The saturated case avoids the consideration of the heat transfer inside the liquid phase. The heat flux is mostly used to vaporise the liquid. However, the main difficulty is the hydrodynamics that contains many scales and high velocities. The representation of the flow with an augmented viscosity was expected to kill the smaller scales and to lead to a more stable film with larger 2D waves. The objective was to determine whether this approach allows to recover the solid heat flux as well as some other features such as the wavelength, the rising velocity or the film thickness.

We consider the example of the saturated case with an overheating ΔT_w of 200 K with a measured heat transfer at mid-height q_w of around 44 000 W m^{-2}. In the following, we assume that this value is consistent with the overall heat flux. This an acceptable assumption thanks to the conclusions of Section 6.2.5.

The value of the augmented viscosity was determined thanks to an equivalent Boundary Layer profile, as shown in Figure 6.15. We set e_{eq}, $\overline{u}_{\text{eq}}$ and η_{eq} to recover an amount of vaporized liquid equivalent to the one of the experiment.

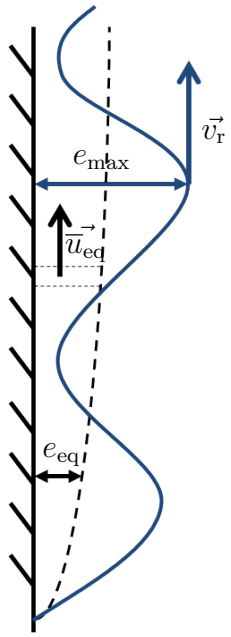

Figure 6.15: The equivalent Boundary Layer profile. e_{eq} and $\overline{u}_{eq}$ are targeted to conserve the mass flux.

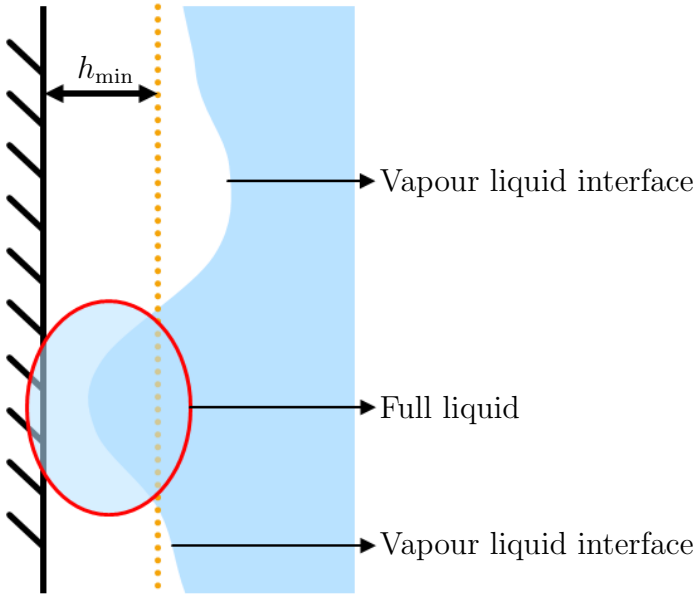

Figure 6.16: Description of the wetting model. If the interface is closer to the solid than h_{min}, then the local thermal quantities are set to those of the liquid. This also impact the conductivity that is used to compute the heat flux jump.

As we aimed to simulate an equivalent behavior of the vapour layer, we tried to keep the same vapour velocity. In the experiment, the vapour velocity is assumed to be equal to the wave rising velocity, as vapour bulks seem to be quite independent of each other. Thus the vapour velocity $\overline{u}$ is assumed to be v_{r} which is 3 m s^{-1} in this configuration. The same value has been considered for the equivalent velocity $\overline{u}_{\text{eq}}$.

To recover an equivalent vapour flux, the product of the vapour rising velocity with the mean film thickness should be constant. Thus e_{eq} has been set to respect this equality. We saw in Section 6.2.6 with the evaluation of q_{Vc} that our approximation with a sinusoidal profile of 3D vapour waves overestimated the vapour flux. We

computed approximately a factor 10 between the experimental and estimated values of q_{Vc}, that is directly linked with $e_{\max}$. Thus $e_{\max}/2$ is not a good approximation of the mean thickness. A better estimation of the equivalent vapour mean thickness is around 1 mm. This value has been taken for e_{eq}.

We then assessed the value of the augmented viscosity by the balance of the shear stress in the vapour film with the hydrostatic pressure for such equivalent values. We recall that the shear stress gradient scales as $\eta_{\mathrm{eq}}\overline{u}_{\mathrm{eq}}/(e_{\mathrm{eq}})^2$, and the pressure gradient as $\rho_{\mathrm{L}}g$. This leads to an equivalent viscosity:

$$\eta_{\mathrm{eq}} = \frac{\rho_{\mathrm{L}} g e_{\mathrm{eq}}^2}{\overline{u}_{\mathrm{eq}}} \tag{6.17}$$

Considering this expression with the order of magnitude taken above leads to a value $\eta_{\mathrm{eq}} = 3{\times}10^{-3}$ Pa s. This value was expected to respect the order of magnitude of the vapour created in saturated conditions, thus the mean heat flux. However, considering the boundary layer model (6.3), such viscosity was expected to lead to a layer approximately four times bigger, meaning a heat flux four times smaller. And the hydrodynamics to be modified with larger waves. Particularly, areas of small proximity where local heat fluxes are intense should be impacted. To account for this areas of small proximity without considering very small mesh sizes, we considered the following wetting model (see Figure 6.16): in areas where the vapour film is very thin, it is assumed to behave as if the liquid was wetting locally the film. Thus in the simulation, local values of thermal interface properties of the fluid will be forced to the liquid's ones whenever the film thickness is lower than the mesh size. This mode was justified by the observations of [24] who noticed transient wetting during vertical film boiling at low subcooling.

The offset on the numerical interface described in Section 5.4.1 was also implemented to a better precision on the vapour film thickness.

6.3.1.2 Numerical parameters

Computations were done for overheating values ΔT_w of 150 K, 200 K and 300 K. The computation domain was believed to reproduce the test bench of Vijaykumar et al. [57]. That is a box of 0.17 m by 0.213 m by 0.46 m with a solid plate of surface 0.063 m by 0.103 m (see Figure 6.17). The mesh was composed of 100 000 nodes and was refined at the interface up to a mesh size of $5{\times}10^{-4}$ m. The time step was set to 10^{-3} s.

Appart from the viscosity of vapour, the vapour conductivity was set to depend on the temperature (see Appendix E). Otherwise properties of the water vapour at $(T_{\mathrm{sat}}+T_w)/2$ were considered [89]. Properties of the liquid were set to those of water at T_{sat} [89]. Values are gathered in Table 6.2.

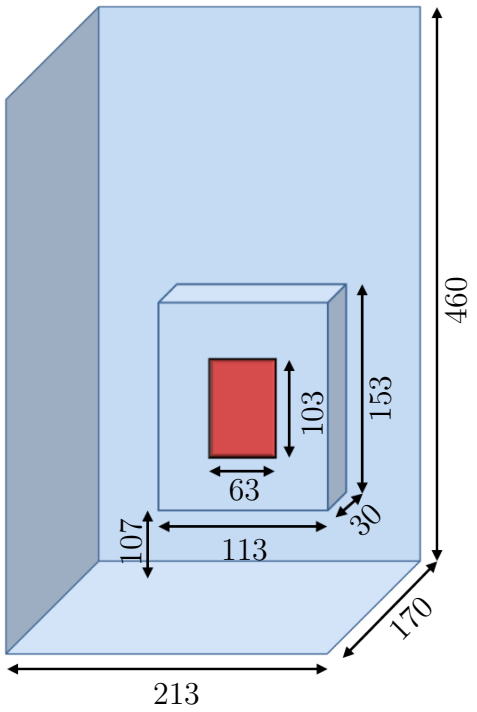

Figure 6.17: Schematic description of the computation domain for the vertical film boiling benchmark. Values of lengths are given in mm.

The interface was initialised with a vapour film thickness of 0.5 mm. As the interface was expected to undergo important displacements and velocities, the mesh was updated every two time steps and the Level Set was reinitialised with the same frequency.

6.3.1.3 Results

For every configuration, two seconds of physical time were simulated. Visualisation of the interface and mass transfer rate at the last increments of the simulations are shown in Figure 6.18. As expected, the proposed approach lead to larger and flatter

	ρ ($\mathrm{kg\,m^{-3}}$)	c_p ($\mathrm{J\,kg^{-1}\,K^{-1}}$)	k ($\mathrm{W\,m^{-1}\,K^{-1}}$)	η ($\mathrm{Pa\,s}$)	$\mathcal{L}$ ($\mathrm{J\,kg^{-1}}$)	γ_0 ($\mathrm{J\,m^{-2}}$)
Vapour	0.48	2030	$f(T)$	3×10^{-3}	2.257×10^{6}	0.059
Liquid	958	4216	0.679	2.80×10^{-4}		

Table 6.2: Physical properties of the considered fluids for the vertical film boiling benchmark.

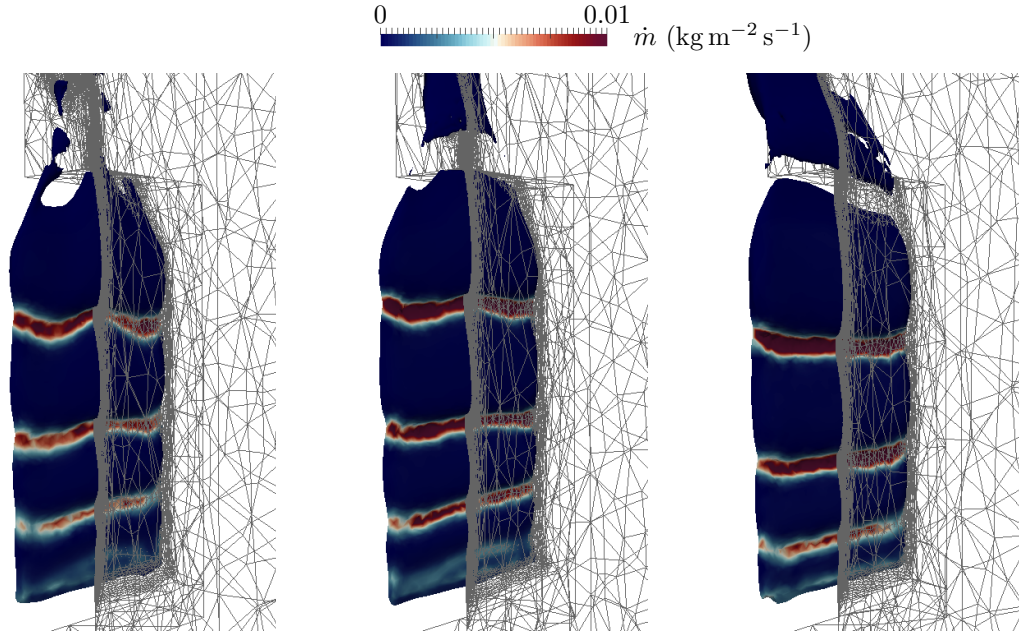

(a) $\Delta T_w = 150\,\mathrm{K}$ (b) $\Delta T_w = 200\,\mathrm{K}$ (c) $\Delta T_w = 300\,\mathrm{K}$

Figure 6.18: Visualisation of the liquid vapour interface at the last increment ($t = 2\,\mathrm{s}$) of the saturated vertical film boiling simulation for different overheatings.

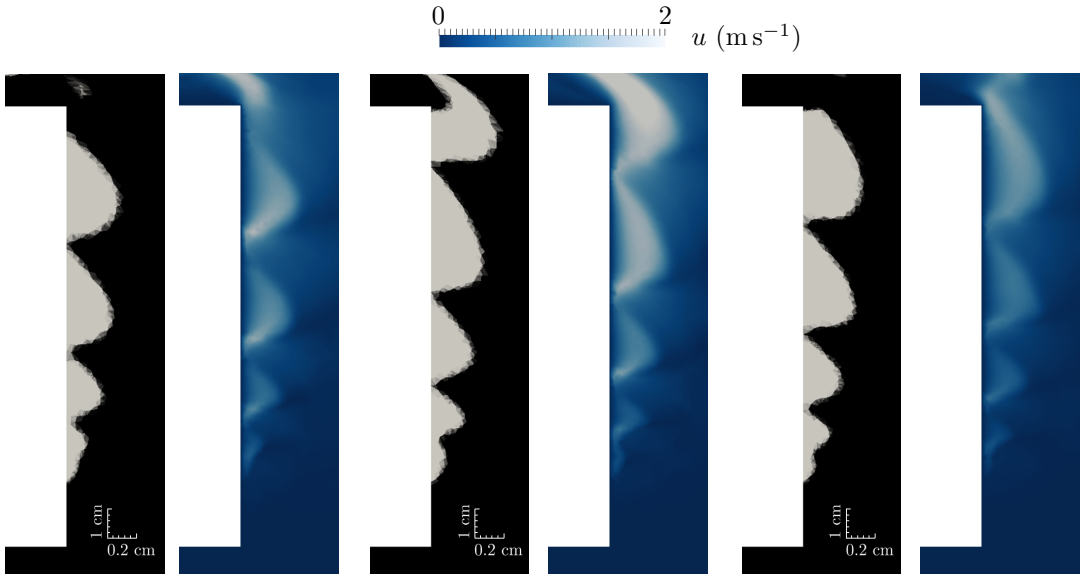

(a) $t = 1\,\mathrm{s}$ (b) $t = 1.5\,\mathrm{s}$ (c) $t = 2\,\mathrm{s}$

Figure 6.19: Visualisation of a cross section view of the vapour film and of the velocity magnitude for the saturated vertical film boiling simulation with $T_w = 200\,\mathrm{K}$ at different time steps. The figures are streched to highlight the waves.

waves with a 2D aspect. Vaporisation occurs the most at the wetting zones, in the valleys of the waves, which is also consistent. The waves were constantly growing and no fixed wavelength was observed. The aspect of the interface is not changing much regarding the overheating. Some tests with higher viscosities had been done and shew that the higher the vapour viscosity, and the flatter the film with larger and thicker waves.

In Figure 6.19 a cross section of the interface and a view of the velocity magnitude is plotted for different times for the $\Delta T_w = 200\,\mathrm{K}$ case. Waves are growing along the heater, fed by the vaporising liquid. The velocity is larger in the vapour phase than in water, which validates the fact that the liquid is not brought along by the vapour.

Values of maximum wave amplitude $e_{\max}$ and wave velocities v_r are compared with experimental values for overheating of 200 K and 300 K in Table 6.3. The mean vapour film thickness $\overline{e}$ is also given for illustration. As the simulated wavelength was not constant, no comparison could be made, but the wavelength was overall larger than the experimental ones. The maximum film thickness and the wave velocity are smaller than the experimental values. Such discrepancies are consistent with the approach with an augmented viscosity. The simulated mean thickness is around three times as big as the targeted one, but this is compensated by a smaller vapor velocity that is close to v_r.

	$e_{\max}$ (mm)		$\overline{e}$ (mm)	v_r ($\mathrm{m\,s^{-1}}$)	
	exp.	simu.		exp.	simu.
150 K	-	4	1.6	-	0.82
200 K	10	4.1	1.7	2.9	0.85
300 K	13	4.3	1.9	2.7	0.92

Table 6.3: Comparison of experimental and simulated hydrodynamic parameters.

Wall heat fluxes for every configurations are plotted in Figure 6.20. The steady state is reached as the mean value of q_w is constant after 0.5 s. This confirms that two seconds of simulation is sufficient.

Values of simulated heat fluxes q_w are compared with experimental values in Figure 6.21. The order of magnitude are respected, though the influence of the overheating is slightly underestimated as the value of q_w is around 20% smaller for $T_w = 300\,\mathrm{K}$. We can also assess the coherence of the simulation regarding the mass/energy conservation. In saturated conditions, the heat is only used to warm up the vapour and vaporise the liquid. We saw earlier that the first effect was energetically negligible in regard to vaporisation. We should then have an equivalence between the vapour top mass flux (see Figure 6.22) and the heat flux.

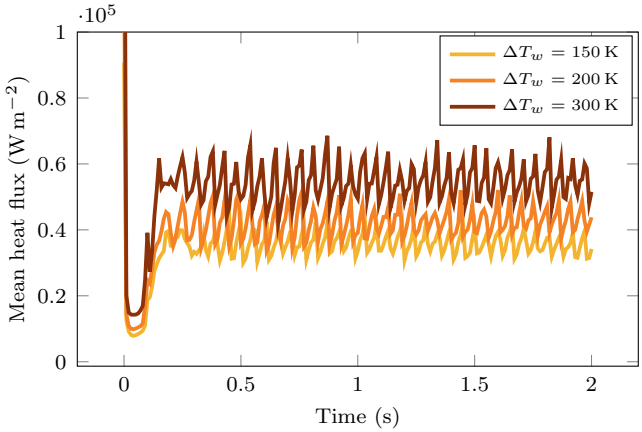

Figure 6.20: Wall heat flux over time for the saturated vertical film boiling simulation at different overheating. 1 s *is shown to be enough for the hydrodynamic steady state to be reached.*

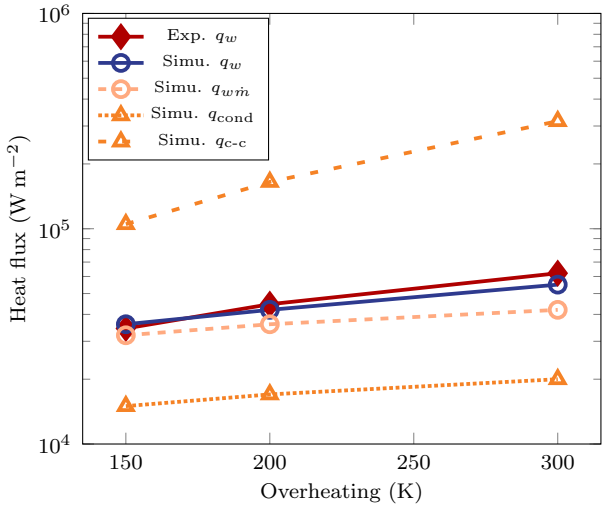

Figure 6.21: Comparison of experimental [57] and simulated wall heat fluxes of the saturated vertical film boiling case. Orders of magnitude and trends are respected between the simulation and the experiments. The evaluation from the mass flux leads to a moderate mass loss at high overheating. The conductive estimation understimates a lot the heat flux, as it does not take into account the wetting model, whereas the conductive-convective overestimates a lot the heat flux.

Writing H the height of the heater and L its length:

$$qHL \simeq \rho_{\text{V}} \vec{u}(z = H)\, \mathcal{L} L\, e(z = H) \tag{6.18}$$

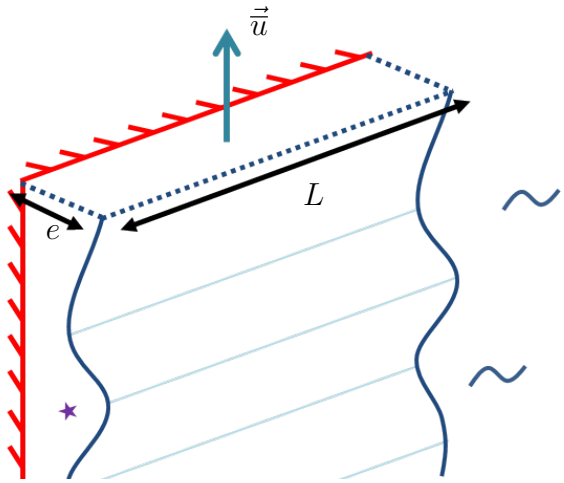

Figure 6.22: Description of the output vapour flux.

Thus, we can assess an equivalent heat flux:

$$q_{wm} \simeq \rho_{\mathrm{V}} \vec{\vec{u}}(z = H)\, \mathcal{L}\, \frac{e(z = H)}{H} \tag{6.19}$$

We computed this equivalent heat flux in the simulation. Results are also gathered in Figure 6.21. We can see that at low overheating, the mass/energy conservation was respected. However, at higher overheating, a loss of 20% was observed. The present method with the moderate amount of computational ressources shows some limits at higher mass transfer rates and velocities. Among other reasons, the present Level Set method approach does not guarantee a proper mass conservation. This bias gets worse with higher velocities, which is consistent with our observations. A smaller time step and mesh size could help reducing this mass loss, but this is beyond the scope of this work.

Though some work has to be done to improve the hydrodynamics model, such simple approach already provides good results and some main features of the flow which is satisfactory.

6.3.1.4 A posteriori estimations

As for the horizontal film boiling benchmark, we assessed the importance of mean conductive and convective effects in the simulation. This time the comparison is done on heat fluxes. The conductive heat flux is computed with the vapour film thickness:

$$q_{\mathrm{cond}} = \frac{1}{S} \int_S \frac{k_{\mathrm{V}} \Delta T_w}{e}\, \mathrm{d}S \tag{6.20}$$

with k_V taken at $(T_\mathrm{sat} + T_w)/2$. The conductive-convective heat flux is computed with the Péclet number:

$$q_\text{c-c} = \frac{1}{S}\int_S (1 + \mathrm{Pe})\frac{k_\mathrm{V}\Delta T_w}{e}\,\mathrm{d}S \tag{6.21}$$

where Pe is computed with:

$$\mathrm{Pe} = \frac{\rho_\mathrm{V} c_{\mathrm{p}\mathrm{V}} e\overline{u}}{k_\mathrm{V}} \tag{6.22}$$

and with the mean velocity estimated with a Poiseuille flow model thanks to the normal gradient at the solid interface.

$$\overline{u} = \left|\frac{\partial \vec{u}_t}{\partial \vec{n}}\right|_{\vec{x}\in w} \tag{6.23}$$

Results of this comparison are presented in Figure 6.21. We observed that the experimental value is framed by the two estimations, which is consistent: pure conduction is the worst case scenario, and the conductive-convective model is based on a strong assumption that any vapour particle is heated from T_sat to T_w. This does not take into account the already heated vapour from below. Observations of [57] lead to the conclusion that the heat transfer mode was mostly conductive, which is not the case in the simulation. This can be explained by the fact that the conductive estimation does not properly take into account the wetting model, as the film thickness never reaches zero in the simulation.

6.3.2 The subcooled configuration

6.3.2.1 Preliminary work: natural convection

Before working on the diphasic system, we assessed numerically the influence of the natural convection in the liquid. To do so, we solved in the liquid the monophasic incompressible Navier–Stokes equations coupled with the convection diffusion equation within the Boussinesq approximation. Taking ρ_L as the density of water at 100 °C the system reads:

$$\begin{cases} \vec{\nabla}\cdot\vec{u} = 0 & \text{(6.24a)} \\ \rho_\mathrm{L}\left(\dfrac{\partial\vec{u}}{\partial t} + (\vec{u}\cdot\vec{\nabla})\vec{u}\right) = -\vec{\nabla}p + \vec{\nabla}\cdot 2\eta\dot{\boldsymbol{\varepsilon}} + \rho_\mathrm{L}(1+\alpha_\mathrm{T}(T_\mathrm{sat}-T))\vec{g} & \text{(6.24b)} \\ \rho_\mathrm{L} c_{\mathrm{p}\mathrm{L}}\left(\dfrac{\mathrm{d}T}{\mathrm{d}t} + \left(\vec{u}\cdot\vec{\nabla}\right)T\right) = k_\mathrm{L}\Delta T & \text{(6.24c)} \end{cases}$$

The Boussinesq estimation was assumed to be valid in the context of water as the coefficient of cubic thermal expansion α_T is small (see Section 3.2.1).

This case was solved in the same domain that the one presented in last Section (see Figure 6.17), with the heater's temperature being set to T_{sat}. This means that the heater was used as an approximation of the liquid vapour interface. We assumed that this approach allowed to capture the scale of magnitude of natural convection effects in the real case. An anisotropic mesh with a constrain of $h_{\text{min}} = 4{\times}10^{-5}\,\text{m}$ normal to the heater was built to properly capture the expected boundary layer. The rest of the domain boundaries was set to $T_{\infty} = 93.4\,°\text{C}$ (subcooling of 6.6 K) except the block that holds the heater that was set with adiabatic conditions.

A time step of 0.01 s was taken, and the simulation ran a physical time of 1 min to ensure a steady state regime. A cross-section view of the velocity and temperature field are plotted in Figure 6.23. The boundary layer is easily identified with a maximum velocity of $0.025\,\text{m}\,\text{s}^{-1}$ and a thermal thickness of around 3 mm. These values are respectively lower and higher than the ones predicted by the scaling law analysis. This means that the computed effect of the natural convection is lower than the estimation.

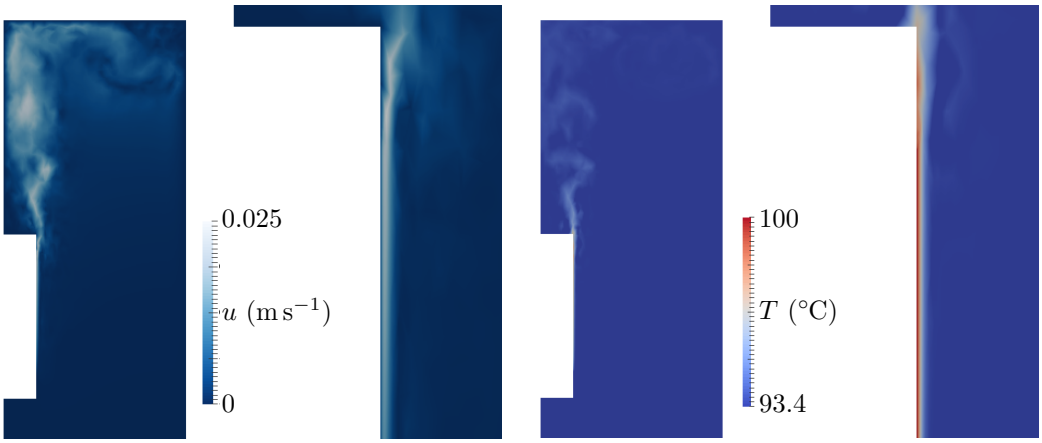

(a) Velocity magnitude *(b) Temperature*

Figure 6.23: Final velocity temperature fields of the monophasic natural convection simulation.

The averaged heat flux over the heater is plotted in Figure 6.24. The steady state is well reached for such time scale. The value of $3612\,\text{W}\,\text{m}^{-2}$ computed is well below the experimental values of liquid side heat fluxes. This confirms that natural convection effects are not dominant in the context of boiling.

6.3.2.2 Modeling approach

Contrary to the saturated case, the difficulty of the subcooled configuration is not linked to the hydrodynamics of the vapour. The vapour film is indeed close to

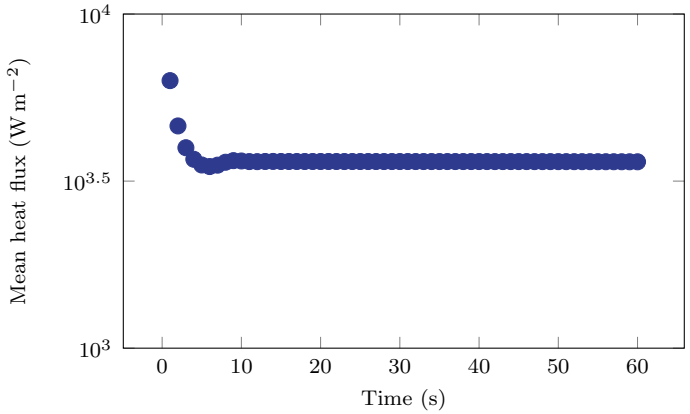

Figure 6.24: Wall heat flux over time for the natural convection simulation. The final time considered it large enough to guaranty the steady state regime.

a boundary layer if we neglects the oscillations of the interface. However, these oscillations have a great impact on the thermics inside the liquid. It creates fine convective flows that improve heat transfers inside the liquid.

We considered the case of Vijaykumar et al. [57] for an overheating of 203 K and a subcooling of 6.6 K. In this configuration, a mean heat transfer q_w of 78 450 W m^{-2} and a mean liquid side heat flux q_∞ of 67 235 W m^{-2} were measured. Considering the Fourier law, this entails a mean thermal thickness of around 0.1 mm in the vapour and of 0.06 mm in the liquid. As the direction of the vapour flow is quite straight, it is possible to model the vapour film. However the second scale of magnitude is specially difficult to capture within the liquid. So, we first studied a case where the liquid side heat flux q_∞ was imposed in the heat flux jump computation.

6.3.2.3 Numerical parameters

We performed two simulations for the same overheating of 203 K. In the first one, the experimental value of q_∞ was taken [57]. For the second one, a reduction of 5% of this value was taken. This second configuration was built to assess the sensitivity of the wall heat flux on the imposed q_∞. It could be related to an estimated variation of 5% of the subcooling. To tackle the vapour film thickness, the mesh size inside the vapour phase normal to the interface was set to $h_{\min} = 4\times10^{-5}$ m. Apart from these modifications, all the parameters were the same as for the saturated configuration simulation.

6.3.2.4 Results

For every configuration, physical times of 2 seconds had been simulated, that was shown to be enough for the hydrodynamics steady state to be reached. Visualisation

of the vapour film, velocity and temperature profiles are plotted in Figure 6.25a. A frontal view of the film thickness field is plotted in Figure 6.25b. As expected, the film was very thin and regular, close from a plane. The temperature was not completely linear and gradients are slightly stiffer near the heater. The velocities inside the vapour layer was more close to a half Poiseuille flow. This was assumed to be due to the volume approach of the mass transfer combined with the offset of the interface. This creates tangential velocity components in the liquid close to the interface.

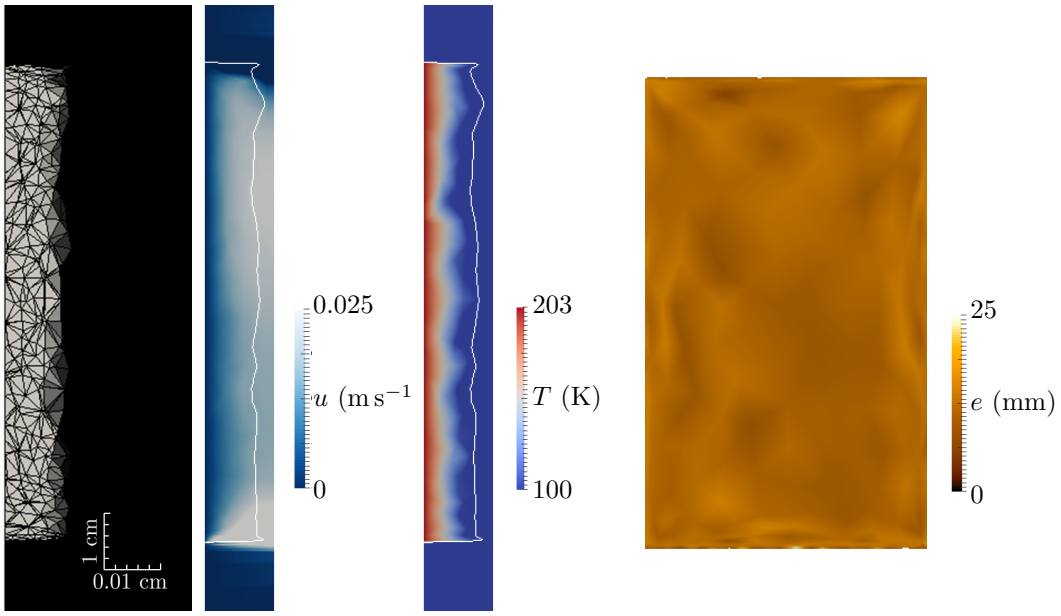

(a) Cross section view of the vapour film and of the velocity and temperature fields.

(b) Frontal view of the film thickness field. The thickness nearly homogeneous.

Figure 6.25: Visualisation of the vapour film with 203 K *for an imposed subcooling taken from [57].*

We challenged the simulated values of the vapour velocity $\overline{u}$ and film thickness e with theoretical estimations $\overline{u}_{\text{th}}$ and e_{th}. Regarding the thickness, the local equilibrium of heat fluxes at the interface reads:

$$q_\infty = \frac{k_{\text{V}} \Delta T_w}{e} \tag{6.25}$$

Regarding the velocity, the computation of the mean velocity inside a half Poseuille flow leads to:

$$\overline{u} = \frac{\rho_{\text{V}} g e^2}{\eta} \tag{6.26}$$

Theoretical and simulated values of these two parameters are gathered in Table 6.4 and are of the same order of magnitude. Differences in e can be explained by the non-linear shape of the temperature that allows the same mean heat flux with a larger mean thickness.

Mean values of the wall heat flux q_w are also gathered in Table 6.4. The first conclusion is that the value of q_w is very sensitive to the value of q_∞, as expected. Considering the associated variation of subcooling to be linear with q_∞, this means that a small variation of around 0.33 K leads to a variation of more than 8000 W m^{-2} which is very large: this confirms the stiff influence of the subcooling on heat transfers, contrary to the conclusions of the sphere quenching experiment.

Secondly, the value for the experimental liquid side heat flux is very close to the experimental value of q_w. This is encouraging. However, if we integrate heat fluxes around the vapour volume, we should recover the same amount of energy from both sides. The mean heat flux difference should be explained by a difference of surface between the heater surface and the liquid vapour interface. It was probably the case in the experiment with such wavy interfaces. But this was not the case in our simulation. This means that the energy conservation is not fully guaranteed by the framework with such numerical parameters. The mesh being quite coarse regarding the interface characteristic length, a further analysis would help explaining the causes of this weakness.

However, the global behavior of the solver is considered acceptable. The next step would be to release the liquid side heat flux. In Table 6.4 the computed value of the liquid side heat flux q_∞ is presented. Its value is far below the experimental one, even with the consideration that the system probably did not reach a thermal steady state in the liquid phase. The same conclusion as in Chapter 5 appears: the high convective effects in the liquid are not simulated with such approach.

6.3.3 General configuration

We saw that a laminar representation enabled to recover some of the features of the saturated configuration, among which the order of magnitude of the heat flux. We also saw that providing that the liquid side heat flux is properly computed, the

$\Delta T_w = 203\,\mathrm{K}$	e (mm)		$\overline{u}$ (m s^{-1})		q_w (W m^{-2})		q_∞ (W m^{-2})
	th.	simu.	th.	simu.	exp.	simu.	simu.
q_∞	0.107	0.115	0.012	0.012	78 450	77 647	4100
$0.95q_\infty$	0.113	0.126	0.013	0.014	-	69 140	3800

Table 6.4: Comparison of experimental, theoretical and simulated parameters for the subcooled vertical film boiling.

global behavior of the film is consistent. As the full description of the interface local hydrodynamics was out of the scope of this study, the model of the modified liquid conductivity k_{Leq} presented in Section 5.4.2.3 was again considered. The numerous measurements provided by [57] allowed to evaluate the relevance of this approach, and to improve our comprehension of the phenomena behind k_{Leq}. We recall the estimation (5.19) based on a simple recirculation model:

$$k_{\mathrm{Leq}} \sim \rho_{\mathrm{L}} c_{\mathrm{pL}} u_n \delta_{\mathrm{c}} \tag{6.27}$$

where δ_{c} was taken as the wave amplitude $e_{\max}$ and u_n the normal component of the liquid velocity close to the interface. We also defined an associated Péclet number $\mathrm{Pe_L} = k_{\mathrm{Leq}}/k_{\mathrm{L}}$. Vijaykumar et al. [57] measured values of u_n ranging from 0.02 to $0.008\,\mathrm{m\,s^{-1}}$ for overheatings between 160 and 207 K and subcoolings between 1.6 and 6.6 K. We saw that $e_{\max}$ was decreasing with the subcooling. Thus the product $u_n\delta_{\mathrm{c}}$ is decreasing with the subcooling. This should lead to a value of $\mathrm{Pe_L}$ that would also decrease with the subcooling.

However, the correlation (6.9) tends to highlight a linear relationship between q_w and ΔT_∞. As we saw that for high enough subcooling, $q_w \sim q_\infty$, this means that $\mathrm{Pe_L}$ should be independant of the subcooling. This argument leads to the point that the description given by (6.27) is not complete.

The reasons of this inconsistency is still not clear. Thus, a constant value of $\mathrm{Pe_L}$ was considered as a first approach. Its value was set thanks to the liquid side heat flux measurements of a reference case of [57]. The configuration for $\Delta T_w = 203\,\mathrm{K}$ and $\Delta T_\infty = 203\,\mathrm{K}$ was chosen.

Another unknown is the nature of the thermal steady state regime. Vijaykumar et al. [57] underlined that the liquid temperature changes were lower than 0.2 K in 1 min and that they managed to avoid thermal stratification. But no more details are provided on the way to have such conditions. Thermal conditions in the liquid are believed to have an important impact on the heat transfer with the vapour. Thus it seems difficult to implement a thermal steady state that would precisely represent one of the experiments. Furthermore, this would require a long simulated time so a lot of computation resources.

To overcome this difficulty, a choice was made to work at "equivalent thermal transient state": The aim was to recover the experimental value on the reference case in a 2 s simulation. Few iterations on the value of $\mathrm{Pe_L}$ were carried out until the experimental value matches the mean value of the simulated q_∞ over the second half of the simulation. Then, we challenged the resulting formulation by simulating different conditions of overheating and subcooling, and comparing the wall heat fluxes with experimental measurements.

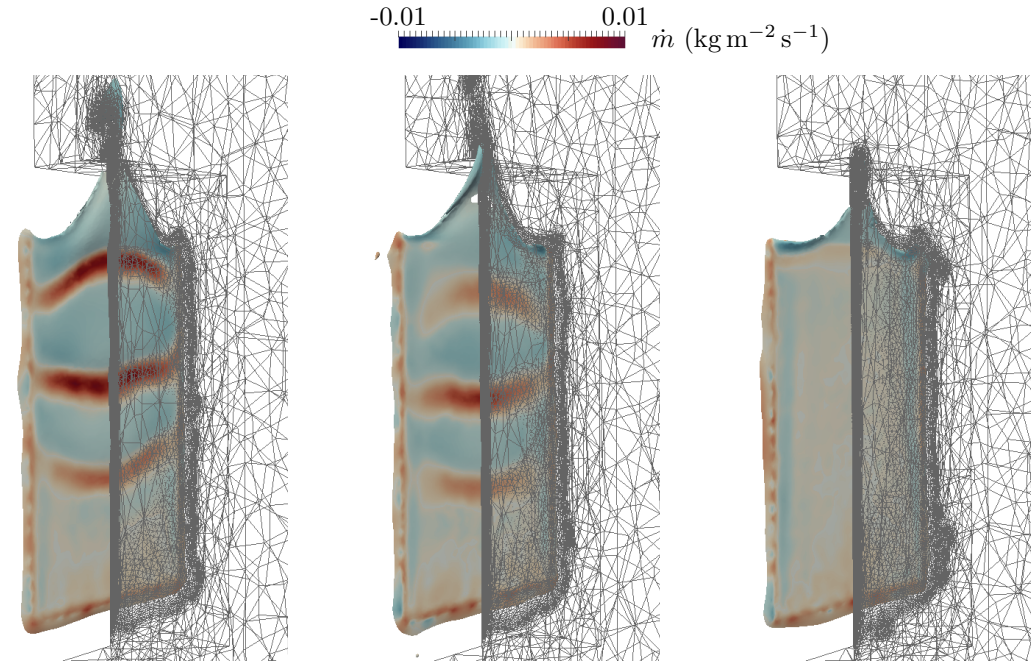

(a) $\Delta T_w = 150\,\mathrm{K}$, $\Delta T_\infty = 5\,\mathrm{K}$

(b) $\Delta T_w = 203\,\mathrm{K}$, $\Delta T_\infty = 6.6\,\mathrm{K}$

(c) $\Delta T_w = 200\,\mathrm{K}$, $\Delta T_\infty = 10\,\mathrm{K}$

(d) $\Delta T_w = 300\,\mathrm{K}$, $\Delta T_\infty = 5\,\mathrm{K}$

(e) $\Delta T_w = 300\,\mathrm{K}$, $\Delta T_\infty = 10\,\mathrm{K}$

(f) $\Delta T_w = 300\,\mathrm{K}$, $\Delta T_\infty = 15\,\mathrm{K}$

Figure 6.26: Visualisation of the liquid vapour interface at the last increment ($t = 2\,\mathrm{s}$) of the subcooled vertical film boiling simulation for different overheatings and subcoolings.

This approach leads to a value of k_{Leq} that is fundamentally dependant on the 2 s thermal transient state. However, if the model of a constant k_{Leq} regarding ΔT_w and ΔT_∞ is relevant, then every transient state can be compared.

Considering the same numerical parameters as in Section 6.3.1 with parameters given by table 6.2, and including the k_{Leq} model, we run the simulation for the following couples of overheating and subcooling (ΔT_w,ΔT_∞) (in K): (150,5), (203,6.6), (200,10), (300,5), (300,10) and (300,15). The simulation of the reference case lead to $\text{Pe}_\text{L} = 156$, thus to $k_{\text{Leq}} = 106\,\text{W}\,\text{m}^{-1}\,\text{K}^{-1}$.

Visualisation of the interface and mass transfer rate at the last increments of the simulations are shown in Figure 6.26. The higher the subcooling, the flatter the interface. This is consistent with experimental observations, as the wave amplitude was shown to decrease with the subcooling. This also causes the vaporisation to be less intense as more heat is absorbed by the liquid. Once again this is consistent with experimental observations. We also observed that the mean thickness decreases with a higher subcooling, but wetting is less present as the hydrodynamic is closer to a BL system.

Mean heat fluxes are compared with experimental data in Figure 6.27. These values are measured at mid-height of the heater, but both works [136] and [61] concluded that these values did not vary much over the height. It is then reasonable to compare these values with mean heat fluxes. We can see that the constant Pe_L approach succeeds well in modeling the liquid convection close to the interface. The "equivalent thermal transient state" is then validated. The power of prediction of this combined approach of a more laminar model with a Pe_L correction is weak, as the value of the convective liquid conductivity seems not to be universal. An

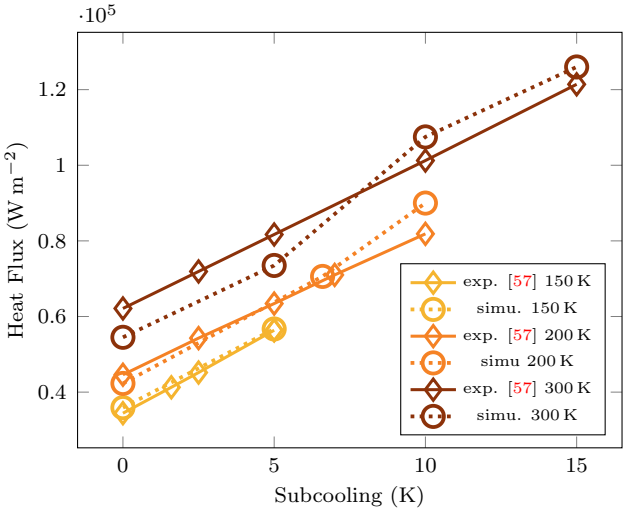

Figure 6.27: Comparison of simulated heat flux q_w with experimental values of [61]. The simulation conductivities were modified to fit the data.

improvement of the capacity of the numerical framework to handle more biphasic complex flows would enable to overcome this difficulty. It may even give more explanation on the sensitivity of liquid side convective effects in regards to the subcooling. This is however beyond the scope of this work.

6.4 Conclusions

- The vertical vapour film is always wavy but gets closer to a Boundary Layer shape at high subcooling. Overall the Boundary Layer model provides a good first approximation of heat fluxes. The heat transfer inside the vapour is close to being conductive whereas the liquid side heat transfer is highly convective.
- The higher the subcooling, and the less vapour is created and the more the liquid is being heated.
- Natural convection has little influence on the heat transfer. However the influence of the subcooling on heat transfer is very important. It is linked with large convective effects close to the liquid vapour interface induced by the interface waves. However the physical explanation of the sensitivity of this effect in regards to subcooling is still an open question.
- Fine scales effects are at play in both the liquid and the vapour phases. A proper resolution of such effects is crucial for the modeling of vertical film boiling.
- The 3D simulation of vapor film boiling at various overheating and subcooling has been performed, that is something that has never been done before according to the autor's knowledge.
- An approximation of the saturated vertical film boiling with an augmented viscosity enables to recover the experimental magnitude of the wall heat flux. However, the sensitivity on the overheating is weaker than what is observed experimentally.
- Subcooled film boiling can be simulated properly providing that the liquid side heat flux is imposed. Empirical laws can be set on the conductivity values to fit experimental data for different degrees of subcooling and overheating. The present configuration revealed small biases on the mass and energy conservation that would require further analyses.

Chapter 7

Full simulation of industrial quenching configuration

Contents

Résumé en Français

Ce chapitre présente la mise en place d'un outil de simulation complet de trempe en bain calme. La considération des nombres adimensionnels rendant compte des phénomènes hydrodynamique et thermiques montre que ce procédé met en jeu des écoulements turbulents avec beaucoup de convection due à la remontée de la phase vapeur. La simulation d'un tel procédé nécessite donc une approche dédiée. De plus, selon la taille de la pièce, le temps caractéristique de trempe varie énormément (de la seconde à l'heure), ce dernier pouvant être estimé par une analyse d'ordres de grandeur.

Étant donné que les temps de calcul en jeu lors de l'utilisation du modèle de changement de phase sont importants, il est inenvisageable de simuler complètement une trempe dès lors que le temps physique de cette dernière dépasse la minute. De plus, le modèle de changement de phase ne permettant pas de simuler tous les modes d'ébullition, la simulation complète d'une trempe nécessite qu'il soit enrichi par un modèle de nucléation. Pour résoudre ces deux problèmes, une approche en deux temps est proposée. Tout d'abord la modélisation complète du mode de caléfaction est simulée sur un temps court, la température étant fixée à celle de la pièce en début de trempe. Ensuite, les informations récupérées par cette simulation sont intégrées à un modèle de résolution de la thermique dans la pièce. Des corrélations issues de la littératures et enrichies par la simulation permettent de rendre compte du mode de nucléation. Un paramétrage est cependant nécessaire pour régler la température de Leidenfrost, qui dépend de facteurs non maitrisés comme l'état de surface de la pièce.

Cette approche est évaluée à travers deux cas de trempe industriels. Les deux cas ont été instrumentés afin d'avoir l'évolution de la température au coeur de la pièce. Le premier est la trempe dans de l'eau d'une brique de 75 mm par 75 mm par 15 mm en Inconel 718, initialement chauffée à 880 °C. La courbe de refroidissement expérimentale montre que le mode de caléfaction est bref à cause de la température froide du bain (25 °C). De fait, la température de Leidenfrost est très élevée. La simulation montre un refroidissement plus rapide sur les arrêtes et au-dessus de la plaque, cohérent avec ce qui est attendu physiquement. Le second cas est la trempe d'un crayon en Inconel de 12 mm de diamètre chauffé à 850 °C dans de l'huile de trempe à 60 °C. On montre que les phénomènes de convection dans le liquide sont aussi présents pour de l'huile, et qu'en prenant ceux-ci en compte, le modèle de trempe prédit correctement le refroidissement de l'éprouvette.

7.1 Introduction

In this Section, we focused our attention on pool quenching, where the solid is immersed inside the liquid. Appendix D presents an analytical and numerical study of a jet quenching configuration.

The simulation of a complete quench is a great challenge. To appreciate the level of complexity of a quench, let us have a look at some meaningful dimensionless numbers associated to a quench of a gear and of a cylinder head. We consider the Reynolds number (Re), the Péclet number (Pe), the Grashof number (Gr), the Biot number (Bi) and the Jakob number (Ja). We recall the definition of these numbers:

$$\mathrm{Re} = \frac{u_\mathrm{c} L_\mathrm{c}}{\nu_\mathrm{L}} \quad \mathrm{Pe} = \frac{u_\mathrm{c} L_\mathrm{c}}{D_\mathrm{L}} \quad \mathrm{Gr} = \frac{g \alpha_{\mathrm{T}\mathrm{L}} \Delta T_\infty L_\mathrm{c}^3}{\nu_\mathrm{L}^2} \quad \mathrm{Bi} = \frac{q_w L_\mathrm{c}}{\Delta T_w k_\mathrm{S}} \quad \mathrm{Ja} = \frac{\rho_\mathrm{L} c_{\mathrm{p}\mathrm{L}} \Delta T_\infty}{\rho_\mathrm{V} \mathcal{L}} \tag{7.1}$$

with u_c the characteristic velocity of the flow and L_c the characteristic dimension of the part.

- Re compares the inertial effects against the viscous effects. It characterizes whether the flow is rather laminar (small Re) or turbulent (large Re).
- Pe compares the conductive heat transfer against the convective heat transfer within the fluid. It characterizes if the temperature profile of the fluid is influenced by the velocity profile (large Pe) or not (small Pe).
- Gr compares the energy variation due to natural convection to the viscous dissipation. It reflects whether the natural convection is intense (large Gr) or not (small Gr).
- Bi compares the heat exchange at the fluid solid interface with the conduction within the solid. It characterizes whether the thermal stress at the interface is rapidly diffused within the solid (small Bi) or not (large Bi).
- Ja compares the sensible heat of the system with the state change latent heat. It characterizes whether the energy given by the solid will be used to warm up (large Ja) or to vaporize (small Ja) the liquid.

We consider that the parts are both made of hardened steel with conductivity $30\,\mathrm{W\,m^{-1}\,K^{-1}}$. For the calculation of Re, Nu, Pe and Gr, we take a length of 10 cm for the gear and 1 m for the cylinder head. For the calculation of Bi, we take a thickness of 1 cm for the gear and 10 cm for the cylinder head. The parts are heated at 1000 °C, which leads to an estimated q_w of $10^5\,\mathrm{W\,m^{-2}}$. We consider that the gear is plunged in hot water at 95 °C whereas the cylinder head is plunged in water at

ambient temperature (25 °C). The flow velocity is estimated to be around $1\,\mathrm{m\,s^{-1}}$, and the following characteristics are considered for water and vapour at 100 °C [89] (see Table 7.1).

ρ_L ($\mathrm{kg\,m^{-3}}$)	ρ_V ($\mathrm{kg\,m^{-3}}$)	η_L ($\mathrm{Pa\,s}$)	$c_{\mathrm{p}\mathrm{L}}$ ($\mathrm{J\,m^{-3}\,K^{-1}}$)	k_L ($\mathrm{W\,m^{-1}\,K^{-1}}$)	$\mathcal{L}$ ($\mathrm{J\,kg^{-1}}$)	$\alpha_{\mathrm{T}\mathrm{L}}$ ($\mathrm{K^{-1}}$)
1000	0.59	10^{-3}	4215	0.68	2.26×10^{6}	0.0003

Table 7.1: Properties taken for the computation of characteristic dimensionless numbers of two reference cases.

Values of the considered dimensionless parameters are gathered in Table 7.2. We can see that in both cases the flow is very turbulent. Heat transfer is mostly due to convective effects all the more since natural convection is intense. In the case of a hot pool, vaporization is the major heat sink. Whereas with cold water the heating of the fluid is where the energy goes the most. Finally, the gear is cooled more uniformly than the cylinder head.

	Re	Pe	Gr	Bi	Ja
gear	1×10^{5}	6×10^{5}	10^{8}	3×10^{-2}	1
cylinder head	1×10^{6}	6×10^{6}	10^{11}	3×10^{-1}	3×10^{2}

Table 7.2: Characteristic dimensionless numbers of the quenching of a gear and of a cylinder head.

Such orders of magnitude are indicators of a complexity to simulate the considered phenomena. With this in mind, it is nearly inaccessible to simulate with a high level of precision a full quench. Hence modeling choices have to be made. Moreover, in the present work, our phase change model does not include the consideration of the interaction between the liquid phase and the hot solid. It is thus adapted for the film boiling mode and can be extended to the transition boiling beginning with a simple wetting model. However, fine wetting phenomena entailed in the nucleate boiling mode prevent any hope to simulate these modes as such. This is the reason why the phase change solver required to be enriched with models and correlations to simulate a full quench. A strategy was adopted to combine the insights given by the simulation with an efficient cooling prediction.

7.2 Quenching model

7.2.1 A priori estimation of the quenching time

It is always interesting to have a first very rough estimation ot a studied case. This is useful for the choice of the adapted mesh and time step as well as the estimated

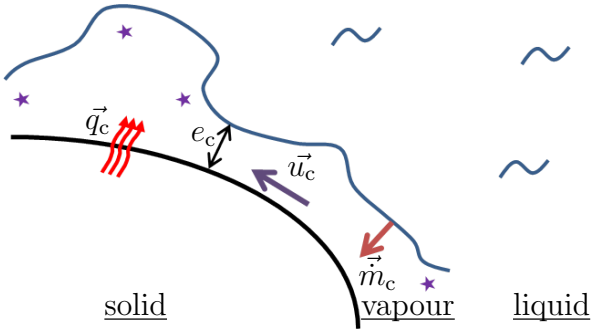

Figure 7.1: Global description of the main characteristic quantities during boiling.

computation time. In this section, we propose to estimate with very approximated scaling laws a general boiling heat flux. We considered an approach similar to the one of the vertical film boiling Boundary Layer (see Section 6.2.2). We studied a vapour particle of velocity u_c that vaporised close to the solid (see Figure 7.1). The characteristic size of the vapour phase between the liquid and the solid is e_c. We considered:

- A balance between the shear stress and buoyancy:

$$(\rho_L - \rho_V)g \sim \eta_V \frac{u_c}{e_c^2} \tag{7.2}$$

- A simplified vision of the interface energy conservation with neglected vapour and liquid heating effects:

$$q_c \sim \mathcal{L}\dot{m}_c \tag{7.3}$$

- The interface mass conservation:

$$\dot{m}_c \sim \rho_V u_c \tag{7.4}$$

- The static Fourier Law inside the vapour:

$$q_c \sim \frac{k_V \Delta T_w}{e_c} \tag{7.5}$$

Doing so, this very rough estimation lead to the following heat flux estimates:

$$q_c \sim \left(\frac{\rho_V(\rho_L - \rho_V)\ g\mathcal{L}k_V^2 \Delta T_w^2}{\eta_V} \right)^{1/3} \tag{7.6}$$

This estimation is mostly valid for a saturated film boiling state and is expected to underestimate fluxes for subcooling situations. Moreover, we know that this

boiling mode is significantly less efficient than nucleation, so we expect to greatly underestimate heat fluxes in this range. In the other hand this mode is more efficient than simple natural convection with a monophasic liquid. This observation is especially important in the case of very large parts whose cores can still be very warm even if the edges are below the saturation temperature. To conclude, we expect this very simple model to overestimate the cooling rate of small parts and to overestimate the cooling rate of bigger parts.

Now we consider a metallic part of volume $\mathcal{V}$ and surface $\mathcal{S}$. We can estimate the time of cooling thanks to the global energy conservation equation

$$\rho_{\mathrm{S}} c_{\mathrm{pS}} \mathcal{V} \frac{\mathrm{d}\Delta T_w}{\mathrm{d}t} = -\mathcal{S} q_{\mathrm{c}} \tag{7.7}$$

An approximation consists in considering that the part is at a uniform temperature. This is an acceptable approximation for small Biot numbers. Then, the equations reads:

$$\frac{\mathrm{d}\Delta T_w}{\Delta T_w^{2/3}} = -\frac{\mathcal{S}}{\rho_{\mathrm{S}} c_{\mathrm{pS}} \mathcal{V}} \left(\frac{\rho_{\mathrm{V}} (\rho_{\mathrm{L}} - \rho_{\mathrm{V}})\ g \mathcal{L} k_{\mathrm{V}}^2}{\eta_{\mathrm{V}}} \right)^{1/3} \mathrm{d}t \tag{7.8}$$

Integrating this equation leads to the first estimation of quenching time:

$$\Delta t_{\mathrm{c1}} = \frac{3 \rho_{\mathrm{S}} c_{\mathrm{pS}} \mathcal{V}}{\mathcal{S}} \left(\frac{\eta_{\mathrm{V}} \Delta T_{\mathrm{c}}}{\rho_{\mathrm{V}} (\rho_{\mathrm{L}} - \rho_{\mathrm{V}})\ g \mathcal{L} k_{\mathrm{V}}^2} \right)^{1/3} \tag{7.9}$$

A second estimation of the cooling time consists in considering that the intense heat flux imposes a temperature close to T_{sat} at the interface. A solution of the heat equation of an infinite slab of thickness L_{c} can be found with Fourier series (see [140]). The approximation of this solution is an exponential function whose characteristic time scale τ_{c} reads:

$$\tau_{\mathrm{c}} = \frac{L_{\mathrm{c}}^2 \rho_{\mathrm{S}} c_{\mathrm{pS}}}{\pi^2 k_{\mathrm{S}}} \tag{7.10}$$

The steady state is considered to be reached at 3 times this characteristic time. Thus the second estimation simply reads $\Delta t_{\mathrm{c2}} = 3\tau_{\mathrm{c}}$. L_{c} is taken as the smallest dimension of the metallic part.

In the context of the industrial Chair INFINITY, partners provided different quenching cases:

1. A large steel brick of around 1 m width.

2. A “multi-hat” shaped titanium part of around 30 cm height.

3. A steel cylinder of 7.5 cm radius.
4. A small nickel brick of 7.5 cm width.
5. A flat steel part of complex geometry and of 5 mm thickness.
6. A "drasticity" test: the quenching of an Inconel cylinder of 6.25 mm radius in oil.

This diversity of configurations gives a good overview of the possibilities of such set up. Different material, geometries, sizes lead to very different behavior. We can assess the relevance of our first approximations thanks to theses cases. They are summed up in Table 7.3. The majority of the quenches are done in water at ambient temperature. Only the last one is done with a quenching oil. The properties for the vapour phase had been estimated with the one of water vapour as no data was available. Our estimations of Δt_{c1} and Δt_{c2} are compared with the experimental value Δt_{exp} for each case in Table 7.3. We can see that overall orders of magnitude of quenching time are roughly respected. As expected, Δt_{c1} model underestimates the quenching time for big parts, and overestimates it for small parts. The estimation given by Δt_{c2} has the inverse behavior. Thus these two estimations give acceptable upper and lower bounds of the quenching time. However, the configurations complexity can lead to adimensional numbers that vary across the space. For example, the Biot number is related to the thickness of the part that is essential for the cooling time estimate. These estimates have therefore to be considered with cautious.

Case	L_c (cm)	$\mathcal{V}$ (l)	$\mathcal{S}$ (m^2)	$\rho_S c_{pS}$ ($J\,m^{-3}\,K^{-1}$)	k_S ($W\,m^{-1}\,K^{-1}$)	ΔT_c (K)	Δt_{c1} (s)	Δt_{c2} (s)	Δt_{exp} (s)
1	50	1600	10.1	4.9×10^6	30	810	2250	12 400	12 600
2	30	600	6	3.8×10^6	20	870	1130	5200	1200
3	15	2.6	0.1	5.3×10^6	20	880	410	1812	860
4	1.5	0.08	0.015	3.5×10^6	11.4	780	53	21	40
5	0.5	0.001	0.001	3.7×10^6	20	500	9	1.4	4
6	1.25	0.017	0.0054	3.7×10^6	20	510	29	9.5	10

Table 7.3: Application of the quenching time estimates on different industrial quenching scenarios.Δt_{c1} and Δt_{c2} are the estimated quenching times and Δt_{exp} is the experimental quenching time.

7.2.2 Modeling approach

Apart from very small parts, the physical time of quenching is at least of the order of the minute, which is an important time scale for our model. With the current phase

change model, the direct simulation of the full quench of a large part would largely exceed acceptable computation times. Moreover, the nucleation part of boiling is not taken into account by this model. A strategy had to be found to overcome these challenges. The proposed approach of this work to simulate a full quench with reasonable computational time is to desynchronize the boiling simulation and the solid cooling. As shown in Figure 7.3, It breaks down into two steps:

- **Thermo-hydrodynamic simulation**: The simulation of the boiling process around the part maintained at a fixed temperature over few seconds. Once a steady regime is reached, time averaged local heat fluxes on the solid surface and film thicknesses are recovered. The boiling model described in Chapter 4 is used. Radiation effects are also considered in the energy conservation equation of the liquid vapour interface with the simplification presented in Chapter 2, as well as in the solid heat flux. The convective conduction corrections is also considered. The value of k_{Leq} is taken from the study of vertical film boiling of Chapter 6. This latter consideration is a strong extrapolation as vertical film boiling is a particular case linked with a specific geometry. Moreover the corrections only hold for water. This extrapolation is considered acceptable in the sense that the modeled phenomena are expected to be present whatever the configuration of film boiling with similar scales. Furthermore, we saw that k_{Leq} was not far from the one of the sphere quenching case that matched heat fluxes. Convection inside the liquid might however still differ regarding the configuration, and this point must be investigated in future studies.

- **Thermal simulation**: The thermal simulation of the part alone. Robin boundary conditions are set considering a Heat Transfer Coefficient (HTC) computed from the thermo-hydrodynamic simulation thanks to the recovered averaged local heat fluxes. At lower temperature when wetting appears, this HTC is modified with a "nucleation-based model" to take into account nucleation phenomena. It relies on correlations and is presented in the following section. In this simulation no phase transformation within the solid is considered.

The two steps are computed on two separated domains that communicate together (see Figure 7.2). This approach relies on several approximations. Fluxes in the calefaction mode do not vary linearly with the temperature, contrary to what is implied by a constant HTC. The strong coupling between the part cooling and the boiling process is not considered. The information of the vapour film thickness of the thermo-hydrodynamic simulation is assumed to hold for other temperatures. It is indeed used to account for the vapour convection from below and thus plays a role in the determination of the Leidenfrost temperature. However, all these biases

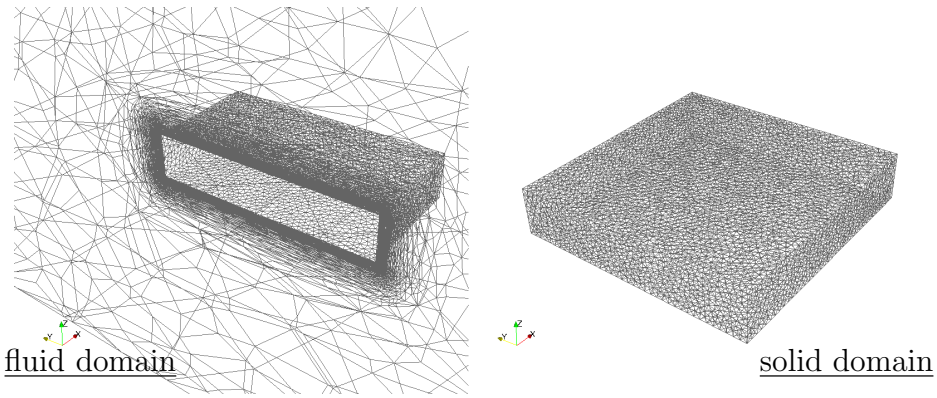

Figure 7.2: Visualisation of the meshes of the two separated computational domains.

could be reduced with few relaunches of the thermo-hydrodynamic simulation with an updated temperature.

The key strengths of this approach are that it combines the precision of the numerical simulation with the simplicity of correlations at a moderate computational cost. The lack of universality of correlations are linked with the context in which they are employed. The information provided by the simulation compensates these biases and enriches the correlation with considerations of geometry and vapour convection.

7.2.3 Nucleation-based model

7.2.3.1 General approach

We present here the model that is used to determine the surface heat fluxes during the thermal simulation. These heat fluxes are used as boundary conditions. Following an approach similar to Kopun et al. [55], the idea is to discriminate the local boiling mode in regards with the local surface temperature T_w. Three different modes are considered with three different heat flux models separated by the critical heat flux temperature T_{CHF} and the Leidenfrost temperature T_{MHF} (see Figure 7.4):

- $T_w < T_{\mathrm{CHF}}$: The combination of natural convection and nucleate boiling (q_{nu})
- $T_{\mathrm{CHF}} < T_w < T_{\mathrm{MHF}}$: The transition boiling mode (q_{tr})
- $T_{\mathrm{MHF}} < T_w$: The calefaction mode (q_{cal})

For each boiling mode, a dedicated model based on correlations or on the thermo-hydrodynamic simulation is set.

This approach requires the determination of the values of T_{CHF} and T_{MHF} as well as the functions q_{nu},q_{tr},q_{cal} that depend on the surface temperature. To do so, the following strategy is proposed:

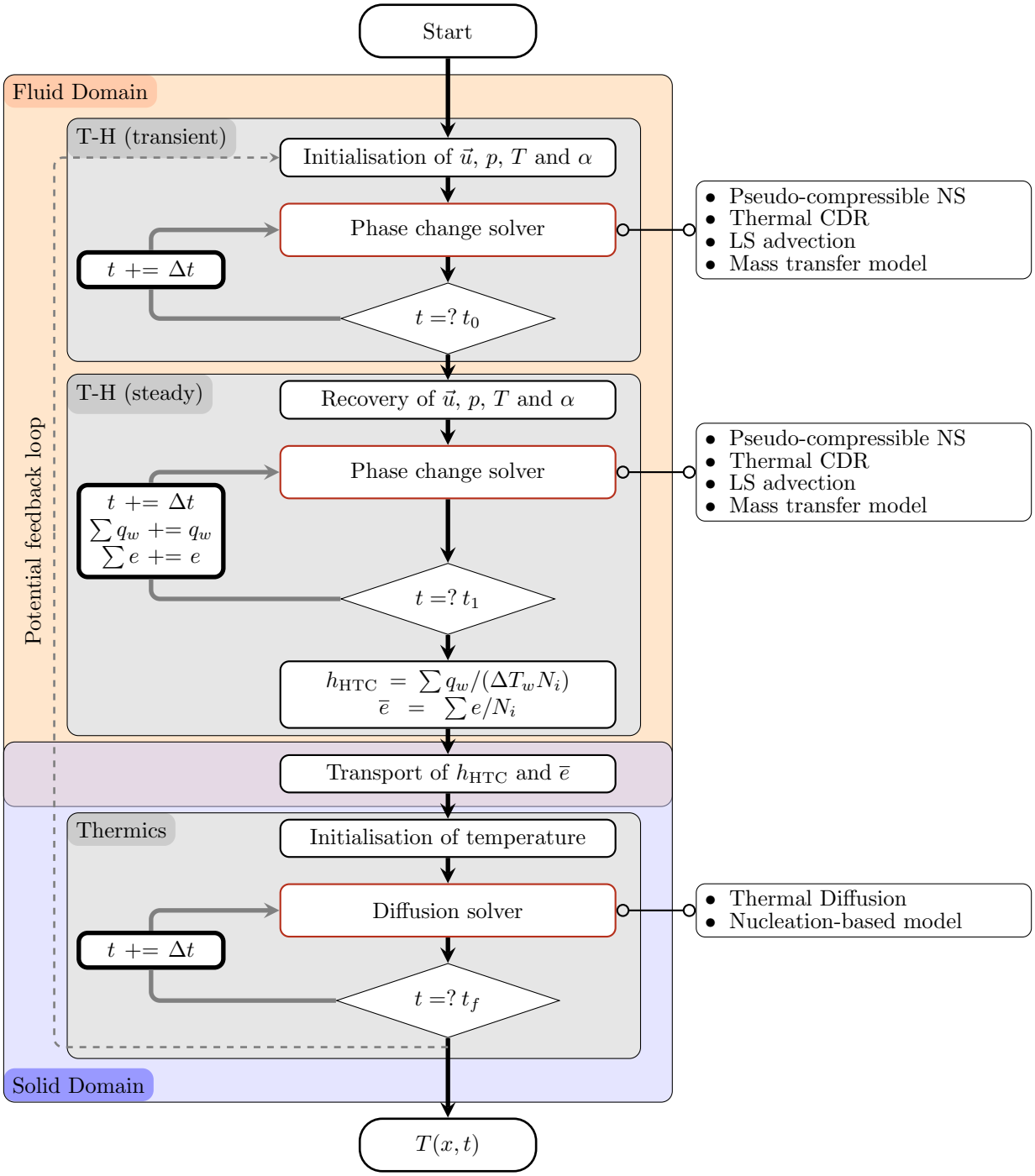

Figure 7.3: Solving procedure of the quenching framework.

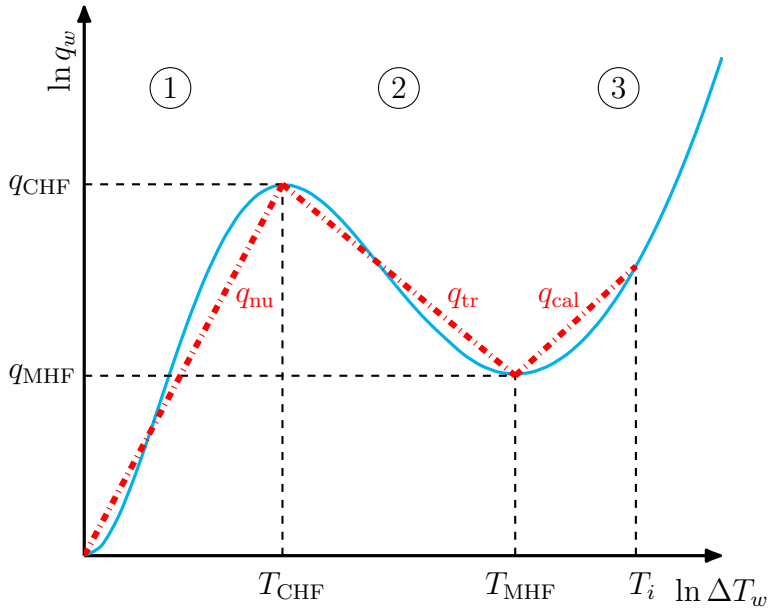

Figure 7.4: Approximation of the boiling curve within the nucleation-based model. It is separated into three sections: natural convection and nucleate boiling (1), transition boiling (2) and calefaction (3).

- Determination of q_{nu} via the correlation of Liu et al. [43]. The value of the convection velocity is given by the bubble elevation velocity of Mendelson et al. [141], whose radius is determined via the estimate of Mikic et al. [38].

- Calculation of the critical flux q_{CHF} by combining several works to include the effects of the subcooling and surface orientation [45, 142, 143].

- Calculation of T_{CHF} by solving $q_{\mathrm{nu}}(T_{\mathrm{CHF}}) = q_{\mathrm{CHF}}$.

- Determination of T_{MHF} via the correlation of Greene et al. [56]. The estimation is modified with fitting parameters to account for surface roughness, and with the vapour film thickness given by the thermo-hydrodynamic simulation.

- Calculation of q_{cal} from the HTC given by the thermo-hydrodynamic simulation.

- Calculation of $q_{\mathrm{MHF}} = q_{\mathrm{cal}}(T_{\mathrm{MHF}})$.

- Calculation of q_{tr} by a linear interpolation between q_{CHF} and q_{MHF} in regards to the temperature.

7.2.3.2 Natural convection and nucleate boiling

q_{nu} is determined with a correlation from the work of Liu et al. [43]. This correlation holds for subcooled boiling and also forced convection below T_{sat}. It had been compared and validated on boiling data in a pipe under forced convection. Even though these conditions are different from a quenching configuration, we estimate that the scales related to nucleation are small enough to be not impacted by the geometry and configuration of the hot plate. A total of 6523 measurement points were confronted with the correlation, of which 2758 with water. The ranges of the data were wide. This therefore allows a good level of confidence in the applicability of this correlation. We recall that $\Delta T_w = T_w - T_{\text{sat}}$ and $\Delta T_\infty = T_{\text{sat}} - T_\infty$. The associated heat flux reads:

$$q_{\text{nu}} = \sqrt{(h_{\text{Liu}}(\Delta T_w + \Delta T_\infty))^2 + (S h_{\text{Cooper}}(\max(\Delta T_w, 0))^2} \tag{7.11}$$

$$S = (1 + 0.055 \text{Re}_{\text{L}}^{0.16})^{-1} \tag{7.12}$$

$$h_{\text{Liu}} = 0.023(k_{\text{L}}/L_{\text{c}})\text{Re}_{\text{L}}^{0.8}\text{Pr}_{\text{L}}^{0.4} \tag{7.13}$$

with $\text{Re}_{\text{L}} = \rho_{\text{L}} u_{\text{c}} L_{\text{c}}/\eta$ the liquid Reynolds number and et $\text{Pr}_{\text{L}} = \eta_{\text{L}} c_{\text{PL}}/k_{\text{L}}$ the liquid Prandtl number.

h_{Cooper} is taken from the work of Cooper et al. [42] with a surface roughness arbitrarily fixed at 1 µm in [43]:

$$h_{\text{Cooper}} = 166375(p/p_{\text{cr}})^{0,36}(-\log_{10}(p/p_{\text{cr}}))^{-1.65} M^{-1.5} \Delta T_w^2 \tag{7.14}$$

with p_{cr} the critical pressure (about 220 atm for water), and M the adimensioned molecular mass (about 18 for water). We consider only atmospheric pressures conditions in this model. The coefficient 166375 is not adimensional, but is expressed in $\text{kg/s}^3/\text{K}^3$

The Reynolds Re_{L} is determined in [43] in the context of boiling inside a pipe. u_{c} is determined with the water flow rate sent into the tube section and L_{c} is determined with the tube section. In the present work, we had to determine L_{c} and u_{c}. We considered the configuration of a relatively calm pool. This means that this approach may not hold for important forced convection configurations. We estimated this velocity as being the rising velocity of the vapour bubbles. This is estimated via the work of Mendelson et al. [141]:

$$u_{\text{c}} = 1.35\sqrt{\frac{\gamma_0}{r_b \rho_{\text{L}}}} \tag{7.15}$$

with r_b is the bubble radius estimated via the work of Mikic et al. [38]:

$$r_b = 7.5{\times}10^{-5}\sqrt{\frac{\gamma_0}{g(\rho_{\text{L}} - \rho_{\text{V}})}}(\text{Ja}^*)^{5/4} \tag{7.16}$$

$$Ja^* = \frac{\rho_L c_{pL} T_{sat}}{\rho_V \mathcal{L}} \tag{7.17}$$

For water $r_b \simeq 1mm$.

The estimation of u_c is made by considering 10 times r_b, i.e. the convective zone created by the rise of the vapour bubbles around the solid. This gives an equivalent Reynolds of 10^4 which is within the range of the comparative data of the study. We therefore considered that this approach remains valid for the correlation use.

This Reynolds number is also considered for the natural convection mode (for $T < T_{sat}$). This is an overestimation of the heat exchange achieved, as convection is less efficient without the presence of bubbles. This point deserves further investigation.

7.2.3.3 Critical heat flux

The critical heat flux q_{CHF} is estimated by combining several works to take into account both surface orientation and undercooling. Liang et al. [44] have done a complete review of the different estimates of q_{CHF}. One conclusion is that the estimation of Zuber [45] is still robust. The corrections are mostly based on the surface roughness and orientation, as well as other parameters such as pressure or viscosity. A few studies reported on subcooling effects, but without any complete comparative study. We focus in this method on orientation and subcooling.

The work of Vischnev et al. [142] is used as a basis for the correction of the plate orientation. Many tests (with water, FC-72, PF-5052, R113) at different pressures shew the relevance of this correction [30]. An estimation of q_{MHF} is proposed as a function of the surface orientation. This connects to the estimate of Zuber in the horizontal case [45]:

$$q_{\text{CHF-Vish}} = \frac{\pi}{24}\rho_V \mathcal{L}\sqrt{\frac{190 - 180\theta/\pi}{190}}\left(\frac{\gamma_0 g(\rho_L - \rho_V)}{\rho_V^2}\right)^{1/4} \tag{7.18}$$

with θ the surface orientation. Its value is 0 for a horizontal downward-facing orientation and π for a horizontal upward-facing orientation.

This model is completed with a factor that takes into account the subcooling [143]. This leads to the final formulation:

$$q_{CHF} = \frac{\pi}{24}\rho_V \mathcal{L}\sqrt{\frac{190 - 180\theta/\pi}{190}}\left(1 + C_0\left(\frac{\rho_V}{\rho_L}\right)^{1/4}\frac{\rho_L c_{pL}\Delta T_\infty}{\rho_V \mathcal{L}}\right)\left(\frac{\gamma_0 g(\rho_L - \rho_V)}{\rho_V^2}\right)^{1/4} \tag{7.19}$$

This correction was also tested with experiments in a boiling pipe with forced flow. Initially, C_0 was fixed at 0.102. The results of Ebrahim et al. [25] in quenching

configurations put forward slightly more important orders of magnitude in the influence of subcooling on the critical flux. They carried out quenching experiments of thin cylinders with the measurement of the intern temperature variation. With 25 cm long specimens that had 1 cm diameters, they found a factor 4 difference between two tests whose liquid temperature were different by 30 K. This is higher than the 2.5 factor predicted by the initial parameter value of [143]. We therefore take $C_0 = 0.2$ to get closer to this last value.

7.2.3.4 Critical heat flux temperature

The calculation of $q_{\text{nu}}(T_{\text{CHF}}) = q_{\text{CHF}}$ is an order 6 polynomial equation:

$$q_{\text{CHF}}^2 = h_{\text{Liu}}^2 (T_{\text{CHF}} - T_{\text{sat}} + T_{\text{sat}} - T_\infty)^2 + (SC_{\text{Cooper}})^2 (T_{\text{CHF}} - T_{\text{sat}})^6 \tag{7.20}$$

where $C_{\text{Cooper}} = h_{\text{Cooper}}/\Delta T_w^2$ is a term not depending on T_w. To simplify the implementation of the model and allow an analytical resolution of this equation, we neglect the first order and second order terms $T_{\text{CHF}} - T_{\text{sat}}$ and $(T_{\text{CHF}} - T_{\text{sat}})^2$. Indeed, the order of magnitude of $T_{\text{CHF}} - T_{\text{sat}}$ is 20 K. In saturation conditions ($T_\infty = T_{\text{sat}}$) the order 6 term is largely dominant. The convection term becomes important only for sufficiently low values of T_∞. In this case, the $(T_{\text{sat}} - T_\infty)^2$ term is preponderant before $T_{CHF} - T_{\text{sat}}$ and $(T_{CHF} - T_{\text{sat}})^2$.

T_{CHF} is thus found by resolving:

$$q_{\text{CHF}}^2 = h_{\text{Liu}}^2 \Delta T_\infty^2 + (SC_{\text{Cooper}})^2 (T_{\text{CHF}} - T_{\text{sat}})^6 \tag{7.21}$$

$$T_{\text{CHF}} - T_{\text{sat}} = \left(\frac{q_{\text{CHF}}^2 - h_{\text{Liu}}^2 \Delta T_\infty^2}{(SC_{\text{Cooper}})^2} \right)^{1/6} \tag{7.22}$$

In Table 7.4, values of T_{CHF} obtained with this simplification ($T_{\text{CHF-s}}$) are compared with exact values ($T_{\text{CHF-e}}$) for various orientations and subcooling for water. The errors made are negligible. The approximation (7.22) is validated.

$T_{\text{sat}} - T_\infty$ (K)	0			20			75		
θ (rad)	0	$\pi/2$	π	0	$\pi/2$	π	0	$\pi/2$	π
$T_{\text{CHF-e}} - T_{\text{sat}}$ (K)	26.21	23.54	15.96	37.35	33.54	22.74	52.64	47.29	32.09
$T_{\text{CHF-s}} - T_{\text{sat}}$ (K)	26.24	23.57	16.06	37.36	33.57	22.84	52.64	47.30	32.16

Table 7.4: Comparison of exact ($T_{CHF\text{-}e}$) and estimated ($T_{CHF\text{-}e}$) values of the critical heat flux temperature. Computations are made for various orientations and subcooling for water thanks to the correlations of [43, 45, 142, 143].

7.2.3.5 Leidenfrost temperature

The estimation of T_{MHF} is very delicate because it has a strong dependancy on the surface roughness and the external vapour supply. The magnitude varies a lot depending on the configuration. It was considered necessary to correct this evaluation with two case-dependent parameters. As a first approximation, we consider the estimate given by Greene et al. [56]

$$T_{\text{MHF-Greene}} = 593 + 5.9\Delta T_{\infty} \tag{7.23}$$

where the values are in kelvin.

This correlation is compared to quenching experiments of copper specimens of 1.3, 2.54 and 3.81 cm diameter and 30 cm length, in a $29\times42\,\text{cm}^2$ pool at atmospheric pressure. The subcooling goes up to 70 K. These conditions are very close to those of industrial hardening though the surface condition is not studied. Several temperature estimates are compared in [55] and the values are very different according to the articles and the tests presented in the study. According to the studies and correlations, we can also fall to values close to 100 °C. A comparison study [25] confirms this dispersion of Leidenfrost temperature estimations. We can push even further the contradiction with the tests of [28] on hydrophilic and hydrophobic spheres. Finaly the present correlation is limited in the case of coolants different from water. For theses reasons, an adjustable parameter C_1 is considered that needs to be fixed empirically. It takes into account unknown quantities such as the surface state:

$$T'_{\text{MHF}} = C_1(T_{\text{MHF-Greene}} - T_{\text{CHF}}) + T_{\text{CHF}} \tag{7.24}$$

The value of C_1 should be smaller than 1 as the temperature given by [56] seems to be an upper limit according to [55]. But it should not be too far from 1 because the surface conditions of industrial parts are usually quite rough and rarely clean. This is believed to make the parts hydrophilic which greatly increases the value of T_{MHF}. By default, C_1 is set to 1.

The other adjustable parameter to be added is the influence of convected vapour. For this, we use the average vapour film thickness information from the thermo-hydrodynamic simulation. The higher this value, the more vapour is convected in the area. We then consider that the estimation given by (7.24) is associated with the zones where the vapour film is thinner. These are the zones where the vapour convection is the weakest and where the vapour film breaks first. Thus, these are the zones where the correlation might be the closest. Then we apply a weight function which will reduce by a factor C_2 the Leidenfrost temperature value in the other areas of the surface. In the absence of further study on the subject, we arbitrarily set the following correction function f:

$$f_{C_2}(e) = \frac{e_{\max} - e}{e_{\max} - e_{\min}} + C_2\frac{e - e_{\min}}{e_{\max} - e_{\min}} \tag{7.25}$$

This modifies the Leidenfrost temperature estimation:

$$T_{\text{MHF}} = C_1 f_{C_2}(e)(T_{\text{MHF-Greene}} - T_{\text{CHF}}) + T_{\text{CHF}} \tag{7.26}$$

By default, values of 0.8 for C_2 is taken. This leads to a gap of around 50 K between the maximum film thickness and minimum film thickness zone. This is in the order of magnitude of experimental observations [55]. However these parameters are expected to be fitted for every quenching configuration.

7.2.3.6 Calefaction and minimum heat flux

q_{cal} is computed thanks to the HTC coefficient given by the thermo-hydrodynamic simulation:

$$q_{\text{cal}} = h_{\text{HTC}} \Delta T_w \tag{7.27}$$

q_{MHF} is then computed thanks to (7.27)

$$q_{\text{MHF}} = h_{\text{HTC}}(T_{\text{MHF}} - T_{\text{sat}}) \tag{7.28}$$

7.2.3.7 Transition boiling

Considering results of the quenching experiments of [25], the cooling rate tends to a linear law between q_{tr} and T. Thus a linear interpolation $q_{\text{tr}} = a(T - T_{\text{sat}}) + b$ is considered for q_{tr}. The resolution of $q_{\text{tr}}(T_{\text{CHF}}) = q_{\text{CHF}}$ and $q_{\text{tr}}(T_{\text{MHF}}) = q_{\text{MHF}}$ allows to write:

$$q_{\text{tr}} = q_{\text{CHF}} \frac{T_{\text{MHF}} - T}{T_{\text{MHF}} - T_{\text{CHF}}} + q_{\text{MHF}} \frac{T - T_{\text{CHF}}}{T_{\text{MHF}} - T_{\text{CHF}}} \tag{7.29}$$

7.3 Pool Quenching

The presented quenching model has been tested in two configurations of moderate dimensions and compared with experimental results. These are the cases 4 and 6 of Table 7.3. The case 4 is the quenching of a small brick proposed by our industrial partner Industeel. The case 6 is a “drasticity” experiment in oil proposed by our industrial partner Faurecia. These two experiments have been chosen for their sizes. The parts are bigger than the sphere considered in our experiments. However, the dimensions are still moderate to have an acceptable computational cost with enough precision regarding the discretisation. Furthermore, the first case had been reproduced by [80] with promising results regarding the cooling rate at the beginning of the quench. The second test case demonstrates the capability of the model to handle other types of fluid. It is considered as a proof of concept as no reliable data was available for the properties of vapour oil. Moreover our nucleation-based model relies on correlations that are not always adapted for coolant different from water. This is especially the case for the Leidenfrost temperature estimation.

7.3.1 Quenching of a 3D brick in water

We first challenged the model on the quenching of a small brick of Inconel 718 alloy of dimensions $75 \times 75 \times 15\,\mathrm{mm}^3$.

We ran the thermo-hydrodynamic simulation on a domain of 0.6 m by 0.6 m by 0.4 m (see Figure 7.5). The brick was placed at the center of the domain at height 100 mm from the bottom. $2{\times}10^5$ nodes were considered, with a minimum mesh size $h_{\min} = 0.5\,\mathrm{mm}$ imposed at the liquid vapour interface.

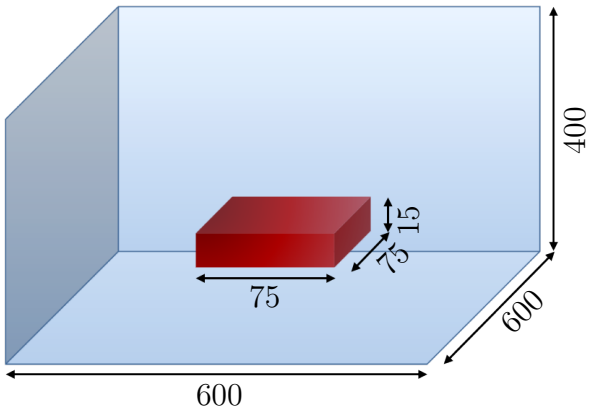

Figure 7.5: Schematic description of the computation domain for the brick quenching. Values of lengths are given in mm.

The water was set initially at $T_\infty = 25\,^\circ\mathrm{C}$, the vapour phase at $T_{\mathrm{sat}} = 100\,^\circ\mathrm{C}$ and the brick at $T_w = 880\,^\circ\mathrm{C}$.

The physical parameters of the simulation are gathered in table 7.5. As for the vertical film boiling benchmark, the viscosity of the vapour was raised to stabilise the thermo-hydrodynamic simulation. The value in Section 6.3.1.1 was taken. Values of vapour conductivity were taken accordingly to the table E.1 from [89]. Otherwise, material properties of water were taken at T_{sat} and at $(T_{\mathrm{sat}}+T_w)/2$ for water vapour. Regarding the thermal simulation, values at T_{sat} were considered. The liquid conductivity for the computation of the liquid side heat flux is taken from Section 6.3.3, thus to $106\,\mathrm{W\,m^{-1}\,K^{-1}}$.

Regarding boundary conditions of the thermo-hydrodynamic simulation, the temperature was fixed at T_w on the brick and at T_∞ on the other domain frontiers. No slip conditions were set on all mesh borders except on the top where zero gauge pressure with free output velocity was set. The remeshing algorithm was called every five steps, and the LS was reinitialised every two steps. The boundary conditions of the thermal simulation was Robin conditions with imposed heat fluxes from the nucleation-based model.

	ρ (kg m^{-3})	η (Pa s)	c_p (W m^{-1} K^{-1})	k (J kg^{-1} K^{-1})	$\mathcal{L}$ (J kg^{-1})	γ_0 (J m^{-2})	ε_w (–)
Thermo-hydrodynamic simulation							
Liquid	958	5×10^{-3}	4216	0.679	2.265×10^6	0.06	–
Vapour	0.4	1×10^{-3}	2030	$f(T)$			–
Thermal simulation							
Liquid	958	2.80×10^{-4}	4216	0.679	2.265×10^6	0.06	–
Vapour	0.597	1.20×10^{-5}	2030	0.0248			–
Solid	8000	–	435	11.4	–	–	0.5

Table 7.5: Properties of the liquid, vapour and solid phases for the 3D brick quenching simulation.

The values of C_1 and C_2 were set to 1 and 0.9 respectively. The thermo-hydrodynamic transient simulation ran for 0.5 s. This was sufficient for the boiling to be steady. Then the steady thermo-hydrodynamic simulation ran for one second to recover the vapour film mean thickness and the heat flux.

Visualisation of four time steps of the transient regime are plotted in Figure 7.6. The simulated film is very flat, which is expected in the case of a strong subcooling with a lot of heat extracted by the water. Thus few bubbles escape from the film. In the Figure 7.7 the mean heat flux and the mean vapour film thickness are shown. Heat transfer is more intense on the top of the part and at the edges, where the film is thinnest. This is coherent as the vapour is trapped below the part. The sharp edges help the solid to cut through the vapour and enter in contact with the liquid, leading to intense heat transfer.

A comparison of the temperature variation in the center of the part is done with experimental data in Figure 7.9. The tendency of the experimental curve seems to highlight the fact that the vapour film is stable only for few seconds. The quench switches very quickly to transition boiling. Computing T_{MHF} thanks to (7.26) leads to a value of 760 °C which is coherent with experimental observations. This high value is due to a large subcooling as the water is at ambient temperature. We also observe that the curve is similar to a decreasing exponential, meaning that the cooling should be close to the cooling model with T_{sat} imposed at the interface of the brick presented in Section 7.2.1.

In the Figure 7.8, various views of the temperature distribution simulated by the thermal solver are presented. The cooling of the part start from the edges and the top, and the core of the brick is the area where temperature is the hotter, which is consistent. Numerical and simulation results are in good agreement regarding the temperature at the center of the part (see Figure 7.9). The choice of the two parameters helped fitting the curve with the determination of a correct Leidenfrost temperature (the slope discontinuity at low overheating is assumed to be due to

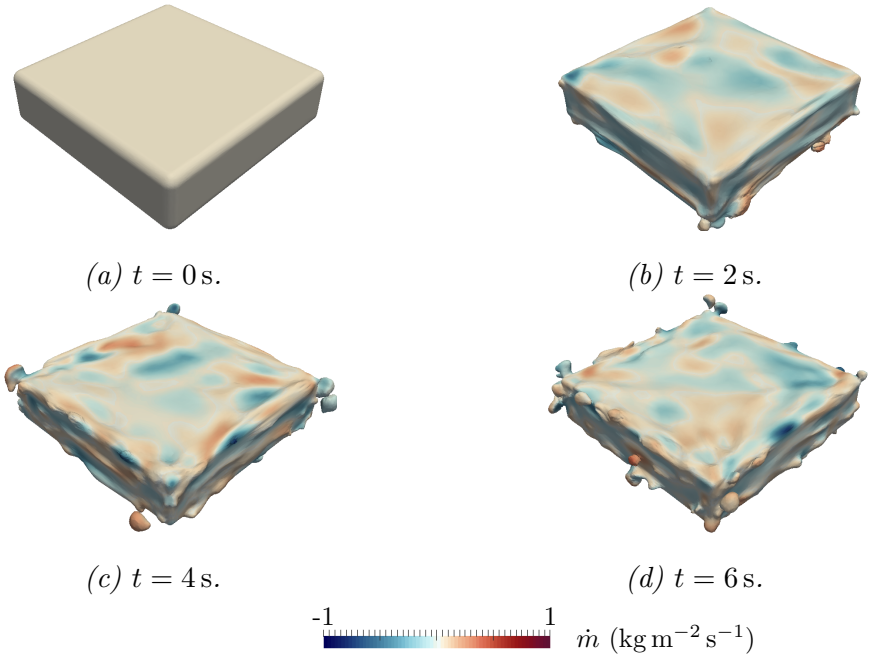

(a) $t = 0\,\mathrm{s}$. *(b)* $t = 2\,\mathrm{s}$. *(c)* $t = 4\,\mathrm{s}$. *(d)* $t = 6\,\mathrm{s}$.

Figure 7.6: Visualisation of the simulated liquid vapour interface and mass transfer rate for the brick quenching simulation. The important subcooling leads to a very flat film. Moreover, few bubble escape from the film, as they condensate mostly before their detachment.

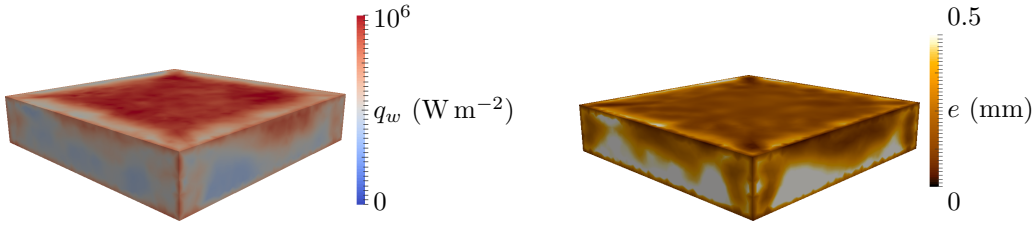

(a) Mean heat flux. *(b) Mean vapour film thickness.*

Figure 7.7: Visualisation of the simulated mean solid heat flux and vapour film thickness for the brick quenching simulation. Heat fluxes are more intense at the top of the brick and at the edges where the vapour film is the thinnest.

some water that enters inside the sensor's hole). The overall behavior of the curve is respected with good cooling slopes that are dictated by the simulation and the correlations.

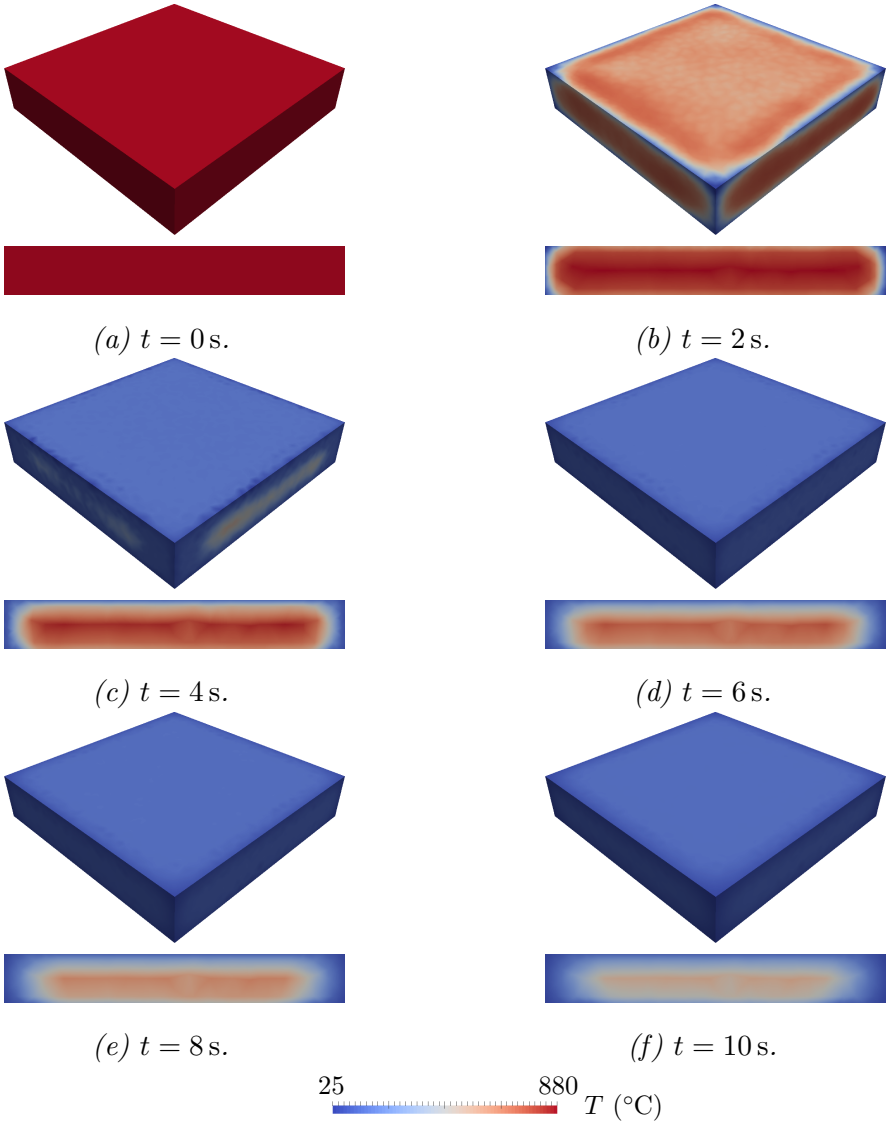

Figure 7.8: Top and cross section views of the temperature field from the thermal simulation of the brick quenching case for different time steps. The edges are the areas where the brick is cooled the fastest, in opposition to the center.

7.3.2 Quenching of a 3D pencil in oil

The following test case is called a "drasticity" test. It consists in quenching a cylindrical rod with an embedded thermocouple inside a liquid (see Figure 7.10). The temperature measurement is a good indicator of the quenching power of the coolant. It is also possible to determine the influence of the material properties and

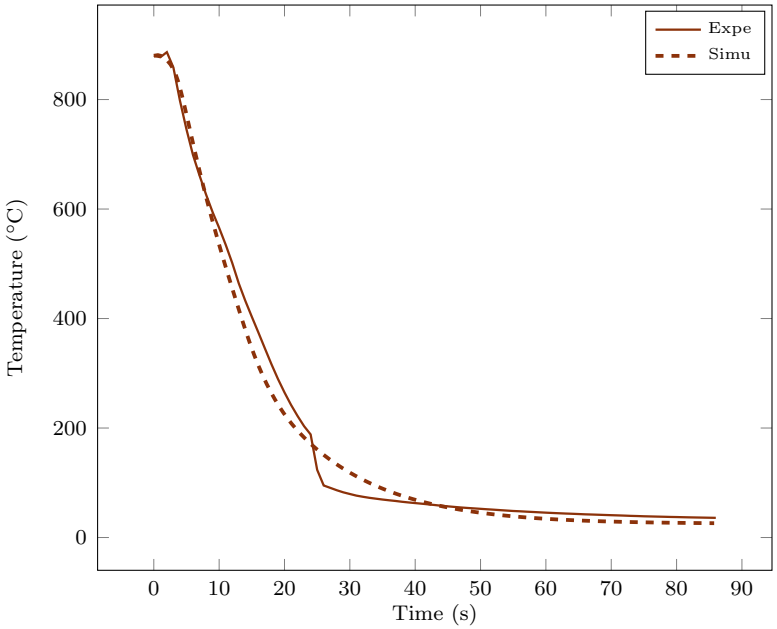

Figure 7.9: Comparison of simulated temperatures with experimental values.

surface quality (see for example [25]). We considered the case of the quenching of a Inconel probe heated at $T_w = 850\,°C$ inside a quenching oil medium at $T_\infty = 60\,°C$.

We ran the thermo-hydrodynamic simulation on a cylindrical domain of radius 62.5 mm and height 180 mm (see Figure 7.11). $3{\times}10^5$ nodes were considered, with a minimum mesh size $h_{\min} = 0.3\,mm$ imposed at the liquid vapour interface.

The physical parameters of the simulation are gathered in table 7.6. Density and heat capacity of the vapour phase were estimated of the same order of magnitude to those of water vapour. The viscosity of the vapour was raised to $8{\times}10^{-4}\,Pa\,s$ to stabilise the thermo-hydrodynamic simulation. According to a model similar to the Boundary Layer model of Section 6.2.2, this lead to an estimation of the mean vapour film thickness (around $5{\times}10^{-4}\,mm$). The conductivity of the vapour was then set to obtain a heat flux of the same order of magnitude as the experimental one (around $10^5\,W\,m^{-2}$). This lead to a value of $0.1\,W\,m^{-1}\,K^{-1}$. Values at T_{sat} were considered for the liquid and vapour phases for the thermal simulation.

Regarding boundary conditions of the thermo-hydrodynamics simulation, the temperature was fixed at T_w on the rod and at T_∞ on the other domain frontiers. No slip conditions were set on all mesh borders except on the top where zero gauge pressure with free output velocity was set. However a special treatment was done for the Boundary Conditions of nodes of inflow velocities at the top. For these nodes, the temperature was set to T_{sat} in the vapour phase and to a linear profile from T_{sat} to T_∞ in the liquid phase. The boundary conditions of the thermal simulation are

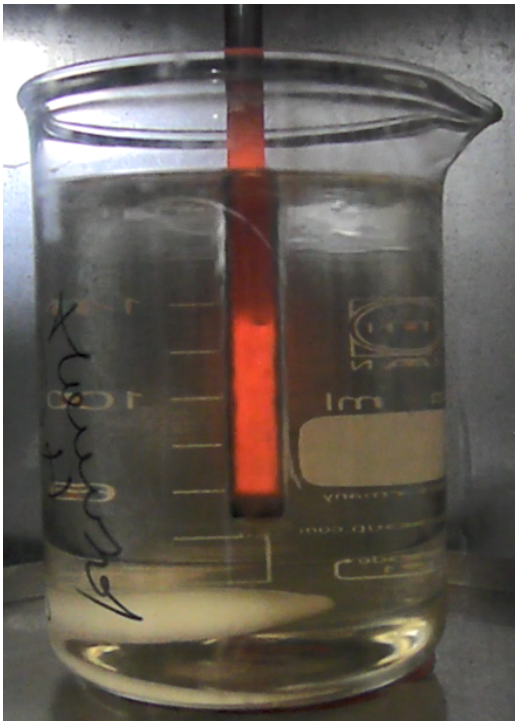

Figure 7.10: Picture of the drasticity test at one second after the start. The vapour film is very flat and regular around the rod.

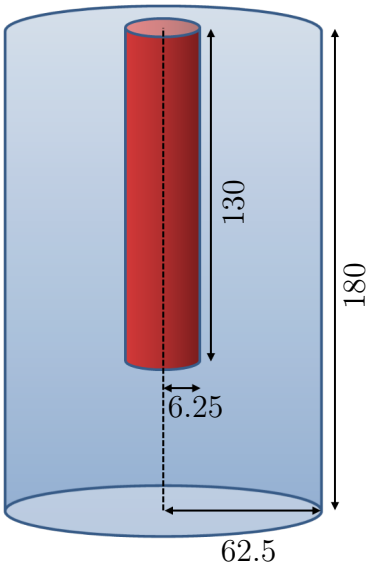

Figure 7.11: Schematic description of the computation domain for the pencil quenching. Values of lengths are given in mm.

	ρ ($\mathrm{kg\,m^{-3}}$)	η ($\mathrm{Pa\,s}$)	c_p ($\mathrm{W\,m^{-1}\,K^{-1}}$)	k ($\mathrm{J\,kg^{-1}\,K^{-1}}$)	$\mathcal{L}$ ($\mathrm{J\,kg^{-1}}$)	γ_0 ($\mathrm{J\,m^{-2}}$)	ε_w $(-)$
Thermo-hydrodynamic simulation							
Liquid	840	1.3×10^{-2}	1770	0.123	2.25×10^{6}	0.06	–
Vapour	1	8×10^{-4}	1000	0.1			–
Thermal simulation							
Liquid	840	1.3×10^{-2}	1770	0.123	2.25×10^{6}	0.06	–
Vapour	1	1.0×10^{-4}	1000	0.01			–
Solid	8470	–	444	20	–	–	0.5

Table 7.6: Properties of the liquid, vapour and solid phases for the drasticity quenching simulation.

Robin conditions with imposed heat fluxes from the nucleation-based model. The remeshing algorithm was called every 5 steps, and the LS was reinitialised every 2 steps.

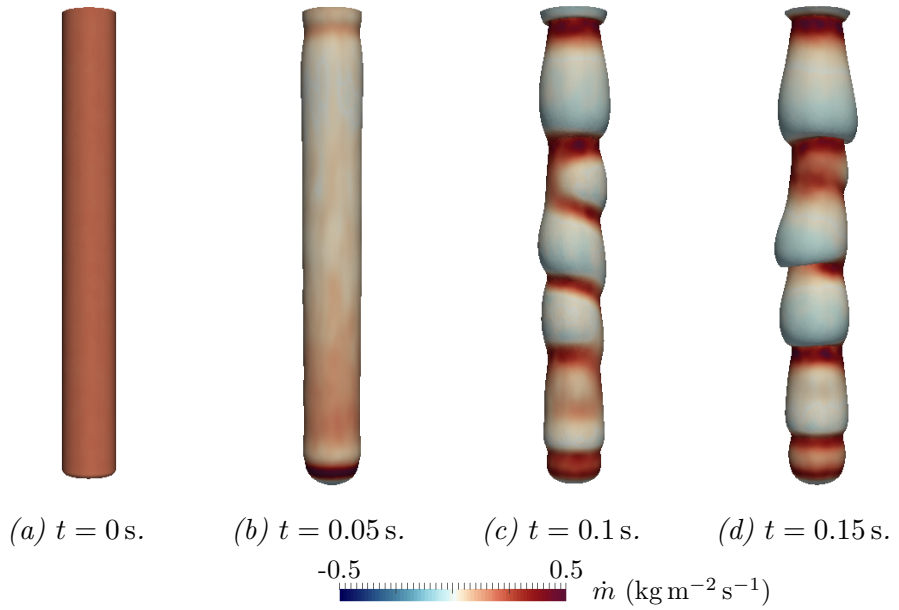

Figure 7.12: Visualisation of the simulated liquid vapour interface and mass transfer rate for the drasticity simulation. The vapour waves are important with vapour created from the bottom and rising along the rod. However this not consistent with experimental observations, as the film should be flatter.

The values of C_1 and C_2 were set to 0.19 and 0.8 respectively to match the experimental temperature profile. The nucleation-based model relies on correlations

that are not always adapted for coolant different from water. This is especially the case for the Leidenfrost temperature estimation. This explains the low value of C_1 to correct this bias. The thermo-hydrodynamic transient simulation ran for 0.5 s and the steady thermo-hydrodynamic simulation for 1 s.

A first simulation was done with no modification of the liquid conductivity on the heat flux jump computation. Visualisation of the liquid vapour interface at four time steps of the transient regime are plotted in Figure 7.12. Waves of vapour similar to the those of the vertical film boiling configuration are observed. The wavelength and wave amplitude are larger than the ones observed in the experiment (see Figure 7.10). As expected, the heat transfer is more intense at the bottom than at the top of the rod where vapour from below feeds the vapour film.

The temperature at the center of the rod is compared with experimental data in Figure 7.13. The first conclusion is that the numerical simulation is underpredicting heat fluxes in the calefaction mode. We conclude from this observation that liquid heat fluxes close to the liquid vapour interface are again underpredicted though oil is a more viscous medium.

Another simulation was performed with a factor 10 on the liquid conductivity used for the heat flux jump computation (model of convective conductivity k_{Leq}). The liquid vapour interface is plotted in Figure 7.14. This time the simulated film is very flat, which is expected in the case of a strong subcooling with a lot of heat

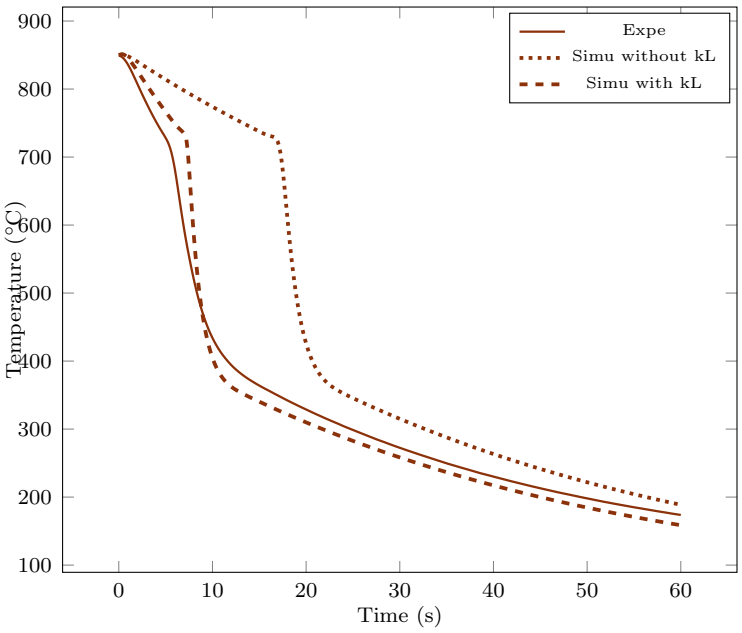

Figure 7.13: Comparison of simulated temperatures with experimental values for the drasticity case.

extracted by the water. The only vapour pockets created are at the bottom of the rod. The sharps edges create important wetting that lead to important heat fluxes and a strong vaporisation.

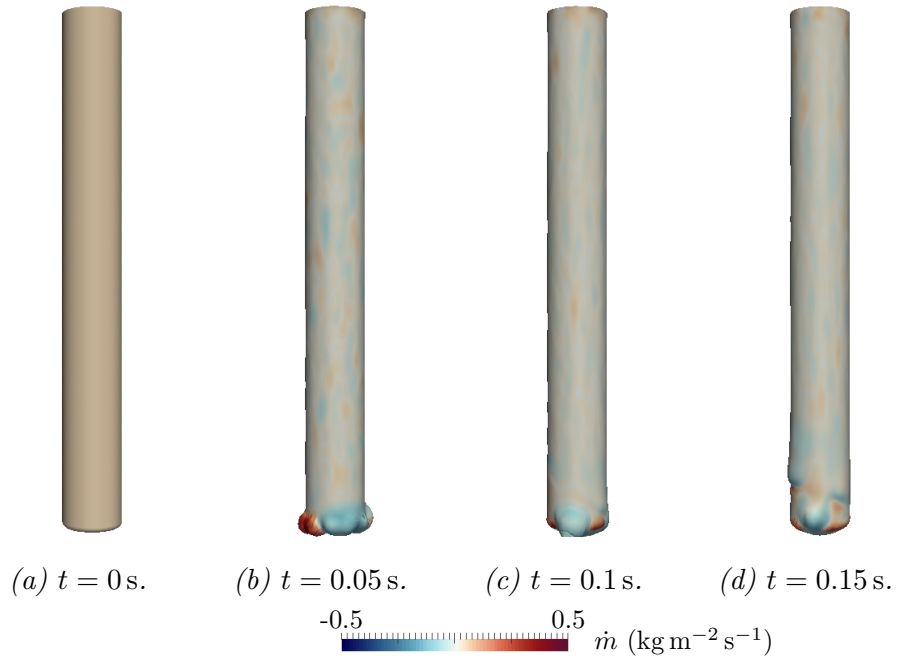

Figure 7.14: Visualisation of the simulated liquid vapour interface and mass transfer rate for the drasticity simulation with convective conductivity model. The film is flatter which is consistent with experimental observations. Mass transfer rates are also reduced.

Regarding the temperature variations, this modification leads to a better prediction of the cooling of the rod. The temperature in a cross section view of the rod as shown in Figure 7.15. The rod is cooled from the bottom. The progression of the vapour film front is more important than the experimental observations. A reason of this observation could be a lack of proper mass conservation as it was observed in Section 6.3.2. This leads to a smaller and more uniform vapour film that overestimates heat fluxes in the upper parts.

7.3.3 Overall observations on the quenching model

This model allows to simulate quenching experiments of long duration with moderate computational resources and acceptable fidelity. The thermo-hydrodynamic simulation performs well in describing the main features of the calefaction mode. And the nucleation-based model is robust for different coolants.

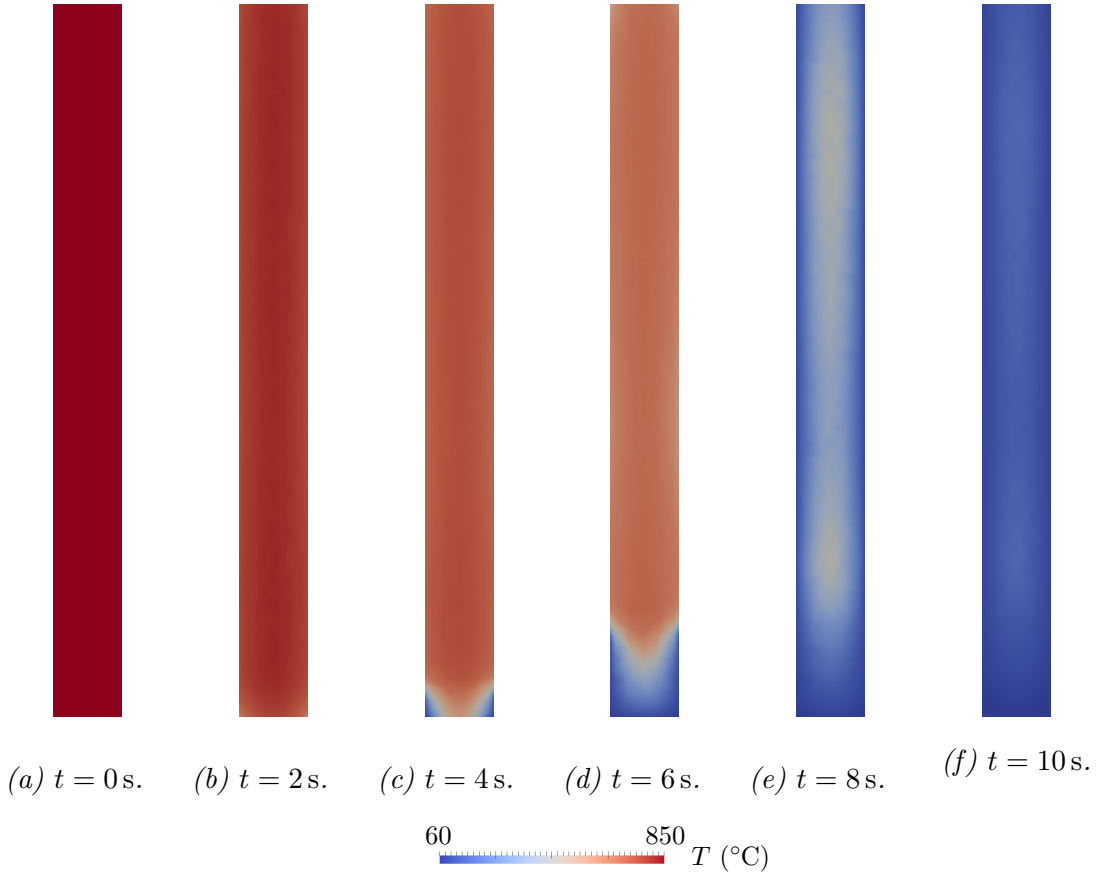

Figure 7.15: Cross section view of the temperature field from the thermal simulation of the drasticity case for different time steps. The bottom edges are the areas where the rod is cooled down the fastest.

We saw in Section 1.1.4.3 that the coupling between the dynamics of the cooling fluid and the thermics in the part is important [9]. This present quenching model offers a weak coupling between the two domains. An improvement would be to relaunch the thermo-hyrdodynamic simulation at different times of the thermal simulation to update the behavior of the vapour film during the calefaction mode, but at a cost.

The use of coefficients on the liquid conductivity reveals the need of further studies on the convection inside the liquid. Regarding the coefficients C_1 and C_2 that shape the Leidenfrost temperature, they highlight the difficulty to predict the effect of surface roughness on the vapour film collapse. Further study could be implemented to tackle this phenomena.

7.4 Conclusions

- The quenching time of an arbitrary part can be bounded by a uniform cooling with an estimated heat flux deduced from scaling laws, and by a temperature imposed cooling.
- A quenching model has been built to allow complete quenching simulations. It is based on an extrapolation of heat fluxes and vapour profiles from few seconds of simulations of the fluid domain. This information is integrated inside a thermal solver along with correlations to account for the entire boiling curve.
- The quenching model has been tested on the quenching of a small brick. It performs well in describing the global cooling of the part despite its simplicity and the assumptions that are considered. The unknown on the surface roughness lead to the consideration of two parameters that need to be evaluated for each case.
- The model has also been tested on a drasticity test with an oil coolant. This simulation demonstrated the potential of the model for other types of coolants than water. It enhanced the fact that the intense liquid side heat fluxes due to strong convection is also at play in oil.
- A jet quenching case has been considered (see Appendix D). A first analytical study has been performed. A strategy has then been adopted to proposed a simulation of the process for a moderate numerical budget. The main features of the process are well described though some parameters have to be evaluated.

Chapter 8

Conclusions and Perspectives

Résumé en Français

Ce chapitre présente les conclusions générales de ce travail de thèse expérimental et numérique, ainsi que les perspectives qui en découlent.

La librairie CIMLib-CFD pré-existante a été enrichie par un modèle complet de changement de phase adapté à une approche par interface régularisée. Ce modèle permet une bonne prise en compte des sauts de vitesse et de flux de chaleur, contrairement à ce qui existait précédemment. Il a été évalué à travers différents cas test analytiques, et montre de bonnes performances dans les configurations en mode film de vapeur. L'importance des effets convectifs proches de l'interface liquide / vapeur dans la phase liquide a aussi été soulignée. Ceux-ci sont estimés être dus aux petites perturbations subies par l'interface. Ce modèle a alors été intégré à un code de simulation de trempe en bain calme qui a été testé et validé sur des cas de tailles caractéristiques modestes.

De nombreuses perspectives ont été tracées. Parmi elles, l'importance d'un travail approfondi sur les solveurs utilisés pour permettre d'attaquer des cas plus complexes sans employer de stabilisation par une viscosité augmentée. Les problématiques de mouillage et de nucléation restent aussi à explorer afin de couvrir tous les modes d'ébullition. En parallèle, l'expérience mise en place offre de nombreuses améliorations afin de couvrir plus de températures et de potentiellement accroître notre compréhension des phénomènes convectifs dans le liquide. Enfin, le modèle de trempe mériterait d'être confronté à des cas industriels plus complexes afin d'évaluer ses capacités et les potentielles améliorations à apporter.

8.1 Conclusions

This thesis was dedicated to the development of a numerical model to simulate boiling flows with an application to the simulation of quenching. In this work, we tackled physical modeling, numerical methods, experimentation and industrial applications. We focused our work on the behavior of the liquid vapor interface and on the heat transfer involved between the boiling fluid and the solid.

We extended the tools available in the pre-existing finite element library of the laboratory by proposing a complete phase change model. The mass conservation was improved with a dedicated solver based on a preexisting version. Interfacial terms were also better modeled, with a new method to properly consider the interfacial energy conservation. This way, the resulting framework was applicable to subcooled configurations. This model was completed by a study of the boiling mode to propose a full quenching model that is applicable at an industrial scale. This work was supported by a series of physical analysis of results of the literature. Validations were conducted through numerical 2D and 3D benchmarks of increasing complexity. An experiment was also set up to provide additional answers on the physics of boiling, and provided an additional benchmark for the phase change solver.

In Chapter 1, the principal features of boiling were presented. An overview of the influential factors in play and of the main experimental observations and correlations was provided. An overview of the numerical solutions available in the literature were presented.

In Chapter 2, relevant approximations on the thermics were considered based on scaling analysis. This lead to the design of a thermal solver adapted to phase change problems. The Level Set method was presented along with a novel approach to compute heat fluxes at the interface. The diphasic solver was validated on three versions of the isochoric Stefan problem.

In Chapter 3, mass and momentum conservation equations were considered and simplified. Relevant approximation were made and justified that lead to the development of a dedicated solver from an existing version. This "pseudo-compressible" Navier–Stokes solver was tested and coupled with the diphasic framework. This mechanical multiphase environment was studied and validated with 2D benchmarks. The discretisation of the Dirac function was shown to be an important parameter for the good precision of the numerical tool.

In Chapter 4 the complete phase change model was presented and validated in benchmarks of increasing complexity. The subcooled Stefan problem proved the reliability of the framework to ensure proper mass and energy conservation at the interface for non oversaturated conditions. The Scriven benchmarks highlighted the limits of the solver in the presence of oversaturated phases. Such conditions were however out of the scope of this study, and did not prevent the framework to be

applicable to boiling simulations. Horizontal film boiling was considered in 2D and 3D and validated this conclusion.

In Chapter 5 an experiment of the quenching of small nickel sphere was presented. The set up of the experiment was detailed along with the measurement techniques and the associated uncertainties. The experiment provided a general description of the film boiling mode. The cooling rate and some hydrodynamical features were measured and compared with numerical simulation results with a laminar approach. A model of convective conductivity was proposed to correct non modeled phenomena in the liquid phase.

In Chapter 6 the vertical film boiling was discussed. A first analytical study was carried out to better understand the physics in play. Dominant terms and asymptotic behaviors were discussed and used to deeper challenge the phase change solver in the context of film boiling. 3D real size numerical simulations were carried out and compared with experimental results. The convective conductivity model was shown to successfully correct the laminar approach bias in subcooled conditions.

In Chapter 7 a quenching model was presented. The phase change framework was enriched with a "nucleation-based" model based on correlations to account for wetting phenomena at low temperatures. This resulted in a quenching model that integrates the boiling numerical simulation, the nucleation model and the interaction with a solid domain. Two real size pool quenches were simulated and compared with the experiments. The model was shown to perform well on small parts quenched in water but also in other types of coolants like oil. An analytical and numerical study of jet impingement quenching was also carried out (in the appendix).

Results of this work are currently being implemented in an industrial tool in the context of the industrial chair INFINITY.

8.2 Perspectives

The present work highlighted some interesting open questions to better understand boiling flows. Some challenges were also stressed to improve the capability of the solver and to provide a ready to use industrial software.

The phase change solver revealed numerical limits that would be interesting to tackle. First, the heat flux jump computation method showed some limits in the context of oversaturated configurations. Furthermore, the order one precision is also an area of improvement. A shock capturing approach for convection dominated flows at the iterface along with a stabilisation work in the context of Finite Element for multiphase flows could improve stability of the solution.

Still on the numerical side, a work could be done on the description of volume terms by the Dirac function. The richness of discretisation of this latter function was shown to be a limiting factor of the precision of the method. More generally,

an important and challenging path was drawn on the numerical stabilisation of the diphasic mechanical solver. This improvement would allow a finer description of the liquid vapor flows and allow numerous studies to improve the understanding of convectives flows at the interface which stressed some open questions.

The quenching model would benefit from a deepening in the modeling of wetting phenomena. A deeper study of the nucleation process and how to simulate it would then be valuable.

Regarding the sphere quenching experiment, it could be used as such to enrich the available data. More pool temperatures could be tackled with other geometries and material for the quenched solids. Different camera angles could be used to improve the accuracy of the measurement. The experiments could also be improved with a better control on the temperature and a more advanced camera set up to provide 3D information. This would reduce the uncertainties and provide a rich description of the boiling process.

Finally, the quenching model could be improved to tackle more complex industrial configurations with a better precision. The full coupling of the thermo-hydrodynamic solver with the thermics inside the part requires the simulation of large spatial domains and long durations. This would require an optimisation of the phase change solver to allow simulations of accessible computation times. A mean field approach could be a possible path to follow that would avoid the resolution of the entire liquid vapor interface.

Appendix A

Radiative effects

This section studies the mechanisms and scales of magnitude of radiation heat fluxes during boiling. The Stefan-Boltzmann law predicts that radiation scales in T_w^4, thus these phenomenon shall be more dominant in high temperatures in the film boiling regime. The film thickness being usually thin compared to the characteristic sizes of the quenched part, we consider a simplified case. Heat fluxes are supposed to be equivalent to those of an infinite solid plan at temperature T_w facing an infinite water plan at temperature T_{sat} and separated by a vapour layer of thickness e.

This study is separated in three questions:

- What is the radiation behavior of a metallic part at T_w, how can it be modeled and what are the order of magnitude of the radiation heat ?
- What is the influence of the vapour film on radiation ?
- How does the water react to radiation effect ?

A.1 Solid modeling

To begin with, most of quenched parts are metallic ones. Most of the time, metals are considered to be colored bodies, that means their emissivity vary and decrease with the frequency. However, the surface state makes the value of emissivity change a lot (from 0.02 to 0.9 for [42], for instance), and no accurate computation can be made without knowing precisely the emissivity (see [144]). Thus, a simple "grey body" model is enough. The emissivity ε_w shall be estimated empirically. For the computations to be conservative, it will be set to one for scaling laws computations.

The global emissive power q_{R} of a grey body of emissivity ε_w is given by the Stefan-Boltzmann law:

$$q_{\text{R}} = \varepsilon_w \sigma_{\text{SB}} T_w^4 \tag{A.1}$$

where $\sigma_{SB} = 5.67 \times 10^{-8}\,\mathrm{W\,m^{-2}\,K^{-4}}$ is the Stefan-Boltzmann constant. As a grey body, its radiation is distributed in the same way as a black body, whose behavior can be evaluated thanks to Planck's law (see Figure A.1)

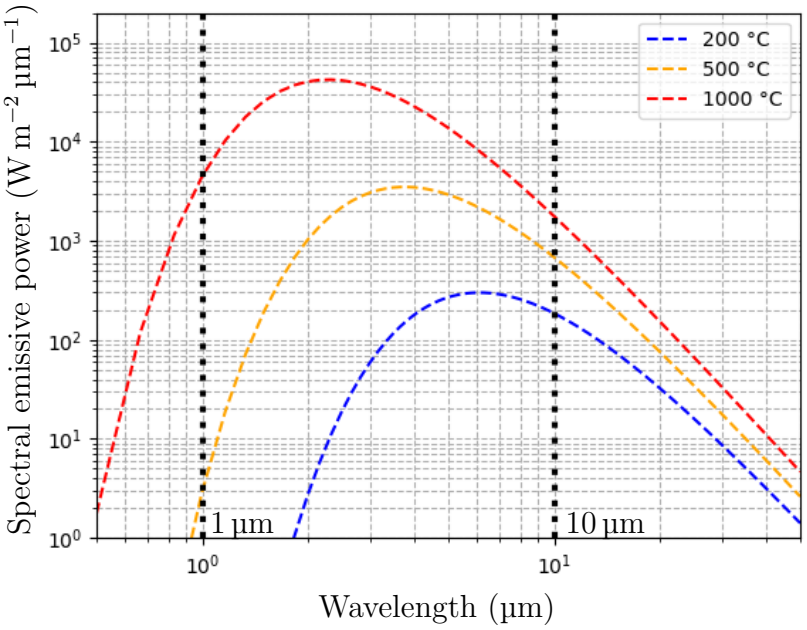

Figure A.1: Spectral emissive power as a function of the electromagnetic wave wavelength for three example temperatures of T_w.

The considered temperature range is from 200 °C (below, the film boiling regime is not valid anymore) to 1000 °C. In this temperature range, most of the heat flux power is approximately distributed for a wavelength $\lambda \in [1, 10]$µm (in the infra red, just after the visible spectrum). For a black body of 1000 °C, the total radiation heat flux is $1.5 \times 10^5\,\mathrm{W\,m^{-2}}$

A.2 Radiation through the vapour film

Considering the vapour film, [145] gives an estimate of the radiation of a layer of water vapour in percentage of the same radiation of a black body at the same temperature [145]. As a single body, and assuming that the Kirchhoff law is valid for such system, this evaluation gives us the magnitude of the absorbance of such vapour layer receiving radiations of a black body of the same temperature. Authors estimate that the radiation for a vapour layer of 10^{-3} m at a partial pressure of 1 bar

is of 1 % of a black body [145]. This is clearly negligible, and this means that the vapour layer can be considered as vacuum for the following radiation calculations.

This conclusion can be challenged by the measurement of the transmittance T of such vapour layer at 1000 °C. This corresponds to the proportion of electromagnetic waves that cross the film layer. The rest is absorbed by the gas. The Beer-Lambert law gives a relationship between the transmittance and the optical depth τ:

$$T = \mathrm{e}^{-\tau} \tag{A.2}$$

where τ is computed with the spectral line strength S, the spectral line profile shape f, the molecule concentration c and the optical length l:

$$\tau = fScl \tag{A.3}$$

The spectral line strength S profile is computed for water vapour at 1000 °C with an online model based on the Hitran database [146]. To be conservative, we consider the maximum value of S between the wavelength of maximum radiation of a black body at 1000 °C, thus between 1 µm and 10 µm (see Figure A.3). Results of the simulation are plotted in Figure A.3.

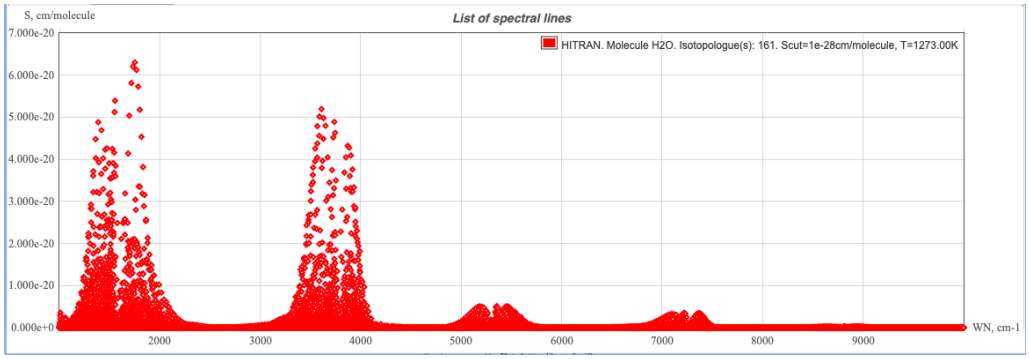

Figure A.2: The spectral line strength S profile is computed for water vapour at 1000 °C *(credits: simulation from Hitran [146])*

The maximum value of S is 7×10^{-20} cm at 5.5 µm. As f is a parameter between 0 and 1 cm, we will take the maximum value to be conservative. Vapour at 1000 °C has a concentration of particles of 7×10^{18} cm^{-3}. And a vapour film of 1 mm is considered for l. This leads to a value of $T = 0.95$. This means that with this extremely conservative consideration, only 5% of the electromagnetic waves are absorbed by the vapour film. Still with a conservative approach, the consideration that this is 5% of the total radiation of the black body leads to an absorbed heat flux of 7500 W m^{-2}. This is negligible in comparison with conductive heat fluxes in the vapour film for this boiling regime.

A.3 Water modeling

Finally, regarding the water side, two questions arise:

- What fraction of heat flux goes through the liquid/vapour interface ? What fraction is reflected back to the solid?
- Does the water let the radiation go through it without any diffusion? Or does it absorb all the heat flux and what size the absorbing layer is?

We obviously do not consider the radiation of water, whose temperature hits 100 °C at most. This is a range of temperature where radiation is negligible.

We answer the first question by considering the Fresnel coefficient r_A that characterize the parts of an electromagnetic wave being reflected and transmitted when going through an interface. The reflection coefficient reads:

$$r_A = \frac{\textbf{Amplitude of the reflected wave}}{\textbf{Amplitude of the incident wave}} = \frac{n_V - n_L}{n_V + n_L} \tag{A.4}$$

n_* being the refractive index of the domain $*$. This value changes with the considered wavelength, but for $\lambda \in [1\,\mu m; 10\,\mu m]$ variations of n_L remain limited (close to 1.3) even for high temperature variations [147, 148]. As for the vapour, it is very close to vacuum. This leads to a reflection coefficient of r_A of -0.14. Considering now the reflected energy, that is linked to the square of the wave amplitude, it is reflected with a ratio $r = r_A^2$. Thus, the heat flux reflection ratio r is about 0.02: most of the heat flux is transmitted to the vapour.

Now, regarding the absorbance of the electromagnetic wave, the characteristic absorbance length could be deduced from the absorbance spectrum of liquid water presented in Figure A.3 [149, 144].

For the considered wavelengths, the characteristic lengths of absorbance vary from 10 cm (1 µm) to 0.01 mm (10 µm). Obviously, all the heat flux is absorbed, and we can also deduce that most of it is absorbed on a layer very close to the liquid/vapour interface. Thus in this case, water can be considered as a grey body of emissivity $\varepsilon_w = 1 - r$ very close to 1, so, very close to the behavior of a black body.

Finally, the vapour being like vacuum and the water surface being close to a black body, the Stefan law A.1 is a good approximation of the radiation heat flux from the solid to the liquid surface. Furthermore, for most of the boiling processes where temperature are lower than 1000 °C, all the heat is absorbed at the liquid vapour interface.

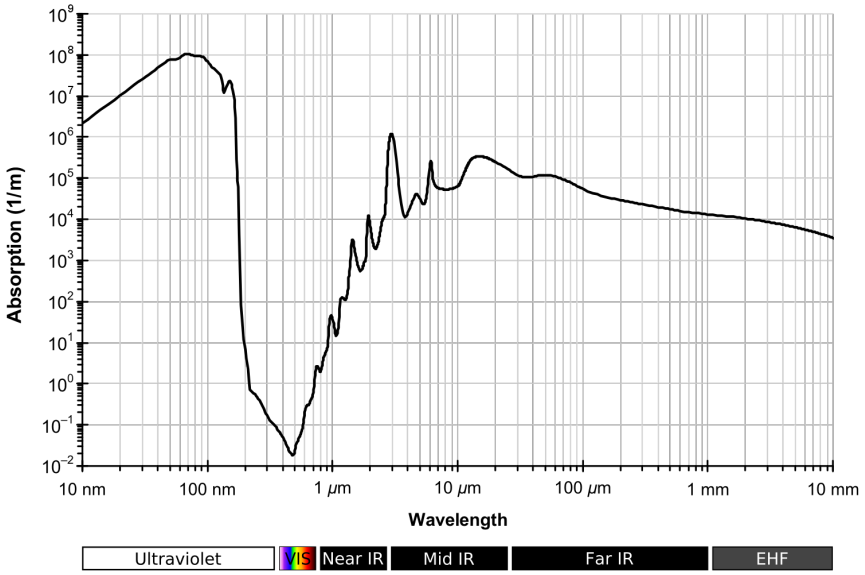

Figure A.3: Absorbance graph of water (credits: Kebes, data from [149])

Appendix B

Coherence between the monolithic and the sharp approach

We demonstrate here that the monolithic approach with a smoothed interface is equivalent to a sharp approach in the limit of a small ε.

On the one hand, we have the equation system of our phase change solver described at the beginning of Chapter 4 that we recall here:

$$
\begin{cases}
\underline{\text{Mass conservation:}} \\
\vec{\nabla}\cdot\vec{u} = \left[\!\left[\frac{1}{\rho}\right]\!\right]\left(\dot{\vec{m}}\cdot\vec{\nabla}\alpha\right)\delta_\alpha & \text{(B.1)} \\
\underline{\text{Momentum conservation:}} \\
\rho\left(\frac{\partial\vec{u}}{\partial t} + (\vec{u}\cdot\vec{\nabla})\vec{u}\right) = -\vec{\nabla}p + \vec{\nabla}\cdot 2\eta\dot{\vec{\boldsymbol{\varepsilon}}} + \rho\vec{g} + \gamma_0\kappa_\alpha\delta_\alpha\vec{\nabla}\alpha & \text{(B.2)} \\
\underline{\text{Energy conservation:}} \\
\rho c_{\text{P}}\left(\frac{\partial T}{\partial t} + \left(\vec{u}\cdot\vec{\nabla}\right)T\right) + A(T-T_{\text{sat}})\delta_\alpha = \vec{\nabla}\cdot k\vec{\nabla}T - \left(\mathcal{L}\dot{\vec{m}} + \vec{q_{\text{R}}}\right)\cdot\vec{\nabla}\alpha\delta_\alpha & \text{(B.3)} \\
\underline{\text{Level Set advection:}} \\
\frac{\partial\alpha}{\partial t} + \left(\vec{u} - \frac{\rho}{\rho_{\text{V}}\rho_{\text{L}}}\dot{\vec{m}} - \left[\!\left[\frac{1}{\rho}\right]\!\right]\dot{\vec{m}}\frac{\kappa_\alpha}{\|\vec{\nabla}\alpha\|}\int_{-\varepsilon}^{0} H_\alpha\,\mathrm{d}\alpha\right)\cdot\vec{\nabla}\alpha = 0 & \text{(B.4)} \\
\underline{\text{Energy conservation at the interface:}} \\
\mathcal{L}\left(\dot{\vec{m}}\cdot\vec{\nabla}\alpha\right) = \left[\!\left[k\vec{\nabla}T\cdot\vec{\nabla}\alpha\right]\!\right] - \vec{q_{\text{R}}}\cdot\vec{\nabla}\alpha & \text{(B.5)}
\end{cases}
$$

On the other hand, we have the three interface conservation equations and the condition on the interface velocity:

$$\begin{cases} \underline{\text{Mass conservation at the interface:}} \\ [\![\vec{u}\cdot\vec{n}]\!] = \left[\!\left[\frac{1}{\rho}\right]\!\right]\dot{m} \qquad \text{(B.6)} \\ \underline{\text{Momentum conservation at the interface:}} \\ \left[\!\left[\frac{1}{\rho}\right]\!\right]\dot{m}^2\vec{n} = -[\![p\vec{n}]\!] + [\![\boldsymbol{\tau}\vec{n}]\!] + \gamma_0\kappa\vec{n} \qquad \text{(B.7)} \\ \underline{\text{Energy conservation at the interface:}} \\ \mathcal{L}\left(\vec{\dot{m}}\cdot\vec{n}\right) = \left[\!\left[k\vec{\nabla}T\cdot\vec{n}\right]\!\right] - \vec{q_{\mathrm{R}}}\cdot\vec{n} \qquad \text{(B.8)} \\ \underline{\text{Interface Velocity:}} \\ \vec{u_{\mathrm{I}}}\cdot\vec{n} = \dfrac{[\![\rho\vec{u}\cdot\vec{n}]\!]}{[\![\rho]\!]} \qquad \text{(B.9)} \end{cases}$$

To recover the jump of a given quantity $(*)$ through the interface, we integrate it on the range $[x(\alpha=-\varepsilon), x(\alpha=\varepsilon)]$, where x is a local coordinate normal to the interface. We notice that a change of variable between x and α allows the following transformation:

$$\int_{x(\alpha=-\varepsilon)}^{x(\alpha=\varepsilon)} (*)\|\vec{\nabla}\alpha\|\,\mathrm{d}x = \int_{-\varepsilon}^{\varepsilon}(*)\,\mathrm{d}\alpha \qquad \text{(B.10)}$$

Finally, we recall that the Dirac function δ_α is such that:

$$\int_{-\varepsilon}^{\varepsilon}\delta_\alpha\,\mathrm{d}\alpha = 1 \qquad \text{(B.11)}$$

In the following section, we will consider a sufficient infinitesimal surface $\mathrm{d}S$ for $\dot{m}$ to be constant. We will also consider that the Level Set is properly built so that:

$$\vec{n} = \frac{\vec{\nabla}\alpha}{\|\vec{\nabla}\alpha\|} \qquad \text{(B.12)}$$

We also recall that $\dot{m}$ is signed. It is positive for vaporization and negative for condensation. As $\vec{n}$ points toward the vapor phase:

$$\vec{\dot{m}} = \dot{m}\vec{n} \qquad \text{(B.13)}$$

B.1 Mass conservation

Let us start with the velocity jump. To recover the velocity jump from the smoothed interface approach, we integrate B.1 following (B.10) :

The right-hand side term is easy to compute as the divergence term is obvious to integrate:

$$\int_{x(\alpha=-\varepsilon)}^{x(\alpha=\varepsilon)} \vec{\nabla}\cdot\vec{u}\ \mathrm{d}x = [\![\vec{u}\cdot\vec{n}]\!]_{x(\alpha=-\varepsilon)}^{x(\alpha=\varepsilon)} = [\![\vec{u}\cdot\vec{n}]\!] \tag{B.14}$$

Thanks to (B.10) and (B.11), integrating the left-hand leads to:

$$\int_{x(\alpha=-\varepsilon)}^{x(\alpha=\varepsilon)} \left[\!\left[\frac{1}{\rho}\right]\!\right] \left(\dot{\vec{m}}\cdot\vec{\nabla}\alpha\right)\delta_\alpha\ \mathrm{d}x = \left[\!\left[\frac{1}{\rho}\right]\!\right]\dot{m}\int_{-\varepsilon}^{\varepsilon}\delta_\alpha\ \mathrm{d}\alpha = \left[\!\left[\frac{1}{\rho}\right]\!\right]\dot{m} \tag{B.15}$$

We recover well the velocity jump from (B.6).

B.2 Interface velocity

Both formulations are consistent in regard to the interface velocity if the advection velocity of the LS from (B.4) at isovalue 0 must corresponds to $\vec{u_\mathrm{I}}$ given by (B.9). As only the normal component is important for the advection velocity:

$$\left(\vec{u} - \frac{\rho}{\rho_\mathrm{V}\rho_\mathrm{L}}\dot{\vec{m}} - \left[\!\left[\frac{1}{\rho}\right]\!\right]\dot{\vec{m}}\frac{\kappa_\alpha}{\|\vec{\nabla}\alpha\|}\int_{-\varepsilon}^{0} H_\alpha\ \mathrm{d}\alpha\right)_{|\alpha=0}\cdot\vec{n} \stackrel{?}{=} \frac{[\![\rho\vec{u}\cdot\vec{n}]\!]}{[\![\rho]\!]} \tag{B.16}$$

First of all, the importance of the second order term is of the order of magnitude of $\varepsilon\kappa_\alpha$ (see Appendix C). As the curvature is a geometric variable independent of numerical parameters, in the limit of a small ε this term vanishes.

Let us rewrite the rest of the left-hand side. First of all, in the same method as for the mass conservation, but this time integrating only from $x(\alpha=-\varepsilon)$ to $x(\alpha=0)$:

$$[\![\vec{u}\cdot\vec{n}]\!]_{x(\alpha=-\varepsilon)}^{x(\alpha=0)} = \frac{1}{2}\left[\!\left[\frac{1}{\rho}\right]\!\right]\dot{m} \tag{B.17}$$

From the velocity jump (B.6), we have:

$$\dot{m} = \frac{\rho_\mathrm{V}\rho_\mathrm{L}}{\rho_\mathrm{L}-\rho_\mathrm{V}}[\![\vec{u}\cdot\vec{n}]\!] \tag{B.18}$$

We define the local normal velocity components $[\![\vec{u}\cdot\vec{n}]\!] = u_V - u_L$. Combining (B.17) and (B.18) leads to:

$$\vec{u}_{|\alpha=0}\cdot\vec{n} = u_L + \frac{1}{2}\left[\!\left[\frac{1}{\rho}\right]\!\right]\frac{\rho_\mathrm{V}\rho_\mathrm{L}}{\rho_\mathrm{L}-\rho_\mathrm{V}}(u_V-u_L) \tag{B.19}$$

Regarding the second term, we recall that the density ρ is defined by an arithmetic weighing between ρ_V and ρ_L regarding H_α. Thus $\rho_{|\alpha=0} = \overline{\rho}$. Thus the second term at $\alpha = 0$ reads:

$$\left(\frac{\rho}{\rho_\mathrm{V}\rho_\mathrm{L}}\vec{\dot{m}}\right)_{\big|\alpha=0} \cdot \vec{n} = \frac{\overline{\rho}}{\rho_\mathrm{L} - \rho_\mathrm{V}}(u_V - u_L) \tag{B.20}$$

Removing (B.20) from (B.19):

$$\begin{aligned}
&\left(\vec{u} - \frac{\rho}{\rho_\mathrm{V}\rho_\mathrm{L}}\vec{\dot{m}}\right)_{\big|\alpha=0} \cdot \vec{n} \\
&\quad = u_L + \frac{1}{2}\left[\!\left[\frac{1}{\rho}\right]\!\right]\frac{\rho_\mathrm{V}\rho_\mathrm{L}}{\rho_\mathrm{L} - \rho_\mathrm{V}}(u_V - u_L) - \frac{\overline{\rho}}{\rho_\mathrm{L} - \rho_\mathrm{V}}(u_V - u_L) \\
&\quad = \frac{2\rho_\mathrm{L}u_L - 2\rho_\mathrm{V}u_L}{2(\rho_\mathrm{L} - \rho_\mathrm{V})} + \frac{1}{2}\frac{(\rho_\mathrm{L} - \rho_\mathrm{V})(u_V - u_L)}{\rho_\mathrm{L} - \rho_\mathrm{V}} - \frac{1}{2}\frac{(\rho_\mathrm{L} + \rho_\mathrm{V})(u_V - u_L)}{\rho_\mathrm{L} - \rho_\mathrm{V}} \\
&\quad = \frac{\rho_\mathrm{L}u_L - \rho_\mathrm{V}u_V}{(\rho_\mathrm{L} - \rho_\mathrm{V})} = \frac{[\![\rho\vec{u}\cdot\vec{n}]\!]}{[\![\rho]\!]}
\end{aligned} \tag{B.21}$$

We recover well the interface velocity from (B.9).

B.3 Momentum conservation

For the momentum conservation, we work with the Eulerian formulation which is equivalent to (B.2):

$$\frac{\partial\rho\vec{u}}{\partial t} + \vec{\nabla}\cdot(\rho\vec{u}\otimes\vec{u}) = \left(-\vec{\nabla}p + \vec{\nabla}\cdot 2\eta\dot{\boldsymbol{\varepsilon}} + \rho\vec{g} + \gamma_0\kappa_\alpha\delta_\alpha\vec{\nabla}\alpha\right)\cdot\vec{n} \tag{B.22}$$

If we integrate this equations, we first have the integral of the divergence term on the left-hand side. Considering only normal terms with the projection on $\vec{n}$:

$$\left(\int_{x(\alpha=-\varepsilon)}^{x(\alpha=\varepsilon)} \vec{\nabla}\cdot(\rho\vec{u}\otimes\vec{u})\,\mathrm{d}x\right)\cdot\vec{n} = [\![\rho\vec{u}(\vec{u}\cdot\vec{n})]\!]_{x(\alpha=-\varepsilon)}^{x(\alpha=\varepsilon)} \tag{B.23}$$

The integration of the time derivative term on the left-hand side is not as trivial. As both ρ and $\vec{u}$ are continuously facing a jump through their interface, we can approximate $\rho\vec{u} \sim [\![\rho\vec{u}]\!]H_\alpha + \rho_\mathrm{L}\vec{u}_L$. In reality, the product of ρ and $\vec{u}$ also leads to cross products between the liquid and vapour components and to a H_α^2 term. We use an approximation of quasi-static state, where variations of quantities around the interface vary less than the integral:

$$\frac{\partial\rho\vec{u}}{\partial t} \sim [\![\rho\vec{u}]\!]\frac{\partial H_\alpha}{\partial t} \sim [\![\rho\vec{u}]\!]\frac{\partial\alpha}{\partial t}\delta_\alpha \tag{B.24}$$

Using (B.5) with $\vec{u_\mathrm{I}}$ the advection velocity of the interface:

$$\frac{\partial \rho \vec{u}}{\partial t} \sim -[\![\rho \vec{u}]\!] \vec{u_\mathrm{I}} \cdot \vec{\nabla} \alpha \delta_\alpha \tag{B.25}$$

Thus in the first approximation of a constant advection velocity on the interface:

$$\int_{x(\alpha=-\varepsilon)}^{x(\alpha=\varepsilon)} \frac{\partial \rho \vec{u}}{\partial t} + \vec{\nabla} \cdot (\rho \vec{u} \otimes \vec{u}) \, \mathrm{d}x \sim -[\![\rho \vec{u}]\!] \vec{u_\mathrm{I}} \cdot \vec{n} \tag{B.26}$$

Adding (B.23) and (B.26)

$$\int_{x(\alpha=-\varepsilon)}^{x(\alpha=\varepsilon)} \frac{\partial \rho \vec{u}}{\partial t} \, \mathrm{d}x \sim [\![(\rho \vec{u}) \, (\vec{u} - \vec{u_\mathrm{I}}) \cdot \vec{n}]\!] = \left[\!\!\left[\frac{1}{\rho} \right]\!\!\right] \dot{m}^2 \vec{n} \tag{B.27}$$

The right hand side terms are more easy to integrate:

$$\int_{x(\alpha=-\varepsilon)}^{x(\alpha=\varepsilon)} -\vec{\nabla} p + \vec{\nabla} \cdot 2\eta \dot{\boldsymbol{\varepsilon}} + \rho \vec{g} + \gamma_0 \kappa_\alpha \delta_\alpha \vec{\nabla} \alpha \, \mathrm{d}x = [\![p]\!] + [\![\boldsymbol{\tau} \vec{n}]\!] + \gamma_0 \kappa \vec{n} \tag{B.28}$$

This first approximation leads to the sharp interface formulation. A better investigation would be required to ensure the proper mathematical equivalence. However, this is not fundamental for the present work as the time derivative term (the one that is not easy to integrate) is negligible in comparison to pressure and surface tension works. We can therefore be satisfied with this estimation.

B.4 Energy conservation

First of all, the energy conservation is by construction guaranteed thanks to (B.5). However this come along another important condition: the conservation of T_sat. Let us study the proper behavior of the stabilisation term on the left-hand side. To study its reliability, we integrate (B.3) on the interface.

Concerning the particle derivative of the temperature, if we approximate that the temperature at the interface is not changing much we have:

$$\frac{\partial T}{\partial t} + \vec{u_\mathrm{I}} \cdot \vec{\nabla} T = \frac{\partial T}{\partial t} + \left(\vec{u} - \frac{\rho}{\rho_\mathrm{V} \rho_\mathrm{L}} \vec{\dot{m}} \right) \cdot \vec{\nabla} T \simeq 0 \tag{B.29}$$

So under the condition of small temperature changes at the interface:

$$\int_{x(\alpha=-\varepsilon)}^{x(\alpha=\varepsilon)} \rho c_\mathrm{p} \left(\frac{\partial T}{\partial t} + (u \cdot \vec{\nabla}) T \right) \mathrm{d}x \simeq \int_{x(\alpha=-\varepsilon)}^{x(\alpha=\varepsilon)} \rho c_\mathrm{p} \frac{\rho}{\rho_\mathrm{V} \rho_\mathrm{L}} \vec{\dot{m}} \cdot \vec{\nabla} T \, \mathrm{d}x \tag{B.30}$$

$\rho^2 c_\mathrm{p}\vec{\nabla}T$ varies along the interface, but its values are finite: obviously $\rho < \max(\rho_\mathrm{V}, \rho_\mathrm{L})$ and $c_\mathrm{p} < \max(c_{\mathrm{p}\mathrm{V}}, c_{\mathrm{p}\mathrm{L}})$. Moreover as T is fixed close to T_sat at the interface, variations of $\vec{\nabla}T$ must be limited even for tiny interfaces. We should at least $|\nabla T| < \max(|\vec{\nabla}T_V|, |\vec{\nabla}T_L|)$. Thus:

$$\left| \int_{x(\alpha=-\varepsilon)}^{x(\alpha=\varepsilon)} \rho c_\mathrm{p} \left(\frac{\partial T}{\partial t} + (u \cdot \vec{\nabla})T \right) \mathrm{d}x \right| < \int_{x(\alpha=-\varepsilon)}^{x(\alpha=\varepsilon)} \left| \rho c_\mathrm{p} \frac{\rho}{\rho_\mathrm{V}\rho_\mathrm{L}} \dot{\vec{m}} \cdot \vec{\nabla}T \right| \mathrm{d}x \tag{B.31}$$

$$\left| \int_{x(\alpha=-\varepsilon)}^{x(\alpha=\varepsilon)} \rho c_\mathrm{p} \left(\frac{\partial T}{\partial t} + (u \cdot \vec{\nabla})T \right) \mathrm{d}x \right| < \frac{2\varepsilon}{\rho_\mathrm{V}\rho_\mathrm{L}} \max(|\rho_\mathrm{V}^2 c_{\mathrm{p}\mathrm{V}} \dot{\vec{m}} \cdot \vec{\nabla}T_V|, |\rho_\mathrm{L}^2 c_{\mathrm{p}\mathrm{L}} \dot{\vec{m}} \cdot \vec{\nabla}T_L|) \tag{B.32}$$

This terms tends towards 0 for in the limit of small ε.

In the limit of small variations of T at the interface, other terms of (B.3) are much easier to integrate:

$$\int_{x(\alpha=-\varepsilon)}^{x(\alpha=\varepsilon)} A(T - T_\mathrm{sat})\delta_\alpha \, \mathrm{d}x \simeq A(\overline{T} - T_\mathrm{sat}) \tag{B.33}$$

$$\int_{x(\alpha=-\varepsilon)}^{x(\alpha=\varepsilon)} \vec{\nabla} \cdot k\vec{\nabla}T \, \mathrm{d}x = [\![k\vec{\nabla}T]\!] \tag{B.34}$$

$$\int_{x(\alpha=-\varepsilon)}^{x(\alpha=\varepsilon)} \left(\mathcal{L}\dot{\vec{m}} + \vec{q_\mathrm{R}} \right) \cdot \vec{\nabla}\alpha\delta_\alpha \, \mathrm{d}x = \left(\mathcal{L}\dot{\vec{m}} + \vec{q_\mathrm{R}} \right) \cdot \vec{n} \tag{B.35}$$

At the end of the day, in the limit of small ε and moderate variations of T around T_sat at the interface, the integration of the energy conservation on the interface reads:

$$A(\overline{T} - T_\mathrm{sat}) \simeq [\![k\vec{\nabla}T]\!] - \left(\mathcal{L}\dot{\vec{m}} + \vec{q_\mathrm{R}} \right) \cdot \vec{n} \tag{B.36}$$

The right-hand side of the equation is exactly the energy jump. Thus if this jump is properly computed, then the stabilization term ensures that $T = T_\mathrm{sat}$ at the interface. This proves that the implementation is consistent.

Appendix C

Second order Level Set advection velocity correction

The goal of this appendix is:

- to demonstrate the origin of the second order bias on the LS advection velocity on a simple case.
- to deduce an expression of a corrective term to account for this bias.

We recall the mass conservation equation and the advection equation of the level set:

$$\begin{cases} \nabla \cdot \vec{u} = \left[\!\left[\frac{1}{\rho}\right]\!\right] \left(\vec{\dot{m}} \cdot \vec{\nabla}\alpha\right) \delta_\alpha & \text{(C.1)} \\ \frac{\partial \alpha}{\partial t} + \left(\vec{u} - \frac{\rho}{\rho_\mathrm{V}\rho_\mathrm{L}}\vec{\dot{m}}\right) \cdot \vec{\nabla}\alpha = 0 & \text{(C.2)} \end{cases}$$

We consider the Growing Bubble theoretical case presented in Section 3.4.2. A vapor bubble of radius $\overline{R}$ is growing inside a liquid phase due to a given mass transfer $\vec{\dot{m}}$ (see Figure C.1.

C.1 Consistence regarding the mass flux

We recall that the theoretical velocity jump reads:

$$[\![\vec{u}]\!] = \left[\!\left[\frac{1}{\rho}\right]\!\right] \vec{\dot{m}} \tag{C.3}$$

The velocity in the vapor being null, this velocity jump entails a mass flux $\mathcal{Q}$ at the interface Γ of the bubble of radius $\overline{R}$:

$$\mathcal{Q} = 2\pi\overline{R} \left[\!\left[\frac{1}{\rho}\right]\!\right] \dot{m} \tag{C.4}$$

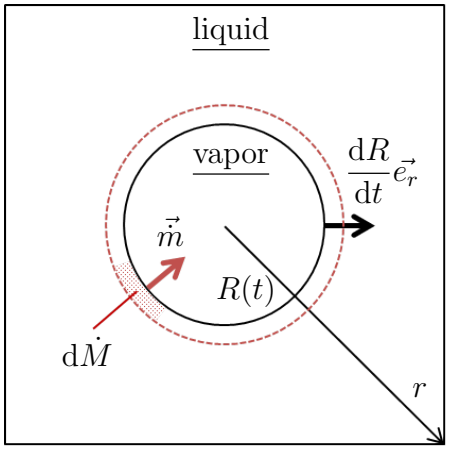

Figure C.1: Representation of Growing Bubble case.

Let us assess if the divergence velocity expression (C.1) is well adapted to respect this velocity jump. To do so, we integrate equation (C.1) on the whole interface Γ between $\overline{R}-\varepsilon$ et $\overline{R}+\varepsilon$. We will compare the result with the velocity flux given by (C.4). We use a cylindrical coordinate system. We assumed that the LS is well reinitialized and that the distance property is respected. This means that $\alpha = \overline{R}-r$. We recall that $\vec{\nabla}\alpha$ points towards the vapor phase, so toward the center of the bubble (as the LS is the distance function, then $\vec{\nabla}\alpha = -\vec{e_r}$). This is also the case for $\vec{\dot{m}}$ with vaporization, with $\vec{\dot{m}} = -\dot{m}\vec{e_r}$ if we consider that $\dot{m}$ is positive.

$$
\begin{aligned}
\int_\Gamma \vec{\nabla}\cdot\vec{u}\,\mathrm{d}S &= \int_0^{2\pi}\int_{\overline{R}-\varepsilon}^{\overline{R}+\varepsilon} \left[\!\left[\frac{1}{\rho}\right]\!\right]\left(\vec{\dot{m}}\cdot\vec{\nabla}\alpha\right)\delta_\alpha r\,\mathrm{d}r\,\mathrm{d}\theta \\
&= \left[\!\left[\frac{1}{\rho}\right]\!\right]\dot{m}\int_0^{2\pi}\int_{\overline{R}-\varepsilon}^{\overline{R}+\varepsilon}\delta_\alpha r\,\mathrm{d}r\,\mathrm{d}\theta \\
&= \left[\!\left[\frac{1}{\rho}\right]\!\right]\dot{m}2\pi\int_\varepsilon^{-\varepsilon}\delta_\alpha(\overline{R}-\alpha)(-\,\mathrm{d}\alpha) \\
&= \left[\!\left[\frac{1}{\rho}\right]\!\right]\dot{m}2\pi\left(\int_{-\varepsilon}^{\varepsilon}\delta_\alpha\overline{R}\,\mathrm{d}\alpha - \int_{-\varepsilon}^{\varepsilon}\delta_\alpha\alpha\,\mathrm{d}\alpha\right) \\
&= \left[\!\left[\frac{1}{\rho}\right]\!\right]\dot{m}2\pi\left(\overline{R} - \int_{-\varepsilon}^{\varepsilon}\delta_\alpha\alpha\,\mathrm{d}\alpha\right) \qquad \text{(C.5)}
\end{aligned}
$$

The function $\delta_\alpha\alpha$ being antisymmetric, the right-hand side integral is null. This means that the mass conservation is respected as we well recover the velocity flux given by (C.4).

C.2 Consistence regarding the liquid velocity profile

Let us verify that the velocity profile in the liquid phase is properly computed. In the case of a static bubble, the vapor velocity is null ($u(r < \overline{R} - \varepsilon) = 0$) and the liquid velocity is that of a point source flow with mass flux $\mathcal{Q}$. Such velocity profile reads:

$$\vec{u} = u_r(r)\vec{e_r} \tag{C.6}$$

with:

$$u_r = \frac{\overline{R}}{r}\left[\!\left[\frac{1}{\rho}\right]\!\right]\dot{m} \tag{C.7}$$

Let us integrate (C.1) between $\overline{R} - \varepsilon$ and r. We have on the one hand:

$$\int_{\overline{R}-\varepsilon}^{r} \vec{\nabla}\cdot\vec{u}\,\mathrm{d}r = \int_{\overline{R}-\varepsilon}^{r} \frac{\partial r u_r}{\partial r}\,\mathrm{d}r = \big(ru_r - (\overline{R}-\varepsilon)u_r(\overline{R}-\varepsilon)\big) = ru_r \tag{C.8}$$

On the other hand:

$$\begin{aligned}
\int_{\overline{R}-\varepsilon}^{r} r\left[\!\left[\frac{1}{\rho}\right]\!\right]\left(\vec{\dot{m}}\cdot\vec{\nabla}\alpha\right)\delta_\alpha\,\mathrm{d}r &= \left[\!\left[\frac{1}{\rho}\right]\!\right]\dot{m}\int_{\varepsilon}^{\alpha}(\overline{R}-\alpha)\delta_\alpha(-\,\mathrm{d}\alpha)\\
&= \left[\!\left[\frac{1}{\rho}\right]\!\right]\dot{m}\left(\int_{\alpha}^{\varepsilon}\overline{R}\delta_\alpha\,\mathrm{d}\alpha - \int_{\alpha}^{\varepsilon}\alpha\delta_\alpha\,\mathrm{d}\alpha\right)\\
&= \left[\!\left[\frac{1}{\rho}\right]\!\right]\dot{m}\left(\overline{R}(1-H_\alpha) - [\![\alpha H_\alpha]\!]_\alpha^\varepsilon + \int_{\alpha}^{\varepsilon}H_\alpha\,\mathrm{d}\alpha\right)\\
&= \left[\!\left[\frac{1}{\rho}\right]\!\right]\dot{m}\left(\overline{R}(1-H_\alpha) - (\varepsilon - \alpha H_\alpha) + \int_{\alpha}^{\varepsilon}H_\alpha\,\mathrm{d}\alpha\right)\\
&= \left[\!\left[\frac{1}{\rho}\right]\!\right]\dot{m}\left(\overline{R}(1-H_\alpha) + \alpha H_\alpha - \int_{-\varepsilon}^{\alpha}H_\alpha\,\mathrm{d}\alpha\right)
\end{aligned} \tag{C.9}$$

Knowing that $\int_{-\varepsilon}^{\varepsilon} H_\alpha \,\mathrm{d}\alpha = \varepsilon$:

$$\begin{aligned}
\int_{\overline{R}-\varepsilon}^{r} r \left[\!\left[\frac{1}{\rho}\right]\!\right] \left(\vec{\dot{m}} \cdot \vec{\nabla}\alpha\right) \delta_\alpha \,\mathrm{d}r &= \left[\!\left[\frac{1}{\rho}\right]\!\right] \dot{m} \left(\overline{R}(1-H_\alpha) + \alpha H_\alpha - \int_{-\varepsilon}^{\alpha} H_\alpha \,\mathrm{d}\alpha\right) \\
&= \left[\!\left[\frac{1}{\rho}\right]\!\right] \dot{m} \left((\overline{R}-\alpha)(1-H_\alpha) + \alpha - \int_{-\varepsilon}^{\alpha} H_\alpha \,\mathrm{d}\alpha\right) \\
&= \left[\!\left[\frac{1}{\rho}\right]\!\right] \dot{m} \left(r(1-H_\alpha) + \alpha - \int_{\varepsilon}^{-\alpha} H_\alpha(-\alpha)(-\,\mathrm{d}\alpha)\right) \\
&= \left[\!\left[\frac{1}{\rho}\right]\!\right] \dot{m} \left(r(1-H_\alpha) + \alpha + \int_{\varepsilon}^{-\alpha} 1 - H_\alpha \,\mathrm{d}\alpha\right) \\
&= \left[\!\left[\frac{1}{\rho}\right]\!\right] \dot{m} \left(r(1-H_\alpha) + \alpha + (-\alpha-\varepsilon) - \int_{\varepsilon}^{-\alpha} H_\alpha \,\mathrm{d}\alpha\right) \\
&= \left[\!\left[\frac{1}{\rho}\right]\!\right] \dot{m} \left(r(1-H_\alpha) - \varepsilon - \left(\int_{\varepsilon}^{-\varepsilon} H_\alpha \,\mathrm{d}\alpha + \int_{-\varepsilon}^{-\alpha} H_\alpha \,\mathrm{d}\alpha\right)\right) \\
&= \left[\!\left[\frac{1}{\rho}\right]\!\right] \dot{m} \left(r(1-H_\alpha) - \int_{-\varepsilon}^{-\alpha} H_\alpha \,\mathrm{d}\alpha\right) \qquad \text{(C.10)}
\end{aligned}$$

If we compare (C.8) and (C.10) we recover the velocity of a fluid particle between $\overline{R}-\varepsilon$ and r:

$$u_r = \left[\!\left[\frac{1}{\rho}\right]\!\right] \dot{m} \left((1-H_\alpha) - \frac{1}{r}\int_{-\varepsilon}^{r-\overline{R}} H_\alpha \,\mathrm{d}\alpha\right) \qquad \text{(C.11)}$$

We verify that u_r connects well with the analytical expression of the fluid flow in the liquid phase (C.7). At $r = \overline{R}+\varepsilon$ we have $\alpha(r=\overline{R}+\varepsilon) = -\varepsilon$ and $H_\alpha = 0$. Thus we recover well:

$$u_r(r=\overline{R}+\varepsilon) = \frac{\overline{R}}{\overline{R}+\varepsilon} \left[\!\left[\frac{1}{\rho}\right]\!\right] \dot{m} \qquad \text{(C.12)}$$

C.3 Consistence regarding the interface advection velocity

In the present case, the vapor phase gains $\dot{m}$ kg of fluid per surface unit and per second. This leads to a displacement:

$$\vec{u_\mathrm{I}} = -\frac{1}{\rho_\mathrm{V}}\vec{\dot{m}} \qquad \text{(C.13)}$$

Let us now verify if the 0 isovalue of the LS is advected with the same velocity. We have from (C.2)

$$\vec{u_\mathrm{I}} = \vec{u} - \frac{\rho}{\rho_\mathrm{V}\rho_\mathrm{L}}\vec{\dot{m}} \qquad \text{(C.14)}$$

What matters is the value of $\vec{u_{\mathrm{I}}}$ at the 0 isovalue. We have $H_\alpha(\alpha = 0) = 1/2$ and as ρ is determined following an arithmetical law, $\rho(\alpha = 0) = (\rho_{\mathrm{V}} + \rho_{\mathrm{L}})/2$. Using (C.11):

$$\vec{u_{\mathrm{I}}}(\alpha = 0) = -\left[\!\left[\frac{1}{\rho}\right]\!\right] \vec{\dot{m}} \left(\frac{1}{2} - \frac{1}{\overline{R}} \int_{-\varepsilon}^{0} H_\alpha \, \mathrm{d}\alpha\right) - \frac{1}{2}\left(\frac{1}{\rho_{\mathrm{V}}} + \frac{1}{\rho_{\mathrm{L}}}\right) \vec{\dot{m}} \tag{C.15}$$

Simplifying:

$$\vec{u_{\mathrm{I}}}(\alpha = 0) = -\frac{1}{\rho_{\mathrm{V}}}\alpha = 0 + \left[\!\left[\frac{1}{\rho}\right]\!\right] \frac{\vec{\dot{m}}}{\overline{R}} \int_{-\varepsilon}^{0} H_\alpha \, \mathrm{d}\alpha \tag{C.16}$$

Which is not the same expression as (C.13). The error is small only if:

$$1 >> \left[\!\left[\frac{1}{\rho}\right]\!\right] \frac{\rho_{\mathrm{V}}}{\overline{R}} \int_{-\varepsilon}^{0} H_\alpha \, \mathrm{d}\alpha \tag{C.17}$$

$[\![1/\rho]\!]$ is usually of the same order of magnitude as ρ_{V}, and $\int_{-\varepsilon}^{0} H_\alpha \, \mathrm{d}\alpha$ is of the same order of magnitude as ε. Consequently the error is small if:

$$\overline{R} >> \varepsilon \tag{C.18}$$

This is usually the case as ε is expected to be at least one scale of magnitude lower than the characteristic length of the flow. This is the reason why this is only an order 2 bias.

The correction of this bias is then easy and only requires to remove the additional term of (C.16) from the interface velocity of (C.2). The new advection velocity reads:

$$\vec{u_{\mathrm{I}}} = \vec{u} - \frac{\rho}{\rho_{\mathrm{V}}\rho_{\mathrm{L}}}\vec{\dot{m}} - \left[\!\left[\frac{1}{\rho}\right]\!\right] \kappa_\alpha \vec{\dot{m}} \int_{-\varepsilon}^{0} H_\alpha \, \mathrm{d}\alpha \tag{C.19}$$

where κ_α is the curvature computed thanks to α. This allows to generalize the result to any kind of interface topology. Attention has to be paid on κ_α which is signed (see Figure 2.3)

This suits for a case where the distance property of the LS is respected. In a case where the LS is not properly reinitialized, the gradient of the LS has to be taken into account. This introduces additional difficulties in the calculations which make them tedious. In a first approximation, we can play on this parameter directly on the final formula of the correction. A sort of "dimensional analysis" is done considering that α is not homogeneous to a length. For (C.19) to be homogeneous, we must divide the second term by $\|\vec{\nabla}\alpha\|$:

$$\vec{u_{\mathrm{I}}} = \vec{u} - \frac{\rho}{\rho_{\mathrm{V}}\rho_{\mathrm{L}}}\vec{\dot{m}} - \left[\!\left[\frac{1}{\rho}\right]\!\right] \frac{\kappa_\alpha}{\|\vec{\nabla}\alpha\|}\vec{\dot{m}} \int_{-\varepsilon}^{0} H_\alpha \, \mathrm{d}\alpha \tag{C.20}$$

C.4 Analytical expression for a sinusoidal smoothing

Considering a sinusoidal smoothing, the analytical expression of H_α reads:

$$H_\alpha = \frac{1}{2}\left(1 + \frac{\alpha}{\varepsilon} + \frac{1}{\pi}\sin\left(\frac{\alpha\pi}{\varepsilon}\right)\right) \tag{C.21}$$

An integral of H_α is:

$$\int H_\alpha = \frac{1}{2}\left(\alpha + \frac{\alpha^2}{2\varepsilon} - \frac{\varepsilon}{\pi^2}\cos\left(\frac{\alpha\pi}{\varepsilon}\right)\right) \tag{C.22}$$

Computing the integral:

$$\int_{-\varepsilon}^{-\alpha} H_\alpha \,\mathrm{d}\alpha = \frac{1}{2}\left(\frac{\varepsilon}{2} - \frac{\varepsilon}{\pi^2} - \alpha + \frac{\alpha^2}{2\varepsilon} - \frac{\varepsilon}{\pi^2}\cos\left(\frac{\alpha\pi}{\varepsilon}\right)\right) \tag{C.23}$$

Thus:

$$\int_{-\varepsilon}^{0} H_\alpha \,\mathrm{d}\alpha = \left(\frac{1}{4} - \frac{1}{\pi^2}\right)\varepsilon \tag{C.24}$$

Appendix D

Jet quenching

The jet quenching consists in cooling a part with a liquid jet at high velocity. This cooling process is usually used for thin metal plates.

The main characteristics of jet quenching are described in Figure D.1. At the very beginning of the quench, a vapour cushion separates the plate from the liquid. However, this vapour film rapidly collapses at the bottom of the jet. Then, a circular wetting fronts appears whose radius increase with time. The velocity of this wetting front is crucial as it is correlated with intense heat fluxes. In the wetted zone, a strong nucleate boiling mode is in play. When the temperature of the part drops below T_{sat}, a single phase forced convection ends to cool down the part to the liquid's temperature.

Heat fluxes in play are very intense, and can go up to few MW m^{-2} [150] even during calefaction [151]. The large momentum of the liquid allows to break the vapour film at very high temperatures. For instance, Agrawal et al. [152] measured

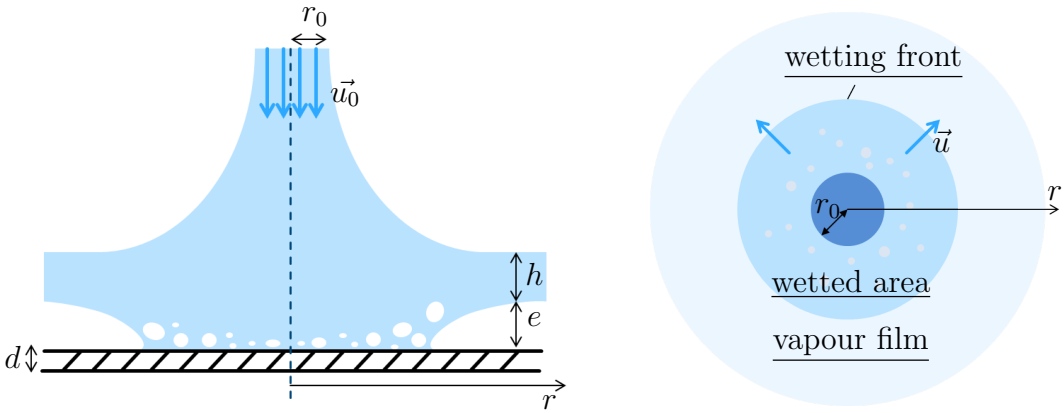

(a) Cross section view *(b) View from the top*

Figure D.1: Global description of the water jet quenching process.

u_0	r_0	T_w	d
$6.1\,\mathrm{m\,s^{-1}}$	$3\,\mathrm{mm}$	$450\,^\circ\mathrm{C}$	$3\,\mathrm{mm}$

Table D.1: Principal characteristics of the considered water jet quenching case.

rewetting temperatures up to 800 °C in water. The wetting temperature is the largest below the jet and then decreases with the distance from the jet.

As expected, the faster the jet, the more intense the cooling [153] with a faster wetting front [152, 154]. The liquid temperature has an impact mostly during the nucleate boiling mode and the single phase mode [155]. Finally, the surface roughness also significantly improves the wetting [156].

This Appendix aims at studying this process as it also interests our industrial partners. We sought to find the scales of magnitude of velocities, lengths and heat fluxes involved in the liquid and vapour phase. We evaluated the relevance of a simple numerical approach to describe the main features of such system. To do so, a combination of numerical simulation and modeling was implemented.

D.1 Main features of jet quenching

We define the input water jet velocity u_0, the input water jet radius r_0, the plate overheating ΔT_w and the plate thickness d. For numerical applications, we considered the values of an experiment carried by Arcelor Mittal research group (see [157]). They are gathered in Table D.1. Properties of the nickel are taken for the plate, and of water and water vapour for the fluid. The study domain is an area of around 50 mm around the jet, which is roughly $10r_0$.

D.1.0.1 Characteristic times

We first computed the characteristic times of thermal conductive and convective effects:

- Estimation of the characteristic time of heat conduction in the part:

$$\tau_\mathrm{c} \simeq \frac{\rho_\mathrm{S} c_{\mathrm{p}\mathrm{S}}}{k_\mathrm{S}} d^2 \simeq 1\,\mathrm{s} \tag{D.1}$$

- Estimation of the characteristic time of heat conduction in the liquid:

$$\tau_\mathrm{c} \simeq \frac{\rho_\mathrm{L} c_{\mathrm{p}\mathrm{L}}}{k_\mathrm{L}} h^2 \tag{D.2}$$

  with h the thickness of the liquid layer. This time equals around $10^2\,\mathrm{s}$ at the level of the jet ($h \simeq r_0$) and 1 s at the edge of the interest domain (with a $1/r$ ratio with h under the jet)

- Estimation of the characteristic time of heat convection in the liquid:

$$\tau_c \simeq \frac{10 r_0}{u_0} \simeq 5{\times}10^{-3}\,\mathrm{s} \tag{D.3}$$

The hydrodynamic regime can then be considered steady in regards to the thermal effects.

D.1.0.2 Interface temperature

In the configuration of a thermal diffusive chock between two phases, the temperature is imposed by the phase of highest effusivity $\sqrt{\rho c_p k}$. In the configuration of a water ($\sqrt{\rho_L c_{pL} k_L} \simeq 10^3\,\mathrm{kg\,K^{-1}\,s^{-2.5}}$) /nickel ($\sqrt{\rho_S c_{pS} k_S} \simeq 10^4\,\mathrm{kg\,K^{-1}\,s^{-2.5}}$) contact, the solid imposes its temperature.

However, convective effects in the liquid phase at the jet impact enhance by far the temperature gradients in the liquid side. We tried to estimate the resulting equivalent conductivity thanks to the following scaling law:

$$\rho_L c_{pL} u_0 \frac{\Delta T}{r_0} T \sim k_{Leq} \frac{\Delta T}{r_0^2} \tag{D.4}$$

This leads to a value of $k_{Leq} \sim 7{\times}10^4\,\mathrm{W\,m^{-1}\,K^{-1}}$ and to an equivalent effusivity 10^5 times higher. This demonstrates that at the impact the liquid imposes its temperature to the solid. This effect is less significant far from the jet as the velocity is mostly horizontal. The latter conclusion holds for a configuration of monophasic impact. In the case of vaporisation, the vapour film insulates the solid surface.

We proposed to specifically study the calefaction mode analytically. During this mode, a vapour film separates the liquid from the heated plate. This vapour film is believed to act as a kind of lubrication layer. Thus it seemed acceptable to break down the problem in two sub-problems:

- A water jet impacting a viscous free plane at T_{sat}.
- A vapour film bounded by the liquid interface at T_{sat} and the solid at T_w.

We considered a steady state regime for both problems as the hydrodynamics is faster than the thermics. The maximum radius considered was $r_{max} = 10 r_0 = 3cm$.

D.2 Hydrodynamics of the liquid film

We first computed the Reynolds number of the considered flow from h and u:

$$\mathrm{Re} = \frac{\rho_L h u}{\eta_L} = \frac{\rho_L Q_0}{2\pi r \eta_L}, \tag{D.5}$$

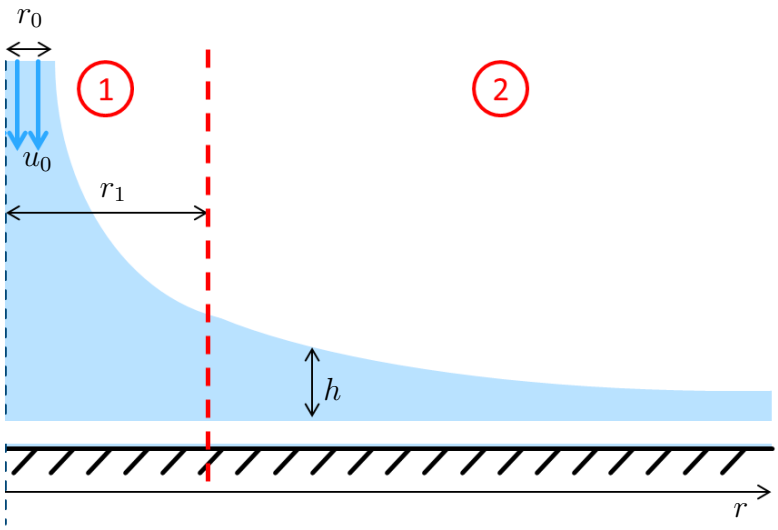

Figure D.2: Model of the liquid film. We consider two domains: a impact domain and a free surface domain.

where Q_0 is the input volume flow rate, and r is the axial coordinate. The second form of the Reynolds number was deduced from the mass conservation of a liquid ring in the approximation of a horizontal flow, which is a good approximation far from the jet:

$$Q_0 = 2\pi r h u. \tag{D.6}$$

Taking the considered flow values for the maximum considered radius, the Reynolds number is around 10^4. This is a convective regime with a flow that is assumed to be decomposed in a very small boundary layer and a free flow above. Thus is seems acceptable to study the water jet independently of the vapour behavior, as if it was evolving on a viscous free surface.

We decompose the liquid film in two domains as shown in Figure D.2. At the impact, a potential flow is considered. Far from the jet, the liquid velocity is assumed to be horizontal.

D.2.1 Liquid model far from the jet

The Reynolds number of the flow being important, it seems acceptable to consider the model of a perfect fluid. We apply Bernoulli's law on a liquid streamline:

$$\frac{p}{\rho} + \frac{1}{2}u^2 + gh = C, \tag{D.7}$$

with C a constant of space and time. Considering a streamline far from the jet, the pressure is close to the atmospheric pressure. Moreover gh is of the order of magnitude of $10^{-2}\,\mathrm{m^2\,s^{-2}}$, compared to u^2 which is rather around $10^{1}\,\mathrm{m^2\,s^{-2}}$. The kinetic energy term is dominant, and we can therefore make the approximation that u is globally constant inside the liquid layer, equal to u_0. This approximation is supported by observations of Bohr et al. [158] for the flow before the hydraulic jump. Considering their estimate of the radius of the hydraulic jump, the considered radii are smaller.

From the mass conservation of a liquid ring in the approximation of a horizontal flow, the thickness of the liquid layer reads:

$$h = \frac{Q_0}{2\pi u_0 r}, \tag{D.8}$$

This gives us a lower bound for the value of h as the viscous effects might slow down the fluid and thus make the water film thicker.

D.2.2 Liquid model at the jet impact

Near the bottom of the jet, the approximation of horizontal velocity is not relevant. We therefore consider a right angle type flow (see [159, 160]):

$$\vec{u} = ar\vec{e_r} - 2az\vec{e_z}, \tag{D.9}$$

where a is a coefficient to be determined. The value of a can be found by considering the radius r_1 away of the jet ($r >> z$) where the velocity field matches the former formulation:

$$u_0 = ar_1 \tag{D.10}$$

A choice has to be make for r_1, that should be of the order of magnitude of few r_0 so that the vertical term of the velocity field is negligible, and that the velocity profile matches the previous one (acceptable for $h(r_1) >> r_1$).

To find the value of h, we consider the streamlines of such flow of the form $azr^2 = C$ with C a constant of the streamline. Connecting h at $r = r_1$ to (D.8):

$$h = \frac{r_1 r_0^2}{2r^2} \tag{D.11}$$

To summarize, the liquid velocity field reads:

$$\begin{cases} \vec{u} = \dfrac{r}{r_1} u_0 \vec{e_r} - 2\dfrac{z}{r_1} u_0 \vec{e_z} & \text{for } r < r_1 \quad \text{(D.12)} \\ \vec{u} = u_0 \vec{e_r} & \text{for } r > r_1 \quad \text{(D.13)} \end{cases}$$

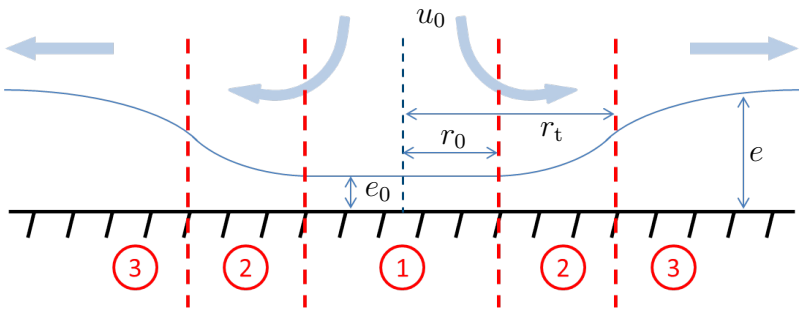

Figure D.3: Model of the vapour film. We consider three domains: (1) the impact zone below the jet where the vapour undergoes a high pressure leading to a large velocity, (2) the viscous zone where the vapour's velocity is reduced, and (3) a vaporisation domain, where vaporisation feeds the vapour film at constant velocity.

with the associated liquid film thickness:

$$\begin{cases} h = \dfrac{r_1 r_0^2}{2r^2} & \text{for } r_0 < r < r_1 \quad \text{(D.14)} \\ h = \dfrac{Q_0}{2\pi u_0 r} & \text{for } r > r_1 \quad \text{(D.15)} \end{cases}$$

D.3 Hydrodynamics of the vapour film

We decompose the vapour film in three domains as shown in Figure D.3. At the impact, a constant thickness is considered and the velocity is assumed to balance the pressure that holds the liquid jet. Close to the jet, the resulting high velocity is reduced by viscous effects. Far from the jet, the velocity is assumed constant and the vapour film is fed by the vaporising liquid.

D.3.1 Vapour film model under the jet impact

We consider the vapour flow always mostly radial ($v_z = 0$), the negligible gravity and the pressure above as constant (free jet above the vapour).

At the impact of the jet, the overpressure that the vapour film experiences to maintain the vapour layer is $\rho_L u_0^2/2$. The vapour then expands radially with an output velocity u_{V0} that is supposed to be high. Momentum variations are then large, and for such Reynolds numbers, the Bernoulli's law is supposed to be once again valid. Considering the atmospheric pressure at the outlet of the vapour disc under the jet:

$$u_{V0} = \sqrt{\frac{\rho_L}{\rho_V}} u_0 \quad \text{(D.16)}$$

that equals $249\,\mathrm{m\,s^{-1}}$ in our context.

With the assumption of linear heat fluxes inside the vapour layer, the mass flux reads:

$$\mathcal{L}\dot{m} = \frac{k_\mathrm{V}\Delta T_w}{e_0} \tag{D.17}$$

where e_0 is the vapour film thickness at the impact of the jet. The mass balance on the disc of vapour below the jet reads:

$$\dot{m}_0\pi r_0^2 = \rho_\mathrm{V} 2\pi r_0 e_0 u_{\mathrm{V}0} \tag{D.18}$$

Combining all the equations together leads to the expression of the vapour film thickness below the jet:

$$e_0 = \sqrt{\frac{r_0 k_\mathrm{V}\Delta T_w}{2\rho_\mathrm{V} u_{\mathrm{V}0}\mathcal{L}}} \tag{D.19}$$

This yields a value of about 0.01 mm, related to a thermal flux of $10^6\,\mathrm{W\,m^{-2}}$. This is the scale of magnitude observed by Bogdanic et al. [151].

D.3.2 Vapour film model outside the impact zone

We now consider the vapour outside the circle $r > r_0$. The velocity is considered steady and radial $\vec{u} = u\vec{e_r}$. A mass balance between r_0 and r reads:

$$\dot{m}_0\pi r_0^2 + \int_{r_0}^{r} \dot{m}(\tilde{r}) 2\pi\tilde{r}\,\mathrm{d}\tilde{r} = \rho_\mathrm{V} 2\pi r e u \tag{D.20}$$

Considering conductive heat fluxes:

$$\dot{m}_0\pi r_0^2 + \int_{r_0}^{r} \frac{2\pi\tilde{r}k_\mathrm{V}\Delta T_w}{\mathcal{L}e(\tilde{r})}\,\mathrm{d}\tilde{r} = \rho_\mathrm{V} 2\pi r e u \tag{D.21}$$

The momentum conservation equation is required to close the system.

Regarding pressure effects the liquid jet is similar to a free flow. As the hydrostatic pressure is negligible, the pressure is considered constant in the whole vapour layer outside of the impact. Regarding viscous effects, normal terms are dominant in regards to tangential terms. The momentum conservation equation then reads:

$$\rho_\mathrm{V} u\frac{\partial u}{\partial r} = \eta_\mathrm{V}\frac{\partial^2 u}{\partial z^2} \tag{D.22}$$

We are mainly interested in finding e. We thus simplify the system by considering the mean velocity $\overline{u}$ along with a model of Poiseuille flow profile for the velocity:

$$u = \overline{u}(r)\frac{6z(e-z)}{e^2} \tag{D.23}$$

This form assumes that the vapour flow is slowed down on its two boundaries. It is therefore valid as long as $\overline{u} >> u_0$. For low vapour velocities away from the jet, we expect the liquid film to drag the vapour. The vapour average velocity should be then around $u_0/2$. The Poiseuille form (D.23) will then be considered with a correction $\overline{u} \longrightarrow \overline{u} + u_0/2$ for low velocity profiles. This last form is the expression of a combination of a slowed down speed $\overline{u}$ and a driven speed $u_0/2$.

Integrating (D.22) between 0 and e:

$$\int_0^e \rho_V u \frac{\partial u}{\partial r} \, \mathrm{d}z = \eta_V \left[\frac{\partial u}{\partial z}\right]_0^e \tag{D.24}$$

Injecting (D.23) into this equation, and after some mathematical manipulations, the considered system to be solved reads:

$$\begin{cases} \dot{m}_0 \pi r_0^2 + \displaystyle\int_{r_0}^{r} \frac{2\pi \tilde{r} k_V \Delta T_w}{\mathcal{L} e(\tilde{r})} \, \mathrm{d}\tilde{r} = \rho_V 2\pi r e \left(\overline{u} + \frac{u_0}{2}\right) & \text{(D.25)} \\ e^2 \dfrac{\mathrm{d}\overline{u}}{\mathrm{d}r} + \dfrac{e\,(\overline{u} + u_0/2)}{2} \dfrac{\mathrm{d}e}{\mathrm{d}r} = -\dfrac{10\eta_V}{\rho_V} & \text{(D.26)} \end{cases}$$

The integration of this system to recover e and $\overline{u}$ is not straightforward. Thus we decompose the vapour film layer in two domains as shown in Figure D.3. The first one for $r \in [r_0, r_t]$ is a viscous domain where the vapour is slowed down by viscous effects to the liquid velocity u_0. The mass flux due to vaporisation is considered negligible. The film thickness variation is due to the deceleration of vapour. The second domain for $r > r_t$ is a vaporising vapour film at constant velocity.

D.3.2.1 Viscous domain

In this domain vaporisation effects are neglected. Thus the mass conservation equation (D.25) reads:

$$\dot{m}_0 \pi r_0^2 = \rho_V 2\pi r_0 e_0 u_{V0} = \rho_V 2\pi r e \left(\overline{u} + \frac{u_0}{2}\right) \tag{D.27}$$

In the approximation of $\overline{u} >> u_0/2$, (D.26) reads:

$$(r_0 e_0 u_{V0})^2 \left(\frac{1}{r^2 \overline{u}^2} \frac{\mathrm{d}\overline{u}}{\mathrm{d}r} + \frac{1}{2r} \frac{\mathrm{d}}{\mathrm{d}r}\left[\frac{1}{r\overline{u}}\right]\right) = -\frac{10\eta_V}{\rho_V} \tag{D.28}$$

This partial differential equation is the expression of two terms on the momentum. The first term is the reduction of the velocity (negative). The second term is the increase in the film thickness for a given velocity (positive). The first term is dominant as the sum of these two terms is negative. Either the second term

is negligible, either it is of the same order of magnitude. To evaluate this, let us approximate the velocity as a power function $\overline{u} \propto r^{\beta}$. Doing so:

$$\frac{1}{r^2\overline{u}^2}\frac{\mathrm{d}\overline{u}}{\mathrm{d}r} + \frac{1}{2r}\frac{\mathrm{d}}{\mathrm{d}r}\left[\frac{1}{r\overline{u}}\right] \propto \beta r^{-\beta-3} - (\beta+1)r^{-\beta-3} \propto -1 \tag{D.29}$$

Thus the only way this relation can hold is for $\beta = -3$. In this approximation:

$$\frac{1}{2r}\frac{\mathrm{d}}{\mathrm{d}r}\left[\frac{1}{r\overline{u}}\right] \propto -\frac{\beta+1}{\beta}\frac{1}{r^2\overline{u}^2}\frac{\mathrm{d}\overline{u}}{\mathrm{d}r} \propto -\frac{2}{3}\frac{1}{r^2\overline{u}^2}\frac{\mathrm{d}\overline{u}}{\mathrm{d}r} \tag{D.30}$$

This means that the two terms are of the same order of magnitude. Back to (D.28), the simplification given by (D.30) leads to the new form of the momentum conservation equation:

$$\frac{\mathrm{d}\overline{u}}{\overline{u}^2} = -\frac{30\eta_{\mathrm{V}}}{\rho_{\mathrm{V}}\left(r_0 e_0 u_{\mathrm{V0}}\right)^2} r^2\,\mathrm{d}r \tag{D.31}$$

This differential equation only describes the variation of $\overline{u}$, thus its integration needs to account for the correction with the driving velocity:

$$\left[\frac{1}{u_{\mathrm{V0}} - u_0/2} - \frac{1}{\overline{u} - u_0/2}\right] = -\frac{30\mu_V}{\rho_{\mathrm{V}}(r_0 e_0 u_{\mathrm{V0}})^2}\frac{1}{3}\left[r^3 - r_0^3\right] \tag{D.32}$$

The velocity profile then reads:

$$\overline{u} = \frac{u_0}{2} + \frac{u_{\mathrm{V0}} - u_0/2}{1 + \left[r^3 - r_0^3\right]/r_{\mathrm{c}}^3} \tag{D.33}$$

with $r_{\mathrm{c}} = \left(\dfrac{\rho_{\mathrm{V}}(r_0 e_0)^2 u_{\mathrm{V0}}}{10\mu_V}\right)^{1/3}$ (the approximation $u_{\mathrm{V0}} >> u_0$ has been made) the characteristic radius of the viscous domain. In the present work: $r_{\mathrm{c}} = 0,8mm \simeq r_0/3$.

The associated film thickness then reads:

$$e = e_0\frac{r_0}{r}\frac{u_{\mathrm{V0}}}{\dfrac{u_0}{2} + \dfrac{u_{\mathrm{V0}} - u_0/2}{1 + \left[r^3 - r_0^3\right]/r_{\mathrm{c}}^3}} \tag{D.34}$$

The velocity then scales like r^{-3}. This validates the simplification (D.30). We consider this velocity and thickness profiles up to a radius r_{t} where the mean velocity is assumed to be stabilised to $u_0/2$ and when the approximations of the negligible influence of vaporisation on e does not hold anymore.

D.3.2.2 Deceleration domain

In this domain, the velocity is assumed to be constant, equal to $u_0/2$. The derivation of (D.25) in regards to r then reads:

$$\frac{e^2}{r} + e\frac{\partial e}{\partial r} = \frac{k_\mathrm{V}\Delta T_w}{\mathcal{L}\rho_\mathrm{V}u_0/2} \tag{D.35}$$

We define $f(r) = e^2(r)$:

$$\frac{f}{r} + \frac{1}{2}\frac{\partial f}{\partial r} = \frac{k_\mathrm{V}\Delta T_w}{\mathcal{L}\rho_\mathrm{V}u_0/2} \tag{D.36}$$

The solutions of this differential equation read:

$$f(r) = \lambda\frac{1}{r^2} + \frac{2k_\mathrm{V}\Delta T_w}{3\mathcal{L}\rho_\mathrm{V}u_0/2}r \tag{D.37}$$

with λ the integration constant that is defined with the condition $e(r = r_\mathrm{t}) = e_\mathrm{t}$. The equivalent vapour film thickness then reads:

$$e = \sqrt{e_\mathrm{t}^2\frac{r_\mathrm{t}^2}{r^2} + \frac{4k_\mathrm{V}\Delta T_w}{3\mathcal{L}\rho_\mathrm{V}u_0}\left(r - \frac{r_\mathrm{t}^3}{r^2}\right)} \tag{D.38}$$

D.3.2.3 Determination of the transition radius

There is a trade-off in choosing r_t. It shall be large enough so that $\overline{u}$ is close to $u_0/2$, but not too large so that vaporization is taken into account as accurately as possible. The final thickness profile does not exactly verify the integrated mass conservation equation, this error is considered acceptable as a first approximation providing that the difference $\overline{u}(r_\mathrm{t}) - u_0/2$ is not too large. A 10 % error leads to a value of $r_\mathrm{t} = 7\,\mathrm{mm}$. Let us have a look at the influence of the choice of r_t on the profile of e which is of particular interest in this work. Profiles e for different values of r_t are shown in Figure D.4. For large r the influence of r_t on e is negligible. Close to the transition, the profile is not strongly impacted by the choice of r_t either.

We therefore choose $r_\mathrm{t} = 7\,\mathrm{mm}$ for our present analysis. At the boundary, we have $\overline{u}_\mathrm{t} = 1.1u_0/2 = 3.37\,\mathrm{m\,s^{-1}}$ and $e_\mathrm{t} = 0.2\,\mathrm{mm}$. The error on the transition speed is acceptable and at the same time the area where vaporization is neglected is small.

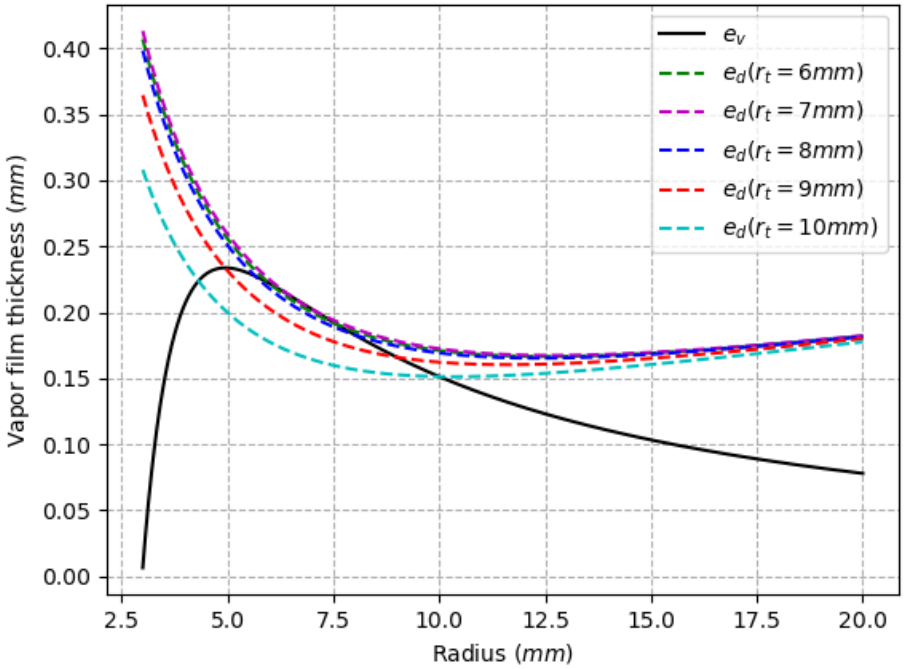

Figure D.4: Profile of the vapour film thickness in the viscous domain and in the deceleration domain for different values of r_t

To summarize, the vapour profile reads:

$$\begin{cases} e = e_0 = \sqrt{\dfrac{r_0 k_V \Delta T_w}{2\rho_V u_{V0} \mathcal{L}}} & \text{for } r < r_0 \quad \text{(D.39)} \\ e = e_0 \dfrac{r_0}{r} \dfrac{u_{V0}}{\dfrac{u_0}{2} + \dfrac{u_{V0} - u_0/2}{1 + [r^3 - r_0^3]/r_c^3}} & \text{for } r_0 < r < r_t \quad \text{(D.40)} \\ e = \sqrt{e_t^2 \dfrac{r_t^2}{r^2} + \dfrac{4k_V \Delta T_w}{3\mathcal{L}\rho_V u_0} \left(r - \dfrac{r_t^3}{r^2} \right)} & \text{for } r > r_t \quad \text{(D.41)} \end{cases}$$

with $e_t = e(r = r_t)$ defined by the viscous expression and with r_c a characteristic radius of viscous effects:

$$r_c = \left(\frac{\rho_V (r_0 e_0)^2 u_{V0}}{10 \mu_V} \right)^{1/3} \quad \text{(D.42)}$$

In the present work: $r_c = 0,8mm \simeq r_0/3$.

Such estimation of the vapour film thickness lead to an estimation of heat fluxes with a conductive estimation: $q_w = k_V \Delta T_w / e$. Values of theses two parameters for different radii are presented in Table D.2. The magnitudes computed are consistent with the measurements of [151] in calefaction mode.

	$r = r_0$	$r = r_t$	$r = 20\,\text{mm}$	$r = 40\,\text{mm}$
e (mm)	0.006	0.2	0.18	0.25
q_w (MW m^{-2})	1.37	0.043	0.048	0.036

Table D.2: Values of vapour film thicknesses and heat fluxes for the saturated calefaction mode of jet quenching at different radius for the studied configuration of [157].

The cooling curves of [157] in calefaction mode lead to a slope of around $5\,\text{K s}^{-1}$ far from the jet. The copper plate being very thin, the cooling is close to be uniform over the height of the plate. Thus this cooling is linked with a heat flux of around $0.07\,\text{MW m}^{-2}$. In practice, this estimate is a bit large because the plate undergoes non negligible radial conductive fluxes that evacuates the heat away from the jet impact. In any case the magnitudes are the same between experimental measurements of and our estimates. This is very satisfactory for a first simple analysis.

D.4 Jet quenching simulation

D.4.1 Modeling approach

The combination of high Reynolds number flow in the liquid jet and of small characteristic lengths at the fluid-solid interface is numerically challenging. The simulation of such intense heat fluxes at small scales with our phase change model would require an important dedicated work. It would also require the design of an adapted mesh as well as a specific attention on wetting phenomena that are even more complex in this configuration.

Such considerations are outside the scope of this present work. We proposed instead a combined analytical and simulated approach with a separation in three zones as shown in Figure D.5. The liquid zone (1) and the solide zone (3) were simulated. The vaporisation zone (2) was modeled. Convective effects are faster than thermal ones. So we first simulated a monophasic mean velocity profile for the liquid zone (1). This was based on the assumption that vaporisation effects do not disturb too much the liquid flow. Then, we computed the thermics both inside the liquid (1) and the solid (3). The vapour phase and vaporisation effects were modeled (zone (2) and drove the thermal conditions between the liquid and the solid.

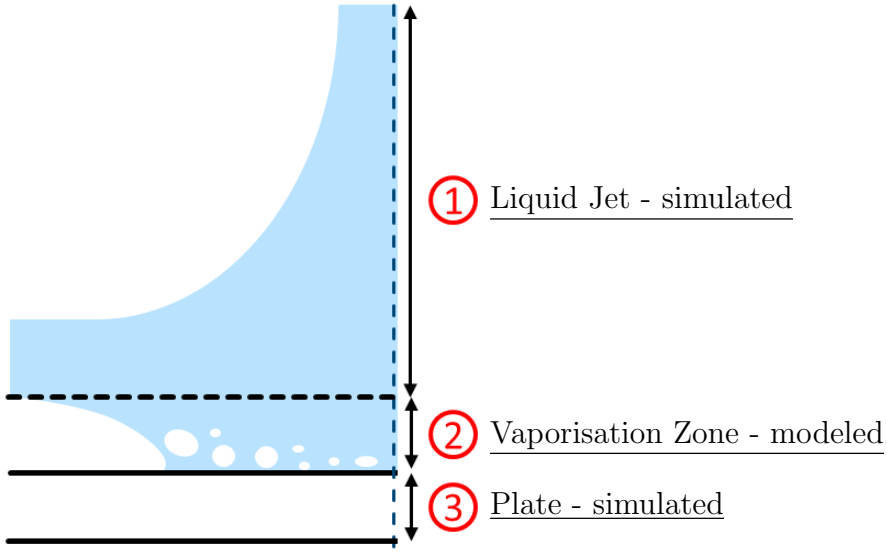

Figure D.5: Separation of the problem of Jet Quenching. The liquid zone (1) and the solide zone (3) were simulated. The vaporisation zone (2) was modeled.

Hydrodynamics The hydrodynamics simulation was undertaken with the Navier-Stokes diphasic solver upon which the phase change is built on. However, no phase change effects were considered between water and air. A Level Set method was used to separated both phases along with a remeshing algorithm to properly capture the interface. To guaranty a proper mass conservation, the Level Set convection velocity was corrected close to the interface thanks to the analytical solution provided by Section D.2.

For the simulated interface to match the analytical interface, the convection velocity of the Level Set close to the interface should be tangent to the interface. In other words, the direction of the convection velocity should be $\left(r, \frac{\mathrm{d}h}{\mathrm{d}r}\right)$.

In practice, diffusive effects at a such high Reynolds number flows can be sources of mass losses. To account for these biases, we integrated the analytical solution of the liquid profile h. We wrote Δh the vertical displacement of the simulated interface with the analytical value. A corrective velocity $\vec{u}_{\text{cor}}$ was added to the velocity $\vec{u}$ obtained from the Navier-Stokes solver:

$$\vec{u}_{\text{cor}} = \frac{\Delta h}{h} u_z \vec{e_z} \tag{D.43}$$

Thermics The thermics was computed in both phases. In the fluid phase, a convection diffusion equation was solved with the velocity field obtained from the hy-

drodynamics simulation. Properties of the fluid were computed thanks to the Level Set also determined from the hydrodynamics simulation. Regarding the boundary conditions, the bottom of the jet was set to an imposed temperature that depends on the solid surface temperature: if this latter is over T_{sat}, then vaporisation is in play and the temperature is set at T_{sat}. Otherwise, the temperature is set at the solid temperature. This first simulation allow us to obtain a subcooling flux q_∞.

Vaporisation effects are integrated as a boundary condition in the numerical simulation of the solid thermal problem. To do so, a heat flux was imposed that depends on the solid surface temperature:

$$\begin{cases} q_w = q_{\text{cal}} = \dfrac{k_{\text{V}} \Delta T_w}{e(r, T_w)} & \text{for } T_w > T_{\text{MHF}} \quad \text{(D.44)} \\ q_w = q_{\text{nu}} & \text{for } T_w < T_{\text{MHF}} \quad \text{(D.45)} \end{cases}$$

e was computed from the analytical saturated calefaction model of Section D.3, and q_∞ from the thermal computation inside the fluid flow. Attention should be paid on the fact that no subcooling was taken into account during calefaction. In theory, this term should be taken into account in the computation of e. However this entails sophisticated computations. Thus an approximation was made to consider only the saturated term. This assumption is considered acceptable in regards to the modest influence of subcooling on calefaction mode heat fluxes close to the jet according to [155].

Regarding nucleation heat fluxes q_{nu}, the complexity of these phenomena are out of the scope of this work. This is the reason why a correlation taken from [155] was considered and modified to take into account inertial effects of the liquid and vapour convection:

$$q_{\text{nu}} = \underbrace{\left(a \left(\frac{\Delta T_w}{T_{\text{sat}}} \right)^b + q_\infty \right)}_{\text{Corr. from [155]}} \underbrace{\left(1 + A_1 e^{-r/2r_0} \right)}_{\text{inertial effects}} \underbrace{\left(\frac{A_2 (T_w - T_{\text{sat}}) + T_{\text{MHF}} - T_w}{T_{\text{MHF}} - T_{\text{sat}}} \right)}_{\text{vapour convection}} \quad \text{(D.46)}$$

with $b = 2.08$ and $a = 9.36\,\text{MW m}^{-2}$ (values from [155]). Regarding the first correction term, it accounts for the fact that under the jet, the important inertial pressure on the vapour bubbles improves the heat transfer. Nobari et al. [161] observed a ratio of 4 at the same temperature between the heat flux under the jet and far from the jet. This is the reason why A_1 is set to 3. The second correction term accounts for the vapour convection that degrades heat transfer. If we consider one point of the plate in the wetted zone, the closer the local temperature T_w to T_{MHF}, the closer the point to the wetting front, thus the more convected vapour is from the center on this point. In the absence of a better argument, the coefficient A_2 is set arbitrarily. These corrections are a first estimation of the biases of the correlation, and would require a dedicated work to further improve the present model.

The wetting temperature T_{MHF} is deduced from the works of Ohtake et al. [162] who observed that the temperature at the vapour film front T_0 was more or less always around 200 °C for water. However the value of T_{MHF} was observed to be higher on a macroscopic scale. To explain this, we propose the following argument described in Figure D.6. The heat flux at the wetting front is very intense. It requires an important gradient of temperature from the vapour film side to supply the energy evacuated. Considering conductive heat fluxes at the surface of the solid from the wetting point to the point of temperature T_{MHF}:

$$q_{\mathrm{nu}}(T_0) \sim k_{\mathrm{S}} \frac{T_{\mathrm{MHF}} - T_0}{L_{\mathrm{c}}} \tag{D.47}$$

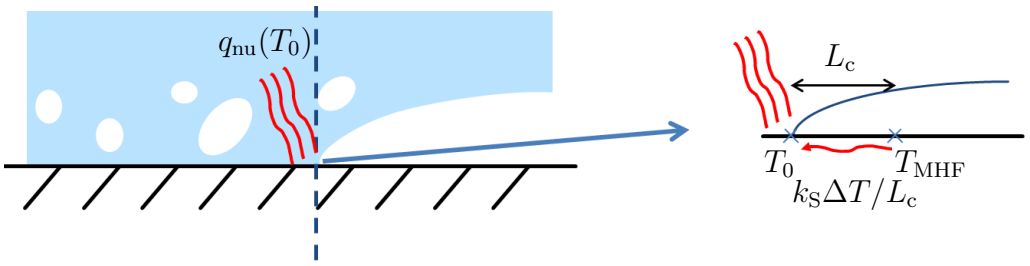

Figure D.6: Schematic description of wetting front. The intense heat flux at the wetting front (for $T = T_0$) is compensate by a diffusive heat flux at the surface of the plate. Thus the "macroscopic" wetting temperature is larger.

This temperature gradient is assumed to exist on a diffusive length $L_{\mathrm{c}} = \sqrt{\dfrac{k_{\mathrm{S}}}{\rho_{\mathrm{S}} c_{\mathrm{PS}} \tau_{\mathrm{c}}}}$ with $\tau_{\mathrm{c}} = \dfrac{u_0}{r_0}$ the characteristic time of the system. This explanation however does not include wetting phenomena that have an important impact of the wetting temperature. Without further analysis, a coefficient A_3 to account for this phenomena is taken. To conclude, the wetting temperature reads:

$$T_{\mathrm{MHF}} = A_3 \left(T_0 + \frac{q_{\mathrm{nu}}(T_0)}{k_{\mathrm{S}}} \sqrt{\frac{k_{\mathrm{S}} r_0}{\rho_{\mathrm{S}} c_{\mathrm{PS}} u_0}} \right) \tag{D.48}$$

D.4.2 Hydrodynamic simulation of the jet

Only a quarter of the liquid jet was simulated. We ran the hydrodynamic simulation on a domain of 50 mm by 50 mm by 30 mm with a cylindrical extension at one corner to include the liquid jet. $1.2{\times}10^6$ elements were considered, with a minimum mesh size $h_{\mathrm{min}} = 0.1$ mm imposed at the liquid air interface. The physical parameters of the simulation are gathered in Table D.3.

	ρ ($\mathrm{kg\,m^{-3}}$)	η ($\mathrm{Pa\,s}$)	c_p ($\mathrm{W\,m^{-1}\,K^{-1}}$)	k ($\mathrm{J\,kg^{-1}\,K^{-1}}$)	γ_0 ($\mathrm{J\,m^{-2}}$)
Liquid	958	1×10^{-2}	4216	0.67	0.06
Air	1	1.0×10^{-4}	2034	0.025	
Solid	8470	-	440	90	

Table D.3: Properties of the liquid, air and solid phases for the water quenching jet simulation.

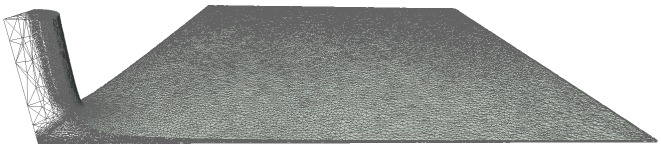

(a) Interface and mesh.

(b) Velocity profile

(c) Temperature profile close at the bottom. The z dimension has been streched by a factor 5 to better see the temperature gradients.

Figure D.7: Simulation results of the quenching jet hydrodynamic simulation. The profile is consistent with experimental observations.

Regarding boundary conditions, free slip conditions were set on the bottom and on the symmetry boundaries. The input velocity u_0 was imposed at the top of the jet. Otherwise zero gauge pressure with free output velocity was set.

The value of A_2 was set to 0.01 to fit the experimental curves (this means a reduction by 100 of the heat transfer efficiency close to the wetting front), and A_3 to 1.01 (a very small deviation in regards to the theoretical estimation of T_{MHF}).

The liquid-air interface, velocity magnitude and temperature fields are shown in Figure D.7. The liquid interface is close to the analytical value. The velocity field is consistent with a null velocity at the jet impact and a constant velocity far from the jet. Finally the temperature gradients are very high with a thin temperature boundary layer which is also consistent with the experiment.

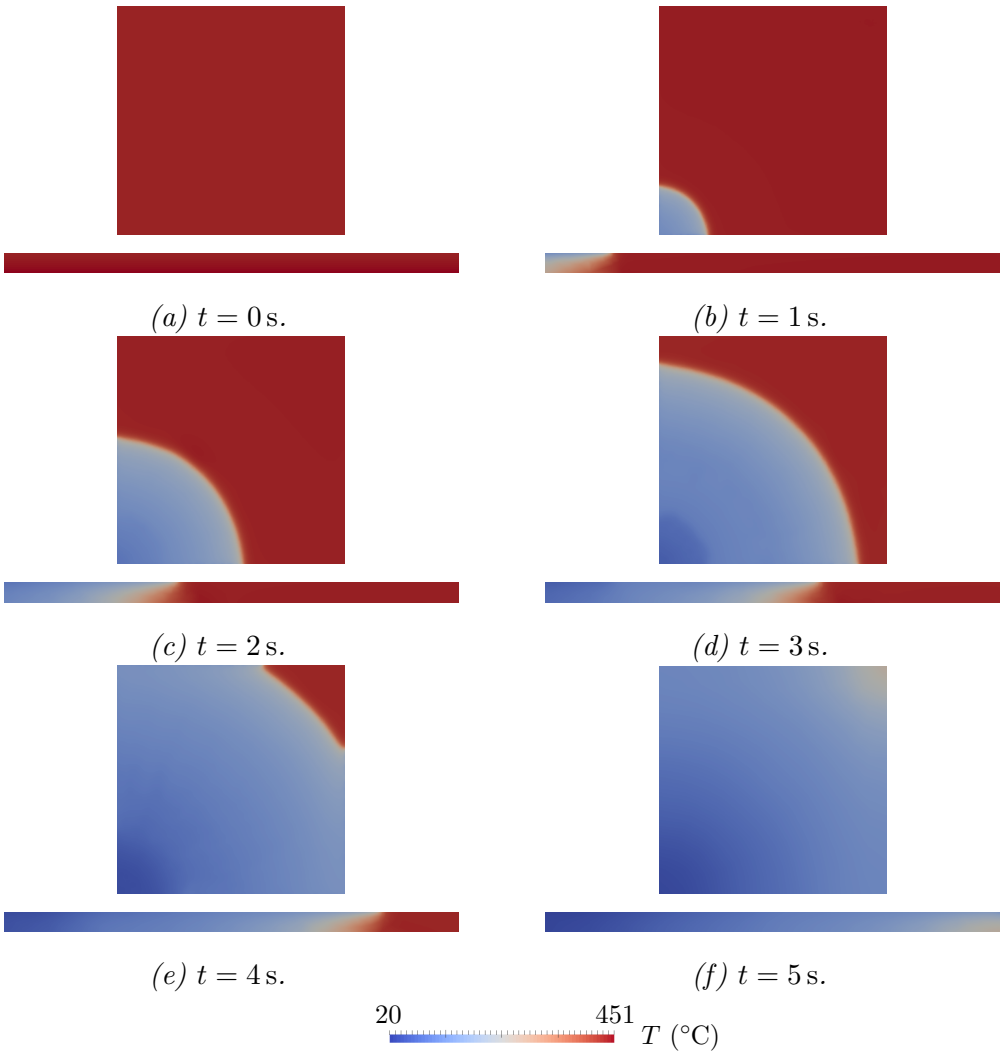

Figure D.8: simulation results of the quenching jet thermics of the plate. The wetting front is the area of great temperature gradient on the top of the plate.

D.4.3 Coupled thermal simulation

The mesh of the last increment of the hydrodynamic simulation was reused for the simulation of thermics inside the fluid. An additional domain of 50 mm by 50 mm by 3 mm was added to simulate the thermics inside the plate. 3×10^5 elements were used inside the solid, with a mesh refinement at the surface of the solid with a minimum mesh size of 0.2 mm. The physical parameters of the simulation are gathered in Table D.3. The boundary conditions inside the solid computational domain are an imposed heat flux at the top, and adiabatic conditions on the other boundaries. In the liquid domain, the temperature was fixed at $\min(T_w, T_{\text{sat}})$ on the bottom at T_∞ on the top. Adiabatic conditions were set on the boundaries of symmetry.

In Figure D.8 the temperature field in the plate on the first times of the simulation is shown. The wetting front is visible, with an important temperature difference before and after the front. The progression of the front is consistent with experimental observations. Three experimental temperature measurements were considered at the surface of the plate: one under the jet and two at 20 mm and 40 mm away from the jet. Temperature variations are compared with the simulation in Figure D.9. The global behavior of the cooling is respected, with proper cooling rates. This result is very satisfactory considering the simplicity of the simulation. This set of parameters shall be challenged in other configurations with varying temperatures and velocities.

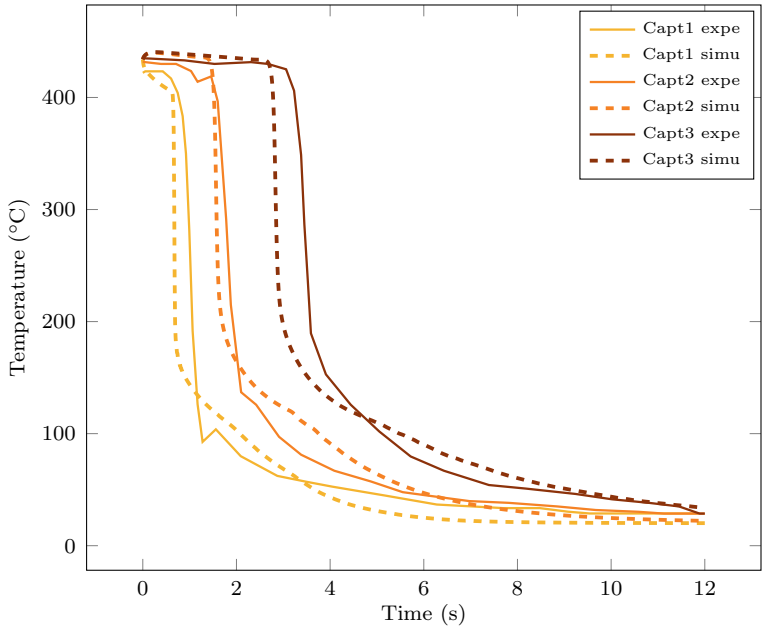

Figure D.9: Comparison of simulated temperatures with experimental values measured

Appendix E

Thermal conductivity of the water vapour

T (°C)	k_V (W m^{-1} K^{-1})
100	0.024
108	0.025
128	0.026
178	0.031
228	0.036
278	0.041
328	0.046
378	0.051
428	0.057
478	0.063
528	0.069
628	0.082
728	0.095
828	0.109
928	0.123
1000	0.14

Table E.1: Thermal conductivity of water vapour at atmospheric pressure (from [89]).

Bibliography

[1] B. Olivier et al. *Chronologie générale du Paléolitique ancien à nos jours* (cit. on p. 3).

[2] M. Radivojević et al. "Tainted ores and the rise of tin bronzes in Eurasia, 6500 years ago". *Antiquity* 87.338 (2013), pp. 1030–1045 (cit. on p. 3).

[3] H. Akanuma. "The Significance of Early Bronze Age Iron Objects from Kaman-Kalehöyük, Turkey". *AAS XVII* (2008), pp. 313–320 (cit. on p. 3).

[4] D. S. Mackenzie. "History of quenching". *International Heat Treatment and Surface Engineering* 2.2 (2008), pp. 68–73 (cit. on p. 4).

[5] G. Murry. "Transformations dans les aciers" (1998), p. 62 (cit. on p. 4).

[6] C. R. Nunura, C. A. dos Santos, and J. A. Spim. "Numerical – Experimental correlation of microstructures, cooling rates and mechanical properties of AISI 1045 steel during the Jominy end-quench test". *Materials & Design* 76 (2015), pp. 230–243 (cit. on pp. 4, 5).

[7] P. Barberis. "Traitements thermiques des alliages de zirconium et de hafnium". *Techniques de l'Ingénieur* M1345 V1 (2018), pp. 1–25 (cit. on p. 7).

[8] P. Archambault, S. Denis, and A. Azim. "Inverse resolution of the heat-transfer equation with internal heat source: Application to the quenching of steels with phase transformations". *Journal of Materials Engineering and Performance* 6.2 (1997), pp. 240–246 (cit. on pp. 8, 9).

[9] G. Ramesh and K. Narayan Prabhu. "Assessment of axial and radial heat transfer during immersion quenching of Inconel 600 probe". *Experimental Thermal and Fluid Science* 54 (2014), pp. 158–170 (cit. on pp. 8, 9, 13, 23, 218).

[10] A. Buczek and T. Telejko. "Investigation of heat transfer coefficient during quenching in various cooling agents". *International Journal of Heat and Fluid Flow* 44 (2013), pp. 358–364 (cit. on pp. 9, 14).

[11] A. Sugianto et al. “A comparative study on determination method of heat transfer coefficient using inverse heat transfer and iterative modification”. *Journal of Materials Processing Technology* 209.10 (2009), pp. 4627–4632 (cit. on p. 9).

[12] C. E. Brennen. *Fundamentals of multiphase flow*. Reprint. OCLC: 316280080. Cambridge: Cambridge Univ. Press, 2006 (cit. on pp. 9, 13, 21, 157).

[13] V. Srinivasan et al. “Numerical simulation of immersion quench cooling process using an Eulerian multi-fluid approach”. *Appl. Therm. Eng.* 30.5 (2010), pp. 499–509 (cit. on pp. 9, 26, 27, 46).

[14] Y. Desalos. “Introduction aux traitements thermiques des métaux et alliages”. *Techniques de l’Ingénieur* M1105 V2 (2003), pp. 1–19 (cit. on p. 9).

[15] S. Nukiyama. “The maximum and minimum values of the heat Q from metal to boilng water under atmospheir pressure”. *Journal of Japan Society of Mechanical Engineering* 37 (1934), pp. 367–374 (cit. on p. 10).

[16] B. Darbois-Texier et al. “La caléfaction”. *Reflets phys.* 37 (2013), pp. 12–16 (cit. on p. 11).

[17] J. Linehard and V. K. Dhir. “Extended hydrodynamic theory of the peak and minimum pool boiling heat fluxes”. *National Aeronautics and Space Administration* CR-2270 (1973), pp. 1–190 (cit. on pp. 12, 19, 20).

[18] P. J. Berenson. *Transition Boiling Heat Transfer from a Horizontal Surface*. Technical Report 17. The National Science Foundation, 1960 (cit. on pp. 12, 19–21, 107, 108, 110–112).

[19] R. Denis. “Modélisation et simulation de l’effet Leidenfrost dans les microgouttes”. PhD thesis. Université de Grenoble, 2014 (cit. on pp. 12, 33, 40, 47, 48, 72).

[20] H. Auracher and W. Marquardt. “Experimental studies of boiling mechanisms in all boiling regimes under steady-state and transient conditions”. *International Journal of Thermal Sciences* 41.7 (2002), pp. 586–598 (cit. on pp. 11, 14).

[21] N. Baudin. “Etude expérimentale et modélisation de l’ébullition transitoire”. PhD thesis. Université de Toulouse, 2015 (cit. on pp. 11, 22, 47).

[22] G. Murry. “Traitements thermiques dans la masse des aciers. Partie 1”. *Techniques de l’Ingénieur* M1126 V1 (2000), pp. 1–25 (cit. on p. 12).

[23] H. Vergara-Hernández and B. Hernández-Morales. “A novel probe design to study wetting front kinematics during forced convective quenching”. *Experimental Thermal and Fluid Science* 33.5 (2009), pp. 797–807 (cit. on p. 13).

[24] H. Jouhara and B. P. Axcell. "Film boiling heat transfer and vapour film collapse on spheres, cylinders and plane surfaces". *Nuclear Engineering and Design* 239.10 (2009), pp. 1885–1900 (cit. on pp. 13, 14, 16, 22, 119, 133, 165, 166, 169, 178).

[25] S. A. Ebrahim et al. "Parametric investigation of film boiling heat transfer on the quenching of vertical rods in water pool". *Applied Thermal Engineering* 140 (2018), pp. 139–146 (cit. on pp. 14, 17, 19–21, 33, 132, 205, 207, 208, 213).

[26] Q. Feng and K. Johannsen. "Experimental results of maximum transition boiling temperature during upflow in a circular tube at medium pressure". *Exp. Therm. Fluid Sci.* 4.1 (1991), pp. 90–102 (cit. on pp. 14, 16, 33).

[27] R. Ikkene, Z. Koudil, and M. Mouzali. "Pouvoir de refroidissement des solutions de trempe à base de polymères hydrosolubles". *CR Chim.* 11.3 (2008), pp. 297–306 (cit. on pp. 14, 16, 33).

[28] I. U. Vakarelski et al. "Stabilization of Leidenfrost vapour layer by textured superhydrophobic surfaces". *Nature* 489.7415 (2012), pp. 274–277 (cit. on pp. 14, 15, 20, 207).

[29] N. Kaneyasu et al. "Effect of surface configuration on nucleate boiling heat transfer". *International Journal of Heat and Mass Transfer* 27.9 (1984), pp. 1559–1571 (cit. on p. 15).

[30] A. H. Howard and I. Mudawar. "Orientation effects on pool boiling critical heat flux (CHF) and modeling of CHF for near-vertical surfaces". *Int. J. Heat Mass Transfer* (1999), pp. 1665–1688 (cit. on pp. 15, 205).

[31] V. K. Dhir. "Boiling Heat Transfer". *Annual Reviews of Fluid Mechanics* 30 (1998), pp. 365–401 (cit. on pp. 15, 16, 18, 19).

[32] H. Ramezanzadeh, A. Ramiar, and M. Yousefifard. "Numerical investigation into coolant liquid velocity effect on forced convection quenching process". *Appl. Therm. Eng.* 122 (2017), pp. 253–267 (cit. on pp. 16, 26, 46).

[33] J. C. Chen. "Correlation for Boiling Heat Transfer to Saturated Fluids in Convective Flow". *Industrial & Engineering Chemistry Process Design and Development* 5.3 (1966), pp. 322–329 (cit. on pp. 17, 18).

[34] V. K. Dhir and S. P. Liaw. "Framework for a Unified Model for Nucleate and Transition Pool Boiling". *Journal of Heat Transfer* 111.3 (1989), pp. 739–746 (cit. on pp. 17, 19).

[35] O. S. Al-Yahia and D. Jo. "Onset of Nucleate Boiling for subcooled flow through a one-side heated narrow rectangular channel". *Annals of Nuclear Energy* 109 (2017), pp. 30–40 (cit. on p. 17).

[36] R. Gaertner and J. Westwater. "Population of Active Sites in Nucleate Boiling Heat Transfer". *Chem. Eng. Progr.* 56 (1960) (cit. on p. 18).

[37] R. Cole. "Bubble frequencies and departure volumes at subatmospheric pressures". *AIChE Journal* 13.4 (1967), pp. 779–783 (cit. on p. 18).

[38] B. B. Mikic and W. M. Rohsenow. "A New Correlation of Pool-Boiling Data Including the Effect of Heating Surface Characteristics". *Journal of Heat Transfer* 91.2 (1969), pp. 245–250 (cit. on pp. 18, 203, 204).

[39] R. L. Judd and K. S. Hwang. "A Comprehensive Model for Nucleate Pool Boiling Heat Transfer Including Microlayer Evaporation". *J. Heat Transfer* 98.4 (1976), pp. 623–629 (cit. on p. 18).

[40] T. Yabuki and O. Nakabeppu. "Heat transfer mechanisms in isolated bubble boiling of water observed with MEMS sensor". *International Journal of Heat and Mass Transfer* 76 (2014), pp. 286–297 (cit. on p. 18).

[41] H. Steiner, A. Kobor, and L. Gebhard. "A wall heat transfer model for subcooled boiling flow". *Int. J. Heat Mass Transfer* 48.19-20 (2005), pp. 4161–4173 (cit. on p. 18).

[42] M. Cooper. "Saturation Nucleate Pool Boiling - A Simple Correlation". *First U.K. National Conference on Heat Transfer*. Elsevier, 1984, pp. 785–793 (cit. on pp. 18, 204, 225).

[43] Z. Liu and R. Winterton. "A general correlation for saturated and subcooled flow boiling in tubes and annuli, based on a nucleate pool boiling equation". *International Journal of Heat and Mass Transfer* 34.11 (1991), pp. 2759–2766 (cit. on pp. 19, 203, 204, 206).

[44] G. Liang and I. Mudawar. "Pool boiling critical heat flux (CHF) – Part 1: Review of mechanisms, models, and correlations". *International Journal of Heat and Mass Transfer* 117 (2018), pp. 1352–1367 (cit. on pp. 19, 205).

[45] N. Zuber. "On the stability of boiling heat transfert". *Trans. Am. Soc. Mech. Engrs.* (1958) (cit. on pp. 19, 203, 205, 206).

[46] S. Kutateladze. "On the transition to film boiling under natural convection". *Kotloturbostroenie* 3 (1948), pp. 10–12 (cit. on p. 19).

[47] H. Sakashita, A. Ono, and J. Nyui. "Critical Heat Flux and Near-Wall Boiling Behaviors in Saturated and Subcooled Pool Boiling on Vertical and Inclined Surfaces". *Journal of Nuclear Science and Technology* 46.11 (2009), pp. 1038–1048 (cit. on p. 19).

[48] V. Yagov. "Physical model and calculation formula for critical heat fluxes with nucleate pool boiling of liquids". *Thermal Engineering (English translation of Teploenergetika)* 35.6 (1988), pp. 333–339 (cit. on p. 19).

[49] J. Galloway and I. Mudawar. "CHF mechanism in flow boiling from a short heated wall—II. Theoretical CHF model". *International Journal of Heat and Mass Transfer* 36.10 (1993), pp. 2527–2540 (cit. on p. 19).

[50] J. M. Ramilison and J. H. Lienhard. "Transition Boiling Heat Transfer and the Film Transition Regime". *J. Heat Transfer* 109.3 (1987), pp. 746–752 (cit. on p. 20).

[51] L. Witte and J. Lienhard. "On the existence of two 'transition' boiling curves". *International Journal of Heat and Mass Transfer* 25.6 (1982), pp. 771–779 (cit. on p. 20).

[52] R. Henry and K. Baumeister. "A correlation for the minimum film boiling temperature". *A.I. Ch. E. Symp. Ser.* 70.138 (1974), pp. 81–90 (cit. on p. 20).

[53] S. Cheng, P. Lau, and K. Poon. "Measurements of true quench temperature of subcooled water under forced convective conditions". *International Journal of Heat and Mass Transfer* 28.1 (1985), pp. 235–243 (cit. on p. 20).

[54] V. Dhir and G. Purohit. "Subcooled film-boiling heat transfer from spheres". *Nuclear Engineering and Design* 47.1 (1978), pp. 49–66 (cit. on pp. 21, 22, 119, 125, 129, 131–133).

[55] R. Kopun et al. "Numerical simulation of immersion quenching process for cast aluminium part at different pool temperatures". *Applied Thermal Engineering* 65.1-2 (2014), pp. 74–84 (cit. on pp. 21, 23, 26, 27, 33, 201, 207, 208).

[56] G. A. Greene and T. F. Irvine. "The effect of water subcooling on film boiling heat transfer from vertical Cylinders" (1994), pp. 940809–940815 (cit. on pp. 21, 132, 203, 207).

[57] R. Vijaykumar and V. K. Dhir. "An Experimental Study of Subcooled Film Boiling on a Vertical Surface—Thermal Aspects". *J. Heat Transfer* 114.1 (1992), p. 169 (cit. on pp. 21, 22, 33, 154–156, 159, 160, 162, 164, 166–174, 178, 182, 184, 186, 187, 189, 191).

[58] V. Klimenko. "Film boiling on a horizontal plate — new correlation". *International Journal of Heat and Mass Transfer* 24.1 (1981), pp. 69–79 (cit. on pp. 21, 107, 108, 110, 112).

[59] N. I. Kolev. "Film boiling on vertical plates and spheres". *Experimental Thermal and Fluid Science* (1998), p. 19 (cit. on p. 22).

[60] K. Nishikawa and T. Ito. "Two-phase boundary-layer treatment of free convection film boiling". *Int. J. Heat Mass Transfer* (1966), p. 13 (cit. on p. 22).

[61] R. Vijaykumar and V. K. Dhir. "An Experimental Study of Subcooled Film Boiling on a Vertical Surface—Hydrodynamic Aspects". *J. Heat Transfer* 114.1 (1992), p. 161 (cit. on pp. 22, 154–156, 159–162, 164–167, 173, 174, 191).

[62] P. K. Meduri, G. R. Warrier, and V. K. Dhir. "Wall heat flux partitioning during subcooled forced flow film boiling of water on a vertical surface". *Int. J. Heat Mass Transfer* 52.15-16 (2009), pp. 3534–3546 (cit. on pp. 22, 33, 174).

[63] D. C. Das, K. Ghosh, and D. Sanyal. "A scale analysis model for film boiling heat transfer on a vertical flat plate with wide applicability". *Int. J. Heat Mass Transfer* 90 (2015), pp. 40–48 (cit. on p. 22).

[64] W. H. Lee. "A Pressure Iteration Scheme for Two-Phase Flow Modeling". *Math. Mod.* (1980), pp. 61–82 (cit. on pp. 24, 46, 48, 69).

[65] A. S. Rattner and S. Garimella. "Simple Mechanistically Consistent Formulation for Volume-of-Fluid Based Computations of Condensing Flows". *J. Heat Transfer* 136.7 (2014) (cit. on pp. 24, 41, 46, 48).

[66] G. Son and V. K. Dhir. "Numerical Simulation of Film Boiling Near Critical Pressures With a Level Set Method". *J. Heat Transfer* 120.1 (1998), pp. 183–192 (cit. on pp. 24, 41, 48, 69).

[67] D. Juric. "Computations of Boiling Flows". *International Journal of Multiphase Flow* (1998), pp. 387–410 (cit. on pp. 24, 41, 48, 69).

[68] S. W. Welch and J. Wilson. "A Volume of Fluid Based Method for Fluid Flows with Phase Change". *J. Comput. Phys.* 160.2 (2000), pp. 662–682 (cit. on pp. 24, 25, 41, 47, 48, 69, 107).

[69] Y. Sato and B. Ničeno. "A sharp-interface phase change model for a mass-conservative interface tracking method". *J. Comput. Phys.* 249 (2013), pp. 127–161 (cit. on pp. 25, 47, 58, 69).

[70] M. Kang, R. P. Fedkiw, and X.-D. Liu. "A Boundary Condition Capturing Method for Multiphase Incompressible Flow". *Journal of Scientific Computing* (2000), pp. 323–360 (cit. on pp. 24, 41, 48, 69).

[71] F. Gibou et al. "A level set based sharp interface method for the multiphase incompressible Navier–Stokes equations with phase change". *Journal of Computational Physics* 222.2 (2007), pp. 536–555 (cit. on pp. 24, 41, 48, 69).

[72] S. Tanguy, T. Ménard, and A. Berlemont. "A Level Set Method for vaporizing two-phase flows". *J. Comput. Phys.* 221.2 (2007), pp. 837–853 (cit. on pp. 24, 41, 48, 69).

[73] A. Esmaeeli and G. Tryggvason. "Computations of film boiling. Part I: numerical method". *International Journal of Heat and Mass Transfer* 47.25 (2004), pp. 5451–5461 (cit. on pp. 24, 48, 69, 107).

[74] N. Kumar Singh and B. Premachandran. "A coupled level set and volume of fluid method on unstructured grids for the direct numerical simulations of two-phase flows including phase change". *Int. J. Heat Mass Transfer* 122 (2018), pp. 182–203 (cit. on pp. 25, 48).

[75] G. Anjos et al. "3D ALE Finite-Element Method for Two-Phase Flows With Phase Change". *Heat Transfer Eng.* 35.5 (2014), pp. 537–547 (cit. on pp. 25, 41, 48).

[76] R. T. Lahey and D. A. Drew. "The analysis of two-phase flow and heat transfer using a multidimensional, four field, two-fluid model". *Nucl. Eng. Des.* 204.1-3 (2001), pp. 29–44 (cit. on pp. 25, 48).

[77] P. Bristiel and N. T. Niane. "Simulation numérique des traitements thermochimiques : applications industrielles". *Techniques de l'Ingénieur* IN209 V1 (2013), pp. 1–24 (cit. on p. 26).

[78] V. Srinivasan et al. "Numerical simulation of immersion quenching process of an engine cylinder head". *Applied Mathematical Modelling* 34.8 (2010), pp. 2111–2128 (cit. on p. 26).

[79] T. Bo. "CFD Homogeneous Mixing Flow Modelling to Simulate Subcooled Nucleate Boiling Flow". *J. Soc. Automot. Eng.* (2004) (cit. on pp. 26, 46).

[80] M. Khalloufi. "Multiphase flows with phase change and boiling in quenching processes". PhD thesis. Mines ParisTech, 2018 (cit. on pp. 27, 28, 49, 50, 74, 79, 107, 109, 208).

[81] M. Khalloufi, R. Valette, and E. Hachem. "Adaptive Eulerian framework for boiling and evaporation". *J. Comput. Phys.* 401 (2020), p. 109030 (cit. on pp. 27, 47).

[82] E. Hachem et al. "Stabilized finite element method for incompressible flows with high Reynolds number". *J. Comput. Phys.* 229.23 (2010), pp. 8643–8665 (cit. on pp. 28, 49, 50, 73, 74).

[83] E. Hachem et al. "Immersed stress method for fluid-structure interaction using anisotropic mesh adaptation: a monolithic approach to fluid-structure interaction". *Int. J. Numer. Meth. Engng* 94.9 (2013), pp. 805–825 (cit. on pp. 28, 94).

[84] T. Coupez and E. Hachem. “Solution of high-Reynolds incompressible flow with stabilized finite element and adaptive anisotropic meshing”. *Computer methods in applied mechanics and engineering* 267 (2013). Publisher: Elsevier, pp. 65–85 (cit. on pp. 28, 73).

[85] R. Valette et al. “Viscoplastic dam-breaks”. *Journal of Non-Newtonian Fluid Mechanics* 287 (2021). Publisher: Elsevier, p. 104447 (cit. on p. 28).

[86] I. Berton et al. “Theoretical and experimental study of the flow of a molten polymer in a micro-compounder”. *Polymer Engineering & Science* 61.12 (2021). Publisher: Wiley Online Library, pp. 3135–3146 (cit. on p. 28).

[87] B. Liscic, H. M. Tensi, and W. Luty. *Theory and Technology of Quenching*. 1992 (cit. on p. 33).

[88] J. Kim, J. F. Benton, and D. Wisniewski. “Pool boiling heat transfer on small heaters: effect of gravity and subcooling”. *Int. J. Heat Mass Transfer* 45.19 (2002), pp. 3919–3932 (cit. on p. 33).

[89] W. M. Haynes. “CRC Handbook of Chemistry and Physics” (2016), p. 2643 (cit. on pp. 33, 36, 37, 70, 140, 178, 196, 209, 261).

[90] E. Guggenheim. *Thermodynamics - An Advanced Treatment for Chemists and Physicists*. Seventh edition. 1985 (cit. on p. 35).

[91] S. O. Unverdi and G. Tryggvason. “A Front-Tracking Method for Viscous, Incompressible, Multi-fluid Flows”. *J. Comput. Phys.* (1992), pp. 25–37 (cit. on pp. 41, 45).

[92] H. S. Udaykumar, W. Shyy, and M. M. Rao. “Elafint: a mixed Eulerian–Lagrangian method for fluid flows with complex and moving boundaries”. *International journal for numerical methods in fluids* 22.8 (1996). Publisher: Wiley Online Library, pp. 691–712 (cit. on p. 41).

[93] J. Glimm et al. “Simple front tracking”. *Contemporary mathematics* 238.2 (1999), pp. 133–149 (cit. on p. 41).

[94] J. Brackbill, D. Kothe, and C. Zemach. “A continuum method for modeling surface tension”. *Journal of Computational Physics* 100.2 (1992), pp. 335–354 (cit. on pp. 41, 79).

[95] S. Osher and R. P. Fedkiw. “Level set methods: an overview and some recent results”. *Journal of Computational physics* 169.2 (2001). Publisher: Elsevier, pp. 463–502 (cit. on p. 41).

[96] S. Osher and R. Fedkiw. *Level set methods and dynamic implicit surfaces*. Vol. 153. Applied Mathematical Sciences. Springer, 2004 (cit. on pp. 41, 46).

[97] S. Florez et al. “A new finite element strategy to simulate microstructural evolutions”. *Computational Materials Science* 172 (2020), p. 109335 (cit. on p. 43).

[98] C. Bahbah. “Méthodes numériques avancées pour la simulation du procédé de trempe industrielle”. PhD thesis. PSL Research University, 2019 (cit. on pp. 43, 44).

[99] M. Shakoor et al. “An efficient and parallel level set reinitialization method - Application to micromechanics and microstructural evolutions”. *Appl. Math. Mod.* (2014) (cit. on pp. 44, 86).

[100] M. Shakoor, P.-O. Bouchard, and M. Bernacki. “An adaptive level-set method with enhanced volume conservation for simulations in multiphase domains”. *International Journal for Numerical Methods in Engineering* 109.4 (2017). Publisher: Wiley Online Library, pp. 555–576 (cit. on p. 44).

[101] T. Coupez, L. Silva, and E. Hachem. “Implicit boundary and adaptive anisotropic meshing”. *New challenges in grid generation and adaptivity for scientific computing*. Springer, 2015, pp. 1–18 (cit. on p. 44).

[102] S. V. Patankar. *Numerical heat transfer and fluid flow*. Series in computational methods in mechanics and thermal sciences. OCLC: 31743097. New York: Hemisphere Publ. Co, 1980 (cit. on p. 44).

[103] E. Hachem et al. “Stabilized finite element solution to handle complex heat and fluid flows in industrial furnaces using the immersed volume method”. *Int. J. Numer. Meth. Fluids* 68.1 (2010), pp. 99–121 (cit. on pp. 44, 73, 74).

[104] M. Sussman, P. Smereka, and S. Osher. “A Level Set Approach for Computing Solutions to Incompressible Two-Phase Flows”. *J. Comput. Phys.* 114 (1994), pp. 146–159 (cit. on p. 46).

[105] S. Tanguy et al. “Benchmarks and numerical methods for the simulation of boiling flows”. *J. Comput. Phys.* 264 (2014), pp. 1–22 (cit. on pp. 46, 47, 58, 107).

[106] M. Khalloufi et al. “High fidelity anisotropic adaptive variational multiscale method for multiphase flows with surface tension”. *Comput. Method Appl. M.* 307 (2016), pp. 44–67 (cit. on p. 46).

[107] M. Li and I. A. Bolotnov. “Interface Tracking Simulation of Phase-Change Phenomena: Boiling and Condensation Verification”. Washington, DC, USA: American Society of Mechanical Engineers, 2016 (cit. on p. 47).

[108] D. Sun, J. Xu, and Q. Chen. “Modeling of the Evaporation and Condensation Phase-Change Problems with FLUENT”. *Numer. Heat Tr. B-Fund.* 66.4 (2014), pp. 326–342 (cit. on p. 47).

[109] S. Badia and R. Codina. "Analysis of a stabilized finite element approximation of the transient convection-diffusion equation using an ALE framework". *SIAM Journal on Numerical Analysis* 44.5 (2006). Publisher: SIAM, pp. 2159–2197 (cit. on pp. 49, 50).

[110] R. Codina. "Comparison of some finite element methods for solving the diffusion-convection-reaction equation". *Computer methods in applied mechanics and engineering* 156.1-4 (1998). Publisher: Elsevier, pp. 185–210 (cit. on pp. 49, 50).

[111] A. C. Galeão and E. G. D. Do Carmo. "A consistent approximate upwind Petrov-Galerkin method for convection-dominated problems". *Computer Methods in Applied Mechanics and Engineering* 68.1 (1988). Publisher: Elsevier, pp. 83–95 (cit. on pp. 49, 50).

[112] A. N. Brooks and T. J. Hughes. "Streamline upwind/Petrov-Galerkin formulations for convection dominated flows with particular emphasis on the incompressible Navier-Stokes equations". *Computer methods in applied mechanics and engineering* 32.1-3 (1982). Publisher: Elsevier, pp. 199–259 (cit. on pp. 49, 50, 73).

[113] T. J. Hughes, L. P. Franca, and M. Balestra. "A new finite element formulation for computational fluid dynamics: V. Circumventing the Babuška-Brezzi condition: A stable Petrov-Galerkin formulation of the Stokes problem accommodating equal-order interpolations". *Computer Methods in Applied Mechanics and Engineering* 59.1 (1986). Publisher: Elsevier, pp. 85–99 (cit. on pp. 49, 50).

[114] T. D. Aslam. "A partial differential equation approach to multidimensional extrapolation". *J. Comput. Phys.* 193.1 (2004), pp. 349–355 (cit. on p. 50).

[115] D. G. Kim, C. H. Jeon, and I. S. Park. "Comparison of numerical phase-change models through Stefan vaporizing problem". *Int. Commun. Heat Mass* 87 (2017), pp. 228–236 (cit. on p. 58).

[116] G. Giustini and R. I. Issa. "A method for simulating interfacial mass transfer on arbitrary meshes". *Physics of Fluids* 33.8 (2021), p. 087102 (cit. on p. 58).

[117] E. Hachem. "Stabilized finite element method for heat transfer and turbulent flows inside industrial furnaces". PhD Thesis. Mines ParisTech, 2009 (cit. on pp. 73–75).

[118] E. Hachem et al. "Unified adaptive Variational MultiScale method for two phase compressible–incompressible flows". *Comput. Method Appl. M.* 308 (2016), pp. 238–255 (cit. on pp. 73, 74).

[119] F. Brezzi and J. Douglas. "Stabilized mixed methods for the Stokes problem". *Numerische Mathematik* 53.1 (1988). Publisher: Springer, pp. 225–235 (cit. on p. 73).

[120] L. P. Franca and T. J. Hughes. "Two classes of mixed finite element methods". *Computer Methods in Applied Mechanics and Engineering* 69.1 (1988). Publisher: Elsevier, pp. 89–129 (cit. on p. 73).

[121] R. Codina et al. "Finite element approximation of the modified Boussinesq equations using a stabilized formulation". *International Journal for Numerical Methods in Fluids* 57.9 (2008). Publisher: Wiley Online Library, pp. 1249–1268 (cit. on p. 73).

[122] J. Sari et al. "Anisotropic adaptive stabilized finite element solver for RANS models". *International Journal for Numerical Methods in Fluids* 86.11 (2018). Publisher: Wiley Online Library, pp. 717–736 (cit. on p. 74).

[123] S. Hysing. "A new implicit surface tension implementation for interfacial flows". *International Journal for Numerical Methods in Fluids* 51.6 (2006). Publisher: Wiley Online Library, pp. 659–672 (cit. on p. 79).

[124] M. Raessi, M. Bussmann, and J. Mostaghimi. "A semi-implicit finite volume implementation of the CSF method for treating surface tension in interfacial flows". *International journal for numerical methods in fluids* 59.10 (2009). Publisher: Wiley Online Library, pp. 1093–1110 (cit. on p. 79).

[125] F. Denner and B. G. van Wachem. "Numerical time-step restrictions as a result of capillary waves". *Journal of Computational Physics* 285 (2015), pp. 24–40 (cit. on pp. 79, 82, 83).

[126] T. Coupez. "Metric construction by length distribution tensor and edge based error for anisotropic adaptive meshing". *Journal of computational physics* 230.7 (2011). Publisher: Elsevier, pp. 2391–2405 (cit. on p. 94).

[127] J. Dolbow and I. Harari. "An efficient finite element method for embedded interface problems". *Int. J. Numer. Meth. Engng* 78.2 (2009), pp. 229–252 (cit. on p. 107).

[128] R. Gracie, H. Wang, and T. Belytschko. "Blending in the extended finite element method by discontinuous Galerkin and assumed strain methods". *Int. J. Numer. Meth. Engng* 74.11 (2008), pp. 1645–1669 (cit. on p. 107).

[129] M. W. Akhtar and S. J. Kleis. "Boiling flow simulations on adaptive octree grids". *International Journal of Multiphase Flow* 53 (2013), pp. 88–99 (cit. on pp. 107, 109).

[130] E. R. Hosler and J. W. Westwater. "Film Boiling on a Horizontal Plate". *ARS Journal* 32.4 (1962), pp. 553–558 (cit. on p. 111).

[131] M. K. Tripathi, K. C. Sahu, and R. Govindarajan. "Dynamics of an initially spherical bubble rising in quiescent liquid". *Nat Commun* 6.1 (2015), p. 6268 (cit. on pp. 111, 135).

[132] R. A. Burns. "Heat transfer studies with application to nuclear reactors". PhD thesis. The University of Manchester (United Kingdom), 1989 (cit. on p. 120).

[133] S. Whitaker. "Forced convection heat transfer correlations for flow in pipes, past flat plates, single cylinders, single spheres, and for flow in packed beds and tube bundles". *AIChE Journal* 18.2 (1972). Publisher: Wiley Online Library, pp. 361–371 (cit. on p. 130).

[134] A. Movaghar et al. "A Subgrid-Scale Model for Large-Eddy Simulation of Liquid/Gas Interfaces Based on One-Dimensional Turbulence". *Turbulent Cascades II*. Springer, 2019, pp. 83–91 (cit. on p. 141).

[135] R. Chiodi, J. McCaslin, and O. Desjardins. "Interactions Between Turbulence and Interfaces with Surface Tension". *Turbulent Cascades II*. Springer, 2019, pp. 249–256 (cit. on p. 141).

[136] T. D. Bui and V. K. Dhir. "Film Boiling Heat Transfer on an Isothermal Vertical Surface". *Journal of Heat Transfer* 107.4 (1985), pp. 764–771 (cit. on pp. 155, 161, 169, 170, 176, 191).

[137] E. M. Greitzer and F. H. Abernathy. "Film Boiling on vertical surfaces". *Int. J. Heat Mass Transfer* (1972), pp. 475–491 (cit. on pp. 160, 161, 171).

[138] J. R. Landel, C. Cossu, and C. P. Caulfield. "Spherical cap bubbles with a toroidal bubbly wake". *Physics of Fluids* 20.12 (2008), p. 122101 (cit. on p. 161).

[139] D. C. Sherman. "Natural convection film boiling on a vertical surface". PhD thesis. California Institute of Technology, 1980 (cit. on pp. 164, 165).

[140] H. S. Carslaw and J. C. Jaeger. *Conduction of heat in solids*. Tech. rep. Clarendon press, 1959 (cit. on p. 198).

[141] H. D. Mendelson. "The prediction of bubble terminal velocities from wave theory". *AIChE J.* 13.2 (1967), pp. 250–253 (cit. on pp. 203, 204).

[142] I. P. Vishnev. "Effect of orienting the hot surface with respect to the gravitational field on the critical nucleate boiling of a liquid". *Journal of Engineering Physics* 24.1 (1973), pp. 43–48 (cit. on pp. 203, 205, 206).

[143] M. J. Brusstar and H. Merte. "Effects of heater surface orientation on the critical heat flux—II. A model for pool and forced convection subcooled boiling". *International Journal of Heat and Mass Transfer* 40.17 (1997), pp. 4021–4030 (cit. on pp. 203, 205, 206).

[144] Y. S. Touloukian and D. P. DeWitt. *Thermal Radiative Properties*. Boston, MA: Springer US, 1970 (cit. on pp. 225, 228).

[145] M. Vigneron and M. Stolz. "Influence du Rayonnement des Gaz Dans les Calculs D'échangeurs de Chaleur". *La Houille Blanche* 43.1 (1957), pp. 50–58 (cit. on pp. 226, 227).

[146] *Hitran on the Web* (cit. on p. 227).

[147] M. J. Weber. *Handbook of optical materials*. The CRC Press laser and optical science and technology series. Boca Raton: CRC Press, 2003 (cit. on p. 228).

[148] H. Rubens and E. Ladenburg. "Les propriétés optiques de l'eau dans le spectre infra-rouge". *Radium (Paris)* 6.2 (1909), pp. 33–39 (cit. on p. 228).

[149] J. E. Bertie and Z. Lan. "Infrared Intensities of Liquids XX: The Intensity of the OH Stretching Band of Liquid Water Revisited, and the Best Current Values of the Optical Constants of H20(I) at 25 degC between 15,000 and 1 cm -1" (1996), p. 11 (cit. on pp. 228, 229).

[150] N. Karwa et al. "Experimental investigation of circular free-surface jet impingement quenching: Transient hydrodynamics and heat transfer". *Experimental Thermal and Fluid Science* 35.7 (2011), pp. 1435–1443 (cit. on p. 243).

[151] L. Bogdanic, H. Auracher, and F. Ziegler. "Two-phase structure above hot surfaces in jet impingement boiling". *Heat Mass Transfer* 45.7 (2009), pp. 1019–1028 (cit. on pp. 243, 249, 254).

[152] C. Agrawal et al. "Determination of rewetting on hot horizontal surface with water jet impingement through a sharp edge nozzle". *International Journal of Thermal Sciences* 71 (2013), pp. 310–323 (cit. on pp. 243, 244).

[153] D. Vader, F. Incropera, and R. Viskanta. "Local convective heat transfer from a heated surface to an impinging, planar jet of water". *International Journal of Heat and Mass Transfer* 34.3 (1991), pp. 611–623 (cit. on p. 244).

[154] N. Karwa and P. Stephan. "Experimental investigation of free-surface jet impingement quenching process". *International Journal of Heat and Mass Transfer* 64 (2013), pp. 1118–1126 (cit. on p. 244).

[155] A. Omar, M. Hamed, and M. Shoukri. "Modeling of nucleate boiling heat transfer under an impinging free jet". *International Journal of Heat and Mass Transfer* 52.23-24 (2009), pp. 5557–5566 (cit. on pp. 244, 256).

[156] R. Dou et al. "Experimental study on heat-transfer characteristics of circular water jet impinging on high-temperature stainless steel plate". *Applied Thermal Engineering* 62.2 (2014), pp. 738–746 (cit. on p. 244).

[157] M. Hamide, J.-L. Borean, and P. Gardin. "CFD modeling of water jet cooling processes". 2011, pp. 1–6 (cit. on pp. 244, 254).

[158] T. Bohr, P. Dimon, and V. Putkaradze. “Shallow-water approach to the circular hydraulic jump”. *J. Fluid Mech.* 254 (1993), pp. 635–648 (cit. on p. 247).

[159] F. Homann. “Der Einfluß großer Zähigkeit bei der Strömung um den Zylinder und um die Kugel”. *Z. angew. Math. Mech.* 16.3 (1936), pp. 153–164 (cit. on p. 247).

[160] W. Timm, K. Weinzierl, and A. Leipertz. “Heat transfer in subcooled jet impingement boiling at high wall temperatures”. *International Journal of Heat and Mass Transfer* 46.8 (2003), pp. 1385–1393 (cit. on p. 247).

[161] A. H. Nobari, V. Prodanovic, and M. Militzer. “Heat transfer of a stationary steel plate during water jet impingement cooling”. *International Journal of Heat and Mass Transfer* 101 (2016), pp. 1138–1150 (cit. on p. 256).

[162] H. Ohtake and Y. Koizumi. “Study on propagative collapse of a vapor film in film boiling (mechanism of vapor-film collapse at wall temperature above the thermodynamic limit of liquid superheat)”. *International Journal of Heat and Mass Transfer* 47.8-9 (2004), pp. 1965–1977 (cit. on p. 257).

RÉSUMÉ

L'ébullition est un mode d'extraction de chaleur efficace utilisé dans nombre de procédés industriels dont la trempe. La trempe consiste à plonger une pièce de métal chaude dans un fluide pour la faire refroidir rapidement. Cette opération permet d'obtenir des microstructures possédant d'excellentes propriétés mécaniques, à condition de bien contrôler le refroidissement de la pièce. Les échanges de chaleur étant gouvernés par le comportement du fluide, il est donc essentiel de bien comprendre les mécanismes d'ébullition.
Cette thèse est intégrée à la chaire industrielle INFinity qui réunit un consortium de douze industriels désirant accroitre leurs compréhension de la trempe. Pour répondre à leur besoin, une approche par simulation numérique des écoulements fluides (CFD) est employée. C'est un outil puissant qui permet la représentation virtuelle des phénomènes physiques en jeu. Appliquée à des cas industrielle, la CFD permet d'anticiper la plupart des problématiques du procédé, et ainsi d'éviter de nombreux essais expérimentaux. Ce travail s'est donc concentré sur le développement d'un outil de simulation de trempe à échelle industrielle. Pour ce faire, la démarche se décompose en quatre étapes: (i) analyser les phénomènes physiques prépondérants afin de simplifier le problème étudiée, (ii) implémenter un modèle Éléments Finis qui résout les écoulement multiphasiques avec changement de phase, (iii) valider ce modèle en simulant le mode de caléfaction lors de la trempe d'une sphère et en ébullition par film vertical, et (iv) enrichir le modèle pour envisager tous les modes d'ébullition afin d'aboutir à un outil complet de modélisation de trempe à usage industriel.
Un travail analytique sur les équations de conservation de la masse, de la quantité de mouvement et de l'énergie dans le cadre de la trempe est présenté. En découle un travail numérique qui a mené à un outil basé sur la méthode Level Set et l'approche Continuous Surface Force. Ce modèle est validé sur différents cas tests 2D et 3D de complexités croissantes. Un travail expérimental sur l'étude de la trempe de billes de nickel a permis de compléter cette approche. Enfin des validations sur un cas académique plus complexe et sur deux cas industriels sont présentées avec une discussion sur les hypothèses et la validité du modèle.

MOTS CLÉS

Ébullition, Caléfaction, Trempe, Écoulements multiphasiques, Changement de phase, Vaporisation, Éléments Finis, Méthode Level Set, Approche Continuous Surface Force.

ABSTRACT

Boiling is an efficient way of extracting heat from a solid. It is used in many industrial processes among which quenching. Quenching consists in the rapid cooling of a metallic part inside a fluid in order to improve the material properties of the microstructure. The control of the temperature variations is of great importance in this process. Thus, the understanding of boiling is fundamental as it drives the cooling rate.
This thesis is part of the industrial Chair INFinity that gathers a consortium of twelve companies. They share a common will to improve their knowledge on quenching thanks to numerical simulation. Computational Fluid Dynamics (CFD) is a solution to reduce the number of full scale experiments for every new quenched part, as well as to provide a powerful tool describing the underlying physics. We thus aimed at developing a tool to simulate the quenching process at an industrial scale. To do so, different aspects have be studied: (i) analyse the most important features of boiling to simplify the problem, (ii) implement a numerical Finite Element framework to properly simulate multiphase systems with phase change, (iii) challenge the model with the simulation of film boiling on a sphere quenching experiment and on a vertical film boiling benchmark and (iv) enrich the model to account for all boiling modes and to implement a quenching model that can handle industrial applications.
An analytical work on the mass, momentum and energy conservation equations in the context of quenching is proposed. A numerical work is tackled to develop a tool based on a Level Set framework and a Continuous Surface Force approach. Validations are then done on 2D and 3D benchmarks of increasing complexities. An experimental work on the quenching of mall nickel spheres has been done. Validations on academic and industrial benchmarks with discussion on the assumptions and the validity of the model are presented.

KEYWORDS

Boiling, Calefaction, Quenching processes, Multiphase flows, Phase Change, Vaporisation, Finite Element Method, Level Set method, Continuous Surface Force approach.